Novel polymer-nanocomposites for enhanced oil recovery

Maje Alhaji Haruna

Submitted in accordance with the requirements for the degree of

Doctor of Philosophy

The University of Leeds
School of Chemical and Process Engineering

December 2019

Declaration

The candidate confirms that the work submitted is his own, except where work which has formed part of jointly-authored publications has been included. The contribution of the candidate and the other authors to this work has been explicitly indicated in the list of publications section. The candidate confirms that appropriate credit has been given within the thesis where reference has been made to the work of others.

Aknowledgement

I would like to express my deepest gratitude to my supervisor Professor Dongsheng Wen for his continued encouragement, guidance, and support for the realization of this research work. His timely and efficient feedback, suggestions, and supervision helped me shape this work into its final form.

I would like to thank the Petroleum Technology Development Funds (PTDF), Nigeria for providing the full funding to undertake this program. I am also extremely grateful to the School of Chemical and Process Engineering at the University of Leeds for providing me with all the facilities to carry out my research.

I would like to take this opportunity to thank Professor Fan Xianfeng (external examiner) and Associate Professor David Harbottle (internal examiner) for their very helpful feedback, suggestions, and comments during the viva.

I am thankful to Professor Jun Zhang, and other team members at Beihang University, Beijing for all the necessary support when I was there for a research visit. My sincere thanks go to the British Council for sponsoring the visit under Newton Funds Grants.

I gratefully acknowledge Dr. David Harbottle and Dr. Xiaodong Jia for their valuable feedback and suggestions during my 1st year transfer viva and 2nd year exam, respectively. I am very thankful to Dr. Saminu Musa Magami for his keen advice from the start to the end of this project.

I am also thankful to the technical support team of Peter Dawson, Dr. Adriane Cunliffe, Mr. David Instrell, Mrs. Karine Alves Thorne, Mr. Stuart Micklethwaite, Dr. Zabeada Aslam, Dr. Ben Douglas, and all the technicians at the University of Leeds who have supported by work.

I am also thankful to Dr. David Harbottle, Dr. Nicole Hondow, and Dr. Nicolas Warren and their students for their support and availing of their facilities to conduct some part of my laboratory experiment.

I also acknowledge the support from Mr. Shahid Pervaiz and Dr. Hui Gao for their continued help and support in the process of synthesis of the nanoparticles used in this work. Heartfelt thanks go to all PhD students and PDRAs whom I worked with during my research at the University of Leeds, in particular, Dr. Jabbar Gardy for his advice and help in the characterization of different prepared materials, Dr. Zhongliang Hu for his great job in setting-up the core-flooding equipment, Dr. Eric Danso-Boateng, Dr. Ehsan Nourafkan, Dr. Antonios Anastasiou, Dr. Muhammad Amjad, Dr. Guice Yao, Mr. Evangelos Daskalakis for their support, great atmosphere and many years of friendship.

I am also thankful to all our research group members for their motivation, acknowledgement, and appreciation of my work.

I am much indebted to all my friends such as Miss Ghinwa Yaghi, Dr. Habib Muhammad, Dr. Muhammad Reza, Mr. Jian Zhai, Dr. Mick Tangparitkul, Mr. Usman Adam Abdullahi, Mr. Idris Amin, Miss Bintu Mustapha and all those who directly or indirectly played a role in the completion of this work that I forgot to mention their names.

Finally, I am always indebted to all my family members for their understanding of the importance of this work and supporting me in all ups and downs with encouragement, love, patience, and prayers. I place on record, my sincere gratitude to my parents, my wife, Maryam, and my daughter Maryam junior (Ummi), for their patience, prayers, moral support, and consistent encouragement throughout my work. This thesis would not have been possible without their help and support.

Dedication

This work is dedicated to my lovely parents, wife and daughter, supervisors, and all friends and family for their constant support and encouragement while carrying out this research.

List of Publications

The work in this project has appeared in the following publications:

- **Maje Alhaji Haruna,** and Dongsheng Wen., 2019. Stabilization of Polymer Nanocomposites in High-Temperature and High-Salinity Brines. *ACS Omega*, *4*(7), pp.11631-11641.

The candidate as a primary author of this publication performed all the experiments and led the drafting of the publication. Dongsheng Wen supervised the work, gave intensive suggestions in explaining the results, and finalizing the paper.

- **Maje Alhaji Haruna**, Zhonglinag Hu, Hui Gao, Jabbar Gardy, Saminu Musa Magami, and Dongsheng Wen, 2019. Influence of carbon quantum dots on the viscosity reduction of polyacrylamide solution. *Fuel*, *248*, pp.205-214.

The candidate as a primary author of this publication performed all the experiments and led the drafting of the publication. Zhonglinag Hu and Hui Gao helped in the synthesis of carbon quantum dots, Jabbar Gardy Helped with TGA measurement and analysis. Saminu Musa Magami improved the review and helped in determining the mechanism for viscosity reduction. Dongsheng Wen supervised the work, gave intensive suggestions in explaining the results, and finalizing the paper.

- **Maje Alhaji Haruna,** Ehsan Nourafkan, Zhongliang Hu, and Dongsheng Wen 2019. Improved Polymer Flooding in Harsh Environments by Free-Radical Polymerization and the Use of Nanomaterials. *Energy & fuels*, *33*(2), pp.1637-1648.

The candidate as a primary author of this publication performed all the experiments and led the drafting of the publication. Ehsan Nourafkan helped in the synthesis of polymers, Zhongliang Hu helped in the core flooding experimental set-up. Dongsheng Wen supervised the work, gave intensive suggestions in explaining the results, and finalizing the paper.

- **Maje Alhaji Haruna,** Zhongliang Hu, Ehsan Nourafkan, and Dongsheng Wen 2019. Improved rheology and high-temperature stability of hydrolyzed polyacrylamide using graphene oxide nanosheet. *Journal of Applied Polymer Science*, *136*(22), p.47582.

The candidate as a primary author of this publication performed all the experiments and led the drafting of the publication. Ehsan Nourafkan and Zhongliang Hu helped to improve the review. Dongsheng Wen supervised the work, gave intensive suggestions in explaining the results, and finalizing the paper.

- **Maje Alhaji Haruna,** Jabbar Gardy, Guice Yao, Zhongliang Hu, Nicole Hondow, and Dongsheng Wen 2019.Nanoparticle modified polyacrylamide for enhanced oil recovery in harsh conditions**.** *Fuel*, 268, 117186.

The candidate as a primary author of this publication performed all the experiments and led the drafting of the publication. Jabbar Gardy, Guice Yao, and Nicole Hondow helped in the characterisation, Zhongliang Hu helped in the core flooding experimental set-up. Dongsheng Wen supervised the work, gave intensive suggestions in explaining the results, and finalizing the paper.

Conference and seminar activities

- **Maje Alhaji Haruna**, Dongsheng Wen, "Hybrid Suspension of Polyacrylamide and Graphene oxide Nano-sheet for Enhanced Oil Recovery", ***Oral presentation*** at 20th Conference on Petroleum Phase Behaviour and Fouling; 2nd to 6th June 2019, Kanazawa, Japan.

- **Maje Alhaji Haruna**, Shahid Pervaiz, Dongsheng Wen, "Improved Rheology and High-temperature Stability of Hydrolysed Polyacrylamide by Using Graphene oxide Nano-sheet", ***Oral presentation*** at 9th Australian Colloid and Interface Science Symposium; 3rd to 7th February 2019, Hobart, Tasmania, Australia.

- **Maje Alhaji Haruna,** and Dongsheng Wen, "Enhanced Oil recovery Using Nanoparticle modified Polymer solutions", ***Oral presentation*** at the School of Chemical and Process Engineering Internal Research Exchange Events, University of Leeds, **18th January 2019.**

- **Maje Alhaji Haruna**, and Dongsheng Wen, "Enhanced Oil recovery Using Nanoparticle modified Polymer solutions", ***poster presentation*** at the School of Chemical and Process Engineering Internal Research Exchange Events, University of Leeds, **18th January 2019**

- **Maje Alhaji Haruna**, and Dongsheng Wen**, "**Polymer nanocomposites for enhanced oil recovery application", ***poster presentation*** at the Bragg Centre Symposium, School of Chemical and Process Engineering, University of Leeds, **15th January 2019.**

- **Maje Alhaji Haruna**, Ehsan Nourafkan, and Dongsheng Wen "Improved Polymer flooding in Harsh environment by free-radical polymerization and the use of nanomaterials", ***poster presentation*** at the Material Chemistry-Division Poster Symposium, Royal Society of Chemistry (RSC) at Burlington House, W1J 0BA London, UK, **23rd November 2018.**

- **Maje Alhaji Haruna**, Hui Gao, Dongsheng Wen, "Rheology of Polymer-Coated Carbon Quantum Dots for Enhanced Oil Recovery"; 13th International conference on material chemistry (MC13), 10th to 13th July 2019, Liverpool, UK

Abstract

Increasing oil production is necessary due to the rise in energy demand and the lack of competitive alternative energy sources. Enhanced oil recovery (EOR) technology aims to retrieve the oil trapped in reservoirs after conventional methods have been exhausted. Many EOR processes are available based on thermal, gaseous, and chemical approaches. One of the most successful EOR methods is polymer flooding, where polymers are dissolved in flooding water to increase sweep efficiency, reduce viscous fingering, and produce more oil. Despite some progress that has been made in polymer EOR, many drawbacks hinder their wide applications due to polymer degradation and instability in harsh reservoir conditions such as high temperature and high salinity (HT-HS).

This project aims to improve the stability, rheology, and flooding performance of polymers in HT-HS conditions by two approaches, i.e., reinforcing polymer chains with desirable nanoparticles to form nanocomposites and engineering new temperature-resistant polymers. In addition, a novel synthesis approach to produce suitable nanoparticles *in-situ* in polymers is developed to further improve the polymer performance. Newly formed materials were carefully characterised, and their stability and rheological properties under HT-HS conditions were investigated, as well as their EOR performance in a pilot core-flooding facility.

The composites of partially hydrolysed polyacrylamide (HPAM), seeded with different nanoparticles (NPs), i.e., graphene oxide (GO) and carbon quantum dots (CQDs) was prepared using direct mechanical mixing approach but appears to be unstable in American Petroleum Institute (API) brine and complex formation brine (FB) solutions. Five different modified acrylamide copolymers (i.e., polymers synthesized from two different monomers) and terpolymers (i.e., polymers synthesized from three different monomers) are produced via free-radical polymerization. Among them, the polyampholytic terpolymer and polyelectrolyte

copolymer containing negative sulfonate groups were found to be stable when multiwall carbon nanotubes (MWCNTs) were introduced in the presence of API brine, but not in the FB solution.

Consequently, a novel modification and *in-situ* synthesis approach were used to alleviate the instability challenge. Whereby covalent functionalization of the copolymer of acrylamide (COPAM) with the partially reduced GO (rGO) was successfully conducted, followed by the addition of 1,3-Propane sultone to further functionalize the obtained rGO−COPAM composites to accomplish the zwitterionic character on the rGO−COPAM surface with excellent stability. Similarly, SiO_2 NPs were modified using (3-aminopropyl) triethoxysilane (M_SiO_2) to create positively charged active groups that enabled stronger interaction with COPAM functional groups. These functionalisation's and *in-situ* synthesis approach led to the formation of highly stable composites with excellent dispersibility and temperature stability, as well as salinity tolerance.

The HPAM rheological properties improve with the addition of GO but behaved differently when CQDs were added. The addition of GO significantly increased the viscosities and high-temperature stability of the base polymer fluid, as well as the elastic properties of the dispersion, due to the formation of covalent linkage and electrostatic hydrogen bond between GO and HPAM functional groups. Contrarily, CQDs addition into HPAM solution decreased both its viscosity and elasticity, demonstrating a phenomenon, which contradicts to the Einstein–Batchelor law, resulting in increased flow activation energy and decreased yield point. The solution became more sensitive to both temperature and shear rate. The mechanism behind the reduced viscosity behaviour of HPAM/CQDs composites appears to be the formation of free radicals and the elimination of ammonia molecules, leading to the deterioration of the polymer backbone. In addition, the viscosity of polyampholytic terpolymer and polyelectrolyte copolymer containing negative sulfonate groups increase in the presence

of MWCNTs in both alkaline and saline conditions. The M_SiO_2/COPAM and SiO_2/COPAM composites synthesised *in-situ* via free radical polymerisation showed improved rheological properties compared to pure polymer solutions after 90 days aging at 80 °C.

The pilot core-flooding experiments showed that zwitterionic-rGO-COPAM composite showed more oil recovery enhancement compared to HPAM and HPAM/GO in both API and complex FB conditions, respectively, with even lower pressure drop. Similarly, M_SiO_2/COPAM and SiO_2/COPAM showed better recovery performance than NP-free COPAM solutions, and the addition of MWCNTs to polyampholytic terpolymer and polyelectrolyte polymers improved the oil recovery in both alkaline and API brine conditions with a lower pressure drop.

Conclusively the work demonstrated that the use of appropriate nanoparticles can reinforce the stability, rheology, and flooding performance of polymers in HT-HS conditions. Among various approaches investigated, nanocomposites synthesised via *in-situ* produced NPs in polymers showed better performance than those prepared via a direct mixture of polymer/NPs solutions, showing great promise for future EOR applications.

Keywords: Enhanced oil recovery; Polymer flooding; Nanotechnology; Rheology; Stability; High temperature-high salinity; Long-term stability.

Content

List of Tables

List of Figures

Nomenclature

API	American Petroleum Institute
APIB	American Petroleum Institute brine
BF	Brine Flooding
CAC	Critical Association Concentration
CEOR	Chemical Enhanced Oil Recovery
CQDs	Carbon Quantum Dots
CMC	Critical Micelle Concentration
CNT	Carbon Nanotube
COPAM	Copolymer of acrylamide
COR	Cumulative Oil Recovery
CSC	Critical Salt Concentration
DLS	Dynamic Light Scatting
$ECOR$	Cumulative Oil Recovery Efficiency
EOR	EOR efficiency
$EIOR$	Increased Oil Recovery Efficiency
EDX	Energy-dispersive X-ray spectroscopy
EOR	Enhanced Oil Recovery
EDL	Electrical Double Layers
FTIR	Fourier-transform infrared spectroscopy
HT-HS	High temperature and high salinity
HPAM	Partially Hydrolysed Polyacrylamide
HPLC	High-Performance Liquid Chromatography
IFT	Interfacial Tension (N/m)

IONP	Iron Oxide Nanoparticle
IPV	Inaccessible Pore Volume
NF	Nanofluid Flooding
NP	Nanoparticle
OOIP	Original Oil In Place
PAM	Polyacrylamide
PV	Pore Volume
PF	Polymer Flooding
PF-EOR	Polymer Flooding Enhanced Oil Recovery
R&D	Research & Development
SCD	Sodium Citrate Dihydrate
SDP	Structural Disjoining Pressure
SDS	Sodium Dodecyl Sulphate
SEM	Scanning Electron Microscopes
TEM	Transmission Electron Microscope
UV-Vis	Ultraviolet-visible
XPS	X-ray photoelectron spectroscopy
G’	Storage Modulus (Pa)
G’’	Loss Modulus (Pa)
tanδ	Damping factor
η^*	Complex Viscosity (Pa·s)
ω	Angular Frequency (rad/s)

Chapter 1 Introduction

1.1. Global energy situation

Currently, the worldwide oil production statistics imply that the ultimate oil recovery efficiency from light and medium gravity by conventional recovery methods is within 25-35% of the original oil in place (OOIP), while only an average of 10% of the OOIP from heavy oil deposit is recoverable. Thus, a substantial amount of OOIP cannot be recovered by the conventional methods, and enhanced oil recovery (EOR) technique target to increase the recovery fraction from the remaining reserves [1]. The global energy demand will be anticipated to increase by as much as 50% by the end of 2030 relative to the current level (**Fig. 1.1**), due to significant population growth and increased industrialization and living standard [2]. How to mitigate the oil demand and production issue requires serious attention and innovative response.

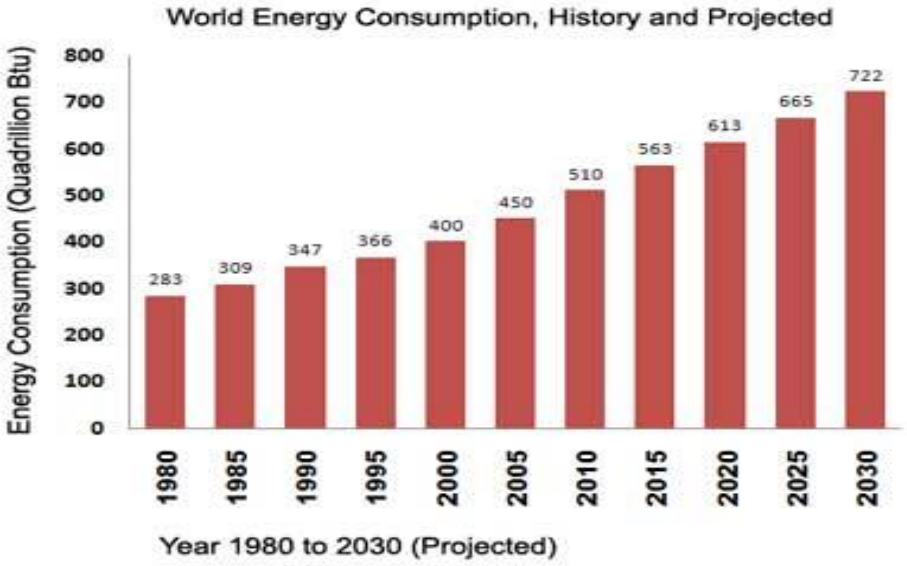

Figure 1.1. Trends showing world energy demand (1980 – 2030) [3].

Renewable energy techniques such as biodiesel, biomass, vegetable oil, photovoltaic, solar thermal, wind power, water, and hydroelectric power, etc. are unlikely to meet the demands effectively, even though the renewable source of energy is environmentally friendly [4]. These

techniques are costly and insufficient for energy demand satisfaction. Correspondingly, in the next coming years meeting the world growth of energy demand will be a major challenge [4]. However, with revolutionary discovery in the oil and gas industries, EOR gained more interest from the research and development phases to oil field implementation. With the current EOR methods including the thermal, chemical, biological and mechanical process, only 30-50% of the OOIP is produced, which indicates that about 50-70% of the OOIP remain trapped after the primary and secondary recovery.

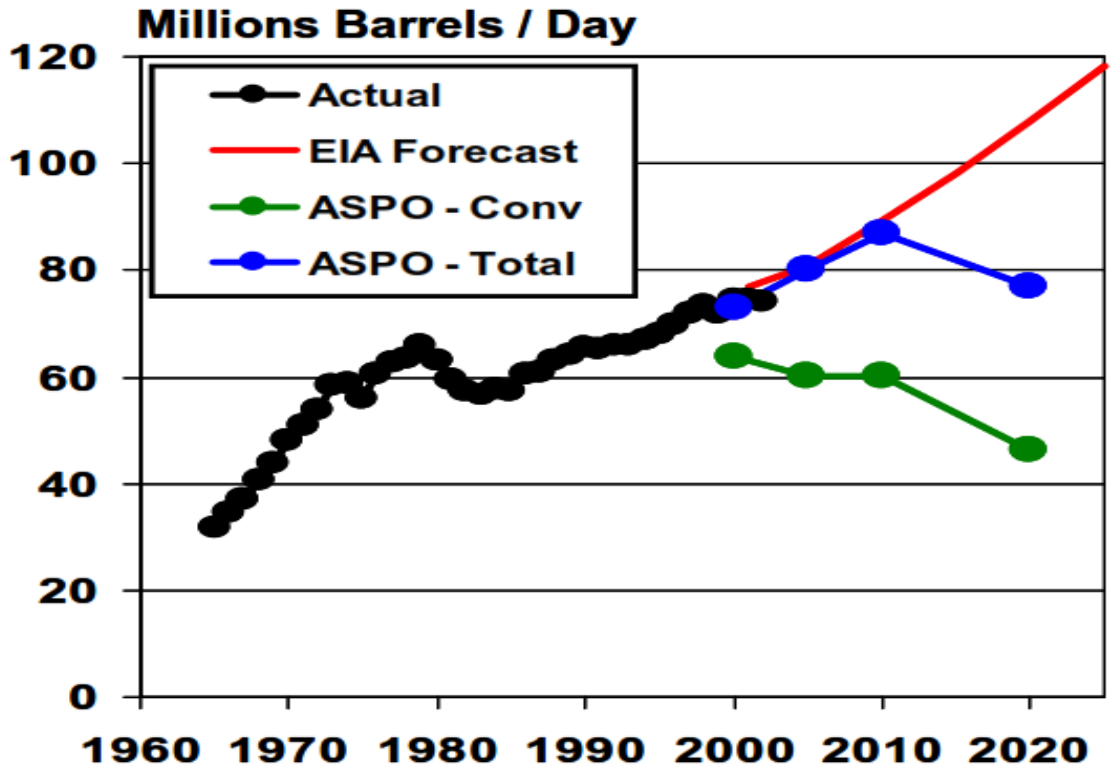

Figure 1.2. World forecasts on conventional oil production [5].

1.2. Enhanced oil recovery

Enhanced oil recovery (EOR) is the implementation of various processes or technologies that improve the oil displacement from the reservoir more than conventional methods [6]. Oil production is divided into three different phases of recovery; primary, secondary and tertiary

recovery. A schematic breakdown of these methods is illustrated in **Fig.1.3**. EOR is divided into thermal injection, gas injection, chemical injection, and others [7].

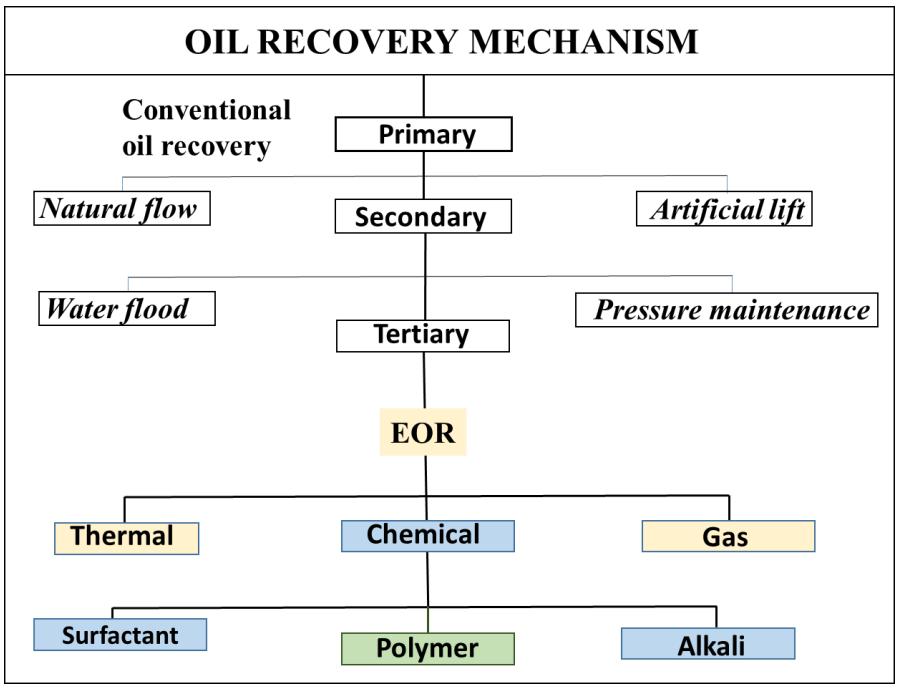

Figure 1.3. Classification of oil recovery mechanisms

1.2.1. Thermal EOR

The thermal injection process comprises the use of thermal energy, commonly in the form of hot water or steam to increase oil recovery. It is usually used when recovering heavy oils. Thermal energy lowered down the viscosity of the oil and boosted reservoir fluid mobility. When applied in the heavy oil field, the steam injection can improve recovery by up to 65% [8]. Technical problems associated with it, include poor sweep efficiency, loss of heat energy to unproductive zone, poor steam or air injectivity, and the reservoir wellbore is damage at the high steam temperature [9].

1.2.2. Gas EOR (CO_2 injection)

This method involves the injection of gasses, either as multi-contact miscible (MCM) or first contact miscible (FCM) with the oil and aid in recovery. In the MCM, the fluid injected is not miscible with the oil in the reservoir; the miscibility is created by mass-energy transfer between the different phases. In the FCM, the gas injected is miscible directly with the oil at reservoir conditions. Most of the lights to the intermediate component are derived out from the oil by CO_2 injection, if the pressure is high enough, the miscible display oil out of the reservoir and provide sufficient viscosity reduction and oil swelling. However, viscous fingering and gravity override occur, as such very low viscosity of CO_2 generates insufficient mobility control [10]. Recovery increase due to the gas injection is mostly between 5-15% [8].

1.2.3. Chemical EOR

The chemical EOR process involves the use of chemicals such as surfactants, polymers, and hydrocarbon (alkali) solvents. These chemical substances are added to the injecting fluid to reduce the interfacial tension and improved the sweep efficiency between the reservoir oil and the injecting fluid.

1.2.3.1. Alkali flooding

The alkaline flooding method is among the fundamental techniques applied in chemical EOR processes. It involves injecting the alkaline solution directly into the reservoir. Alkalis are water-soluble materials that discharge hydroxide ions (OH^-) when dissolving in water. Alkalis can be classified by being organic or inorganic or can be categorized as strong or weak. In chemical EOR, alkalis are used to accomplish the following; wettability alteration, reduce surfactant loss, and interact with a crude carboxylic acid to generate *in-situ* surfactant.

1.2.3.2. Surfactant flooding

The word surfactant originated from the surface-active agent. The surfactant is the substance that adsorbs into the system surface of the interface to change the degree of interfacial or surface free energy of that interface [11]. The molecules of surfactant formed adjusted monolayers at the interface and display surface activity (lowering the interfacial tension between the two phases) [12]. The surfactant ability to adsorb to the various interfaces depends on the surfactant molecules, which consist of a hydrophilic head and hydrophobic (lipophilic) tail [12, 13]. A schematic diagram representing surfactant molecules is illustrated in **Fig. 1.4**. The head group can be ionic or polar and actively interact with the aqueous environment and solvated via ion-dipole or dipole-dipole interaction [11, 12].

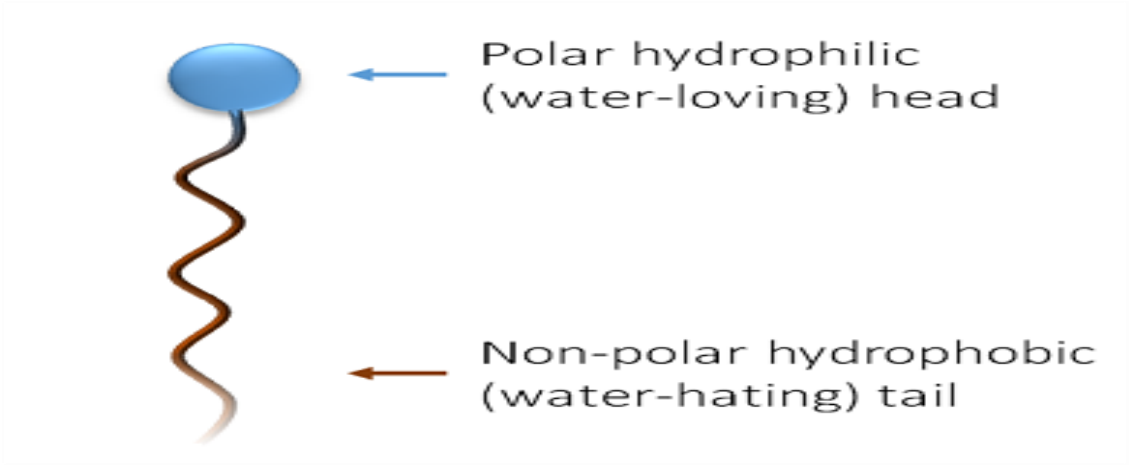

Figure 1.4. Schematic of a general surfactant molecule.

The main group of the surfactant such as cationic, anionic, and amphoteric is classified by the nature of the surfactant molecules head group. The tail section or hydrophobic of the surfactant molecules usually consist of hydrocarbon chain which can be branched or linear [11, 12]. Some unique surfactants such as a perfluorocarbon or a polydimethylsiloxane surfactant can have a non-hydrocarbon chain tail [11]. The surfactants have the tendency to reduce the contact

between their hydrophobic group and water in aqueous solution by either association in the solution or adsorb at the interface [14].

1.2.3.3. Polymer EOR

Polymer flooding is among the chemical enhanced oil recovery methods (CEOR) and is a most straightforward technique with proven results and lengthy commercial history. This technology outnumbers other CEOR processes because the risk associated with the application of polymer flooding is indeed low. Over the past years, the application has enormously widened with field cases in high salinity and temperature reservoirs. Mobility ratio has been known as one of the most influential factors that deteriorate oil recovery by waterflooding because water is unable to completely sweep the oil due to its lower viscosity [15]. However, polymer flooding emerged as an alternative method for EOR. Polymer mix with water to form a polymer solution and the polymer addition in water boosts the apparent viscosity of the displacing fluid to lower the mobility ratio. With controlling mobility ratio the sweep efficiency also improved by creating a smooth flood front with less viscous fingering, and water breakthrough is postponed hence more oil recovery is achieved.

1.2.3.3.1. Polymer flooding mechanisms

Mobility control

The viscosity of the reservoir oil is considerably higher than the injected fluid viscosity. The polymer is added to the solution to increasing the fluid viscosity (e.g. water), and the mobility will become less than that of the oil phase in place. Mobility ratio (M) is the ratio of the mobility of displacing fluid to the mobility of the displaced fluid [7].

If the mobility ratio (M) is greater than one $M > 1$ indicates that water is more mobile than oil and would pass through the oil zone creating an early breakthrough, and therefore results in

low displacement efficiency. If the mobility ratio is below or equal to one $M \leq 1$, it is considered to be favorable for oil displacement. **Fig. 1.5** illustrates how oil recovery is influenced by the mobility ratio.

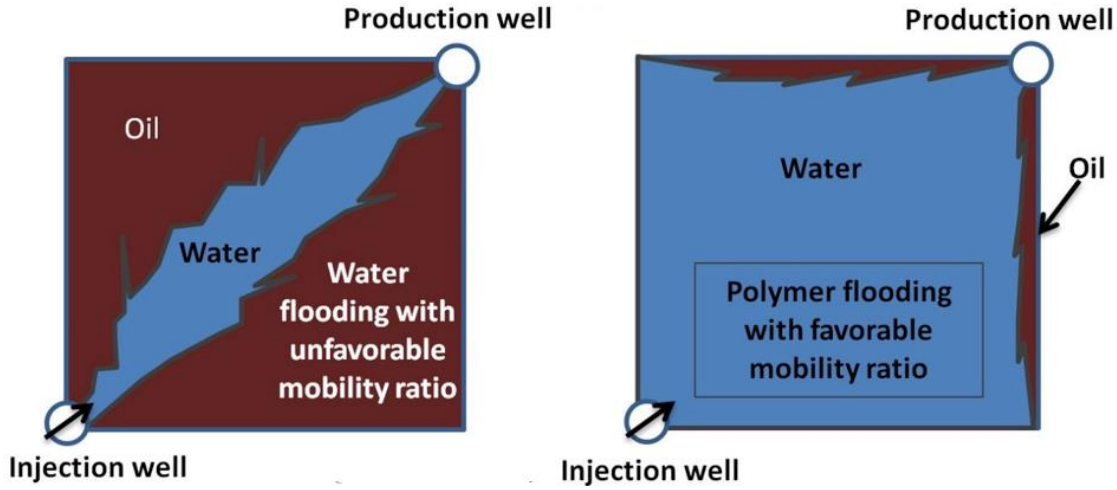

Figure 1.5. (a) Fingering effect due to unfavourable mobility ratio and (b) good mobility control facilitated by the use of polymer flooding.

Fractional factor

Fractional flow (f_w)is another important concept associated with the flow of two immiscible phases. The mobility ratio does not remain constant in the immiscible displacement process. However, it differs from the saturation of the flowing phases. Fractional flow is the ratio of the flow rate of water to the oil flow rate. Buckley-Leverette analysis has been used to obtain the overall fractional flow of water for the water-oil system. The methods work under the assumption, assuming the oil and water flowing through porous media simultaneously no capillary diffusion at the front [16].

The fractional flow of the water is changing by altering the mobility ratio. The f_w-curve moves towards the right as the mobility ratio reduced (become more favourable) as shown in **Fig. 1.6.**

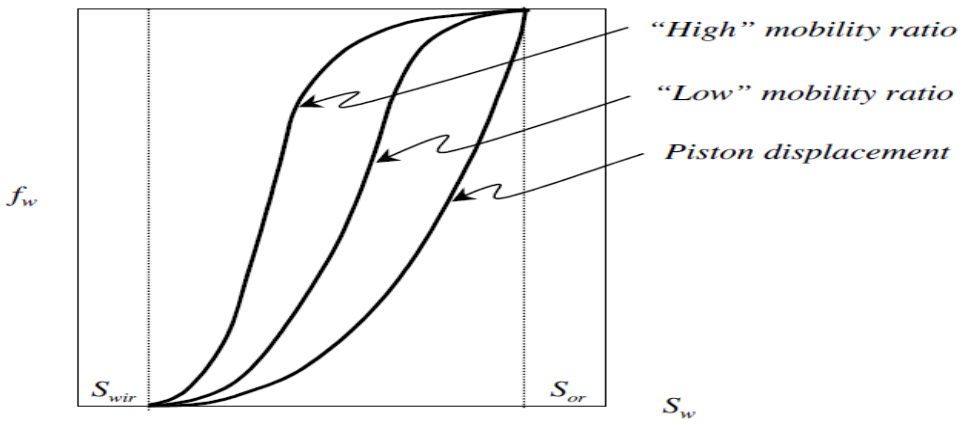

Figure 1.6. Showing the effect of mobility ratio in a fractional flow of water.

Resistance factor (R_f)

The term resistance factor is applied to indicate the flow resistance encountered by polymer solution as compared to water flow. For example, a resistance factor of 7 means that the difficulty for the polymer solution to flow through the system is 7 times more than that of water. At room temperature and pressure, water has the viscosity of 1cp, in this instance polymer solution would flow through porous media with predicted apparent viscosity of 5cp, although measured viscosity in viscometer could be much lower. Thus, the apparent viscosity could be measured accurately by the resistance factor [17].

Resistance factor (R_f) can be expressed as a water mobility ratio to the polymer solution mobility ratio.

Sweep efficiency

Sweep efficiency is an essential part that in association with the mobility ratio acts as a benchmark in judging the degree of accomplishing a flooding process. The total efficiency factor, E, stands for the amount of original oil in place that can be recovered before the starting point of a secondary or tertiary displacement process [18].

$$E = E_D + E_{AS} + E_{VS} \ldots\ldots\ldots\ldots 1.1$$

Where, E_D = Displacement efficiency, E_{AS} = Aerial sweep efficiency and E_{VS} = Vertical sweep efficiency. **Fig. 1.7** represents all the three efficiencies in a reservoir.

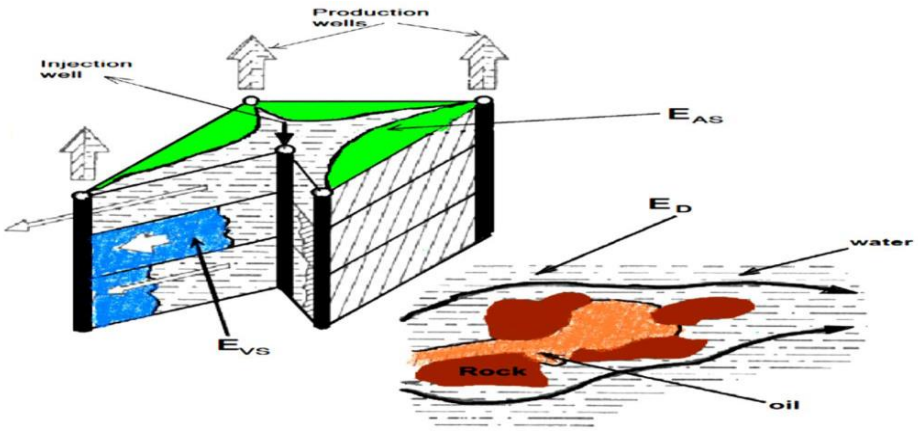

Figure 1.7. Sweep efficiencies [19].

1.2.3.3.2. Problems associated with polymer flooding

Many laboratory studies and field implementation of polymer flooding has been completed with encouraging diverse achievement [20]. However, despite having promising results in polymer flooding EOR, the following drawbacks still need to be considered to make the process more successful.

- **Formation damage:** In polymer flooding, the retention of polymer in the porous media occurs due to the mechanical entrapment, adsorption, and/or precipitation. This retention results in the formation damage. In the polymer EOR, adsorption can be critical, because it can occupy a large pore area and it can sometimes become irreversible which leads to high oil blockage. Making it difficult to recover a significant quantity of oil, because the formation permeability reduced as well as the recovery factor.
- **Polymer degradation:** Polymers are expensive, and the flooding process is limited due to the polymer degradation caused by high reservoir temperature, hardness, and make-up brine salinity.

- **Polymer stability:** Among the highest challenges facing polymer EOR is polymer stability which occurs as a result of polymer degradation. The degradation that is caused by a chemical constituent in the reservoir due to the effect of oxidation or ionic ions, and is called chemical degradation. Degradation can also thermal when the polymer is subjected to higher temperatures. A high flow rate results in mechanical degradation, while biological degradation is caused by the action of microorganisms.

1.3. Research motivation

Nanotechnology refers broadly to the application of science and technology that deals with the control of matter on the atomic or molecular scales smaller than 1 µm, ranging normally within 1 to 100 nm [21-23]. Nanotechnology has been widely used for many industrial applications including cosmetics, pharmacy, and energy transformation and conversion [24]. The use of nanotechnology in the oil and gas industries is a recent development that holds many promises [24, 25].

Nanoparticles (NPs) are considered to be a class of materials that have numerous functionalization abilities and can be coated with polymer or surfactant to form hybrids. In EOR applications, various NPs have been added into the injection fluid to alter oil and water interfacial tension, substrate wettability, and flow characteristics, leading to different EOR results. When NPs are mixed with the polymer to form nanocomposites, it is expected to improve the polymer rheological properties, thermal stability, and resistance to saline conditions, which could lead to better control of the mobility and consequently improved EOR performance.

This project aims to improve the stability, rheology, and flooding performance of polymers in HT-HS conditions by two approaches, i.e., reinforcing polymer chains with desirable NPs to

form composites and engineering new temperature-resistant polymers. In addition, a novel synthesis approach to produce suitable NPs *in-situ* in polymers is developed to further improve the polymer performance. Newly formed materials were carefully characterised, and their stability and rheological properties under HT-HS conditions were investigated, as well as their EOR performance in a pilot core-flooding facility.

The above aim of this project is accomplished through the following research **objectives**:

- **Task 1**: Design and fabrication of different new materials (i.e., polymers and polymer nanoparticles composites).
- **Task 2:** *In-situ* synthesis and characterization of new polymer nanoparticle composites under the influence of high ionic strength brine and long-term temperature stability.
- **Task 3:** Investigation of the stability and rheological properties (Viscosity, viscoelasticity) of the new materials.
- **Task 4:** Investigation of the flooding performance and EOR effect of the new materials.

1.4 Thesis outline

Chapter one: This Chapter provides a research background related to global energy demands, enhanced oil recovery methods with a focus on polymer EOR.

Chapter two: This Chapter conducts a detailed literature review of polymer EOR and nanotechnology for improving oil recovery, as well as polymer nanoparticle interactions and their applications in EOR.

Chapter three: This Chapter investigates the formulation and characterisation of different polymers and polymer-nanoparticles composites via direct mechanical mixing. The Chapter is subdivided into three parts, descriptions of the equipment, formulation, and characterizations

of the polymer nanocomposites via direct mechanical mixing process, and synthesis and characterization of different co/ter-polymers via free-radical polymerization. Suitable nanoparticles and polymers are identified for enhanced oil recovery under the influence of pH and API brine.

Chapter four: This Chapter develops novel technology for *in-situ* formation and modification of polymer-nanoparticles composites. The nanoparticle synthesis was conducted *in-situ* under the influence of high ionic strength brines. The first section of this Chapter explores the *in-situ* production of rGO/polymer nanocomposites via the covalent functionalization of polymer with the partially reduced graphene oxide (rGO). The second part focusses on the *in-situ* synthesis of modified SiO_2/polymer composites using (3-aminopropyl) triethoxysilane to create positively charged active groups that allow stronger interaction with COPAM functional groups, leading to high dispersion stability and temperature stability of the formulated material.

Chapter five: This Chapter investigates the stability and rheological properties of different formulated materials synthesized in Chapters 3 and 4. The rheological investigation of the HPAM seeded with GO and CQDs is conducted. The impact of various nanoparticle concentrations, temperatures, and electrolyte concentrations on the long-term thermal stability and rheological behaviour are investigated. In addition, the investigation of the influence of MWCNTs on the rheological properties (viscosity and viscoelasticity) of the five polymers synthesised via free radical polymerization, is conducted and appropriate polymers are identified for EOR at API brine and alkaline pH conditions. The effect of modified rGO and modified SiO_2 on the polymer rheological properties is also observed.

Chapter six: This Chapter investigates the influence of different materials prepared in Chapters 3 and 4 (i.e., polymers and polymer-nanoparticle composites) on EOR using a core flooding experimental set-up. The effect of MWCNTs on the recovery enhancement of the two

selected polymers are evaluated at high temperature under the influence of API brine and alkaline pH condition, respectively. The effect of different GO concentrations on the HPAM oil recovery efficiency at high temperature (up 80° C) condition is investigated, the effect of modified rGO and modified SiO_2 are also evaluated at complex salinity and high-temperature conditions.

Chapter seven: This Chapter presents the overall conclusions and suggestions for future work. The layout of this thesis is shown in **Fig. 1.8**.

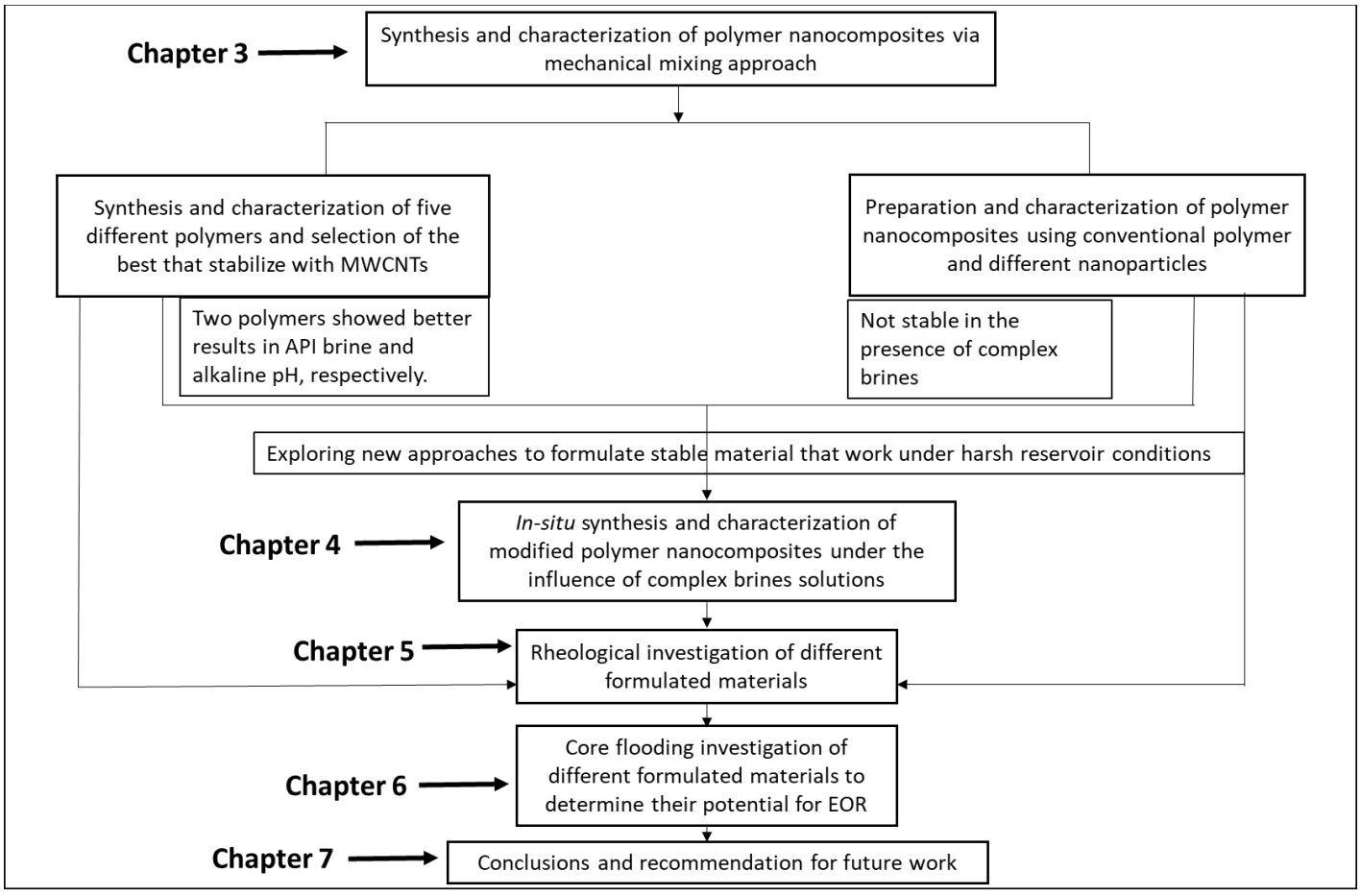

Figure 1.8. The layout of the thesis.

Chapter 2 Literature review

2.1. Polymer-based EOR

Polymer flooding (PF) is one of the chemical enhanced oil recovery (CEOR) methods and is the most straightforward technique with proven results and lengthy commercial history [20, 26]. This technology outnumbers other CEOR processes because the risk associated with the application of PF is indeed low, and over the past years the application has enormously widened with field cases in high salinity and temperature reservoirs [20]. PF involved the addition of water-soluble polymers into injection water to form a polymer solution. The polymer-augmented water is injected into a subterranean oil formation with the aim to improve reservoir sweep efficiency. Increasing the water viscosity improved mobility control between the injected slug (water) and the hydrocarbons (oil) within the reservoir [20].

After injecting the polymer-augmented water, the solution moves freely through the rocks to increase oil recovery [27], and however, by mobilizing the capillary-trapped oil, the volumetric sweep efficiency will improve. Polymer slug is considered as the solution with shear thinning and non-Newtonian behaviour.

The PF process efficiency could be affected by many factors and parameters either positively or negatively. These parameters could be related to the economic, technical, and reservoir conditions, or related to the characteristics of the polymer solution itself. Polymer solution features and its physicochemical behaviour is affected by the following parameters; viscoelastic properties, molecular weight, concentration, salinity, the degree of hydrolysis and pH of the make-up solution. However, when preparing a polymer solution with high concentration and high molecular weight, care should be considered to avoid economical and technical limitations [28].

The reservoir rock's initial wettability state has an essential impact on the performance of the PF method. Some reports revealed that the flow behaviour of polymer in porous media includes polymer retention due to adsorption mechanism, pressure build-up, residual resistance factor is substantially not the same with wettability state. During PF in an intermediate-wet reservoir, the interaction between the injected polymer and some portion of the oil-wet rock will occur. The adsorption site of polymer in the rock is reduced by adsorption of crude oil components, and the interaction between the polymer molecules and the rock surface decreased. Too much adsorption of polymer on the water-wet rock surfaces caused poor sweep efficiency of polymer solution because of the retention in porous media and aggregation of the trapped oil in the blocked pores [28-30].

2.1.2. Types of polymers used in EOR

Two types of polymers are the most commonly used for EOR application: synthetic polymers and biopolymers. Polyacrylamide (PAM) and its derivatives are the typical synthetic polymers. Xanthan gum is a commonly used biopolymer. Hydrolysed polyacrylamide (HPAM) is usually used for the majority of field projects because it is less costly and it is applicable for large scale production [31, 32]. According to Wang *et al.* [33]. HPAM solution is expected to exhibit significantly higher viscoelasticity compared to the Xanthan polymer solution. PAM/HPAM are long-chain molecules with an effective small diameter. Therefore, at a higher flow rate, they are relatively sensitive to mechanical shear which results in viscosity reduction. HPAM is also sensitive to saline conditions, its molecules curl up at high brine salinity and loss their viscosity building effect. Biopolymers were not commonly used, but few projects have proposed its applicability, although a lot of research work was conducted in the 1970's and 1980s. Contrary to PAM's group, xanthan polymers are more tolerant to saline conditions and mechanical shear but susceptible to reservoir biological degradation. However, both polymers

are sensitive to the high-temperature environment and do not provide long-term thermal stability [13, 28].

Modification of polymers was proposed to alleviate the challenges facing polymer EOR. Research conducted by Li *et al.* [34] proposed the addition of the hydrophobic branch in the copolymer with hydrophilic skeleton showed enhanced polymer viscosity. In a similar finding, the flowability and viscosity of thermos-sensitive copolymer containing single, double and triple hydrophobic chains increases after the modification with diallyl ammonium salt [34, 35]. Consequently, the tendency of this polymer was evaluated by testing their EOR performance, it was revealed that after one month of aging at a high temperature of 45 and 85 °C, the oil recovery factor by thermos-sensitive polymer was 16.4 and 15.5%, respectively while that of pure PAM was found to be 12%.

Despite the positive results of these new polymers, they come with many problems including low solubility, high chemical cost, and elevated resistance factor. Natural or synthetic inorganic materials have been also used to fill the conventional polymers to enhance their performance and have become economically viable [36]. However, these added fillers bring many other problems for the application resulting in opacity, brittleness and weight increase [36, 37].

2.1.3. Polymer behaviours in the reservoir

2.1.3.1. Polymer adsorption

In this context, adsorption is referred to as the interaction between the surface of the rock and polymer molecules, which cause molecules of the polymer to bind to the rock surface. Some portions of the polymer injected are left behind which eventually results in the reduction of concentration. Polymer adsorption does not decrease with the decrease in concentration, therefore, it is considered as the irreversible process [38]. However, adsorption increase

resistance to flow, account for the loss of polymeric additives and generate the stripped water bank at the dominant edge of the slug [38]. The degree of polymer adsorption on the rock surface rely upon the following; (i) types of polymer, (ii) the accessibility to the active surface (iii) mineralogy of the rock (iv) temperature (v) rock wettability (vi) relative permeability to water and solvent (salinity).

A high degree of hydrolysis reduces the adsorption of hydrolysed polyacrylamide in sandstones reservoirs because it has a large amount of COO^- groups. Compared to sandstone reservoirs, HPAM has very high adsorption behaviour in carbonate reservoirs. Unlike non-ionic PAM, electrostatic attraction between the charged polymers and the reservoir rocks plays a good role in the polymer adsorption [39]. Therefore, the strong interaction between COO^- and Ca^{2+} causes the HPAM adsorption significantly in carbonate reservoirs. A high concentration of salt brings about the cations that promote the polymer/rock interaction due to the decrease in the size of the HPAM flexible chain, which results in adsorption [40-42]. The adsorption of HPAM could be enhanced by the effect of temperature, due to the high temperature the negative charges on the rock surfaces increases, and lead to the decrease in adsorption by increasing the electrostatic repulsion.

2.1.3.2. Polymer retention

There is a solid relationship between retention and adsorption of polymers, retention of polymer includes; hydrodynamic retention, mechanical trapping, and adsorption. Retention by mechanical trapping occurs when large molecules of the polymer are lodged in channels with the narrow flow. This may result in a material build-up near the injection well that can cause pore blockage and well plugging. Based on that, it is recommended not to use low permeability for polymer flooding [43]. Hydrodynamic retention has a small impact on total retention and therefore should be neglected in field operations. But in contrast with alkaline and surfactant,

mechanical trapping and hydrodynamic retention of the polymer are significant because of the polymer large molecules. Polymer retention includes adsorption, therefore retention increase with the increase in adsorption and vice versa [44]. The influence of permeability and polymer concentration on the retention behaviour of non-ionic polyacrylamide with high molecular weight were examined by Zitha *et al.* [45].

The retention mechanism for many conventional polymers such as PAM and HPAM, in porous media, is widely known [46, 47]. However, despite several claims regarding the high viscosity and enhance flooding performance of hydrophobically associated polyacrylamide (HAPAM) [46, 48], there is still a lack of sufficient study about their retention behaviour in porous media. This shows a large difference in terms nature of the retention between PAM and HAPAM, due to the presence of a hydrophobic domain on the HAPAM backbone [49]. In research conducted by Lu *et al.* [49], there is relatively smaller static and dynamic retention by PAM compared to HAPAM, although the static retention was found higher than the dynamic retention in both polymers. Another important factor that influences the retention of polymers in reservoir rock is permeability, according to the reports, low permeability rock often has higher mechanical entrapment than high permeability rock [50].

Polymer retention and adsorption have shown to be independent on concentration [51] in concentrated and dilute regions [51], but dependent on concentration in the semi-dilute region. It was also reported that polymer retention could be decreased when the solution with low concentration is injected. In the dilute region, most of the molecules of the polymer are in contact with the rock surface and behave freely like a coil. In the concentrated zone polymers covered all sites of the rock. While in a semi-dilute region where the effect of concertation is observed, there is mixed behaviour, some segments of the molecules are partially adsorbed while others are fully adsorbed. **Fig. 2.1** illustrates the polymer retention mechanisms.

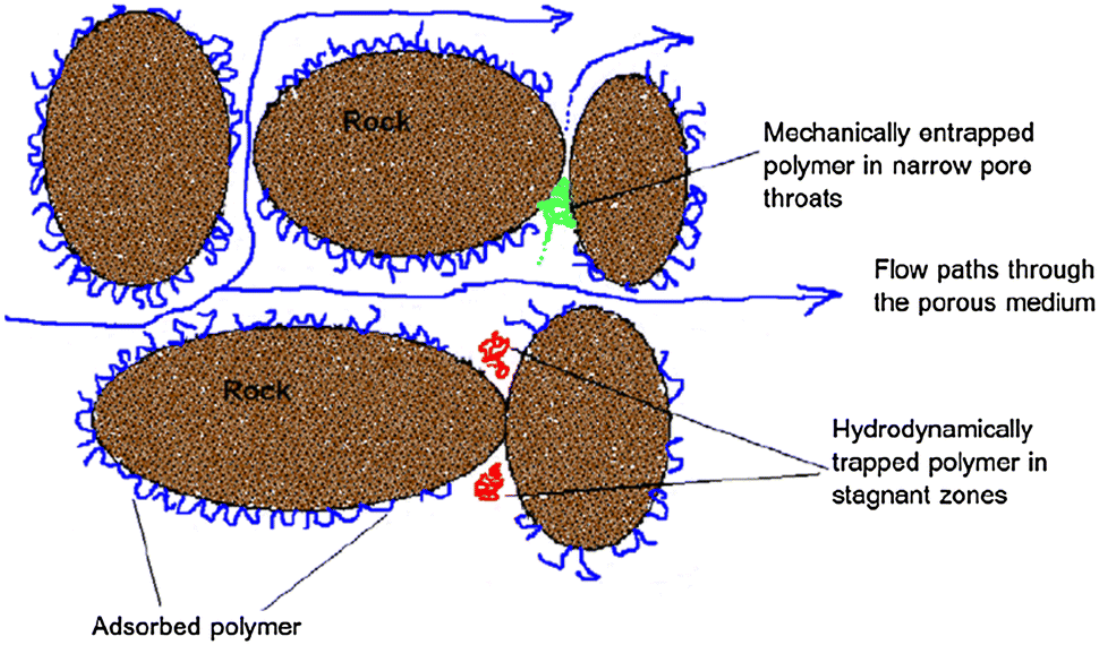

Figure 2.1. Polymer retention in porous media [52].

2.1.3.3. Polymer degradation and stability

Polymer degradation and stability is an important factor in designing the flooding process. In industrial PF processes, the polymer is required to undergo long-term treatment under harsh conditions in the reservoir. Persistent aging of the polymer under severe circumstances would cause viscosity reduction and hence drawbacks to the oil recovery [53]. Polymers need to be thermally or chemically stable for many months after injection. The thermal effect results in viscosity reduction while chemical (salinity) effect may lead to precipitation. Selecting of EOR polymer is not limited to good adsorption, injectivity, rheological properties, and cost, but rather excellent thermal, brine, biological and shear stability. HPAM is the most commonly used polymer for oil reservoirs mobility control, and it has been tested at field scale [46, 54, 55]. Despite the tremendous use of HPAM in EOR, it suffers a common problem of instability and degradation at harsh reservoir conditions such as high temperature, high pressure or high salinity [56].

It is observed that HPAM would undergo a significant reduction in viscosity and a decrease in the percentage of oil recovery in most of the high-temperature reservoirs [57]. The viscosity reduction could arise because of the effect of hydrophobic impairment due to the increase in polymer mobility and the eventual damage of inter-chain linkages [58, 59]. When reservoir temperatures go above 60 °C, it is highly likely that the acrylamide functionality would undergo hydrolysis to form acrylate derivatives [56] or carboxylic acid [60] groups, which have high affinity to salts in the reservoir.

Also, lack of salt tolerance causes HPAM degradation, which consequently hinders its application in EOR, for instance, the presence of any sodium ions can neutralise the negative charges, which can cause the shrinkage of the polymer chains and a consequent decrease of the hydrodynamic radius. The addition of NaCl solution can enhance the ionic strength of the system, leading to the compression of the double electrical layers (EDL) on HPAM molecular chains. Also, the electrostatic repulsion among the anions would be altered. The addition of $CaCl_2$ was reported to significantly decrease the viscosity of the HPAM as well as pseudo-plasticity due to the presence of the doubly charged cations [61]. Increasing the degree of hydrolysis causes the HPAM to precipitate from the bulk phase due to the formation of the complexes between the divalent cations and the polymer [62]. Moreover, prevention of the mutual repulsion that can exist between carboxylic groups on the backbone of the HPAM would lead to a shrinkage of the hydrodynamic volume, and subsequently more viscosity reduction [61, 63]. From another point of view, the many challenges that HPAM solutions could encounter in EOR applications could range from thermal challenges, leading to low thermal stability to tolerate severe reservoir conditions, leading to early degradation, or mechanical challenges, leading to inadequate durability and toughness. Other challenges could be related to swelling, leading to deficient swelling ability or elasticity challenges, leading to insufficient, required viscoelasticity properties.

2.1.3.4. Inaccessible Pore Volume (IPV)

Inaccessible pore volume or IPV was studied by Dawson and Lantz [64]. It is the phenomenon whereby large polymer molecules can have less or not have access to small pores in porous media. Therefore, water with no polymer occupied the IPV and creates changes in polymer concentration [64]. As shown in **Fig. 2.2** it has been observed in an experiment that the polymer-water solution velocity in a reservoir is higher than the trace velocity. Showing the occurrence of the polymer breakthrough earlier than tracer and these confirmed the inaccessibility of polymer molecule to some pore volume [65].

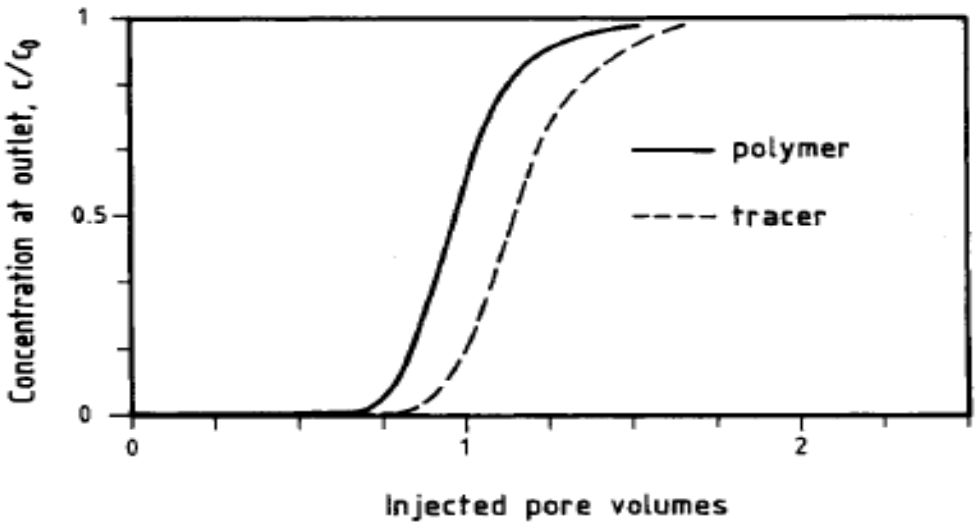

Figure 2.2. Injected pore volume versus concentration at the outlet [65].

2.1.4. Rheological properties of polymer solutions

Rheology is the study of the material flow and deformation behaviour under the applied force, which is frequently, tested using a rheometer. The word "Rheology" was revealed in the 1920's, in Greek referred to as "Panta rhei" meaning everything flows, and it defined the study at which the matter flow [66]. A rheometer is an equipment used for measuring the fluid viscosity and to determine how strain and stress affect the material being investigated. The parallel plate model was the easiest way to describe rheological properties [66], where different liquid layers

are viewed on the top of one another. In the rheometer, the force is generally applied rotationally (**Fig. 2.3** b & c) in the rheometer rather than axially (**Fig. 2.3 a**).

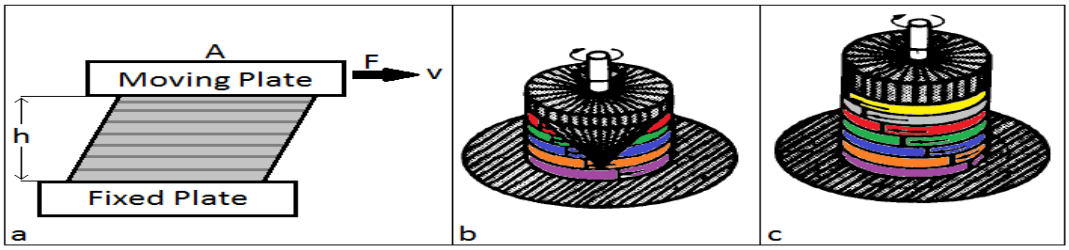

Figure 2.3. Rheometer plates [67].

a) Represent parallel plate model, (b and c) stand for a flow of sheared liquid represented by bands with different colour, b- represent cone on the plate, and c- represent plate on cone [66].

2.1.4.1. Viscosity

Viscosity is the measure of the fluid's resistance to flow with a gradual deformation under the influence of stress on its cross-sectional surface. The greater the viscosity, the greater the resistance of the fluid to stress. Viscosity is often expressed in Pas unit and is mathematically defined in equation 2.1:

$$\eta(\mathrm{Pa.s}) = \frac{\tau(\mathrm{Pa})}{\gamma(\mathrm{s}^{-1})} \ldots\ldots\ldots 2.1$$

Where

η is the viscosity (Pa.s)

τ is the shear stress (Pa)

Υ is the shear rate (s^{-1})

Fluids are classified categorically in two different ways, Newtonian and Non-Newtonian fluid [66] **(Fig. 2.4)**. The letter is classified by using a single coefficient of viscosity, with increasing shear rate, and the viscosity remains constant at the desired temperature, i.e. viscosity does not

depend on shear rate. A fluid whose viscosity changes when flow speed changes are referred to as Non-Newtonian fluid, at different experimental conditions such as temperature, shear rate, etc., the fluid viscosity tends to decrease or increase accounting for shear thickening or shear thinning behaviour.

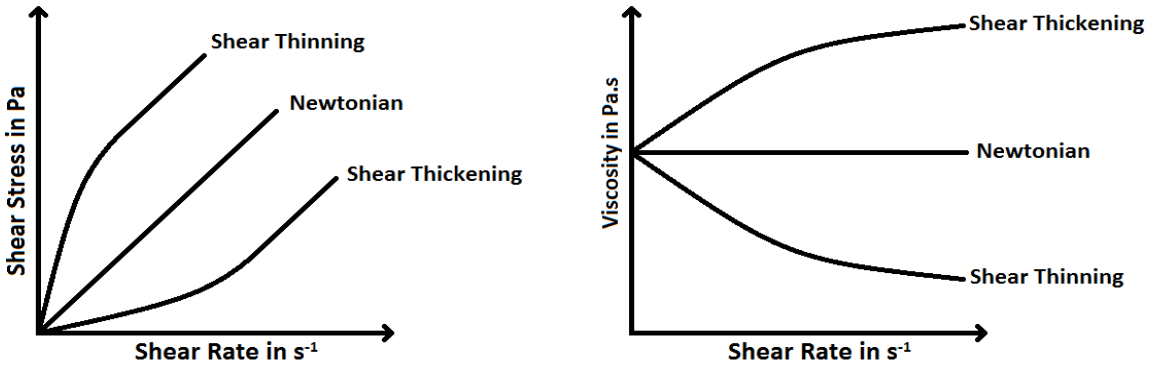

Figure 2.4. Plot showing the effect of shear rate on fluid viscosity demonstrating the Newtonian and Non-Newtonian nature with respect to both the (right) viscosity and (left) shear stress [67].

2.1.4.2. Viscoelasticity

The viscoelastic properties of materials are measured with an oscillatory test, where sinusoidal strain is applied [68]. The viscous (loss) modulus, G", is deformation energy used up by the sample during the process and thereafter lost, while elastic (storage) modulus, G', is a measure of the deformation energy deposited by the sample during the shear process. The loss factor, $\tan\delta$, is defined as the ratio between the viscous and elastic modulus of the viscoelastic behaviour (equation 5.2) [69, 70].

$$\tan\delta = \frac{G''}{G'} \ldots\ldots\ldots 2.2$$

Frequency independent viscous and elastic moduli were used to characterize ideal viscous and elastic behaviour. For a fluid with ideal viscous behaviour, G'' dominates G' and indicate that $\delta = 90^0 \; and \; \tan\delta = \propto$, while on the other hand, if G' dominates G'', the loss factor $\delta =$

$0^{\circ}\ and \tan\delta = 0$ [69]. For viscoelastic fluids, at higher frequencies, the storage modulus is higher than the loss modulus and lower at lower frequencies. However, at the medium frequency, normally called crossover frequency, ω^{*}, G' = G'', and thus, $\tan\delta = 1$.

2.1.5. Influential factors on polymer viscosity

2.1.5.1. Shear rate

When a solution of polymer is injected into the oil well, the shear rate (flow rate) to the in-depth of the reservoir from wellbore will change; thereby causes the viscosity to change accordingly. A series of experiments was conducted by Tang *et al.* [71] using an unconsolidated core holder packed with the glass beads. After secondary flooding polymer injection was performed in each experiment. The relationship of shear vs. HPAM solution viscosity was measured using viscometer before the experiment as shown in **Fig. 2.5.** The blue diamond and red boxes are apparent viscosity and bulk viscosity obtained by core flooding experiments and viscometer. Delshad *et al.* [72] used viscoelastic and shear-thinning models to compare with the experimental results as shown in **Fig. 2.5.** A Newtonian, near-Newtonian, or mild shear thinning is seen at low velocities in a porous media, and bulk viscosity has been observed with the same trend while measured using a capillary viscometer. The bulk viscosity curve begins to diminish, with the increasing shear rate, showing shear-thinning while the apparent viscosity starts to deviate from the diminishing bulk viscosity. The bulk viscosity obeyed the similar decreasing slope when the shear rate continues to extend, but the apparent viscosity in porous media begins to increase demonstrating a shear thickening behaviour [71]. A similar trend in HPAM solution viscosity is also observed by other researchers [72-76].

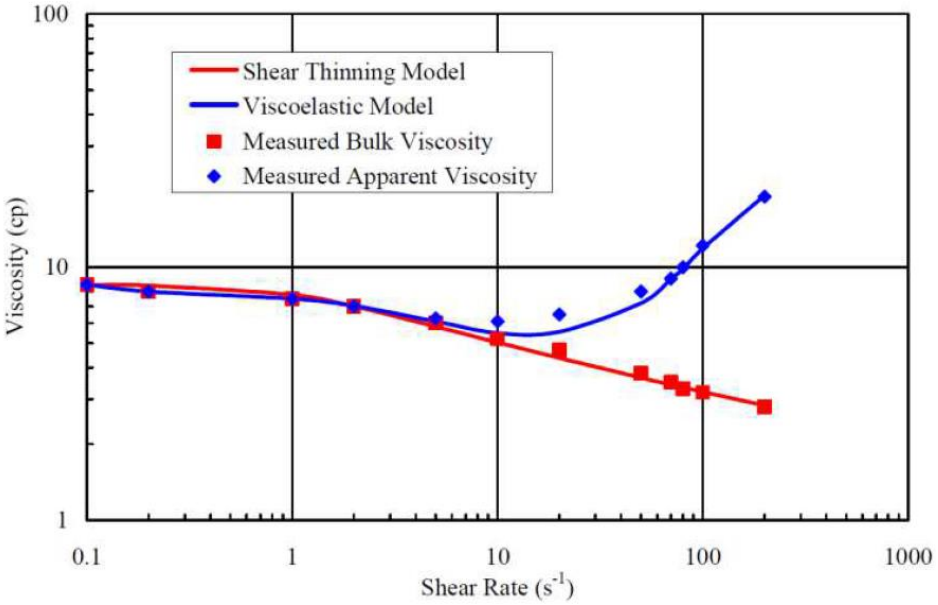

Figure 2.5. The viscosity of HPAM against shear rate measured by viscometer and within the porous media [77].

2.1.5.2. Molecular weight

Molecular weight (Mw) is the ratio of the polymer molecular mass to the 1/12th of the carbon-12 [78], which was used to illustrate the size of macromolecule materials. It has a unit of g/mol, or Dalton (Da), 1 Da = 1g/mol. In many cases, the flow behaviour of a polymer is affected mainly by Mw. The Mw of the polymer is related proportionally to its molecule size, i.e., the higher the Mw the larger the size. In simple terms, the polymer with higher Mw possesses a higher viscosity and greater resistance as illustrated in **Fig. 2.6** [79].

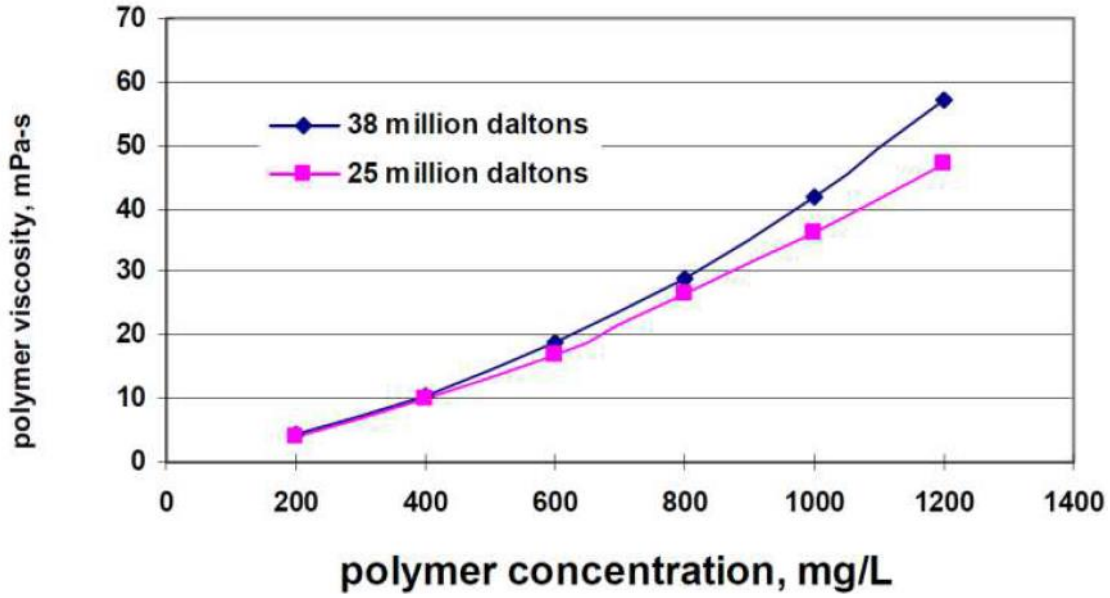

Figure 2.6. The apparent viscosity of polymer with different molecular weight against the concentration [79].

In many cases, a larger polymer Mw also leads to higher oil recovery. Dong *et al.* [79] conducted a core flooding experiment with different Mw polymers (Table 2.1) to investigate the effect of Mw on oil recovery. They found that after water injection about 32 to 33 % of the oil was recovered in each case. These followed by injecting the polymer with different Mw, as shown in **Table 2.1** the polymer with 18.6 million Daltons appeared to have a higher oil recovery. However, for the reservoir with low to moderate permeability, higher Mw polymers require high injection pressure and might result in more unswept PV, which results in smaller recovery factors as shown in **Fig. 2.7** [80].

Other previous work reported that polymer with high Mw is considered to be shear sensitive [81]. Due to the macromolecule chain breakage, and reversibility of shear degradation. Six polymers and co-polymer with variation in Mw (2 to 18.5 million Daltons) were tested through a capillary tube of stainless steel with a 5 cm long and internal diameter of 125 µm [77]. The finding showed that the polymer sensitivity to shear was observed with increasing Mw. This is because a large number of coiled molecules were found to be more stretched at the same

deformation regime. Notwithstanding, when chosen the polymer Mw, some important factors had to be considered. (1) The higher Mw polymer could reduce the amount of polymer required for the injection. (2) The relation between permeability and Mw should be given proper consideration. (3) The Mw should not be too large, so that it can propagate through the pore channels easily [79], however, for field application the lower or moderate Mw polymer can be more appropriate to avoid polymer entrapment and shear degradation that results in viscosity loss [77].

Table 2.1. Polymer Mw effect on oil recovery [79].

Mw, 10^6 Daltons	% recovery by Waterflooding	% recovery by polymer flooding	% overall recovery
18.6	32.2	22.6	54.8
11	32.9	17.9	51.8
5.5	32.7	10.6	43.3

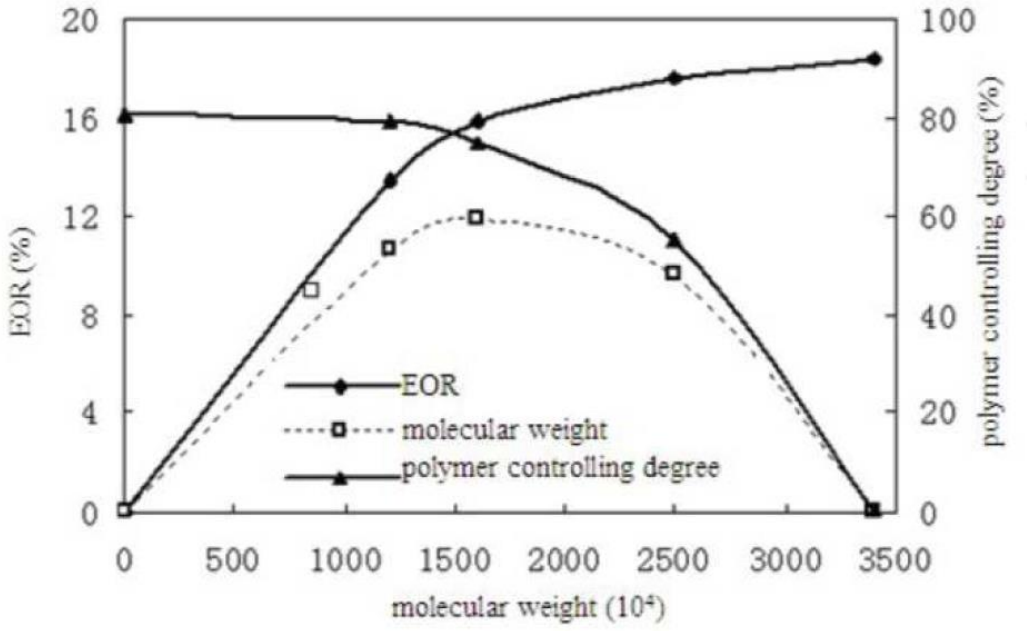

Figure 2.7. The polymer molecular weight versus oil recovery enhancement [80].

2.1.5.3. Polymer concentration

Polymer concentration is among the vital factor to consider when discussing its viscosity. Aluhwal and Kalifa [82] observed the effect of HPAM viscosity against various concentrations experimentally as shown in **Fig. 2.8**. According to the finding as concentration increases, the increase of apparent viscosity was observed. However, the rheological behaviour of tested fluid was separated into a semi-dilute and dilute region by a critical association concentration (CAC) or critical concentration (C*). In a semi-dilute region, the rheological properties of the polymer being controlled by the intermolecular associations around the chains of the polymers [83]. Generally, the concentration of polymer is directly proportional to the viscosity in which an increase in the polymer viscosity occur as its quantity increases, and vice-versa.

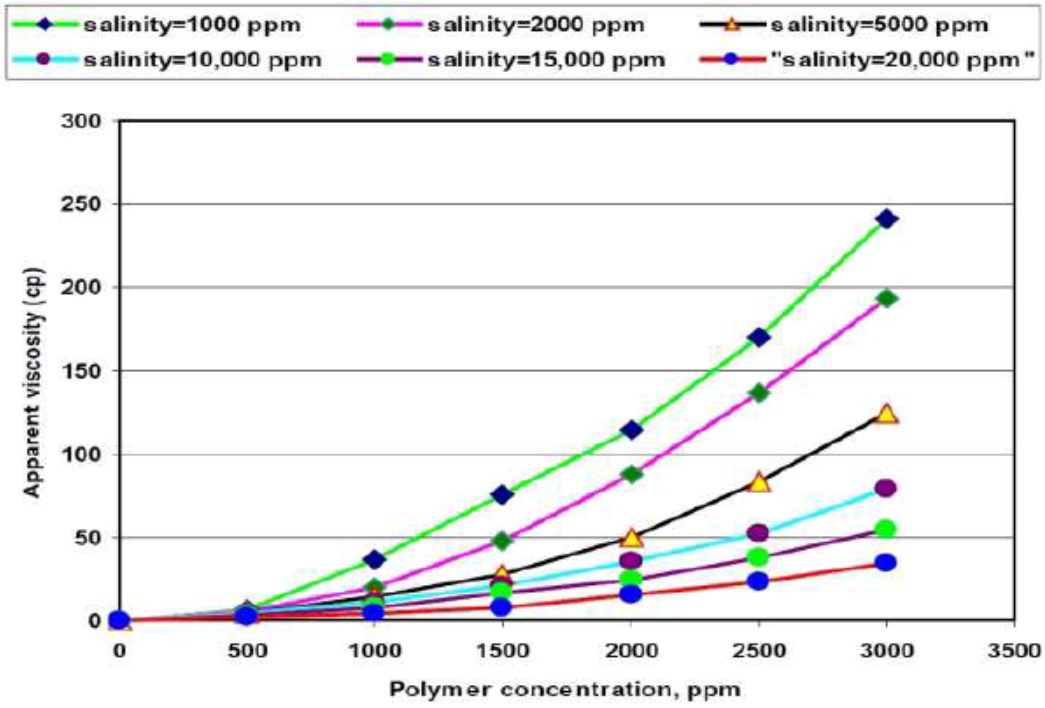

Figure 2.8. Polymer viscosity as a function of concentration and salinity [82].

2.1.5.4. Salinity

Polymer used in EOR is sensitive to salinity and that plays a significant role in the viscosity. When polymer, such as HPAM, is exposed to water with high salt content, it cationic and

anionic would have caused repulsion/attraction to the chain of the polymer, and compose a stretched or compressed like nature. If used in pure water or low salinity condition, the anionic group's electrostatic repulsion between polymers would be de-shielded, thereby allowing the polymer molecules to remain expanded. This makes it relatively hard to propagate through porous media and make the viscosity so high. On the other hand, when reaching the higher salinity, the electrostatic repulsion is shielded by the double electrolytes layer. This results in the polymer chains to stretch by decreasing the molecules, which consequently lower down the viscosity at higher salt content. As shown in **Fig. 2.8**, the influence of salt content was examined by Aluhwal and Kalifa [82]. They found that the apparent viscosity is lower at high salinity concentration, and the effect is strengthened with increasing polymer concentration. This is due to the electrostatic interaction between the charged groups.

2.1.5.5.Temperature

Water-soluble polymers are susceptible to temperature. As heat is applied, the polymer chains can undergo chemical or physical changes, which can result in unwanted changes to the significant properties of the polymer, leading to polymer degradation. In many cases, molecular degradation often called thermal degradation occurs due to overheating, especially when the polymer is subjected to high temperature. The long-chain molecular component of the polymer backbone begins to separate at a high temperature which can eventually cause molecular scission. Typically at a specific temperature, the strength of the bonds deteriorates and causes the attached elements on the polymer to be detached. Gao *et al.* [84] examined the effect of temperature on the apparent viscosity of HPAM as shown in **Fig. 2.9.** The results showed that the viscosity decrease with the increasing temperature. The higher temperature would necessarily continue to break down intermolecular hydrophobic associations changing the HPAM backbone and then hydrolyse its acrylamide group into acrylate groups.

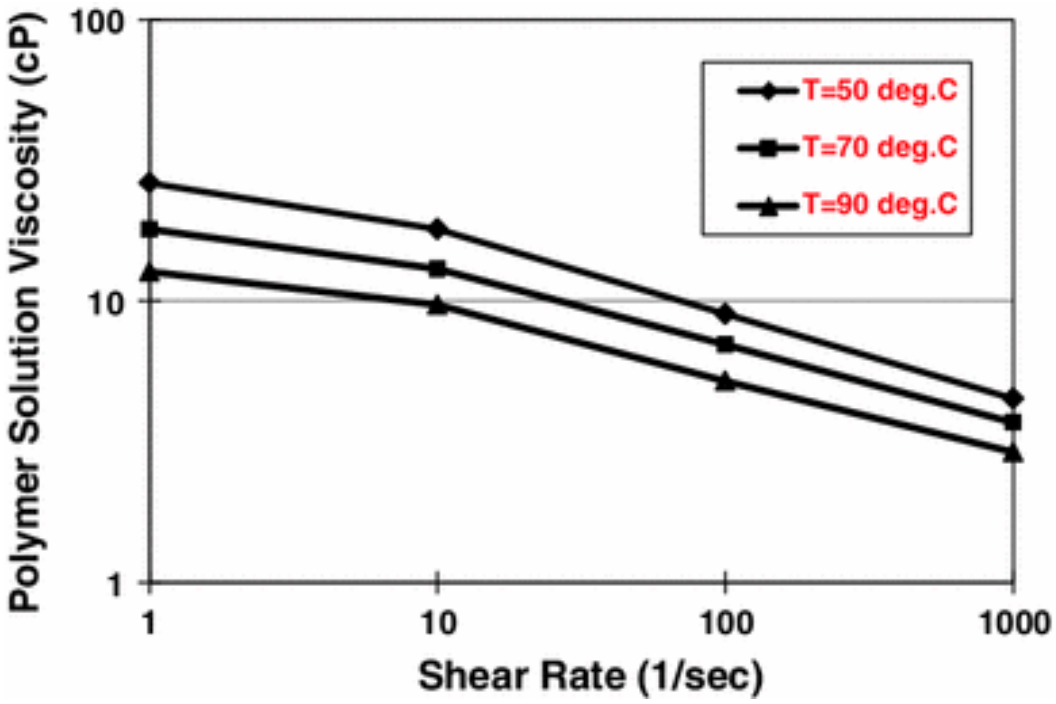

Figure 2.9. Effect of temperature on the HPAM viscosity [84].

2.2. Nanotechnology-based EOR

Nanotechnology refers broadly to a field of applied science and technology that deals with the control of matter on the atomic or molecular scales smaller than 1 µm, ranging normally within 1 to 100 nm [21-23]. Nanotechnology is the term that was used to cover construction, design, and utilization of functional structures with one characteristics dimension at least measured in nanometre. Nanostructure and nanotechnology are distinguished from other technologies by their unique properties regarding nanoscale proportion. In the coming years, it is believed that nanotechnology will open a door for many cutting-edge technologies [85].

Nanomaterials can be fabricated in two ways, "Bottom-up" process and "Top-down" Process. The nanofabrication using the "bottom-up" method depends on building nanostructure atom by atom or molecule by molecule using either manipulation of atoms or self-assembly technique by applying scanning probing microscopy [86]. The "top-down" method is more elementary and relies either on the division or removal of bulk material to produce the desired

structure with suited properties by minimizing the bulk fabrication process [85]. The method is based on microlithographic and physical philosophy, contrary to the "bottom-up" process where molecular or atomic units are used to gather molecular structures. In the "top-down" approach, different ways such as milling and lithographic process are used in the fabrication of nanomaterials [85].

Nanomaterials have a relatively large surface area in comparison to the material of similar mass, which can enhance electrical properties, strength, and better chemical reactivity. Secondly, the quantum effect can be domineering affecting the electrical, optical, and magnetic behaviour of materials [87]. In the nano-structural frame, the nanoparticle is the basic component that is smaller than commonly used daily objects (Newton law of motion) but larger than atoms or molecules regarding size (quantum mechanics). **Fig. 2.10** illustrated how nanoparticles could improve the surface area instead of bulk material.

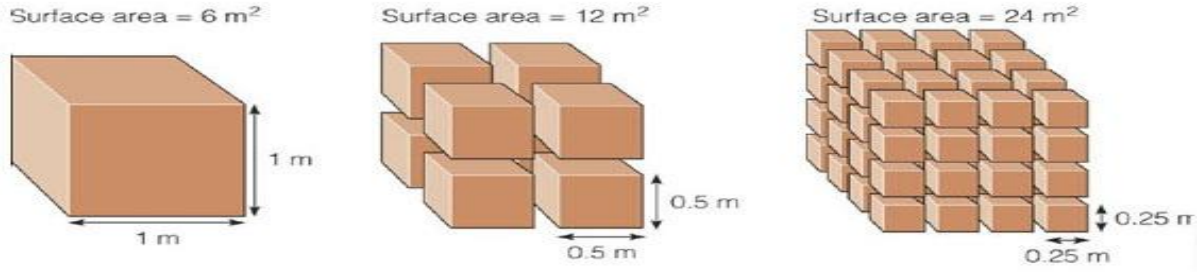

Figure 2.10. Surface area modified using nanoparticles

2.2.1. Factors (mechanisms) influencing nanotechnology for EOR application

Recently, many investigations have presented that, nanoparticles (NPs) overture promising prospective for the EOR process [88-94]. Depending on the flooding methods many possible mechanisms trigger the application of NPs in EOR, which include mobility ratio, interfacial tension, wettability alteration, disjoining pressure, particle retention, preventing asphaltene

precipitation, the appearance of climbing films, and nanocatalyst [95-99]. Overviews of some of the mechanisms are highlighted below.

2.2.1.1. Mobility control

The oil viscosity is considerably higher than that of injected fluid, and lack of good mobility ratio between the oil and injection fluid often results in viscous fingering which leads to inappropriate sweep efficiency [100-103]. Therefore, it is paramount to control the oil/water mobility to improve the sweep efficiency for higher oil recovery. The idea of adding NPs into the fluid was proposed to increase the viscosity up to the optimum level with net effect to improve mobility ratio and hence better oil recovery [104-107].

Due to the NPs addition, the solution becomes thicker because of the NPs ability to form a network structure through chemical bonding. Hu *et al.* [108] reported the use of SiO_2 NPs to improve the HPAM viscosity showing a promising future for nano EOR. Sharma *et al.* [109] also observed the viscosity increase by almost three times factor after 1 wt.% SiO_2 NPs was introduced in both polymer and polymer-surfactant solutions. In another finding addition of 3 wt.%, SiO_2 NPs into the fluid improved the solution viscosity and changed the overall flow profile to show shear-thinning behaviour [110]. Maghzi *et al.* [107] investigated the influence of SiO_2 NPs dispersion during polymer flooding. They reported that at high SiO_2 content the trapped oil can be mobilized easily, and the overall recovery efficiency is higher compared to the conventional polymer and waterflood.

Nanoclay has been used to enhance the solution viscosity and improved oil recovery by 11% during EOR [92]. Cheraghian *et al.* [111] reported a 5-6 % higher recovery after nanoclay was added to improve the solution viscosity. Metal oxide such as TiO_2 [112, 113], FeO [114] have also been reported to improve the injection fluid viscosity, which leads to better sweep efficiency during oil recovery.

NPs are reported to reduce oil viscosity, Ogolo *et al. [115]* observed a 12% increase in oil recovery by adding Al_2O_2 in a sand pack. One of their hypothesis was that Al_2O_3 had the tendency to decrease oil viscosity. However, there was no data provided showing the oil viscosity reduction. Therefore the mechanism was reported based on observation and assumption that Al_2O_3 is a good catalyst for heavy oil upgrading [116] Kashefi *et al.* [117] observed that addition of zeolite beta NPs into crude oil could reduce rock permeability of a sand pack. This phenomenon of oil viscosity reduction by NPs could increase the oil flow and consequently improved the mobility ration between oil and injected fluid.

The above review showed the promising perspective of NPs to improve the mobility ratio between oil and injection fluid, in which a solution containing silica-based NPs were frequently used. However, there is a lack of proper investigation on the NPs effect on the mobility control at reservoir conditions with high temperature and high salinity.

2.2.1.2. Interfacial tension

For more than 35 years, surfactant flood tertiary oil recovery have been employed, particularly in the depleted USA oil reservoirs after water flooding [118, 119]. Oil and water are two immiscible liquids that have high interfacial tension (IFT) between them. It has been examined that, introducing nanoparticles into the system will alter the IFT and show better potential for oil recovery enhancement [109, 120-123].

Several studies demonstrated the ability of NPs to reduce IFT. It has been reported that around 70-90% of oil/water IFT reduction was observed by using nonferrous metal nanofluid [112], while another report showed up to 91% of oil/water IFT reduction [124]. Frijters *et al.* [125] observed how the NPs adsorption mechanisms tend to affect the IFT compared to surfactants. They explained that surfactant adsorption at the interface was due to the hydrophilic head and hydrophobic tail while neutral NPs adsorption was due the less energy required for maintaining

the particle-fluid interface. It was reported that neutral NPs changed the IFT by applying a cheaper particle-fluid interface to replace the energetically fluid-fluid expensive interfaces. Free energy term F_σ can be used to illustrate these statements as a function of surface tension and oil droplet area as shown in **Fig. 2.11.**

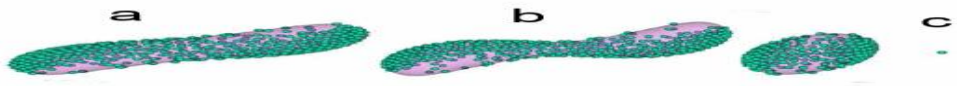

Figure 2.11. The breakup of oil droplets due to the adsorption of nanoparticles [125].

An experimental and theoretical study was performed on the induced effect of adding SiO_2 in natural surfactant adsorption on sandstone rock. Hydrophilic SiO_2 was less efficient than its hydrophobic counterpart in obstructing adsorption damage on to the shale-sandstone [126]. SiO_2 NPs were employed to change the adsorption of the surfactant on a rock surface. Based on the results obtained, the NPs addition lowered the surfactant adsorption on the rock surface and boosted the surfactant flooding performance. Hence, better oil recovery was observed [127]. The spinning drop was used to observe IFT reduction between brine/nanofluid and synthetic oil. 0.01 wt.% SiO_2 NPs lowered the IFT from 14.7 mN/m to 9.3mN/m. Further increase in particle concentration up to 0.05% decrease the interfacial tension to about 5.2 mN/m. In a similar experiment, 19.2mN/m was employed as reference IFT value for a brine-crude oil phase. Almost half decreased of this value was observed after 0.1 wt.% SiO_2 NPs were added to the solution [128]. From the above findings, it has been noticed that IFT is sensitive to the specific NPs.

NPs dispersion in the aqueous phase is reported to reduce the interfacial properties of the solution. Although NPs alone without surfactant has less implication on IFT reduction. Most of the studies investigated the NPs influence to reduce IFT between surfactants and oil during oil recovery. Notwithstanding, it could be immensely important to investigate the influence of

NPs on the IFT reduction of the solution containing polymers, especially when amphiphilic particles like graphene oxide are used to improve polymer performance.

2.2.1.3. Wettability alteration

The wetting preference idea of the rock for the ultimate oil recovery is a much more debated topic. The actual oil reservoir can be oil, intermediate, or water wet [90, 129] as shown in **Fig. 2.12**. Several researchers reported that production by water wet formation is more prepared than oil-wet formation [130]. While the production by intermediate wet formation is better than water wet formation [131]. Most oil production will occur before water breakthrough in the water-wet system, after which the rate will decline. Certainly, in an intermediate or oil-wet system, the water breakthrough will occur earlier than in the water-water system. Haven a reliable wettability modifier with improved mobility properties is important in EOR. Many studies proposed the use of NPs to alter the wettability in EOR because of its possible applications under broader oil reservoir conditions [89].

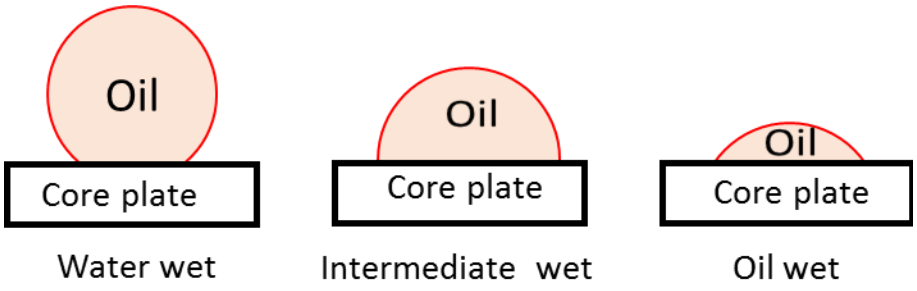

Figure 2.12. Wettability alteration conditions of a rock/brine/oil system.

Change of rock wettability and its effect by the use of NPs has been reported by several authors [115, 130, 132-139]. Karimi *et al.* [140] reported that the nanoparticle addition into the solution alters the wetting from oil-wet to strongly water-wet condition. The oil recovery and nanoparticle transport system was investigated, the lower particle concentration provides more oil recovery compared to higher particle concentration. A maximum of 33% increase in oil

recovery was observed after water flooding with 20 ppm concentration of rutile TiO_2 nanoparticle-assisted brine flooding. This phenomenon was believed to be observed by the possible wettability changes, improvement in the mobility ratio, and log-jamming effect [123]. Although, TiO_2 showed a rapid reduction in oil-water/rock contact angle, in another work AlO_2 showed more contact angle reduction than TiO_2, proven better EOR potential [141]. A similar study was performed to investigate the effect of TiO_2 and Al_2O_3 on wetting behaviour in comparison with the SiO_2 NPs. The finding showed that TiO_2 provides a high impact on oil recovery than SiO_2 and AlO_2 [142].

Li *et al.* [143] observed the increase in oil wetness using hydrophobic and hydrophilic SiO_2 NPs in neutral wet sandstones. The nanoparticle is driven by the bulk pressure to decrease the contact angle, hydrophilic/hydrophobic nanoparticles increases the wettability alteration at high particle concentrations while surface wettability was measured by the contact angle. Flooding experiment was conducted at ambient pressure and temperature to monitor the effect of wettability alteration by SiO_2 NPs as a dispersant, the oil recovery was observed to be 8.7% higher than that of conventional water flooding which was believed to be as results of the change in porous media wettability [144].

The influence of particle concentration on wettability was also studied by other researchers. Vafaei *et al.*[145] reported the effect of bismuth tellurite NPs concentrations on contact angle. It has been revealed that the contact angle increased with increasing NPs concentration followed by a decrease after the critical concentration was reached. The results indicate that the contact angle as a function of particle concentration was dependent on the size and size distribution of the particle. At the same concentration, a larger variation in contact angle in particle with smaller size [145]. Hendraningrat *et al.* [88] also reported the influence of lipophobic and hydrophilic (LHP) SiO_2 NPs concentrations on the wettability alteration. As

shown in **Fig 2.13**, the contact angle decreases with the increase in concentrations of the NPs, and the wettability also changes to more water-wet. The smaller size NPs are found to have more impact on contact angle reduction because of the higher electrostatic repulsion. Moreover, changes in wettability could be a result of salinity, exposure time, a solid system, ionic composition [146]. Some evidence has shown NPs can alter wettability in both sandstone [147] and carbonate rocks [148].

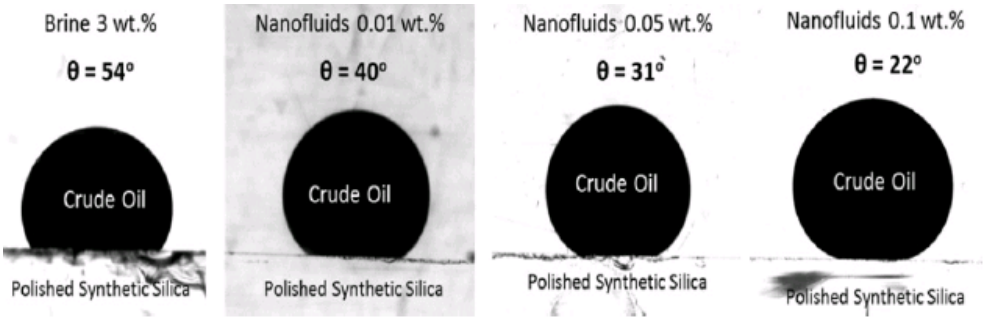

Figure 2.13. Contact angle variation with the change in nanoparticle concentrations [88].

2.2.1.4. Structural disjoining pressure

The effect of structural disjoining pressure (SDP) was proposed by Wasan and Nikolov [138]. The forces that drive this phenomenon are electrostatic force, Van der Walls force and Brownian motion [138, 149]. The NPs with smaller size has bigger electrostatic repulsion between them which results in larger SDP. As the number of particles increases, the working forces on the wedge film will also increase [138].

When NPs are dispersed in a fluid (aqueous) approach hydrophilic solid surface, the NPs will arrange themselves orderly with the solid-like structure at the three-phase contact region (**Fig. 2.14**). This arrangement when it is towards the bulk phase it becomes more disordered and attains a fluid-like structure. Studies have shown that in the confined region, pressure rising from such an ordering manner will enhance the spreading of NPs behaviour [138]. The particles that are in the three-phase contact region will contribute to generating a wedge-like structure

and push themselves to stay in between the solid rock and discontinuous phase. The available particle in the bulk fluid will employ a pressure that forces particles towards the wedge structure forward. This kind of force applied is known as SDP or film tension gradient [149]. An experiment was conducted and revealed that NPs that contained in the three-phase region between oil, water, and rock tend to force themselves to be placed between the solid rock surfaces and a discontinuous phase. A wedge-like structure is formed by the particles, which performed some action to separate the fluid (oil) from the pore wall and spreading behaviour of nanofluid resulting in SDP[106, 149].

Because of that structural force, NPs could display a good ability to spread in a confined space. Which was observed to (a) stabilized liquid films [150], (b) change the microscopic contact angle of a liquid droplet [145], and (c) lift an oil droplet from the wall in an aqueous solution [137, 139]. In general, SDP is considered an important mechanism that describes the surface force which is suitable for thin liquid films.

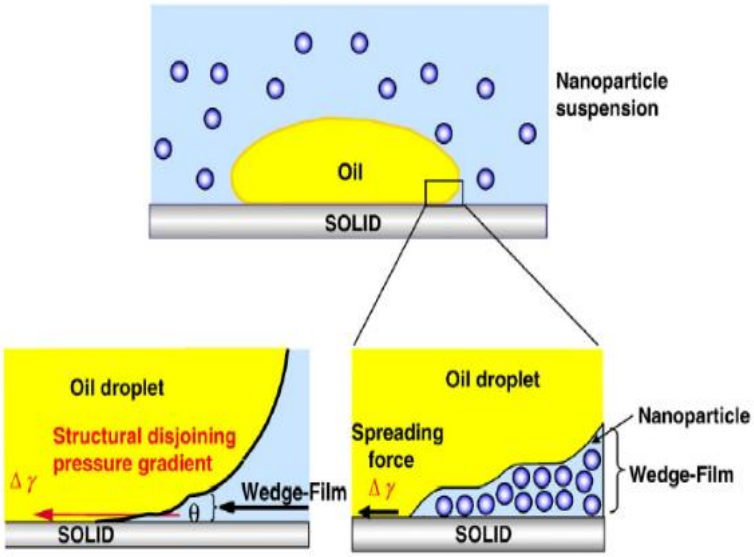

Figure 2.14. Nanoparticle establishing a wedge-film resulting in structural disjoining pressure [151].

2.2.1.5. Retention in porous media/pore channel blockage

Pore channel blockage caused by either log-jamming and mechanical entrapment [152]. Mechanical trapping occurs when the pore channel is smaller than the diameter of the injected material, while log-jamming occurs due to the plugging as the accumulation of the material inside the pore channel (**Fig 2.15**). Core flooding experiment performed by Li *et al.*[147] showed NPs to have a greater tendency of altering the porosity and permeability of the porous rock. The transport of NPs to the porous media is governed through hydrodynamics, convection, and diffusion. At the beginning of the flooding, adsorption and desorption of particles occur at the pore wall [147]. It is the combined forces of hydrodynamics, Born repulsion, van der Walls forces, the repulsion between electrical double layer (EDL) and acid-base interaction that play a role in this process. In this, the dynamic balancing process could reach an equilibrium state, and here the NPs can move through pore systems with fewer or no adsorption and diffusion.

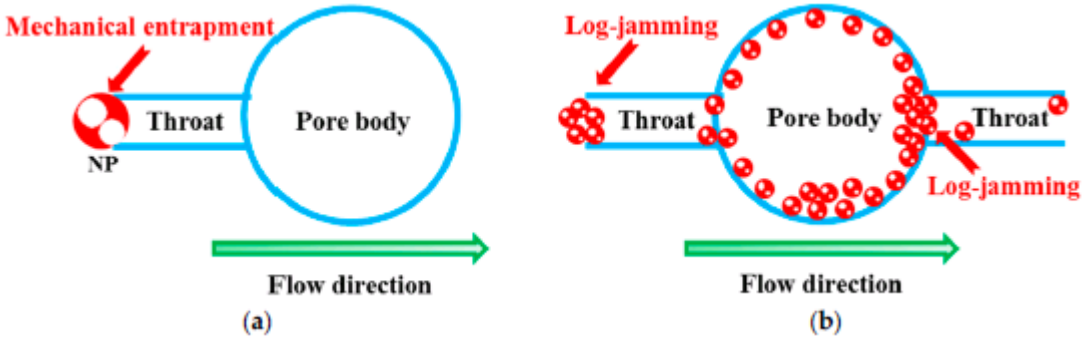

Figure 2.15. The schematic of two mechanisms causing pore channels plugging: (a) mechanical entrapment; (b) log-jamming [153].

The size and shape, the flow rate, the concentration of suspended particles, and the chemistry of carrying fluids also control the migration and retention of solid particles in the porous media [154, 155]. Skauge *et al.* [152] demonstrated an experiment in which SiO_2 NPs propagate through a pore system so quickly, and pose no damage to the environment due to their natural

existence in the reservoir. They cannot also strain or block pores because they are too small, which makes them preferable for EOR applications [152].

The flows of a nanofluid from pores to throats, lead to an increase in fluid velocity due to the differential pressure effect and narrowing of the flow area. Due to the smaller size of water molecules, it flows faster than NPs in the pore channel, causing the NPs to accumulate at the pore throats entrance as shown in **Fig 2.16**. Due to log-jamming, this accumulation will result in blockage of small pore throats which lead to the building up of the pressure in adjacent pore throat and thereby forcing to oil to be trapped. The NPs start to flow once the plugging starts to disappear after the oil is freed [106, 152]. The effect of NPs on the log-jamming phenomenon was examined by Hendraningrat *et al.* [88] during single-phase flooding on the water-wet system. They observed that the impairment of permeability and porosity in the core plugs increases when the concentration of nanofluids increases.

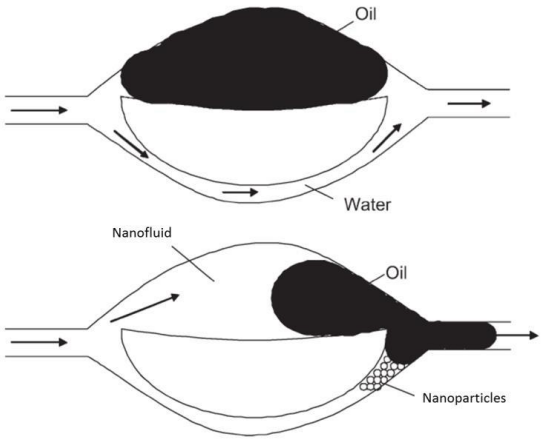

Figure 2.16. Schematic of pore channel plugging caused by log-jamming [152].

2.2.1.6 Summary of the nano-EOR mechanisms

According to the above review on different NPs mechanisms for EOR, many studies have demonstrated that NPs could improve oil recovery efficiency. As summarized in **Table 2.2** majority of the reported literature proposed more than one mechanism for nano-EOR based on

assumption and experimental analysis. Therefore, it could be the most acceptable idea if agreed that the nano-EOR is derived by the combination of different mechanisms. But which mechanisms are the dominant? Which of the mechanisms are dependent or independent on one another? According to the summary in **Table 2.2,** wettability alteration may seem to be the most acknowledge and highly influential mechanism of nano-EOR. Some works of literature reported the reduction in IFT, some analysis reported the effect of SDP and log-jamming. However, mobility control appears to be the most important mechanism in polymer flooding EOR.

One can conclude that most of the reported studies by different researchers are not all consistent or rather in conflict with one another. This conflict arises as a result of using some surfactant or surfactant-like substances along with the NPs in the same fluid. This surfactant would equally alter rock wettability as it does for IFT. Another possible reason lack of clear understanding of the nano-EOR mechanisms, and lack of experimental control.

The majority of the EOR mechanisms reported as a result of NPs into water (without polymer or surfactant) are complex and might be a combination of log-jamming effect, increasing fluid viscosity, or wettability alteration from oil-wet to the more water-wet system. Although the majority seems to agree the change in wettability is the most dominant mechanism in the situation where only NPs are used without surfactant or other chemical agents.

The influence of NPs on IFT reduction is perhaps insignificant when stabilizers or other surfactant-related chemicals have been included in the NPs solution, but it can enhance the surfactant ability to reduce IFT, although it could not alone reduce the IFT significantly. Therefore, in this case, it is less likely to agree that the IFT reduction is influenced by NPs addition.

Some studies showed a promising perspective of NPs such as metal oxide and SiO_2 to improve the mobility ratio between oil and injection fluid. Although NPs alone did not significantly increase the water viscosity when mixing with polymeric material the viscosity increases. However, there is a lack of proper investigation on the NPs effect on mobility control at the high salinity condition of the reservoirs. Metal oxide NPs are reported to reduce the oil-phase viscosity, which helps to improve the mobility ratio.

Log-jamming is recorded as a possible nano-EOR mechanism. Nonetheless, log-jamming may also affect the oil recovery in a negative way by reducing the amount of the produced oil, because NPs blocking the pores may decrease the permeability. When the NPs have high concentration and/or big size which will results in permeability reduction due to a log-jamming effect, and consequently lower the oil production.

The majority of the reported literature focussed on using SiO_2 NPs to improve the performance of EOR fluid, however, a large amount of SiO_2 is commonly used to achieve a targeted concentration. This results in SiO_2 NPs to agglomerate or even precipitate if they are not carefully dispersed, which greatly decreases NPs potential for field application. Therefore, there is a need to explore a way to improve the SiO_2 performance at a smaller concentration.

Although some other studies were performed to evaluate the influence of metal oxide NPs and demonstrated their capability as EOR agents, and evaluate their advantage over SiO_2 based fluid, but there are still some discrepancies among themselves that limited their use in EOR. In this regard, the influence of other NPs such as graphene oxide (GO), carbon NPs should be explored to understand their potential use in EOR.

Table 2.2. Summary of the study of nanofluid EOR and mechanisms.

NP Type	Fluids	NPs concentration	Mechanisms	EOR (%)	Source
TiO_2	Surfactant	0.001 wt.%	Reduce IFT Decrease θ Increase μ	12–17	[112]
ZrO_2	Water	0.05, 0.10 gr/cc	Decrease θ	10	[140]
SiO_2	Surfactant	10 vol. %	Reduce IFT Decrease θ	33	[124]
SiO_2	Water	0.1 mass %	Reduce IFT Decrease θ	23.5	[122]
SiO_2, Al_2O_3	Polymer	0.05 mass %	Decrease θ Reduce IFT Log-jamming	7-24	[88]
SiO_2	Water	3 wt. %	Change SDP Change θ Log-jamming	5-35	[106]
SiO_2	Polymer Polymer-surfactant	1 wt. %	Reduce IFT Change mobility	21	[109]
TiO_2	Brine	10–500 ppm	Change θ Change mobility Log-jamming	9.5-13.3	[123]
ZrO_2, NiO	Water	0.004–0.05 wt.%	Change θ		[132]
SiO_2	Water	1.0 wt.%	Change θ	8.7	[133]
SiO_2	Water	10 wt.%	Reduce IFT Decrease θ	22	[149]
SiO_2	Water	3 wt.%			[130]
Al_2O_3, ZrO_2, MgO, Fe_2O_3, SnO, SiO_2, Ni_2O_3, ZnO	Ethanol, brine, and Water	0.3	Reduce IFT Change mobility Change θ	12	[115, 156]
SiO_2	Polymer	0.1 wt.%	Change mobility	10	[107]
TiO_2	Brine	0.01 and 1 wt.%	Change mobility Reduce IFT	51	[113]
LHP SiO_2	Brine	0.1 wt.%	Change θ	10	[134]
HLP & LHP SiO_2	ethanol	0.1–0.4 wt.%	Change θ	19.31	[135]
Fe_2O_3, Al_2O_3	propanol	0.05–0.3 wt.%	Change θ Reduce IFT	22.5	[141]
ZrO_2, CeO_2, MgO, CNT, TiO_2, $CaCO_3$, SiO_2, Al_2O_3	Brine	5 wt.%	Change θ Reduce IFT	8–9	[90]
Al_2O_3, TiO_2, SiO_2	Brine	0.05 wt.%	Change θ Reduce IFT	7–11	[142]
TiO_2	polymer and water	1.9–2.5 wt.%	Change mobility	4	[92]

			Reduce IFT		
Nanoclay	Water	0.9 wt.%	Reduce IFT Change θ	5.8	[93]
SiO_2	Water	3 wt.%	Change θ Reduce IFT	29	[106]
SnO_2	Water	0.1 wt.%	Change θ	22	[94]
SiO_2	Polymer	5 wt.%	Increase viscosity	NA	

2.3. Polymer nanoparticle interactions

Polymer systems are used extensively in different industrial applications due to their unique characteristics. These characteristics include lightweight, ductile nature, and ease of production. However, polymers can have lower strength and modulus as compared to ceramics and metals. To enhance their properties, such polymers have to be reinforced with inclusions (particles, whiskers, or platelets) [157]. Using this approach, properties of the polymers can be improved and at the same time maintain their ductile nature and lightweight [157]. Improving properties can be found so often even at nearly low filler content. Depending on the particle shape, size, chemical nature, and specific surface area, the properties of polymers can be improved [158].

Therefore, polymer and NPs mixing becomes the breach pathway for flexible engineering composites. Such improvements are induced by the physical presence of the NPs, and polymer-particle interaction and the state of dispersion [159]. Polymer nanocomposites are at the lead of advanced materials applications, where the incorporation of dispersed NPs into a polymer matrix renders materials with tailored and controlled properties without compromising the processing ease of the parent polymer [105, 160].

2.3.1. Polymer nanocomposite preparation

Polymer nanocomposites can be fabricated either by a mechanical or chemical process. One of the major problems in polymer nanocomposite preparation is achieving homogenous and uniform dispersion of nanoparticles in the polymer matrix [159]. The nanofillers have a tendency to form micro size and aggregate clusters, limiting the nanoparticle dispersion in the polymer and hence deteriorate the properties of the nanocomposites [158, 159]. Many attempts have been made to homogeneously and uniformly fabricate polymer matrix by the polymerisation reaction, chemical reaction, or surface modification of filler materials [161, 162]. The following methods are used for the fabrication of polymer nanocomposites.

2.3.1.1. Direct mixing or *ex-situ* process

Direct mixing involved the breakdown of aggregated particles while mixing [161, 162]. This method consists of two main ways; *melt compounding* and *solvent method*.

Melt compounding method: This process involves the mixing of polymer without any solvents followed by the nanofillers addition into the polymer solution [161, 162]. In this method the hydrodynamic force (shear stress) is induced in the melt polymer by viscous drag, thereby using the shear stress to breakdown the particle aggregates, leading to the homogeneous dispersion of polymer nanocomposites.

Solvent/solution method: This method involves mixing nanoparticles and polymer with solvents. The nanoparticles are dispersed in a solvent and polymer is dissolved in a co-solvent. The nanocomposites are then collected via solvent coagulation or a solvent evaporation method. The shear stress in this method is lower than that of the melt compounding method. In order to breakdown the particle aggregate the NPs are pre-dispersed in the solvent followed by sonication [162].

The process involved using magnetic stirrer or ultrasonicator. The sonication could be either high-power sonication using a tip or horn, or mild sonication in a bath. An early experiment conducted to prepare polymer and nanotube using direct mixing and found to have a good dispersion [163-166]. Hu *et al.* [108] prepared the hybrid suspension of SiO_2 and HPAM via direct mechanical mixing and a solution with good dispersion was obtained under the influence of 8 wt.% NaCl. The solution of different acrylamide-based polymers with MWCNTs was prepared via a direct mixing technique [167].

2.3.1.3. *In-situ* polymerization method

In-situ polymerization methods consist of the NPs dispersion into the monomer followed by polymerization process under the influence of free-radical initiator [162]. The monomer is polymerized between interlayers to form either intercalated or exfoliated nanocomposites. In a similar method which is called *in-situ* template synthesis, the NPs are synthesized in the presence of polymer chains. Both NPs layers and polymer matrix are diffused in an aqueous phase and the gel undergoes refluxed under high temperature. The nucleation and growth of NPs occur after the polymer chains are trapped inside the particle layers at high temperatures. The major limitation of this method is the polymer decomposition causes by high temperature [162].

Jia *et al.* [168] produced CNT/PMMA based composite via *in-situ* radical polymerization using 2,2-azobisisobutyronitrile as a free-radical initiator. They found that the CNT π-bonds were opened to form a network with PMMA molecules which lead to homogenous dispersion of the composite. Cheng *et al.* [169] conducted the preparation of transparent nanocomposites of *N*, *N*-dimethyl-acrylamide, styrene, and divinylbenzene with ZnS NPs via free-radical polymerization using 2,2-azobisisobutyronitrile as initiator. Many NPs such as TiO_2, ZnO, and CdTe have been

incorporated into polymer matrices to form a composite by *in-situ* polymerization methods [169-176].

2.3.2. Polymer nanoparticles used in EOR

In an attempt to surmount the multiple limitations of polymer EOR, recently, making polymer nanocomposites with highly dispersed inorganic particles has attracted great attention due to their excellent properties, such as mechanical toughness, large deformability, thermal stability, etc. [177-187]. They have been reported to dramatically affect the melt [188, 189], and solution [184, 190] viscosities, and rheological behaviours of polymeric materials. Thus, the application of NPs inclusion in the polymer EOR process to improve the rheology and stability is reviewed below.

2.3.2.1. Rheology

Rheology is the study of flow and deformation behaviour of the material under the applied force, which is frequently, tested using a rheometer. Therefore, in EOR, the oil viscosity is considerably higher than the injected fluid viscosity, and water-soluble polymers were widely used in EOR processes to boost the fluid viscosity because of its cost-effectiveness and good rapport with other chemicals [102]. Consequently, the application is still limited to certain conditions of the reservoir as explained in **Section 1.2**. However, adding NPs into the fluid will improve its efficiency and increase the viscosity up to an optimum level with net effect targeting improved mobility and hence better oil recovery efficiency.

SiO_2 is the most widely applied NPs to improve the rheological performance of polymers used in EOR [101, 107, 191, 192]. For example, Saito *et al.* [110] investigated the effect of adding 3 wt.% SiO_2 NPs into a polymer solution and found an improvement in the solution viscosity and changed in the overall flow profile displaying a shear thinning behaviour. Dingwe Zhu *et*

al. [48] demonstrated the rheology and flooding experiment with HAPAM/SiO_2 hybrid; the hybrid exhibits better viscosity and more heat and salt tolerance than HAPAM alone, this improvement is as a result of hydrogen bond formation between the hybrids. Similar results were observed in HAHPAM/SiO_2 solution with a better increase in apparent viscosity and elastic modulus and more oil recovery compared to pure HAPAM solution [63]. Hu *et al.* [108] found that there is a formation of a bridge between SiO_2 NPs and HPAM which enhanced the rheological properties of HPAM. In another experiment, the addition of 0.1 wt.% SiO_2 into the HPAM solution increases its viscosity showing a promising future for the EOR application [193].

SiO_2 NPs was used as a thickening additive for high molecular weight anionic PAM and HPAM which are commonly applied as EOR mobility controllers. In contrast to the above finding, SiO_2 has less impact here, and it may even cause a reduction in viscosity because the interaction between the SiO_2 and polymer matrix is not properly monitored. However, these finding doubt the applicability of combining SiO_2 and high molecular weight PAM/HPAM solution, more specifically at the reservoir with high salinity. But surface treatment can alter the behaviour of the polymer by introducing partial attachment of the hydrophobic group to reduce the unwanted interaction between the SiO_2 NPs and polymer [194].

Other NPs that are used to improved polymer rheological properties include TiO_2 [92, 195], CNTs [105, 167, 196], nanoclay [100, 101, 184, 197-199], layered double hydroxide [200-202], and iron oxide [203]. High and low molecular weight polyisobutylene in decalin solution was used in combination with hydrophilic and hydrophobic TiO_2 particles to investigate the shear viscosity behaviour. In both cases, viscosity increase was observed with less effect at a high shear rate. Classical rheological behaviour was observed with the Newtonian plateau followed by the shear-thinning region using TiO_2/polymer composite. However, the plateau disappears after the solutions were filled with particles, even at low volume fraction (e.g. 4 wt.

%). The viscosity increase was noticed actively as the shear stress decreases, and therefore at a low-stress level, the viscosity-shear stress curves are concave upward [195]. It has been reviewed that the polymer/CNTs composites rheological properties were improved due to the establishment of a state of the dispersion of the CNTs in the mixture [105]. Anthony *et al.* [203] conducted experiments to improve the magnetic NPs (iron oxide) mobility using polymers and surfactants, their finding suggests that addition of only 0.1 wt.% polymers and surfactant will significantly improve the mobility of NPs in the porous medium. Laponite XLG clay was used to evaluate the fracture-plugging and mobility control of polymer in mature the reservoir. The clay addition improved the polymer viscosity effectively leading to better sweep efficiency, thereby improving the recovery efficiency [100, 101]. In another experiment, Cheraghian *et al.* [197] showed that the addition of nanoclay to PAM had positive effects on the viscosity properties of the polymer solution.

Some studies have shown that the inclusion of NPs into polymer matrices could cause viscosity reduction [204-208], in clear disagreement with the expression developed by Einstein [209]. This phenomenon brings great attention to controversial explanations and perceptions [210-215]. It has been observed that the radius of nanoparticles, their radius of gyration, and the molecular weight of the polymers are the leading factors affecting the behaviour of the polymer-nanoparticle composites [204-206]. According to studies by Mackay and co-workers [204-206], viscosity reduction occurred when the polymer molecular weight was larger than the entanglement molecular weight and the inter-particle half-gap was smaller than the gyration radius. Other studies show that degradation of the polymer [216, 217], adsorption of polymers with high molecular weight [218], constraint release of the entangled polymer chain [205, 206, 215], free volume expansion induced around the NPs [205, 206], changes in the entanglement density of polymer chains [208] and slip between the sample and the geometry during

rheological testing [219] are possible mechanisms that enable viscosity reduction in polymer–nanoparticle composites.

In this section different NPs have been reviewed to improve the rheological performance of EOR polymers, some NPs showed less performance and may course reduction in viscosity. Even SiO_2 which is the most commonly used NPs in this process, if not carefully dispersed it may cause a reduction in polymer viscosity. Therefore, careful consideration of the composites' preparation method has to be given. Also, other NPs types that can form a strong linkage with EOR polymers has to be explored. Furthermore, there is a lack of an in-depth understanding of the key process-structure-property relationships, which are required to understand the chemistry of these novel materials fully.

2.3.2.2. High temperature-high salinity Stability

Thermal stability is an important factor in the polymer flooding process. Also, polymer and polymer nanocomposites stabilization in an aqueous environment with extreme salinity (high ionic strength) has been considered recently as a key subject in the research. For instance, in the petroleum industries, nanomaterials have been recently proposed to deliver into oil reservoirs acting as sensors or imaging enhancers to provide useful information regarding the reservoir condition. However, applying polymer nanocomposites into the reservoir is a challenging task due to the high salinity and high temperature of the environment, which can easily destabilize the injected nanomaterials. Several approaches such as physical dispersion methods, covalent bonding, and non-covalent bonding methods have been implemented to address this stabilization issue. In recent years, the improvement of polymers stability by modification of the structure or by the use of NPs has gained a great interest [34, 35, 63, 220, 221].

Earlier studies have demonstrated the potential of CNTs, which would improve the stability of the polymer solution [222-224]. However, the ability of CNTs to forms π-π interactions and strong Van der Waals force makes it prone to forming an insoluble solution with many media and forms tight bundles [225, 226]. An experiment conducted by Han *et al.* [227] to analyse the phenomenon of polymeric stabilized MWCNTs and its transport behaviours through a saturated column of quartz sand consisting of humic acid as a natural organic matter, model clays, and electrolytes materials. The results showed that pure MWCNTs without polymer inclusion were vulnerable to electrolyte effects and much less transportable, compared to polymeric stabilized MWCNTs. Functionalizing of CNTs with nitrene cycloaddition reaction has been used for the modification of CNTs to increase solubility and stability in aqueous solution [222, 223]. But none of the investigations was conducted using polyacrylamide or its derivatives, and neither in HT-HS conditions.

A composite of carbon NPs and ionic polymer (Poly (vinyl alcohol)) was shown to be stable in API brine. The polymer was grafted onto the NPs surface by acidic treatment using chlorosulfonic acid. It has been reported that the NPs that are partially sulfonated showed better dispersion stability at 100 °C in API brine than highly sulfonated NPs, while unsulfonated NPs were not dispersed. The long-term temperature stability, however, was not examined, which prevented their use as reservoir sensors [228]. Vanso *et al.* [229] also observed the stability of polyimidazole betaine in 22.6 wt. % NaCl solution without reporting long-term thermal stability. Johnston and co-workers [230] attempted to stabilize nanocomposites containing poly-acrylate/acrylamide-type polymers and iron oxide NPs wrapped with sulfonic salt in reservoir conditions with API brine for one month at 90 °C. The finding showed that the stabilization was favoured by the ionic nature of the polymer and NPs repulsion against agglomeration.

SiO_2 NPs have been widely investigated to improve polymer stability owing to their availability and easy surface functionalisation nature [48, 108, 231-233]. As shown in **Fig. 2.17** Hu *et al.* [108] demonstrated that the formation of a bridge and hydrogen bonding between SiO_2 NPs into HPAM molecules led to the improvement of temperature stability after aging at 80 °C for up to 12 days, but the effect of complex brine solution was not investigated due to the aggregation of the polymer solution, this improvement was due to the formation of a hydrogen bond between silanol functionalities of SiO_2 and PAM amide groups. It was also observed that SiO_2 could improve the PNIPA viscosity at high temperature through carbonyl groups of the polymer acting as physical cross-linker between macromolecules, thereby reinforcing the structure of the polymer to provide better mechanical properties [231, 232]. However, none of the studies investigated the long-term thermal stability and effect of complex brine solution. It has been observed that under a high ionic strength of brine, the SiO_2 NPs start to agglomerate causing large numbers of silanol groups that shelter the SiO_2 surface to create aggregates of NPs in the polymer solution. This lack of good SiO_2 dispersion was likely due to their preferred face-to-face stacking in agglomerated/aggregated tactoids [233], which leads to severe agglomeration and sedimentation in a harsh environment [234]. Also, when SiO_2 NPs and a polymer are mixed, it takes a long time to form a well-dispersed mixture, which greatly decreases the potential field application of NP-based systems [48]. It has been shown that the hydrophilic nature of SiO_2 NPs decreased the physical strength to interact with the polymer matrix that has hydrophobic structure, making the dispersion more difficult in HT-HS conditions [235, 236].

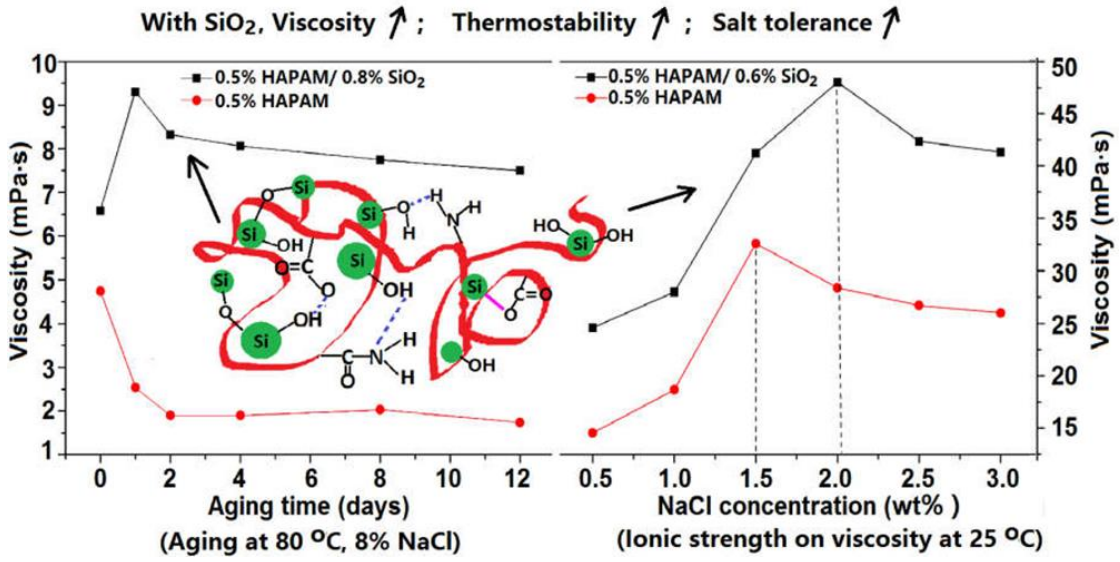

Figure 2.17. Influence of SiO_2 on long-term temperature stability and salinity tolerance of HPAM [108].

Several approaches, including grafting of polymers, chemical (through covalent bonding), and physical (through physisorption) strategies are previously used for surface modification [237, 238] to reduce the stability challenge. Jafarnezhad *et al.* [194] also consider surface treatment to alter the behaviour of the polymer by introducing partial attachment of the hydrophobic group to reduce the unwanted interaction between the SiO_2 NPs and polymer. But all these approaches have different limitations. Therefore, surface modification and stability in the presence of complex salt remain a debated topic.

However, to address the challenges facing SiO_2 dispersion into the polymer solution, there is need to produce a novel surface modification approach to produce well-dispersed SiO_2 dispersion is proposed, and use them for *in-situ* synthesis of a copolymer of acrylamide (COPAM) to form a stable nanocomposite. This can be achieved by creating a positively charged active sites on the NPs surface. In addition to the conventional hydrogen bonds, positively charged surfaces allow strong coordination bonds with the polymers' negative charged side chain, reinforcing its stability under HT-HS conditions.

Additionally, there is a need to explore the applicability of different other NPs with distinguished mechanical, thermal, and electrical characters such as graphene oxide (GO). Not directly related to EOR, several investigations showed a strong interaction between GO and polymers, due to its layered structure and a large number of oxygen-containing groups (i.e. carboxyl, epoxide, and hydroxyl) on its surface [239], also, shown to improve polymer physical and mechanical properties [240, 241]. GO/polymer composites have been assembled via chemical cross-linking to generate a self-assembled network that led to their application in various systems [242-248]. These improvements are a result of strong interfacial interaction between polymer matrix and GO [249, 250], high conductivity, large surface area, and atom-thick two-dimensional conjugated structures of GO [242].

2.4. Summary of the state-of-the-art

The application of the polymer flooding has been reviewed in this Chapter, which shows better performance compared to the water flooding process. However, despite promising achievement in polymer EOR, many drawbacks hinder the application at harsh reservoir conditions, causing polymer degradation and instability due to HT-HS conditions of the reservoirs.

Nanotechnology has been recently used for EOR with various mechanisms proposed. It has been used with a polymer to form composites to improve the polymer EOR efficiency.

Polymer nanocomposite using different NPs such as SiO_2, TiO_2, CNTs, clay, and iron oxide NPs have been investigated. Despite promising achievements in terms of increasing polymer viscosity and stability to some extent, the following areas still need to be addressed.

- There is a limited investigation on different polymers and NPs types. Therefore, exploring the applicability of other NP types with distinguished mechanical and thermal properties is required.

- Processing polymer nanocomposite should be carefully considered to achieve a long-lasting and stable dispersion of NPs into the polymer solution.
- For EOR applications, however, the stability of these nanocomposites have to be examined under high temperature and high saline conditions. Some studies showed that under a high ionic strength of brine, NPs start to agglomerate and create aggregates of NPs in the composite solution.
- Some NPs such as SiO_2 takes a longer time to form well-dispersed in polymer solutions, which greatly decrease the potential field application of NP-based systems. This issue needs to be addressed.
- There is a lack of in-depth understanding of the key process-structure-property relationships, which are required to understand the chemistry of these novel materials fully.
- Some NPs need higher concentration to achieve a target viscosity while other particles may cause a reduction in polymer viscosity. Finding NPs that can contribute to high viscosity at lower concentrations would be needed. Also, there is a lack of understanding of the mechanisms behind the viscosity reduction by some NPs.
- Most of the studies did not investigate the effect of long-term thermal, brine, and dispersion stability. Proper stability analysis is of great importance to fully understand the composite EOR potential.

The overall aim of this project is to improve the stability, rheology, and flooding performance of polymers in HT-HS conditions by two approaches, i.e., reinforcing polymer chains with desirable NPs to form composites and engineering new temperature-resistant polymers. In addition, a novel synthesis approach to produce suitable nanoparticles *in-situ* in polymers will

be developed to further improve the polymer performance. Base on the above summary, the following novel ideas will be considered in this project.

- As many of the current investigations focus on SiO_2 and metal oxides NPs, research in this thesis will explore the potentiality of new NPs (GO and CQDs) that have not been investigated previously to examine their applicability in rheology, stability and EOR performance under HT-HS conditions. This will include the modification of nanofluids under reservoir-like conditions.
- This work will also build on the previous studies to improve the performance of SiO_2 NPs via a novel surface modification approach to produce well-dispersed SiO_2 dispersions, and use them for *in-situ* synthesis of COPAM to form stable nanocomposites, and investigate their effects on thermal stability, long term aging at HT-HS condition and to conduct a pilot-scale of core-flooding investigation to ascertain their potential use in EOR.
- This project will also produce new temperature resistance polymers with acrylamide backbone and use suitable NPs to identify the best polymer for EOR application at HT-HS and alkaline conditions. MWCNTs will be used in this because it was reported to improve the stability of other polymer types.
- Newly formed materials will be carefully characterised spectroscopically using different techniques to fully understand the chemistry behind the processed composite materials.

The thesis layout and ideas have been summarized and illustrated in **Section 1.4** and **Fig. 1.8**, respectively.

Chapter 3 Synthesis and characterization of polymer and polymer nanocomposites via direct mixing

3.1. Introduction

This Chapter investigates the formulation and characterisation of different polymers and polymer-nanoparticles composites via mechanical mixing. The Chapter is subdivided into three parts, descriptions of the equipment, formulation, and characterizations of the polymer nanocomposites via direct mechanical mixing process, and synthesis and characterization of different copolymers via free-radical polymerization. Suitable nanoparticles and polymers are identified for enhanced oil recovery under the influence of pH and API brine.

3.2. Description of the instruments

3.2.1. Scanning electron microscopy (SEM)

SEM is a technique that produces an image by scattering electrons onto a target surface, this will allow the morphological examination (size and shape) of the material (organic or inorganic) ranging from nano to micro-scale. The principle of SEM operation is that the surface of the sample (solid) is bombarded by electrons through an electron gun. The electron gun generates an electron beam from the top of the microscope. The beams move down to the vacuum zone passing through the electromagnetic lenses. The electron hit on the sample, generating the loss in energy as characteristics X-rays, secondary electrons, backscattered, and other photons of different energies [251]. The detector collected the ejected signals (X-rays, backscattered and secondary electrons) from the sample and converts them into a signal to create a final image. The resolution and magnification of SEM depend primarily on the working

distance between the sample and the detector. **Fig. 3.1** is a photo of the SEM image taken from LEMAS.

In the current project, the surface structure, the morphology, and the particle size of the powdered samples were examined by a high-performance cold field emission scanning microscope (Hitachi, CFE-SEM SU8230) operating between 1kV and 20kV in secondary electron imaging mode. The preparation of the sample was carried out adding a drop of the suspended sample on the SEM sample holder and remove the contamination in SEM cleaner using UV radiation/Ozone at 1 Pascal/10 min. Different magnifications were to capture the images using Gatan Digital Micrograph software.

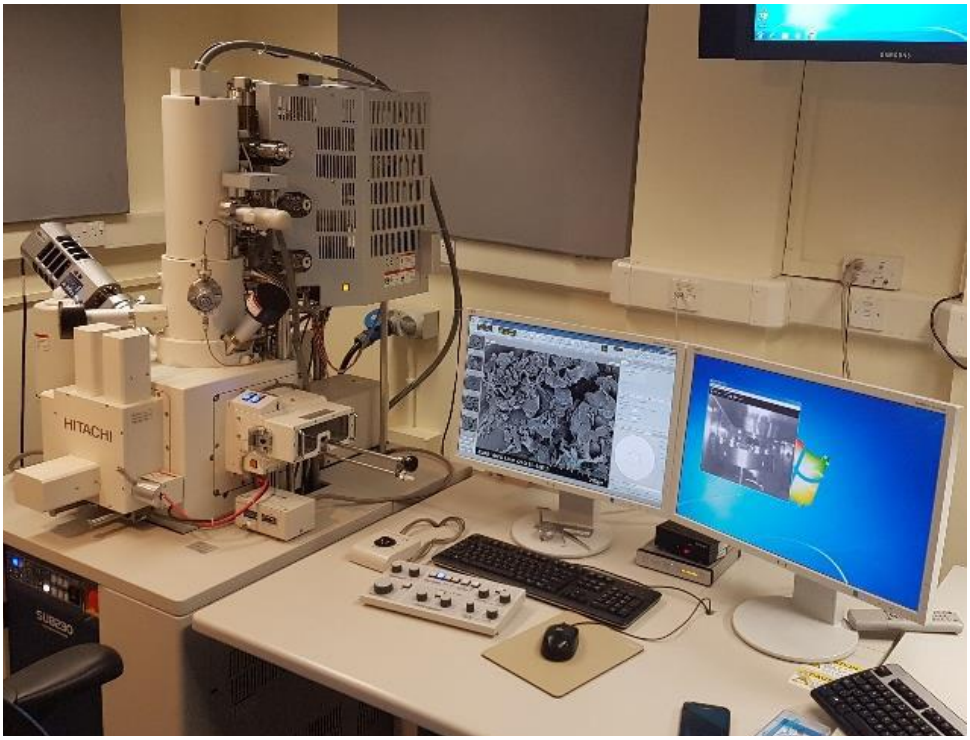

Figure 3.1. SEM instrument used for the morphology analysis.

3.2.2. Transmission electron microscopy (TEM)

Like SEM, TEM is also a class of electron microscopy where an electron beam of light is transmitted via an ultra-thin sample dispersed on the TEM grid (**Fig. 3.2**). The image is formed

when the electron beam interacts with the sample. The diffraction (degree of interaction) between the sample and beam depends on the variation in density, atomic mass, and thickness of the sample. TEMs are capable of imaging at a much shorter than X-ray and visible radiation and at high resolution, it can enhance to atomic level [252].

In general, TEM comprises the single or double tilt sample holder, electromagnetic lens system, imaging source, and electron source [252]. A tungsten filament electron gun emits a high-velocity beam of electrons while heated with 100 to 300 kV voltage. The electromagnetic lens was used to accelerate the beam towards the sample and transmits it through the sample. After the electrons are re-focus or adjusted by the magnetic lens system after passing through the sample, and also to get enlarge the image to obtain higher magnification. While analysing the samples the column is maintained under a high vacuum to allow the electrons to travel a long distance.

In the current project, TEM images were recorded on an FEI Titan Themis Cubed 300 and FEI Tecnai TF20 FEG operated at 300 kV and 200 kV respectively. The system investigated the high-resolution morphology, and particle size distribution of the selected area electron diffraction (SAED) to examine the inter-planner spacing from the diffraction of electrons, the internal and surface structural properties, the location of elements (TEM-mapping), and also, the connected energy X-ray spectroscopy (EDS) were used to detect the composition. For the measurement, the sample was prepared by dropping a small sample on a carbon-coated gold/copper grid for TEM.

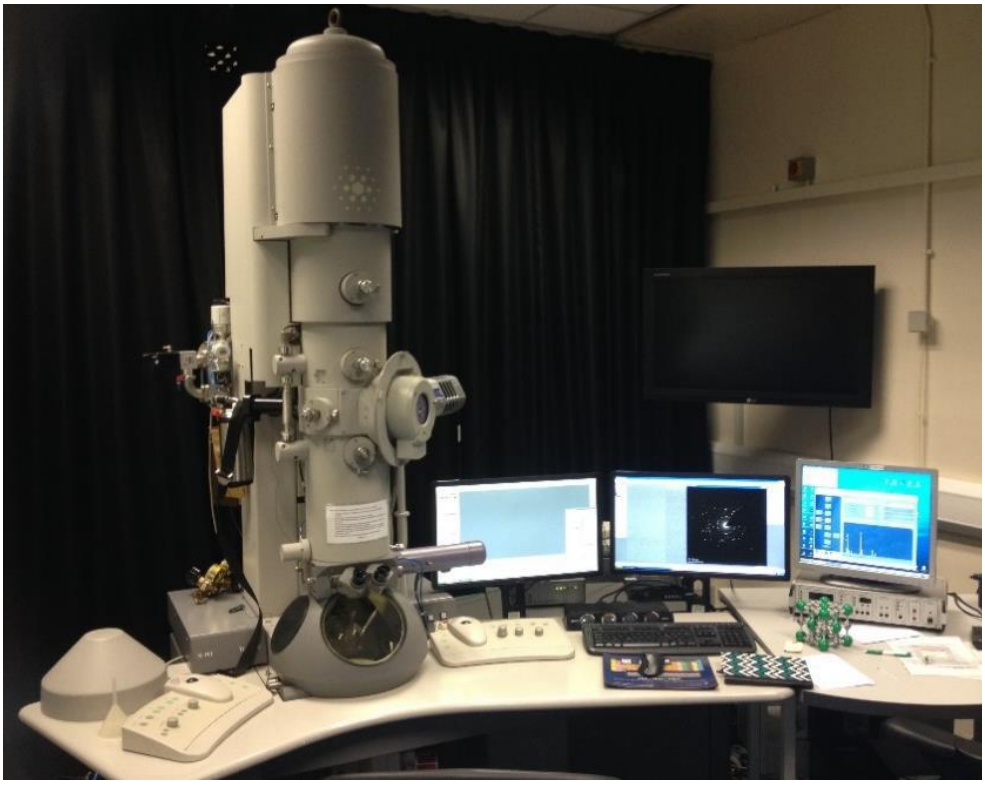

Figure 3.2. TEM instrument used for the morphology analysis.

3.2.3. Thermogravimetric analysis (TGA)

TGA is a thermal analysis method that used microbalance to monitors the changes in the weight of a sample as a function of temperature and time under the control of an inert atmosphere like N_2 gas. The technique is used to characterise either solid or liquid materials that exhibit a change in weight (gain or loss) as a result of dehydration, decomposition, oxidation, reduction, and desorption [253]. In this project, TGA was used to examine the thermal degradation of polymer, nanoparticle, and polymer nanoparticle composites and to quantify the volatile part of the sample.

The operation principle of TGA is that the sample is loaded in an empty platinum pan. The pan is then put inside the furnace and applied the constant heating rate and monitor the changes in mass through microbalance against temperature and time. The system temperature and sample are being monitored precisely through thermocouples and the resulting outcome is plotted as a

mass of the sample with respect to temperature/time. An inert gas is used to purge the atmosphere in the sample chamber to prevent oxidation and any other unwanted reactions while carrying out the experiment. The thermal stability of the sample is determined by monitoring the amount of weight gain or loss [253].

In this project, the thermal degradation of the prepared samples was investigated using Mettler Toledo (TGA/DSC-2) star^{e} system. The system was programmed to perform within the heating range from 25 °C to 900 °C at 10 °C/min under the constant flow rate (50 mL/min) of nitrogen gas (**Fig. 3.3**). The STAR^{e} and TAS infinity PRO software were used to export the data for all the samples. Although it is not directly related to EOR or the stability of the colloidal material, the TGA analysis was measured in this to understand further the degradation behaviour of the powdered samples Fused in the current experiments. Also, it has been used as an indicator to understand the mechanisms behind the viscosity reduction of HPAM/CQDs.

Figure 3.3. TGA/DSC-1 instrument

3.2.4. CHNS analysis

CHNS analyser is an instrument used to quantify the percentage of the elements present in each sample. The technique principle of operation is based on the Pregl-Dumas method. Thermo Scientific™ FLASH 2000 CHNS Analyzer was used in this work, at first it was calibrated by different standard components. Around 2-3 mg of the sample was weighed into a silver capsule and pressed, the capsule with the loaded sample is put into the CHNS analyser and later the sample undergoes combustion in oxygen under the temperature influence (1000 °C) using flash combustion. Helium as an inert gas was used to remove the combustion products (H_2O, SO_2, and CO2) and separated by a chromatographic column, the thermal conductivity detector (TCD) detected them as an output signal. These recorded signals are proportional to the concentration of the particular component in the mixture [254]. The result was manipulated and exported using is SQL-based software by EA 2400 Data Manager.

3.2.5. X-ray photoelectron spectroscopy (XPS)

XPS is also called Electron Spectroscopy for Chemical Analysis (ESCA). It is a fundamental technique for providing information on the elemental composition, purity, oxidation state, and analysis of surface (external) layers in solid materials by evaluating the electronic structure of ions/atoms [255]. The technique is operated based on Einstein's principle (E=hv) with regards to photoelectron spectroscopy. In the mid-1960s, the technique was developed at the University of Uppsala by Kai Siegbahn and co-workers [255]. A mono-energetic soft X-ray photon beam (Al Kα (*hv*=1486.6 eV) and Mg Kα (*hv*=1253.6 eV)) were used to irradiate the surface of the sample *in vacuo*.

In this project, the XPS analysis was performed on a KRATOS XSAM 800 fitted with an energy analyser. Al Kα X-ray (monochromatic radiation 1486 eV) was employed as an X-ray

source, the X-rays are generated from an aluminium anode operating at the emission voltage 5 mA and 15 keV. 6.5x10-10 bar was used within the spectrometer as a base pressure during the examination to prevent contamination on the surface during data acquisition. The sample films were prepared by putting a few grams of the particular sample on the aluminium surface. To make a thin film, the surfaces were later exposed to near-infrared light to escape the solvent. The CasaXPS were used for spectral fitting and correcting the binding energies charge to the C 1s peak at 285 eV to reimburse for residual charging effects because of the increase in positive charge at the analyte surface. The positions intensities of the peak from the XPS spectra were used to understand how much of at the surface and the chemical/elemental composition of the measured sample.

3.2.6. Lumisizer

The Lumisizer is a transformative development based on the LUMiFuge platform with extra important capabilities that spontaneously measures the time- and space-resolved (extinction) of the transmitted light across the entire sample length. In this work, the dispersion stability of polymer nanoparticle composite was observed to investigate the sedimentation and flocculation behaviour by measuring the transmission of near-infrared (NIR) light under the influence of centrifugal force using (LUMiSizer, Lum GmbH, Germany), a dispersion analyser centrifuge. The measurement was conducted by pipetting 400 µl of the sample into a polycarbonate tube cell. The tube was then inserted into equipment to measure the sedimentation profiles along the sample length during the centrifugation. The software attached to the system recorded the real-time transmission profiles at certain intervals. **Fig. 3.4** shows (a) Lumisizer instrument and (b) Measurement scheme of the multi-sample analytical centrifuge with photometric detection.

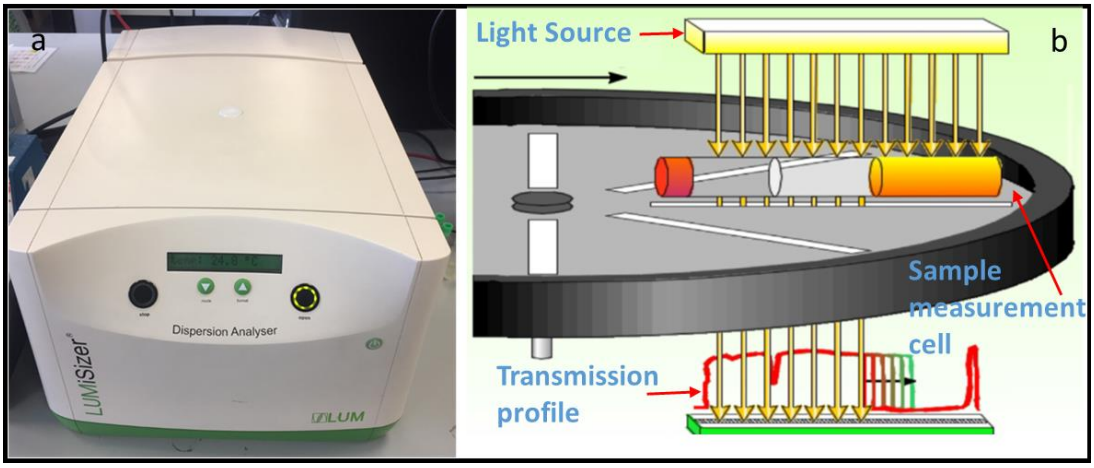

Figure 3.4. (a) Lumisizer instrument (b) Measurement scheme of the multi-sample analytical centrifuge.

3.2.7. Turbiscan

The Turbiscan is widely used to characterise the dispersion state of the liquid material. It is used to directly monitor the flocculation and sedimentation behaviour of the material in realistic conditions. In this project, the stability of the composites samples was determined with a vertical scan analyser Turbiscan MA 2000 (Formulation, Toulouse, France), as reported by Hebishy *et al.* [256]. In each case, a flat-bottomed cylindrical glass tube (external diameter 27.5 mm, height 70 mm) containing the suspension was used. The backscattering or transmission of light from the suspension was then measured periodically along the height axis at every 40-µm interval. The results are displayed as the sedimentation profile such that the backscattering was against time, along with the sample height. **Fig. 3.5** shows the image Turbiscan instrument used in this work.

Figure 3.5. Turbiscan instrument.

3.2.8. Size and Zeta Potential

Malvern instrument (Zetasizer Nano ZS) can be used to measure the size and zeta potential of the nanofluid. Dynamic light scattering (DLS) is a common technique used to measure the size distribution. The size measured is hydrodynamic size, which the sphere diameter that diffuses at the similar speed at which the particle is being measured. The size measurement by the zetesizer system is determined first by measuring the particle Brownian motion in a solution using DLS followed by size interpretation using established theories. The particle with smaller size diffuse will move quickly while bigger particles move slowly. On the other hand, the measurement of zeta potential is done by the combination of measuring techniques. Electrophoresis and Laser Doppler velocity, which in many cases called Laser Doppler is used. This approach measures how fast the particle moves in the liquid when applying the electrical field – i.e. its velocity. Once the velocity of the particle is known and the electrical field is applied, then by using the two other known constant of the sample – dielectric constant and

viscosity, the zeta potential can be determined. **Fig. 3.6** shows the Photo of Malvern instrument used for size and zeta potential measurement.

Figure 3.6. Photo of Malvern instrument used for size and zeta potential measurement.

3.2.9. Fourier transform infrared spectroscopy (FTIR)

FTIR is a sensitive technique that is widely applied to obtain an infrared spectrum of emission or absorption of gas, liquid, or solid. The instrument is particularly used for identifying organic chemicals in a whole range of applications, although some inorganic materials can also be characterized using the technique. Over a wide spectral range, the FTIR spectrometer collects high spectral resolution simultaneously.

Infrared (IR) refers to electromagnetic radiation at the wavelength range of 0.7 µm to 1000 µm (far-IR: 400-20 cm^{-1} shows the changes in rotational energy level; mid-IR 4000-400 cm^{-1} shows changes in the fundamental vibrational level of most molecules; near IR: 40000-4000 cm^{-1} shows the changes in rotational and vibrational levels, some low energy electron transitions and overtone region, even though, for much chemical analysis the most interesting region by the scientist is the vibrational portion (mid-IR 4000-400 cm^{-1}) between 2.5 µm and 25 µm [257].

The technique can be applied for the quantitative and qualitative analysis since the IR spectrum can provide a fingerprint of each determine functionality in the measured sample, corresponding to the vibration frequencies between the atomic bonds within the material. Wavenumber is the most typical used unit for radiation in vibrational IR, which proportional directly to the energy. The band intensities are assigned to the concentration of the absorbed material and the path length of the light via the Beer-Lambert Law as illustrated in equation 3.1. [257, 258].

$$A_\lambda = log\frac{1}{T_\lambda} = log\frac{I_0}{I} = \varepsilon_\lambda bc \dots\dots\dots 3.1$$

Where A_λ is the absorbance at a given wavelength (the relative quantity of the light absorbed by sample); b is the path length in cm (usually 1 cm for the distance light pass through the chemical species); ε_λ is the molar absorptivity at a particular wavelength (L/mole.cm); and c is the molar concentration of the chemical species in the sample (mol/L)? Also, expressed in transmittance mode as in equation 3.2:

$$T_\lambda = \frac{I}{I_0} = e^{-\varepsilon_\lambda bc} \dots\dots\dots 3.2$$

Where T_λ is the transmittance at a particular wavelength (the relative quantity of the light absorbed by sample); I_0 is the incident radiation and is the intensity of transmitted light.

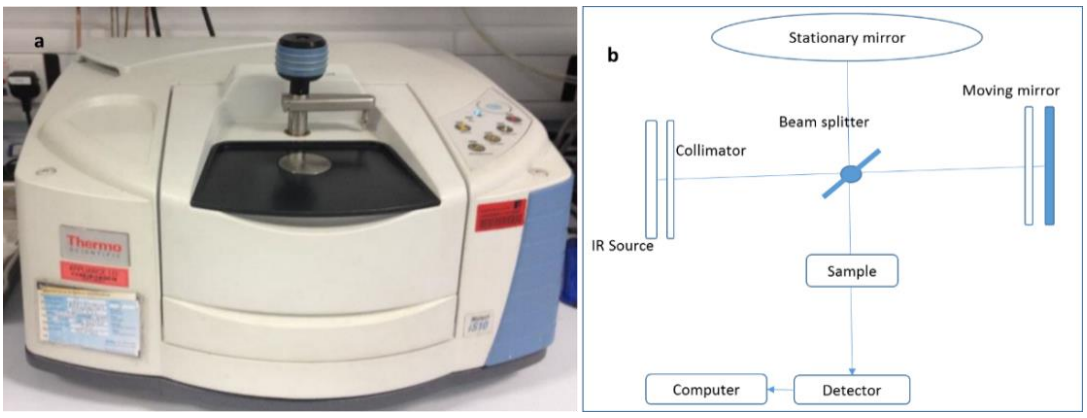

Figure 3.7. FT-IR instrument (a) and schematic diagram of a Michelson interferometer (b).

In this work, the FT-IR spectra of all the polymers and nanoparticles, and polymer nanoparticle composites were recorded at ambient conditions (room temperature and pressure) using a Nicolet iSO FT-IR spectrometer equipped with a deuterated triglycine sulfate (DTGS) diamond detector to examine the chemical vibrational modes in each sample (**Fig. 3.7**). At the beginning of each measurement, a spectrum of the background was recorded. Afterward, a different scan up to 36 was performed at the average signal of infrared within the range of 400 cm^{-1} to 4000 cm^{-1}.

3.2.10. X-ray diffraction (XRD) analysis

XRD analysis is the most commonly used technique for the identification of unknown crystalline materials (e.g. inorganic compound, minerals). It generates information on the crystal structure, preferred crystal orientation (texture), phase, and more structural parameters such as crystallinity, average grain size, crystal defect, and strain. The XRD pattern of some samples in this project was obtained using XRD Philips X'Pert and/or Bruker D8 (**Fig. 3.8)** X-ray diffraction connected with a LynxEye detector, the radiation source was CuKα (λ=1.54 Å) operating at 40 mA and 40 kV, calibrated using Si standard. To ascertain the accuracy of the measurement, each sample was scanned twice from 2θ angle ranging 10º to 70º with step size 0.0495º at 1 second per step and 35 seconds per step.

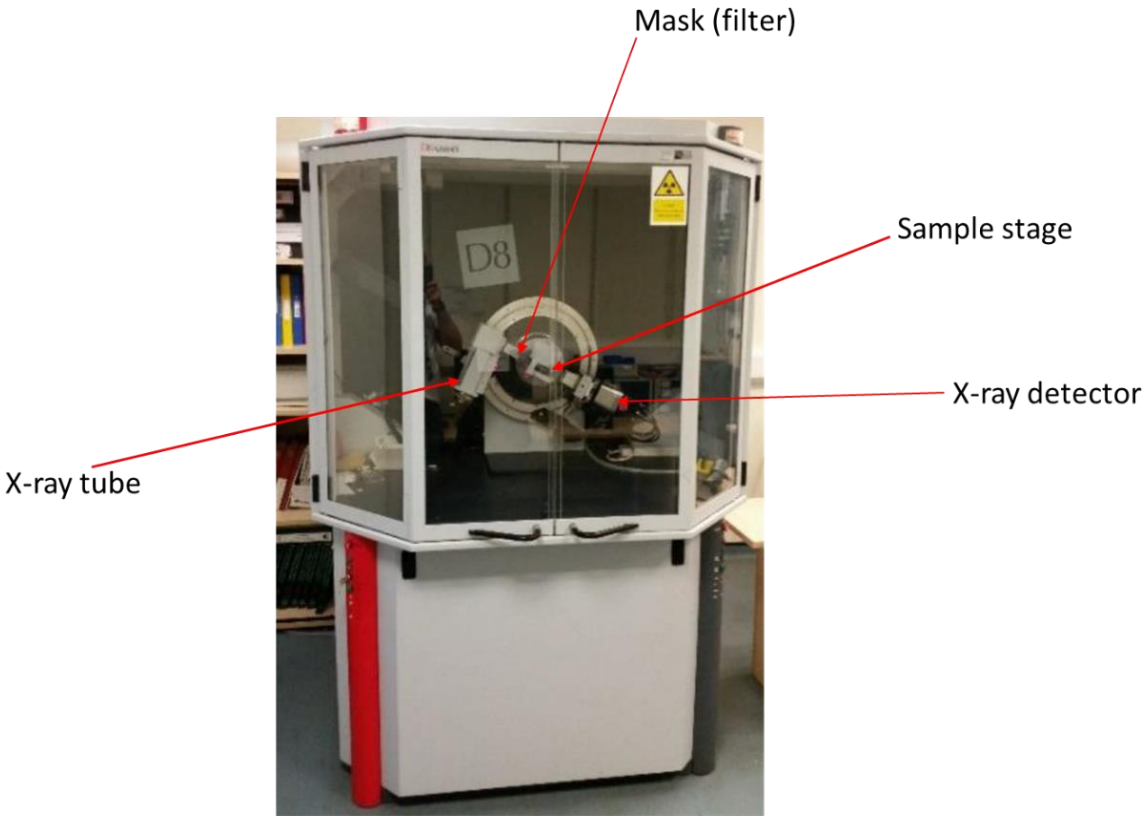

Figure 3.8. Brucker Powder D8 advance X-ray diffractometer

3.3. Synthesis and characterizations of polymer nanocomposites using commercial polymers

3.3.1. Reagents

Hydrolysed polyacrylamide (HPAM) was provided by SNF FLOERGER, France, having a molecular weight of 10 mDa and a density of 0.9 g/cm^3. Sodium chloride with the purity of around 99.0% was purchased from Sigma-Aldrich. Graphene oxide and carbon quantum dots are synthesized prior to the experiment using the procedure mentioned below.

3.3.2. Synthesis of graphene oxide

Modified Hummers' method was used to synthesise a stable graphene oxide [259]. Graphite powder ≈20 µm in size, hydrogen peroxide (H_2O_2, 36%), and potassium permanganate ($KMnO_4$, 99%) were purchased from Sigma-Aldrich. Nitric acid (HNO_3, 69%) and sulphuric acid (H_2SO_4, 95%) were obtained from VWR Chemicals. Graphite powder was used as the starting material. A mixture of sulfuric acid and nitric acid was used for oxidation of graphite powder in a water-based solution. In a typical synthesis, 12 grams of graphite powder was prepared in a mixture of 100 ml H_2SO_4 and 50 mL HNO_3 and stirred for 24 hours at room temperature. 100 ml of DI water was subsequently added to the mixture and then stirred continuously for another day. $KMnO_4$ (12 grams) was added slowly in the solution keeping the temperature of the mixture low. This was followed by stirring for five hours. 60 ml of 36% H_2O_2 was added in an ice bath to keep the temperature low, and this suspension was stirred overnight. The resultant suspension was filtered using a Whatman filter paper. The filtrate was then washed three times with 10% HCl, centrifuged (13000 rpm for 1 hour) and the supernatant was discarded.

3.3.3. Synthesis of carbon quantum dots (CQDs)

CQDs were facilely synthesised by one-step hydrothermal carbonisation of D-(+)-Xylose, according to published procedures [260, 261]. Firstly, 0.2 g of D-(+)-Xylose were dissolved in deionised water (20 ml). Afterward, the solution was moved into a Teflon-lined, stainless steel autoclave. The solution was subsequently heated for 6 h at 200 °C and then cooled to room temperature. The cooled solution was centrifuged for 30 min at 10,000 rpm to obtain a solid black carbon precipitate. The supernatant containing carbon quantum dots was filtered using a standard syringe filter paper and then used in the next stage.

3.3.4. Preparation of the polymer nanocomposite mixture

Composites of HPAM/NPs were prepared using mechanical mixing. 0.025 g of the HPAM were dissolved in 50 ml deionised water to achieve 0.05 wt. % HPAM solution through continuously stirring at room temperature. Different concentrations (0.01, 0.02, 0.0.4, 0.06, 0.08 and 0.1 wt. %) of the NPs suspension were separately added dropwise into the designed HPAM solution under gentle stirring at room temperature, for example, the ratio of HPAM/GO/water is 1:2:100 when 0.05 wt.% of HPAM and 0.1 wt.% of NPs were dispersed in water. The HPAM/NPs suspension was continually mixed by gentle stirring using a magnetic stirrer (SB 162-3, Stuart) for 24 hours to allow sufficient time for the NPs to form a network with the graft polymer to achieve a stable composite material. Different brine (NaCl) concentrations were then added to the individual solutions followed by a further 24 h stirring at room temperature to investigate the effect of electrolytes. While for CQDs composites with Shandong Tongli polymer, (0.05, 0.1, 0.2, 0.4, and 0.5 wt. %) of the NPs were used. **Fig. 3.9 (a)** and **(b)** showed the schematic illustration of the synthesis procedure, taken HPAM/CQDs as an example of synthesis methods. The HPAM/NPs composites were oven-dried to obtain a powdered sample for further characterization. However, for SEM analysis a freeze-dried method was used resulting in the

powdered HPAM/NPs composites. In this section detailed characterization of the HPAM/GO and HPAM/CQDs composites were presented, the mechanisms behind stable composites formation were also provided.

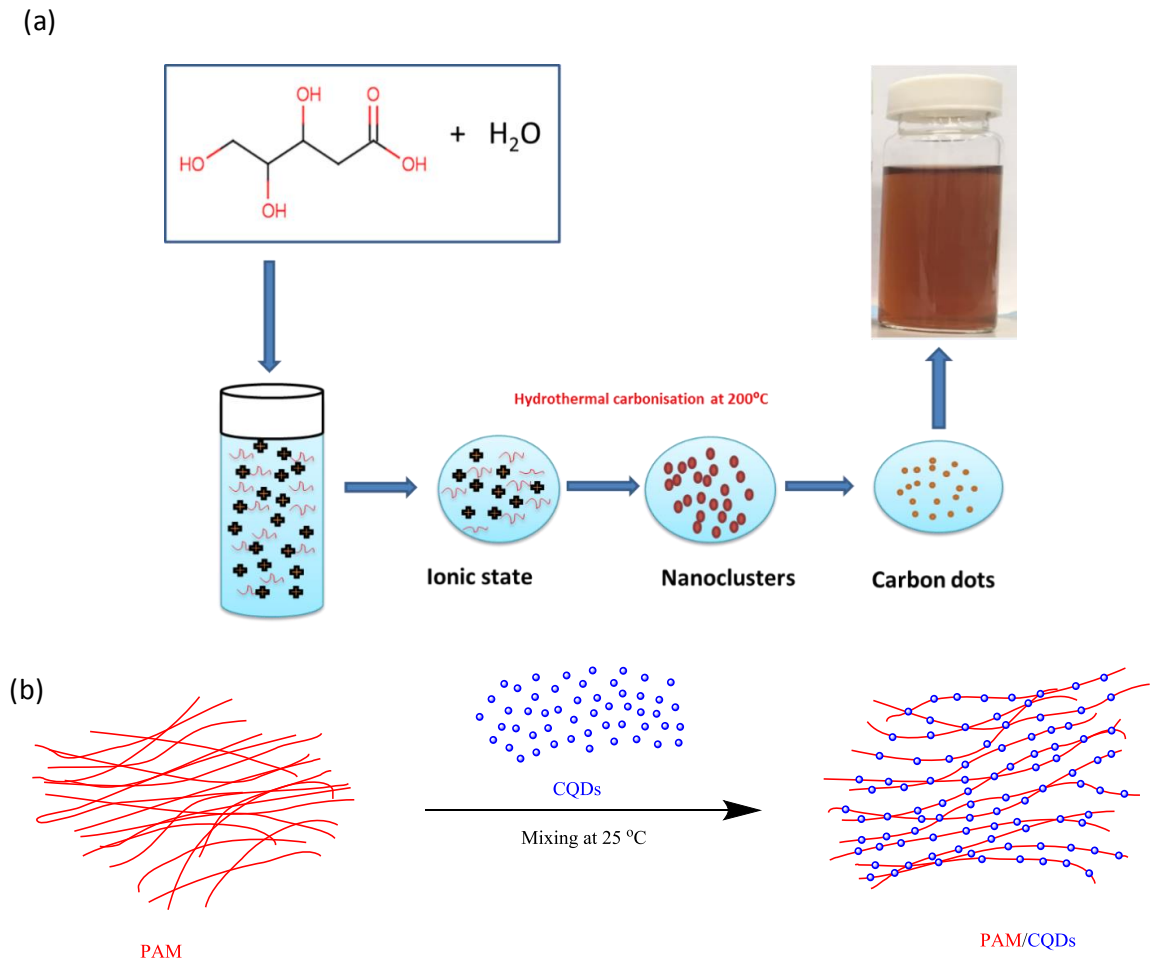

Figure 3.9. Schematic of the synthesis of carbon quantum dots by one-step hydrothermal carbonisation of D-(+)-Xylose (a) and illustration of the synthesis of the HPAM/CQDs composite materials (b).

Table 3.1. Variation in the salt's components of brine's mixtures.

Salt components	Brines (%)
$MgCl_2.6H_2O$	1.3
NaCl	7.5
$Na_2.SO_4$	0.006
$NaHCO_4$	0.005
$BaCl_2$	0.001
$CaCl_2.2H_2O$	5.0

Notwithstanding, while making the HPAM/NPs composites, an attempt has been made to prepare the solution in the presence of high ionic strength brines containing different salt components as shown in **Table 3.1.** But unfortunately, the stable dispersion was not achieved in these conditions, even after using different dispersion stabilizers, the solution tends to sediments, agglomerate, or even precipitate after the preparation. An example is showing in **Fig. 3.10** for GO/HPAM composite. However, new approaches have been explored to modify the NPs surface and make an *in-situ* synthesis of the polymer/NPs solution, the process is discussed as a separate section in **Chapter 4**.

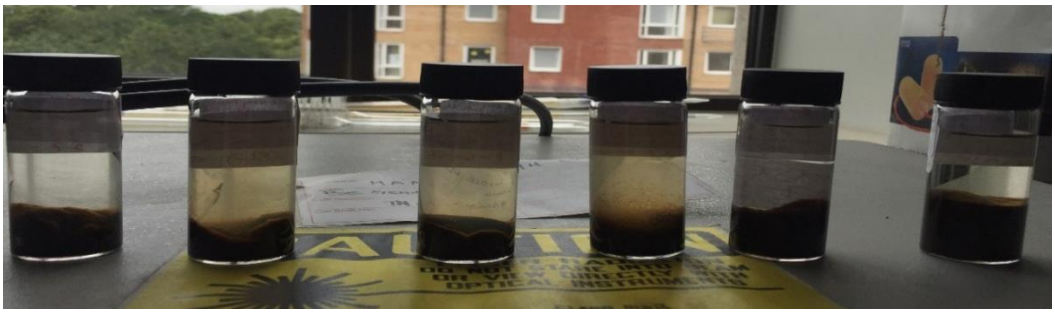

Figure 3.10. Below show some of the unstable samples prepared for GO/HPAM composite under the influence of complex brine salinity.

3.3.5. Characterisation

Morphologies of the fabricated NPs, HPAM, and HPAM/NPs composites were determined by scanning electron microscopy (SEM, SU8230 Hitachi). The microscope was operated at 2 kV. Also, a transmission electron microscopy (TEM, FEI Tecnai TF20, LEMAS center, Leeds, UK) was used, operated at 200 kV. The zeta potential was measured using a dynamic light scattering (DLS) technique (Zetasizer Nano ZS, Malvern Instruments Ltd., Malvern, UK). A UV-visible spectrometer (UV-1800, Shimadzu, Kyoto, Japan) was used to determine the particle concentrations, based on the Beers-lambert law. For this, measurements were carried out at a wavelength of 310 nm [262]. The stability of the HPAM/NPs composites was determined with a vertical scan analyser Turbiscan MA 2000 (Formulation, Toulouse, France)

[256]. The functionality of the PAM, the CQDs, and the HPAM/NPs composites was measured by a Nicolet iS10 Attenuated Total Reflectance (ATR)-Fourier transform infrared (FTIR) spectrometer. The pH value of the composites was determined by a Mettler Toledo pH-meter (Seven Compact S210). The XRD analysis was carried out on dried samples to evaluate the degree of polyacrylamide intercalation between the NPs layers, using a Bruker D8 X-ray diffraction, fitted with a Cu Kα radiation (1.54 A˚, 40 kV, 40 mA). Data was collected from a 2θ angle ranging from 10 – 70° with a step size of 0.0495˚ at 35 s per step. The pH of the dispersion was measured on a METTLER TOLEDO pH meter (seven Compact S210). The thermal degradation of the dried samples was studied using a TGA/DSC-1 instrument (Mettler Toledo, England), covering the temperature range of 35 to 900 °C. A heating rate of 10 °C/min was used during each measurement, the system was operated under a constant flow rate of nitrogen gas at 50 ml/min. Proton NMR spectroscopy was carried out on the HPAM and the PAM/NPs composites, using advanced 600 MHz nuclear magnetic resonance spectrometer (Bruker Company, Ettlingen, Germany). Each specimen was tested in the deuterium oxide (D_2O) solvent.

3.3.6. Results and discussion

3.3.6.1.Characterization of HPAH/GO composites

The TEM images show typical wrinkles and a crumble-like structure of GO **(Fig. 3.11a)**, the selected area of electron diffraction (SEAD), as shown in **Fig. 3.11b** indicates that a clear diffraction brightness and spotty rings that indexed to a hexagonal crystal structure of graphite. The SEM images show that the surface of GO is smooth, indicating that the GO nanosheet is attached **(Fig. 3.11c). Fig. 3.9d** shows that the GO exhibits strong ultra-violet light absorption and a clear absorption at 280 nm. The Raman spectrum of HPAM, GO, and HPAM/GO composites are shown in **Fig. 3.12a,** GO spectrum demonstrated a D-band at 1357 cm^{-1} and a

G-band at 1591 cm^{-1} respectively. The D-band is linked with the structural deformity relevant to the partly disorganised network of graphitic domains or generated by the functional group's attachments on the carbon basal plane. While the G-band is referred to as the E2g mode first-order scattering. The HPAM showed a tiny symmetrical band centred at around 481 cm^{-1} due to skeletal deformation [269] and a wide sloppy band at 1667 cm^{-1} due to the amide-1 vibration. Similarly, there is a change in the frequency of amide II (primarily -NH_2 bending) from 1600 cm^{-1} to 1625 cm^{-1}. The change of the amide I frequency indicates the formation of hydrogen bonding between two polymer chains [269]. However, the GO D-band and G-band become broadened in the HPAM/GO composite becoming more prominent and wide, indicating a considerable interaction between HPAM and GO.

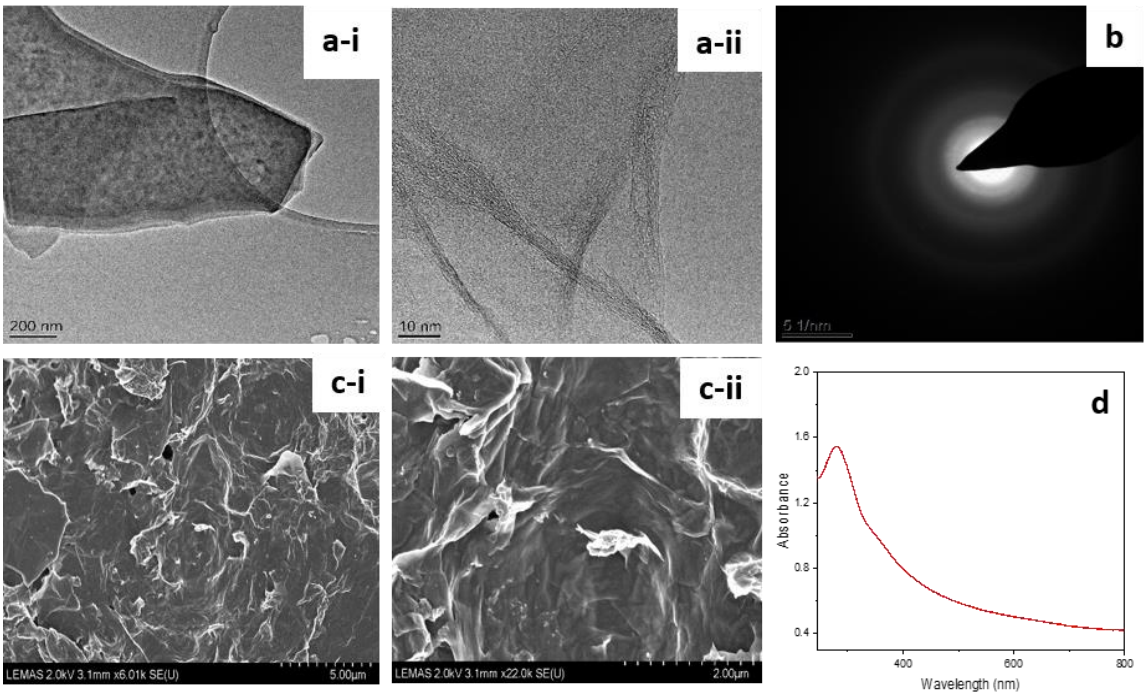

Figure 3.11. (a) TEM images (b) SAED (c) SEM images (d) the UV-vis spectrum of Go nanosheets.

The essence of the chemical bonding structure between the HPAM and GO was evaluated using FT-IR spectroscopy to understand the formation mechanisms of GO/HPAM composite as shown in **Fig. 3.12b.** For the HPAM spectrum, 1117, 1449, and 2953 cm^{-1} correspond to ring structure vibration of C-O-C stretching, methyl C-H bend, and C-H stretching vibration respectively. The peaks observed at 3321 and 2923 cm^{-1} can be attributed to the carbonyl and the amino group of the HPAM amides chain. The peak at 1700 cm^{-1} is attributed to the C=O (carbonyl functional group) stretching vibration while the peak at 3424 cm^{-1} is related to the N-H stretching vibration. The amide I and amide II vibrational bands appear at 1650 and 1548 cm^{-1} [270]. The GO sheets FT-IR spectrum shows bands at 3420, 1395.5, and 1069.7 cm^{-1} which are referred to as the symmetric and asymmetric stretching vibration of O-H, the bending vibration of O-H and the stretching vibration of the C-O bond in epoxide group, respectively [271, 272]. For HPAM/GO composites, the formation new peak at 1660 cm^{-1} demonstrated that the GO -COOH was transformed into $-COO^-$ with $-NH_3^+$ of HPAM as the counter-ions. Other than electrostatic interaction, hydrogen bonds also formed between the epoxy groups and OH of GO, and $-NH_2$ and C-O of HPAM presence in the composite material. In GO the epoxide group C−O stretching (1069.7 cm^{-1}) became weaker gradually and the GO OH bending peaks (1395.5 cm^{-1}) shifted to the higher wavenumber, confirming the existence of hydrogen bonds. The same peaks observed at 3321, and 2923 cm^{-1} in the HPAM spectrum were also shown in the HPAM/GO spectrum but was shifted to lower wavenumber (3302 and 2859 cm^{-1}), indicating stable dispersion of GO/HPAM nanocomposites. New peaks appear in HPAM/GO at 1081 and 1451 cm^{-1} which were not observed concerning the near HPAM are due to the formation of C-O-C stretching ring structure vibration and methyl C-H bending vibration, respectively. These might be due to the hydrolysable covalent cross-links formation between HPAM and GO [108, 273]. Besides, in GO/HPAM hybrid spectrum another peak appears at 2953 cm^{-1}, which indicates the formation of C-H stretching vibration, confirming

the formation of a covalent bond between carbon present in the GO backbone and hydrogen from the amide group of HPAM.

Moreover, the formation of the N-H group at 3228 cm^{-1} in the spectrum of the composite is as a result of electrostatic interaction between the polar hydrogen in the GO and highly electronegative nitrogen atom present in the HPAM amide, which bound together to form hydrogen bond and further increases the hybrid suspension stability. Also, the absorption band formed at 1741 cm^{-1} is ascribed to carbonyl stretching vibration, the bands at 1568 cm^{-1} are responsible for $–CO-NH_2$ bonds and a band at 1376 cm^{-1} represent the C-N stretching vibration. Accordingly, the –CO-N-H mode contributes to the C-N stretching vibration and N-H bending vibration, which emerges from bonding between the amide group of HPAM chains and the carboxylic group of the GO. **Table 3.2** shows the elemental compositions for HPAM, GO and HPAM/GO samples analysed by SEM-EDS.

Table 3.2. Summary of elemental compositions for dried HPAM, GO and HPAM/GO samples.

Sample	Elemental compositions			
	C (%)	O (%)	N (%)	S (%)
HPAM	64.54	23.25	10.42	1.17
GO	59.47	40.25	0.00	0.28
HPAM/GO	40.10	46.54	9.84	3.52

NMR spectroscopy was also employed aiming to present the confirmation that HPAM molecules were incorporated into GO sheets using an Advanced 500 nuclear magnetic resonance spectrometer (Bruker Company, Ettlingen, Germany) in deuterium oxide (D_2O). **Fig. 3.13a and b** show ^{1}H-NMR of HPAM and HPAM/GO respectively. For pure HPAM, the absorption peaks at 1.407, 2.113, and 3.321 ppm represent $-CH_2$ protons. C-H and $R-CO-NH_2$ were denoted in the absorption peaks of 6.868 and 7.609 ppm, respectively. All of these indicated that the major polyacrylamide functional groups are found in the spectrum [274-276]. Compared to HPAM/GO

spectrum, the -NH_2 and -CH_2 peaks in HPAM become broader and wide indicating modification in HPAM backbone after interacting with GO sheet, however, there are the existence of new peaks marks with the different shapes and symbols at 6.873 ppm for Ar-OH and 3.639 ppm representing R-CO-NH_2 which certainly indicated how oxygen atom in GO interact with -NH_2 of HPAM to form a hydrogen bond. The emergence of this new characteristic attraction peaks proves the successful grafting of HPAM chains onto the GO sheets.

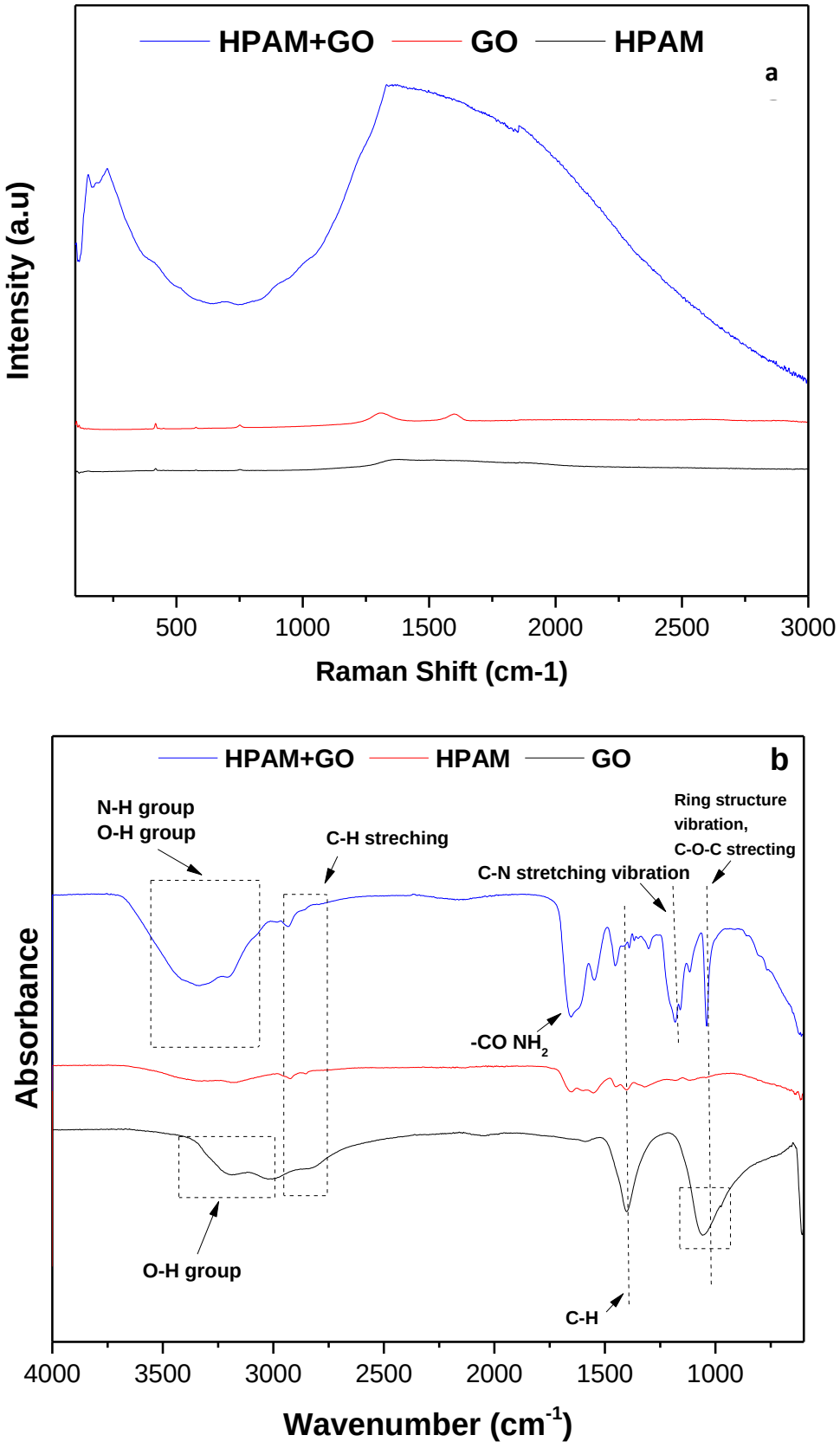

Figure 3.12. (a) Raman Spectroscopy for HPAM, GO and HPAM/GO composites, and (b) FTIR spectra for HPAM, GO and HPAM/GO composites.

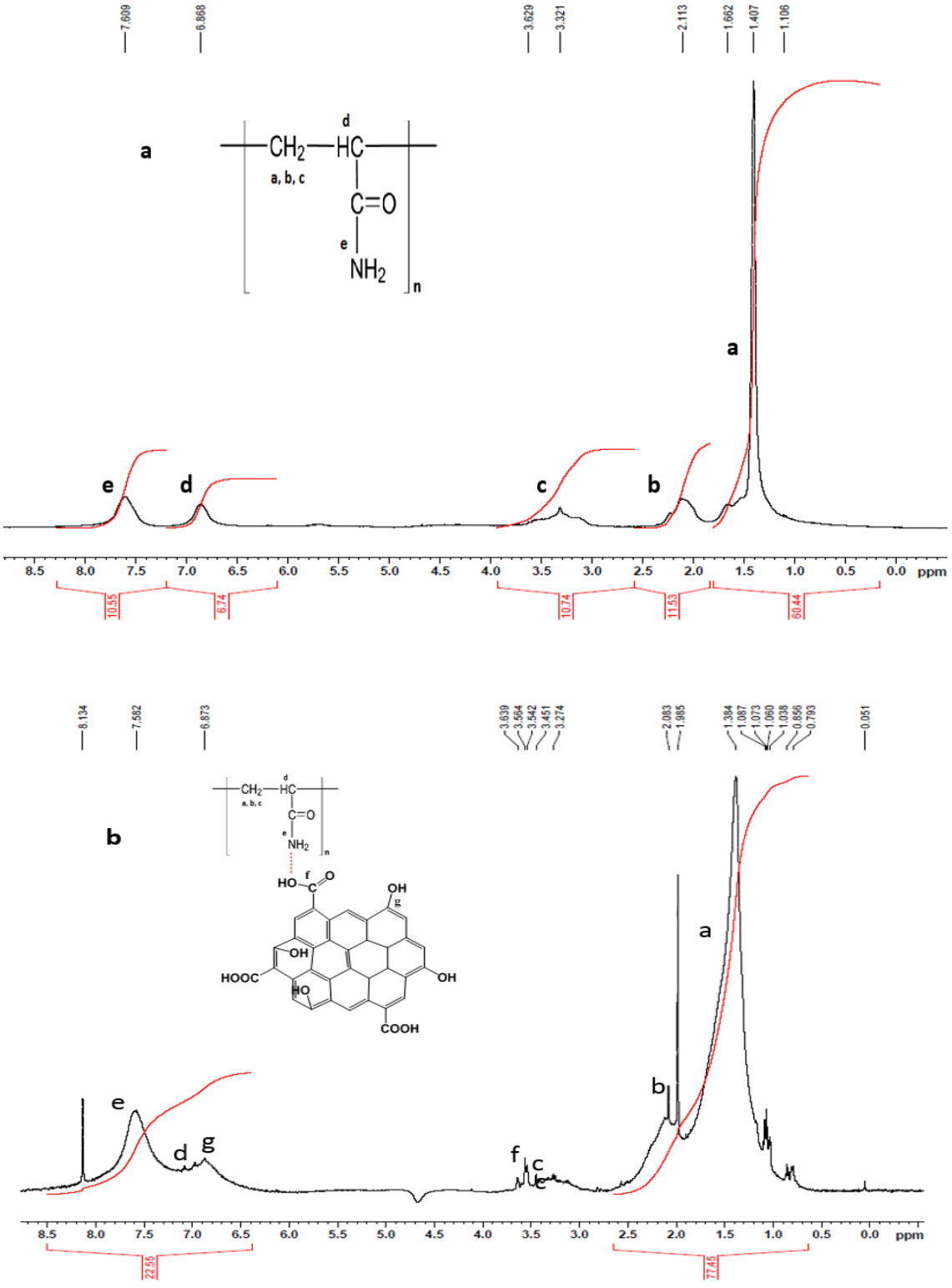

Figure 3.13. 1H-NMR for (a) HPAM and (b) HPAM/GO composites in D_2O.

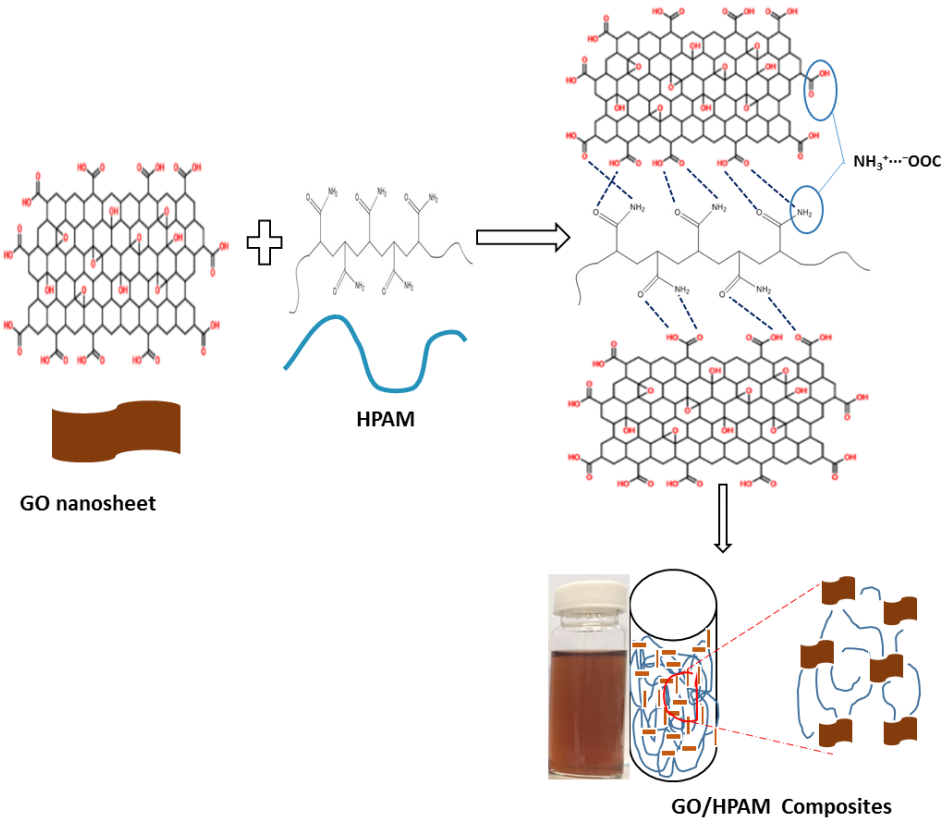

Figure 3.14. Schematic representation of the network structure of GO/HPAM composites.

Considering the characterization findings, a proposed mechanistic illustration of GO/HPAM nanocomposite is shown in **Fig 3.14**. The numerous functional groups containing oxygen (carboxyl, hydroxyl, and epoxide groups and so on) were on the edges and basal planes of GO nanosheet. After interacting with the HPAM, the -COOH group presence in the GO can protonate the HPAM $-NH_2$ group to generate the pairs of $-NH_3^+\cdots{}^-OOC-$ ion. Similarly, three sorts of hydrogen bonds were also observed in the composites in addition to the electrostatic interaction, viz: among the HPAM carboxyl groups and GO hydroxyl groups, and the remaining two prevailed midway around the protonated $-NH_3^+$ of HPAM together with the GO epoxy groups and carboxyl groups, respectively, as proved by FT–IR analysis. Remarkably, the results suggested the evolution of chemical ligation between HPAM segments and GO in the nanocomposites. However, the composites were observed and considered stable enough to

circumvent the possible phase separation that can easily happen in the fabrication of the nanocomposites via the physical mixing of the polymer and GO.

The static position method is the most generally used method to decide the stability of nano composition. It allows the sample to stand in a container for a particular period, and the distance or colour difference in sedimentation was observed by the naked eye [277-279]. However, this method cannot evaluate the true stability of our composite suspensions. As shown in **Fig. 3.15**, the sedimentation behaviour was monitored and recorded every 5 minutes for 2 hours using Turbiscan analyser, backscattering intensity/transmission intensity profiles versus the sample height. The backscattering profiles interpretation explained the changes in the backscattering light caused by the particle sedimentation within the sample cell. Over the period, the change in backscattering varies with the sample height when sedimentation occurs. However, if the particle dispersion is stable, over the entire sample cell no noticeable change in the backscattering profiles is observed. The suspensions containing 0.01, 0.02, 0.04 and 0.08 wt. % GO in HPAM/GO composites showed a representative example of a highly stable suspension**.** The results indicate that since there is no particle precipitation throughout the height of the container, no sedimentation takes place in all range of GO concentrations. This improved stability is associated with the change of the particle surface charge. Therefore zeta potential was used to investigate the incorporated amount of GO state of the surface charge in the HPAM/GO composites and pure samples at 70 °C. The results in **Table 3.3** indicate negative zeta potential for all the measured samples showing improved stability. The zeta potential of the composites shows stronger intercalation between the HPAM and GO nanosheet, indicating that improved dispersion stabilisation has been achieved [274, 280].

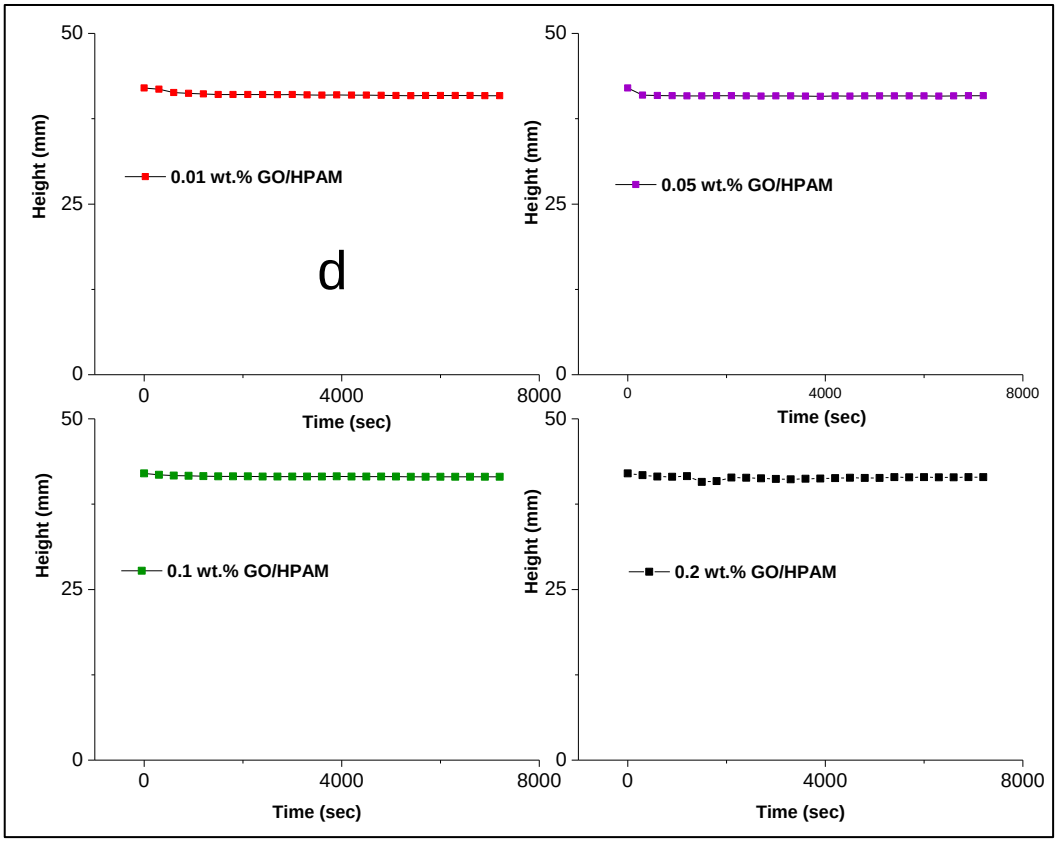

Figure 3.15. Turbiscan stabilization test for 2 hours duration with scan every 5 minutes for HPAM, GO, and HPAM with different loadings of the GO at 60 °C.

Table 3.3. Zeta potential of HPAM, GO, and HPAM/GO nanocomposites at 70 °C for different pH.

Concentrations	Zeta Potential (mV)
Pure HPAM	-45.1
Pure GO	-24.2
GO/HPAM	-50.5

3.3.6.2. Characteristics of the fabricated CQDs, HPAM and HPAM/CQDs composites

Fig. 3.14a shows images depicting the morphological characteristics of the HPAM/CQDs composites. The TEM image, (**Fig. 3.16a**), reveals that the CQDs are spherical particles, having diameters in the region of ~5 nm. In this, no clear aggregations were observed. Similarly, the

SEM of the HPAM/GQDs composites showed how CQDs nanoparticle was incorporated into the polymer. Thermal degradation characteristics of the CQDs, the HPAM, and the HPAM/CQDs composite material are presented in **Fig. 3.16b**. In the case of the CQDs, the thermogram indicates an initial weight loss (~13 wt. %) after the commencement of the heating, until about 100 °C. This weight loss arises due to the evaporation of loosely held water molecules. Tightly held water was then steadily lost (~3 wt. %) as the heating continued up to 150 °C. A steady decrease in weight (~66 wt. %) was then observed until 600 °C, indicating the decomposition of the CQDs material. This decomposition is consistent with previous literature reports [281-284]. It can be seen that the HPAM and the HPAM/CQDs composite material showed a limited weight loss (~7 wt. %), corresponding to the evaporation of loosely bound water molecules. This occurs through the desorption of the molecules from the surface of the HPAM and the HPAM/CQDs composite at room temperature up until 150 °C. However, water molecules that are tightly bound to either the HPAM or the HPAM/CQDs composites were desorbed between 150 and 230 °C. This result indicates that water desorption occurred at a higher temperature in both PAM and HPAM/CQDs materials in comparison to temperature it occurs in the CQDs particles. The decomposition curve corresponding to heating between 230 and 460 °C indicates the slow decomposition of the HPAM molecules compared to the behaviour of the HPAM/CQDs composite. This could be attributed to the amount of oxygen (as hydroxyl and carboxylic acid) reduction that occurs at elevated temperatures in the HPAM/CQDs material. It should also be noted that a significant weight loss in the HPAM material was observed in the region of 460 - 900 °C. This can be attributed to the release of ammonia molecules (deamination of HPAM), accompanying the decomposition of formed carboxylic groups through pyrolysis at a higher temperature. The thermal degradation and stability mechanisms of the HPAM and HPAM/CQDs are very complicated, which deserves further detailed studies by using differential scanning calorimetry (DSC), thermogravimetric

analysis/mass spectrometry (TGA-MS) and/or thermogravimetric analysis-Fourier transform infrared (TGA-FTIR) techniques.

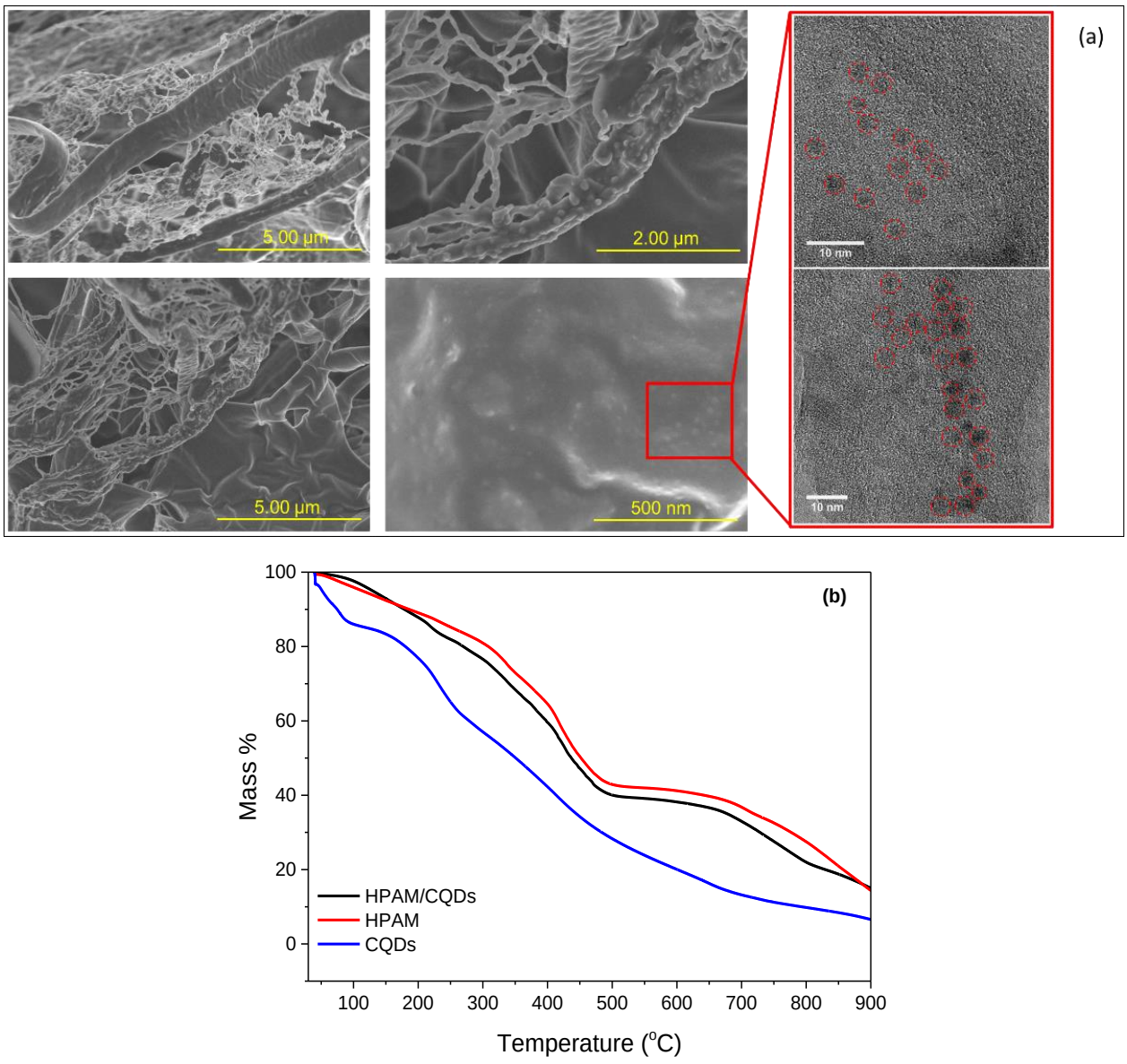

Figure 3.16. (a) Morphological SEM (left) and TEM (right) images of the HPAM/CQDs composite and (b) TGA profiles for CQDs, PAM, and PAM/CQDs composites.

The static position method is the most generally used method to decide the stability of nanofluids. The static position method allows nanofluids to stand in a container for a particular period, and the distance or colour difference in sedimentation between nanofluids was observed by the naked eye [277-279, 285]. In this study, the stability of nanofluids was determined using

static and dynamic tests. The selected samples were evaluated via eye test investigation, Turbiscan analysis, and zeta potential measurement. In the static position method, all samples remained standing for 10 days, and the stability difference between samples was observed by the naked eye. However, as shown in **Fig 3.17** the differences were difficult to detect using naked eye observation. The stability behaviour of the various materials was examined by the sedimentation method monitored every 1 h, continuously for 24 h, using a Turbiscan analyser (**Fig. 3.18**). The technique detects changes in the backscattered light that are caused by the particle sedimentation within the sample cell. All of the samples with different CQD concentrations demonstrated no particle precipitation throughout the height of the container, indicating excellent stabilities. In comparison with the zeta potential of bare HPAM, the zeta potential of the HPAM/QCDs composite is much stronger, indicating that improved dispersion stabilization was achieved. For example, the zeta potential of 0.4 wt. % CQDs are ~ -20 mV while that of HPAM/CQDs composite reached up to ~ -55 mV due to the enhanced surface charges that were achieved through the addition of the HPAM material.

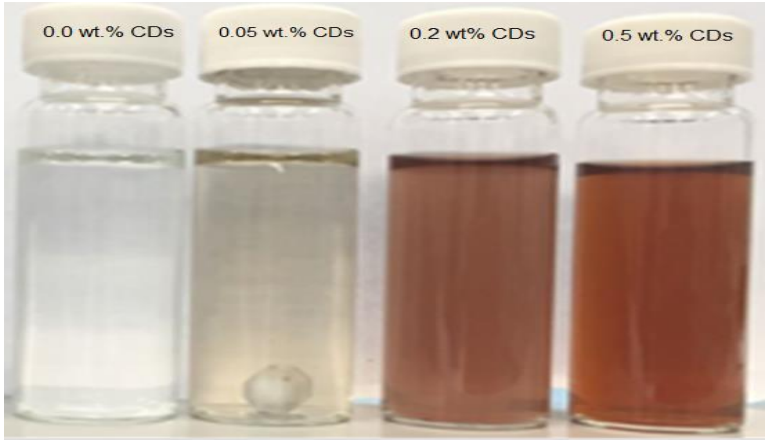

Figure 3.17. Static position stability test for the addition of different amounts of CQDs into HPAM.

In this study, the case of the suspension containing 0.05, 0.2, and 0.5 wt. % CQDs, with neat HPAM sample as a reference, shows a representative example of highly stable suspension (**Fig. 3.18b**). The results indicate that since there is no particle precipitation throughout the height of

the container, therefore, no sedimentation takes place in all ranges of CQDs concentration. This improved stability is related to the variation of the surface charge of the particles. The state of the surface charge with the incorporated amount of CQDs was investigated by measuring the zeta potential of HPAM/CQDs composites at different temperatures, in addition to measuring the zeta potential of neat HPAM and pure CQDs. The results in **Fig. 3.18** indicates that, compared with the zeta potential of bare HPAM and neat CQDs, the zeta potential of the composites is much stronger, indicating that improved dispersion stabilization is achieved.

ATR-FTIR spectroscopy was employed at ambient conditions to confirm the functional group appearance in the prepared materials, as shown in **Fig. 3.19a**. In the spectrum of the CQDs, three peaks appear at 1117, 1449, and 2953 cm^{-1}. These peaks correspond to the vibration of C–O–C stretching, the methyl C–H bending, and the C–H stretching, respectively. The peaks observed in the HPAM spectrum at 3321 and 2923 cm^{-1} can be attributed to the hydroxyl (O–H) and the amino (N–H) groups in the HPAM material. On the other hand, a broader peak has shifted to lower wavenumber (3302 cm^{-1}). This could have arisen due to the formation of carboxylic acid in the backbone chains of the polymer in the HPAM/CQDs composite. Moreover, a peak at 2953 cm^{-1} in the HPAM/CQDs spectrum could be related to the C–H stretching vibration. New peaks also appeared in the spectrum of the HPAM/CQDs at 1081 and 1451 cm^{-1}. These peaks are related to the formation of C–O stretching vibration and to methyl C–H bending vibration, respectively. This could be due to the existence/formation of the ester cross-link bond between the HPAM and the CQDs materials [108, 273]. Additionally, the absorption band formed at 1741 cm^{-1} is ascribed to carbonyl stretching vibration for the CQDs, as is the band at 1568 cm^{-1} which relates to –CO–O–C vibration stretching. There are other characteristic strong peaks between 1325 and 1386 cm^{-1}, representing the fingerprint region of C–O–C bonds and/or ester bonds (–CO–O–C). The appearance of new peaks proof

of the formation of chemical linkage between the carboxyl group in the deaminated polymer and the hydroxyl group in the CQDs.

Remarkably, the results from the ATR-FTIR analyses suggest the evolution of chemical ligation between the HPAM segments and the CQDs in the composite material. Concerning that, the composites are observed and considered stable enough to circumvent the possible phase separation that can easily happen in the fabrication of the nanocomposites via the physical mixing of polymer and carbon dots. The measured pH values (**Fig. 3.19b**) showed an increased acidity corresponding to an increase in the concentration of the CQDs. This is consistent with the release of $-NH_2$ molecules, forming NH_3. A more detailed explanation of this mechanism and chemical linkage is discussed in **Chapter 6**.

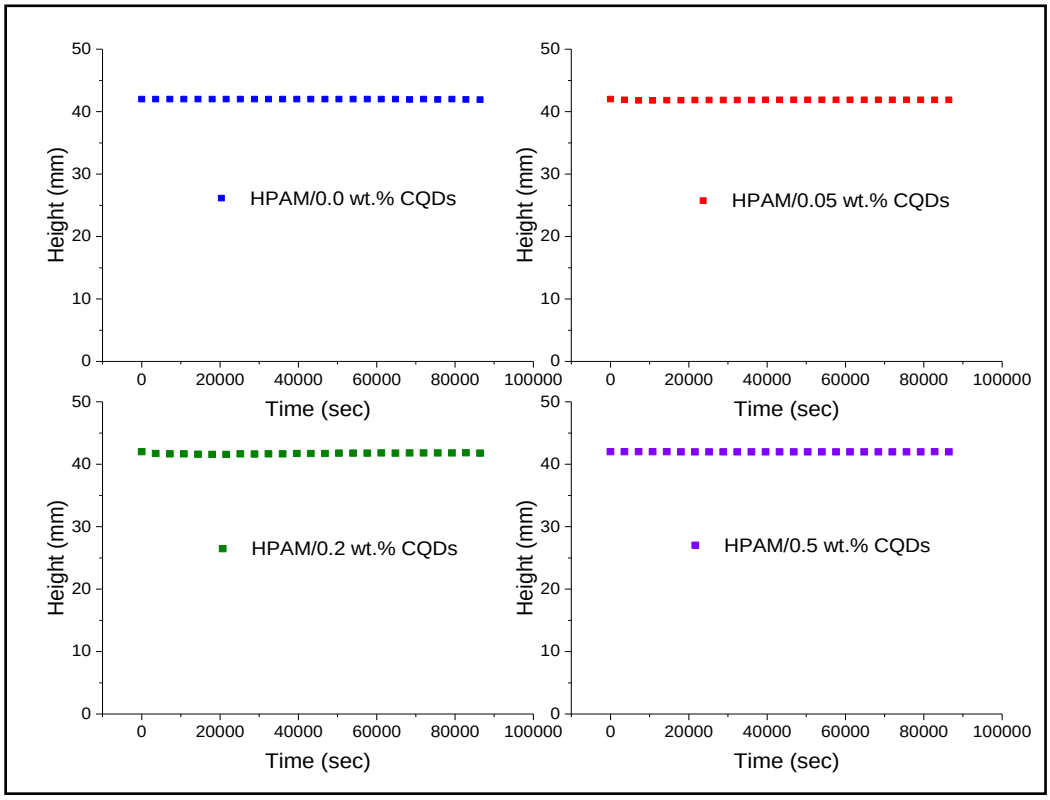

Figure 3.18. Turbiscan stabilisation tests after 24 h of HPAM and HPAM/CQDs composites containing different amounts of CQDs.

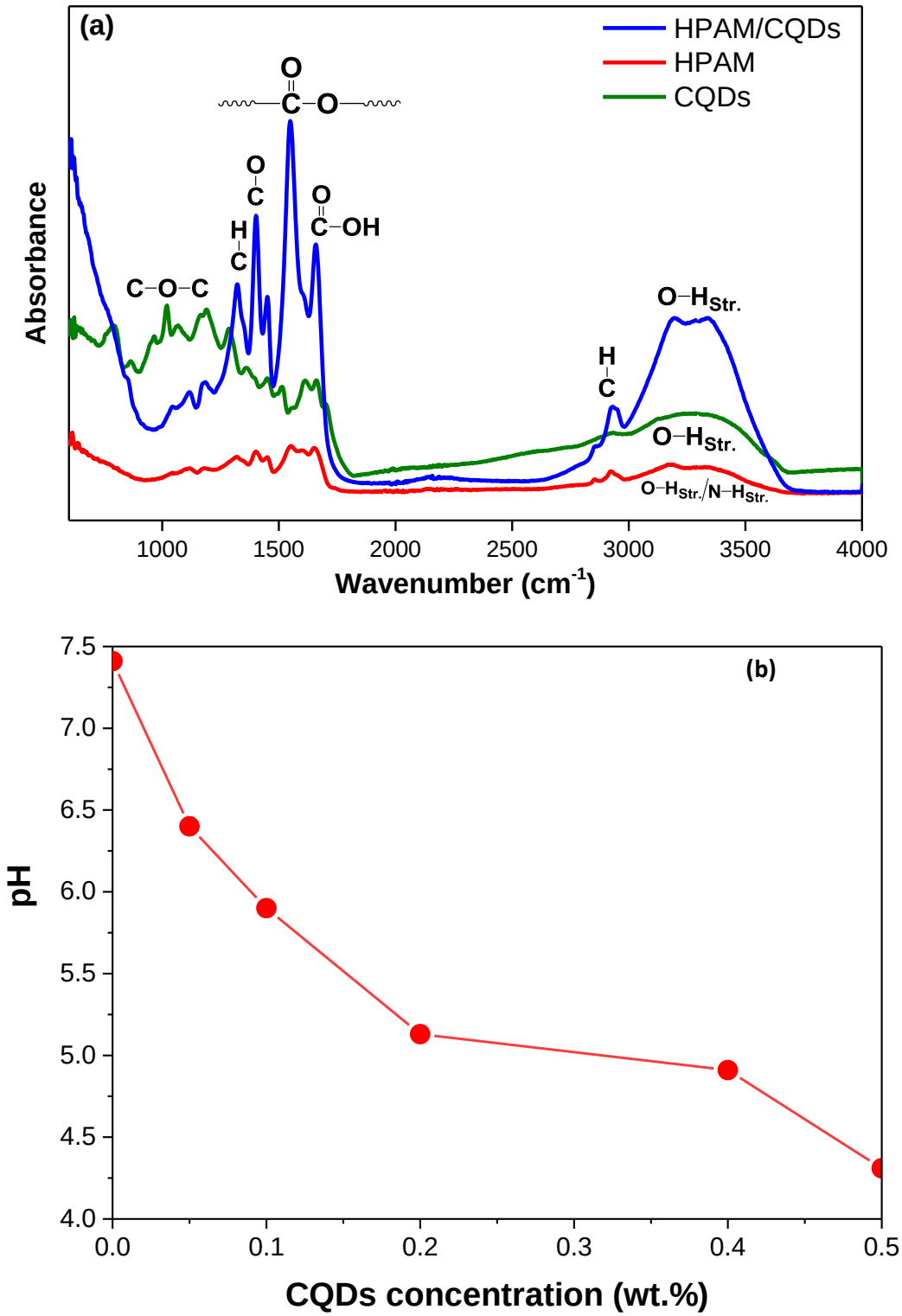

Figure 3.19. (a) ATR-FTIR spectra and (b) monitoring of pH while the addition of CQDs to the HPAM solution was undertaken.

The XRD profiles for the PAM and the HPAM/CQDs composites are contained in **Fig. 3.20**. In the case of the HPAM/CQDs composite, two extra sharp diffraction peaks appeared at 2θ of 31.7 and 45.5°. These are related to the existence of small crystalline fractions of the HPAM/CQDs composites. This suggests that introducing the CQDs into the HPAM transformed it from an amorphous status into a low degree of crystallinity. The NMR spectroscopy was used to evaluate the influence of the addition of the CQDs into the HPAM. **Fig. 3.21,** shows the proton NMR results of the HPAM solutions and the HPAM/CQDs composites, respectively. The peaks appear at 1.4 and 2.1 ppm represent protons in $–CH_2$. In the HPAM material, $–CO–NH_2$ and C–H peaks were observed around 6.3 ppm and 6.9 ppm, respectively. These confirmed the formation of major polyacrylamide functional groups in the spectrum [274-276]. However, the $–NH_2$ peaks in the HPAM spectrum disappear in the HPAM/CQDs composite, certainly proving the deamination from the polymer backbone by the presence of the CQDs.

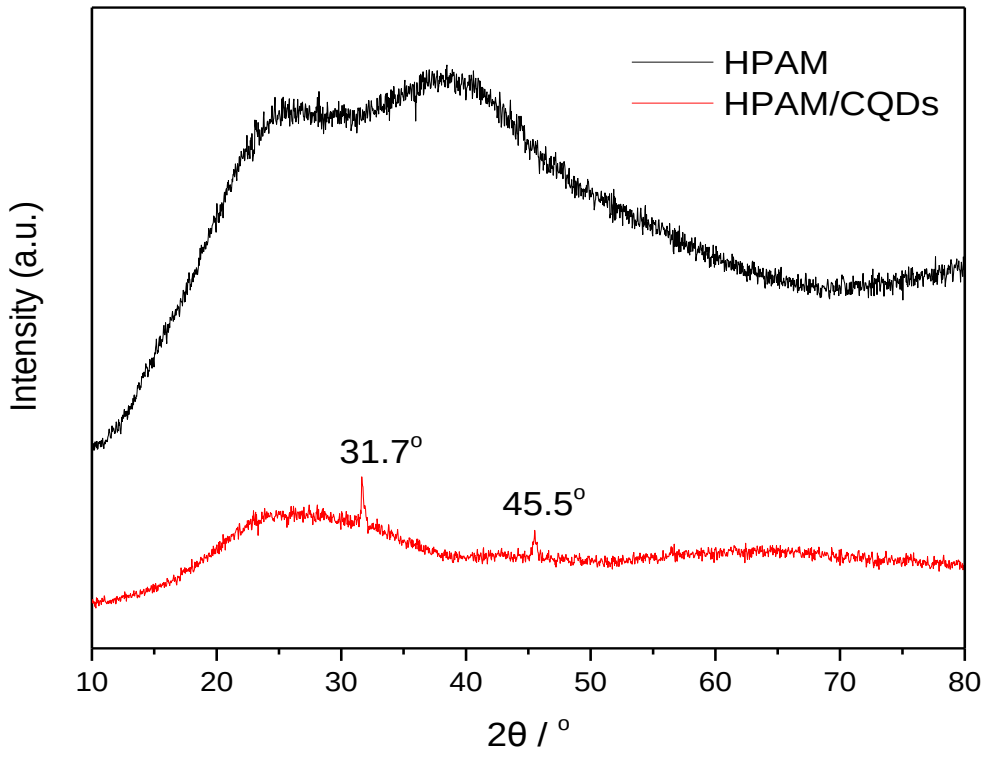

Figure 3.20. XRD profiles for HPAM and PAM/CQDs composites.

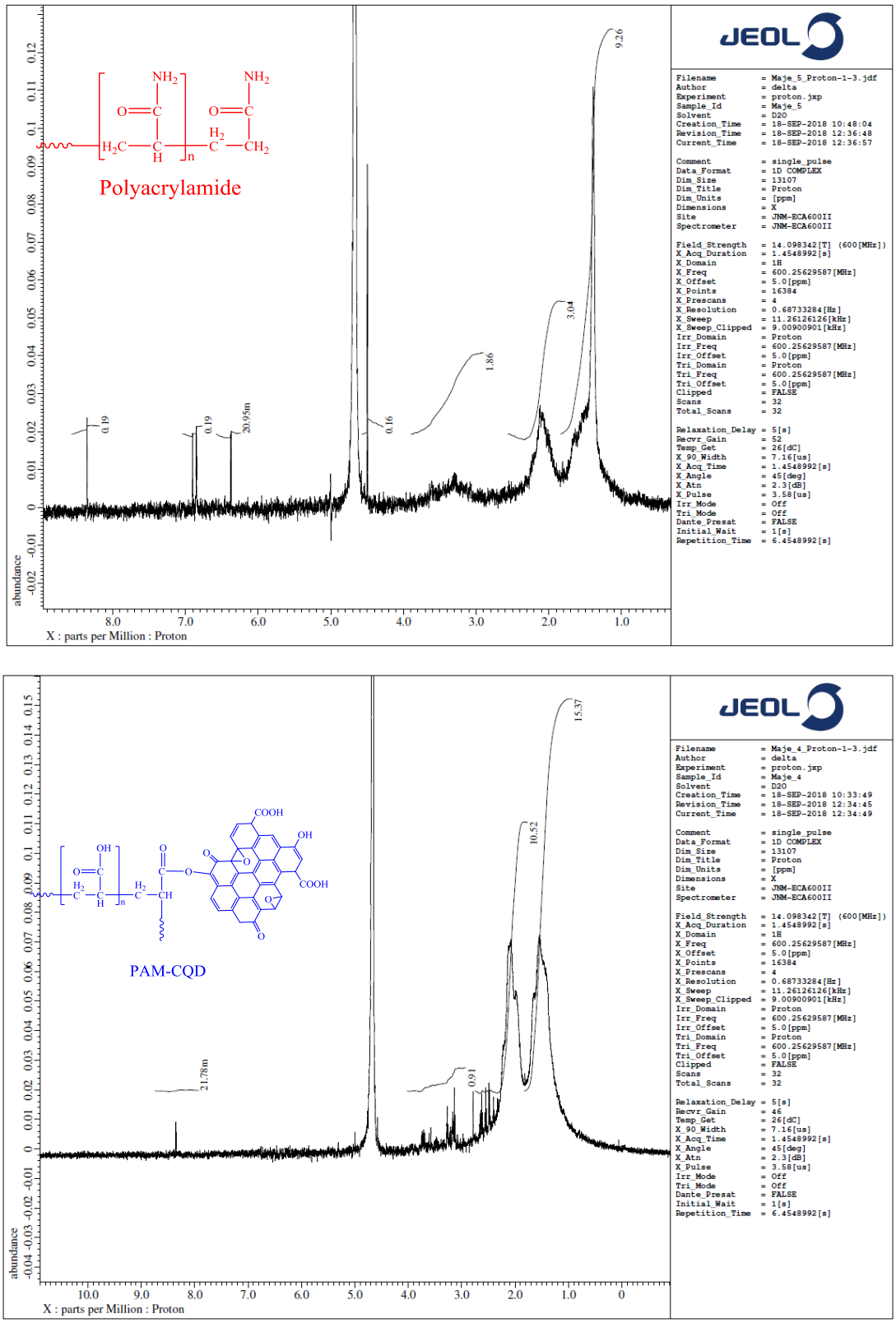

Figure 3.21. 1H-NMR for (top) HPAM, (bottom) HPAM/CQDs composites.

3.4.Synthesis and characterizations of polymer using free-radical polymerization method

3.4.1. Reagents

Monomer of acrylamide (AA), isopropyl acrylamide (IAA), (3-acrylamidopropyl) trimethyl-ammonium chloride (ATAC), 2-acrylamido-2-methyl-1-propanesulfonic acid (APSA), 4-4'-azo-bis-4-cyanopentanoic acid (ACPA), calcium chloride, magnesium chloride, and sodium chloride were obtained from Sigma-Aldrich. Mineral oil with a viscosity of 42 mPas and a density of 0.82 kg/m^3 were purchased from Kerax Ltd. (UK).

3.4.2. Polymer synthesis methods

The polymers were synthesized from AA, IAA, APSA, and ATAC monomers based on the mass percentage describe in **Table 3.4**. The measured concentrations were individually dissolved in 180 ml deionized water in a round-bottomed flask. The flask was stirred in a water bath at 80 °C for 6 hours under reflux in the presence of nitrogen gas following the addition of 10 mg ACPA as an initiator to obtain free radical polymerizations as shown in **Fig. 3.22**.

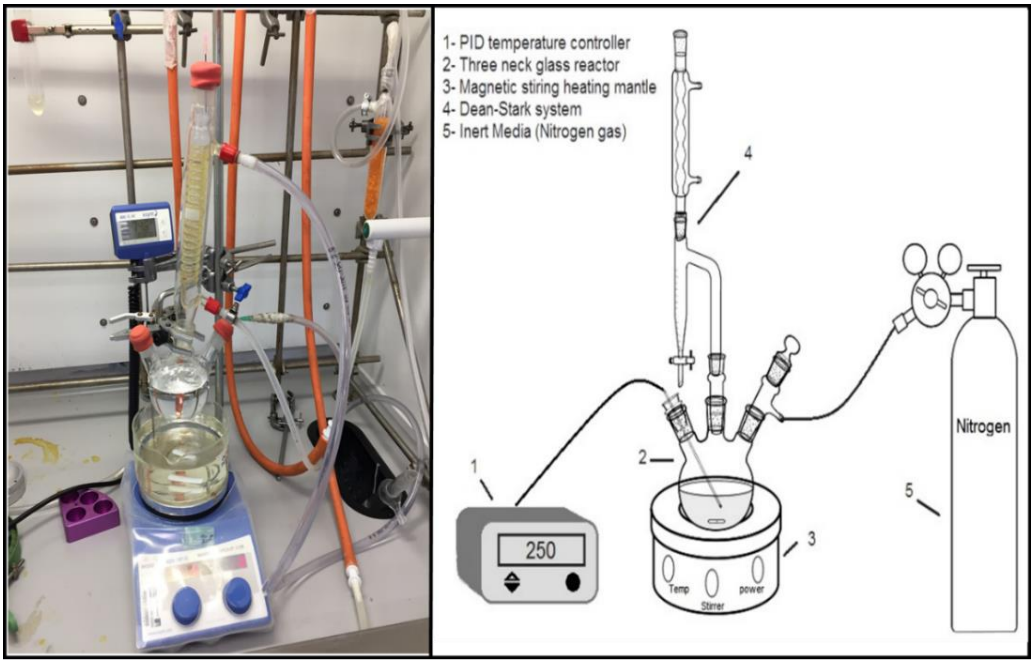

Figure 3.22. (Left) Set-up for the synthesis of co/ter-polymers, (Right) schematic design of the experimental set-up.

Table 3.4. Different mixture of AA monomers during the polymerization process.

Properties	Sample A	Sample B	Sample C	Sample D	Sample E
AA (g)	7.5	3.75	3.75	3.75	3.75
IAA (g)	0	0	0	0	1.875
APSA (g)	0	3.75	0	1.875	1.875
ATAC (g)	0	0	3.75	1.875	0
Conversion %	100	85	83	81	81
PDI	1.68	2.03	2.14	4.59	5.11
$M_{w,GPC}$ (g/mol)	499573	696575	636557	721406	1106656
$M_{n,GPC}$ (g/mol)	295696	343140	297457	157055	157055
Substitution ratio (%)	AA:100	APSA:51.6- AA: 48.4	ATAC:53.9-AA:46.1	APSA:32.9-ATAC:28.7-AA:38.4	APSA:25.3-IAA:30.5-AA:44.1

3.4.3. Preparation of polymer nanocomposite using multi-wall carbon nanotubes (MWCNTs)

To obtain polymer nanoparticle dispersions, the desired concentration of the MWCNTs were dispersed in brine (2 wt. % $MgCl_2$, 2 wt. % $CaCl_2$ and 8 wt. % NaCl), or solution with an extreme alkaline condition (pH=11). PH=11 is selected in this project because extreme pH affected the PAM performance in the EOR application causing the electrolyte double layer to shrink, which eventually reduces its viscosity and consequently leads to poor EOR performance. The mixture was sonicated using a probe sonicator (Fisher scientific ultrasound probe) at an amplitude speed of 25 percent for 5 minutes to avoid particle aggregation. The synthesized polymer was then added into the suspension to obtain MWCNTs/polymer dispersion and mixed by gentle stirring using an SB 162-3, Stuart magnetic stirrer for 24 h to allow sufficient time for the MWCNTs to associate with the graft polymer. A pH of the solution was regulated to acidic and alkali conditions with hydrochloric acid and sodium hydroxide, respectively using pH meter (Seven Compact Mettler Toledo, UK). The brine solution was stored at a fixed temperature of 80 °C in an oven, and the stability test of immovable samples was conducted after 7 days.

3.4.4. Characterizations

Proton NMR (^{1}H-NMR) was used to evaluate the modification of co/ter-polymers using Advanced 500 Bruker Nuclear magnetic resonance (NMR) (resonance frequency of 400 MHz). Gel permeation chromatography (GPC) was also used to analyse the polymers to obtain the molecular weight and polydispersity using 0.1 M $NaNO_3$ as the mobile phase. The Agilent Technologies Infinity 1260 MDS instrument was used for the analysis, which was equipped with light scattering (LS), differential refractive index (DRI), UV detectors, and viscometry (VS). Tosoh TSKGel GPWXL columns were set and operated at 40 °C with a 1 mL/min flow

rate. The calibration was conducted between 106 to 1,368,000 g/mol using Poly(ethylene oxide) standards (Agilent Easy Vials). The analysed samples were filtered before injection through 0.22 μm pore size hydrophilic GVWP membrane. Agilent GPC/SEC software was used to determine the experimental molar mass and dispersity values of synthesized polymers.

The nature of surface functionality species of the synthesised co/ter-polymers and their composites with MWCNTs was examined using ATR-Fourier-transform infrared spectroscopy (Nicolet iS10 FT-IR spectrometer). The morphology of the polymer/MWCNTs dispersion was investigated using a transmission electron microscope (FEI Tecnai TF20 TEM). The stability of MWCNTs was performed to observe the flocculation and sedimentation during centrifugation of MWCNTs/polymer dispersion using a dispersion analyser centrifuge (LUMiSizer, Lum GmbH, Germany) by recording the transmission of near-infrared light. Viscosity (η) of MWCNTs/polymers solution was measured using a Physica Anton Paar rheometer (Cone plate CP75-1, model MCR 301) at a shear range of 10-1000 s^{-1} at 22 °C. Different frequencies ranging between 1 and 100 rad/s (i.e., 0.159 to 15.92 Hz) were used for dynamic frequency sweep measurement. Interfacial tension (IFT) and contact angle (CA) measurements were performed using a pendent drop tensiometer, equipped with a temperature controller and digital camera used for capturing the image of the droplet.

3.4.5. Results and discussion

3.4.5.1. Characterization of Co/ter-polymer and MWCNTs/polymer hybrid

The structure of the synthesized polymers consisted of hydrophilic molecular chains with different neutral random side chains viz: hydrophobic, cationic, or anionic as shown in **Fig. 3.23**. ^{1}H-NMR spectra of the co/ter-polymers were recorded after dissolving 10000 ppm in 1:10 deuterium oxide (D_2O) and water solution at 25 °C. The analysed NMR spectra of the synthesized polymers are shown in **Fig. 3.24**. The conversion of polymers was obtained by

calculating the NMR resonance ratio between the monomers and polymer units, as proposed by the equation 3.4 [286].

$$Conversion = \frac{S_p}{S_p + S_m} \ldots\ldots\ldots\ldots\ldots\ldots\ldots\ldots 3.4$$

Where S_m stands for the peak area of the monomer and S_p represent the peak area of the obtained polymer. The conversions at the end of co/ter-polymerization have been reported in **Table 3.4**. The MastReNova software, (Mestrelab research S.L., version 6.0.2) was used to measure the integration peaks that contributed to the functional groups. For instance, in the ^{1}H-NMR spectra of sample B, the integration peaks that appear for the functional groups of APSA and AA monomers after they react are 3.41 and 3.2 (equivalent to 51.6 and 48.4 substitution percent), respectively as illustrated in **Fig 3.24i.** Substitution percent of the remaining samples are shown in **Table 3.4**.

The polydispersity index (PDI), the weight average molecular weight (M_w), and the number average molecular weight (M_n) of the polymers obtained by GPC are compiled in **Table 3.4 and Fig. 3.25**. The outcome shows that the polydispersity of polymers increased when different monomers were used during polymerization. The minimum and maximum PDI belong to pure acrylamide polymer and partially hydrophobic polymers respectively. The higher M_w and PDI of partially hydrophobic polymers show the high molecular weight in sample E has a significant influence.

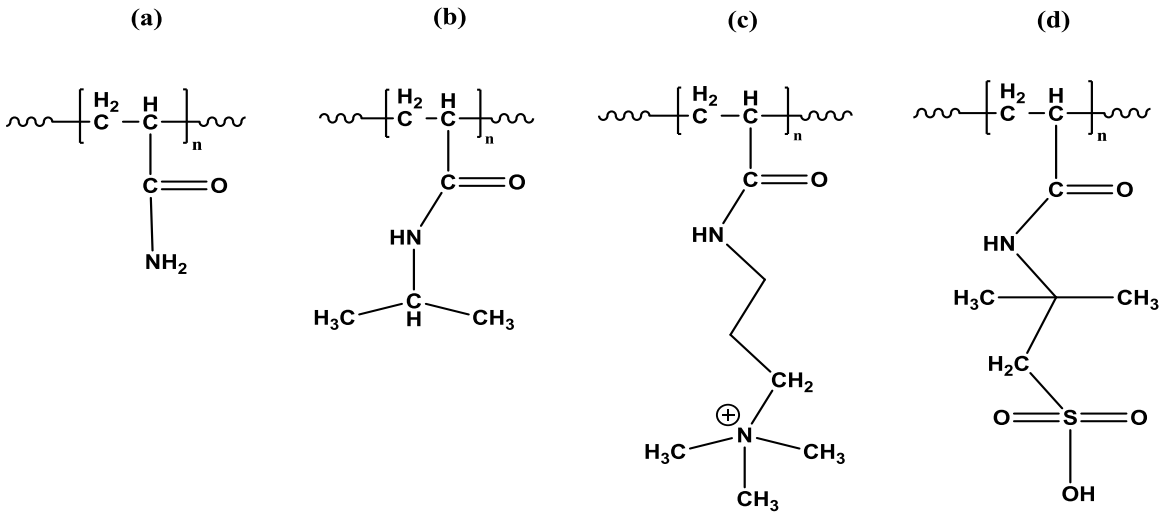

Figure 3.23. Schematic of side chains in co/tar-polymers molecular structure (a) Amide side chain, (b) Hydrophobic side chain (c) Cationic side chain, and (d) Anionic side chain.

(a)

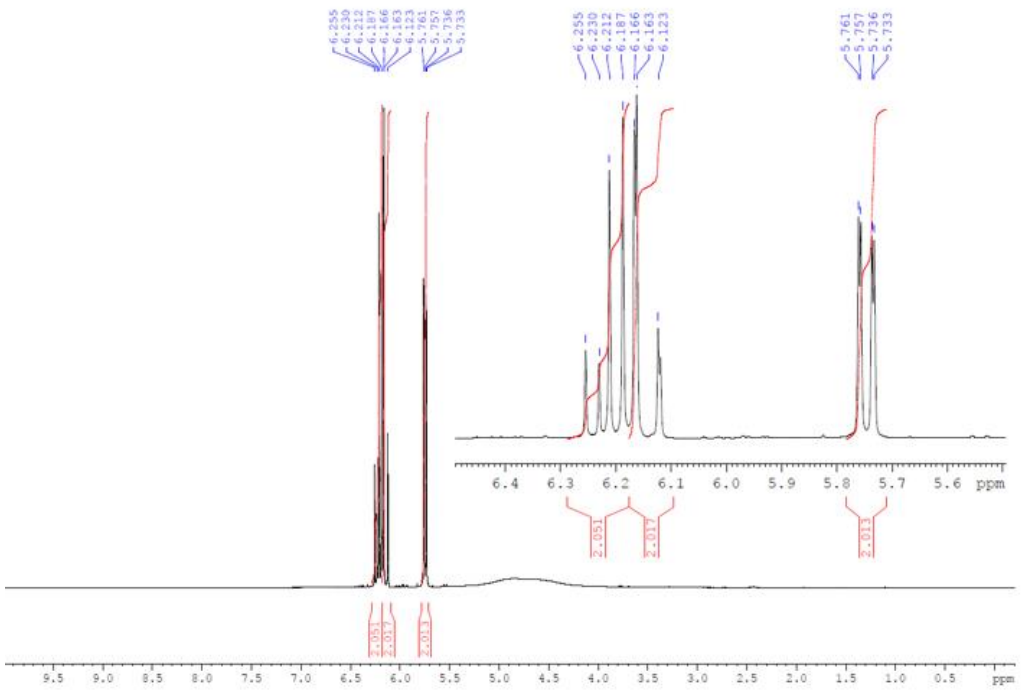

Figure 3.24. 1H-NMR spectra for different sample A: (a) AA monomer, (b) PAA, sample B: (c) AA-APSA monomers blend, (d) AA-APSA copolymer, sample C: (e) AA-ATAC monomers blend, (f) AA-ATAC copolymer, and sample D: (g) AA-APSA-IAA monomers blend, (h) AA-APSA-IAA terpolymer, (i) integration of peaks for sample B.

(b)

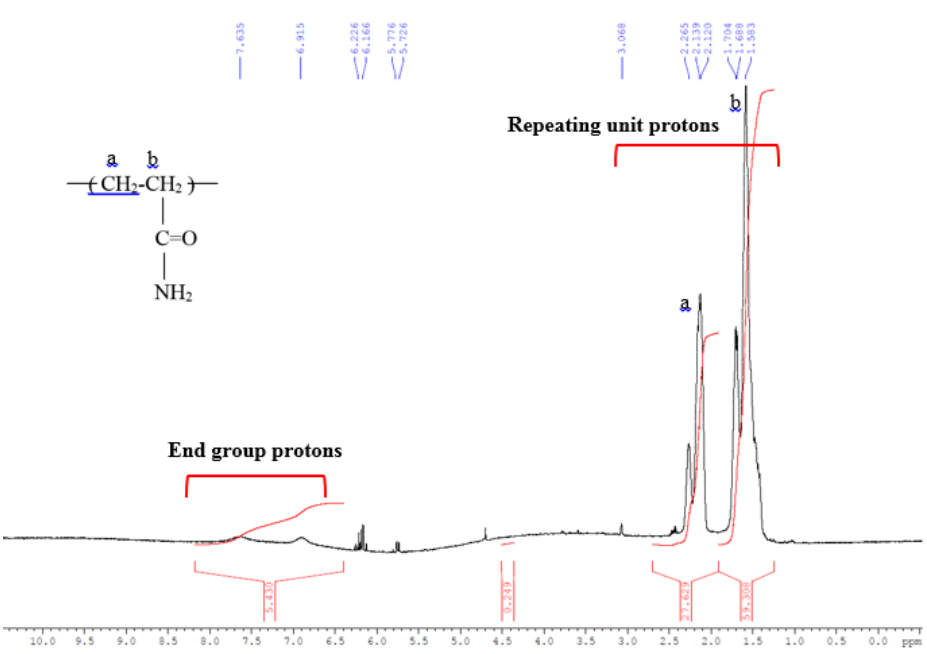

(c)

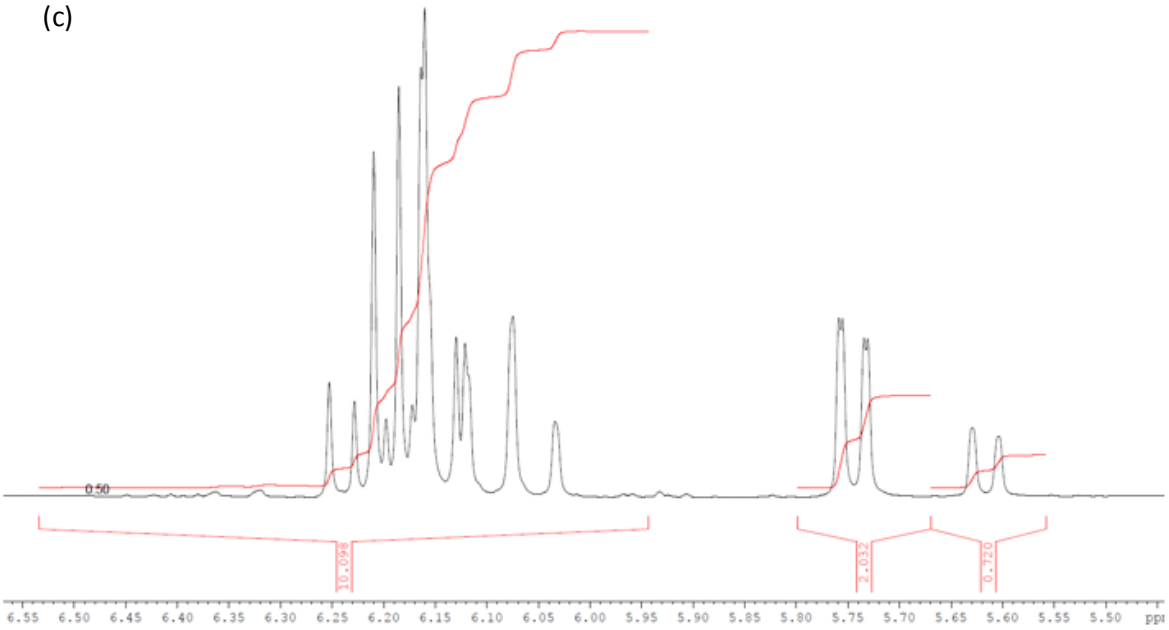

Figure 3.24: Continues.

(d)

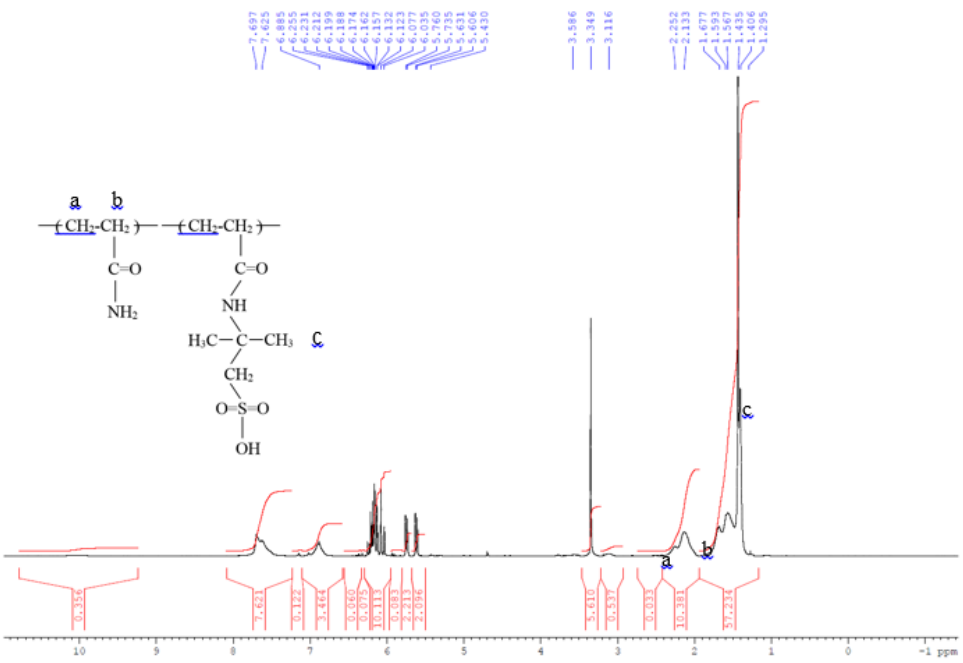

(e)

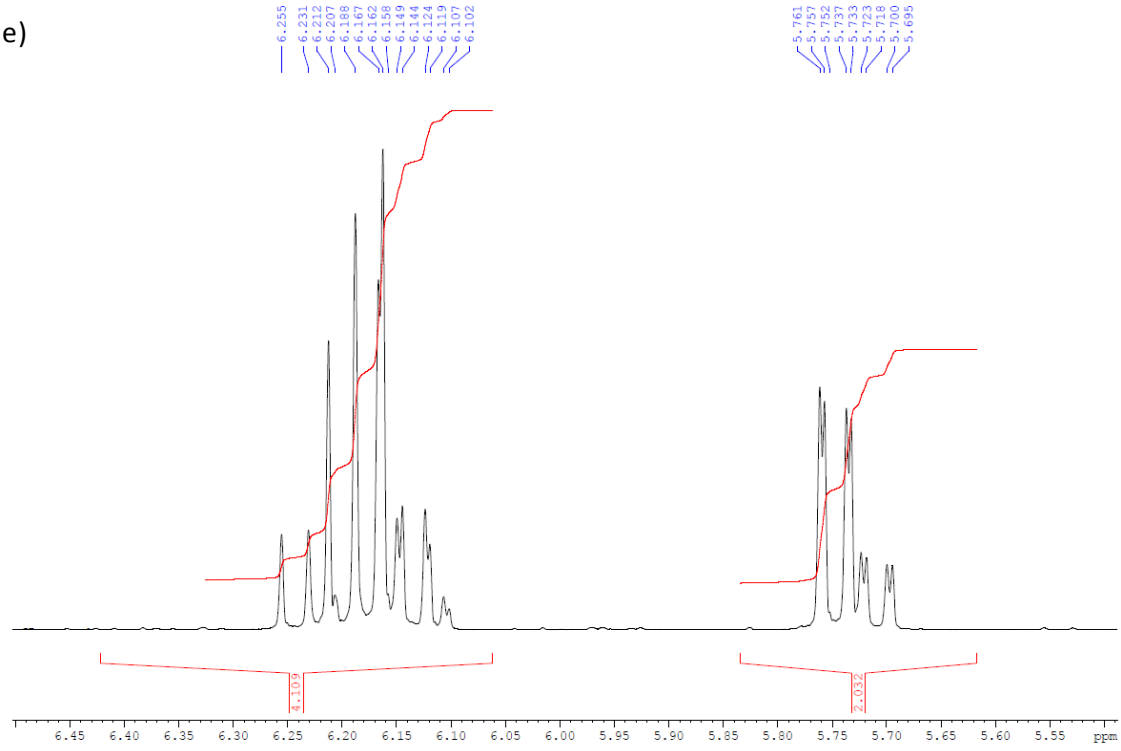

Figure 3.24: Continues.

(f)

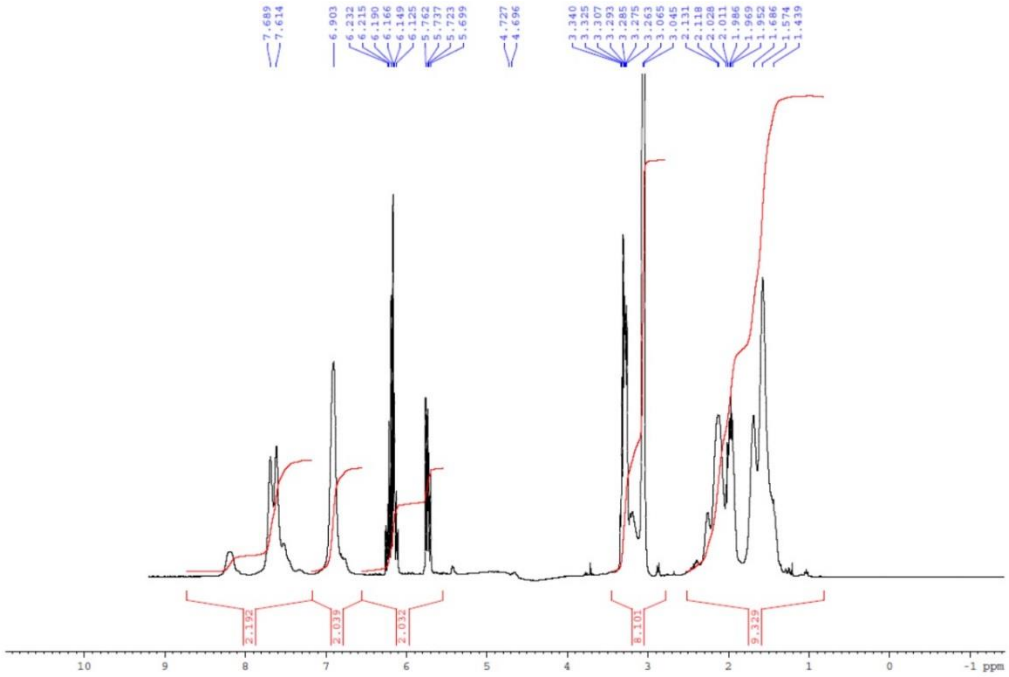

(g)

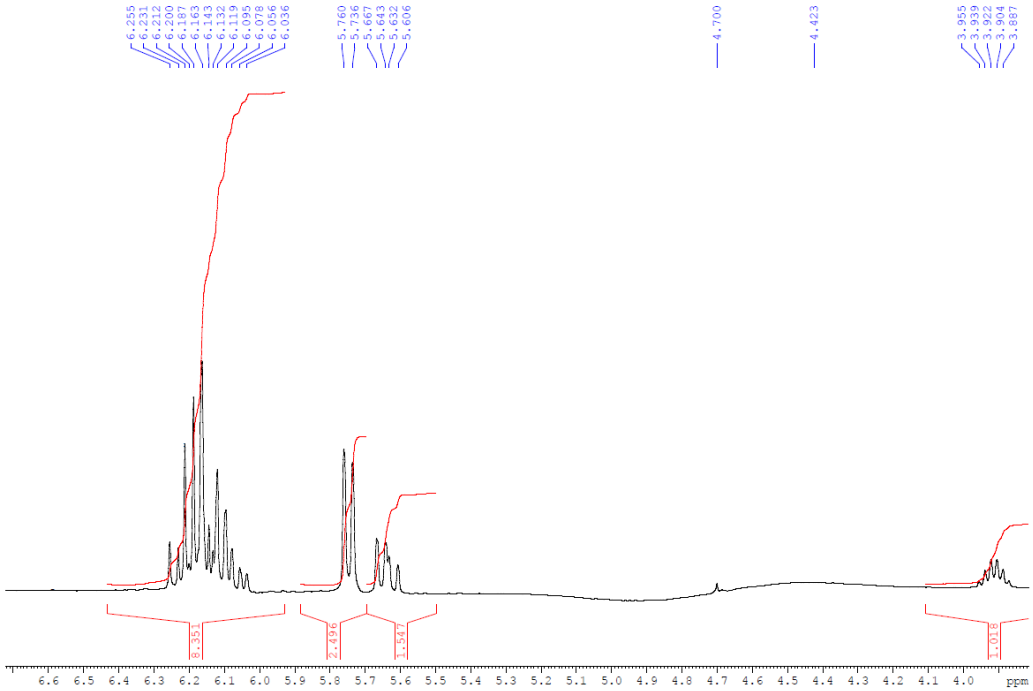

Figure 3.24: Continues.

(h)

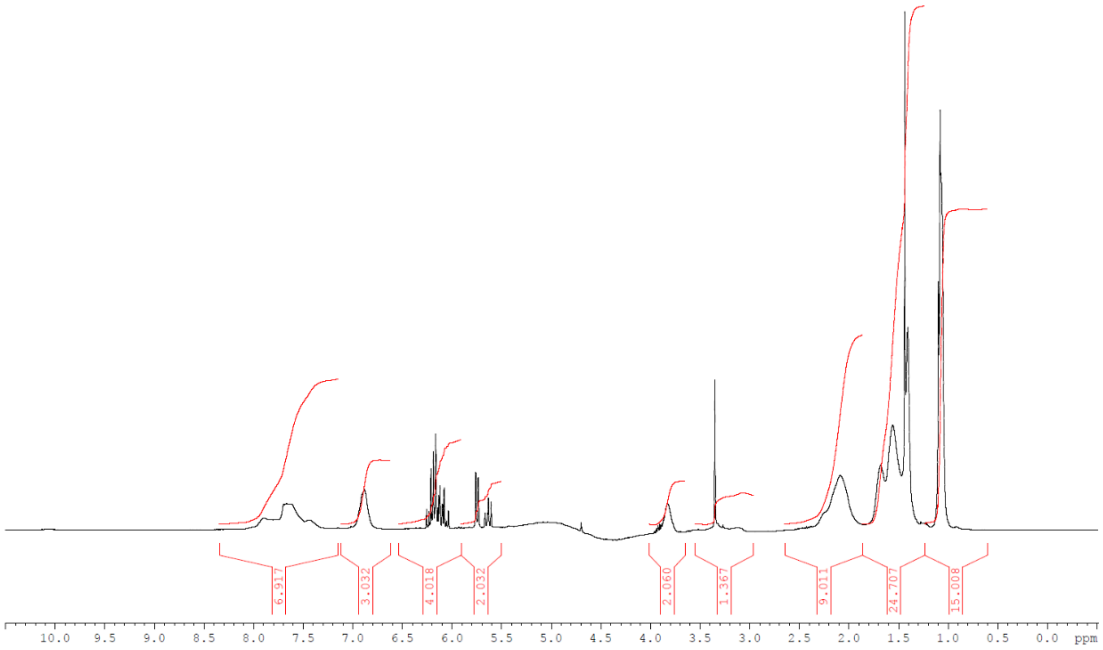

(i)

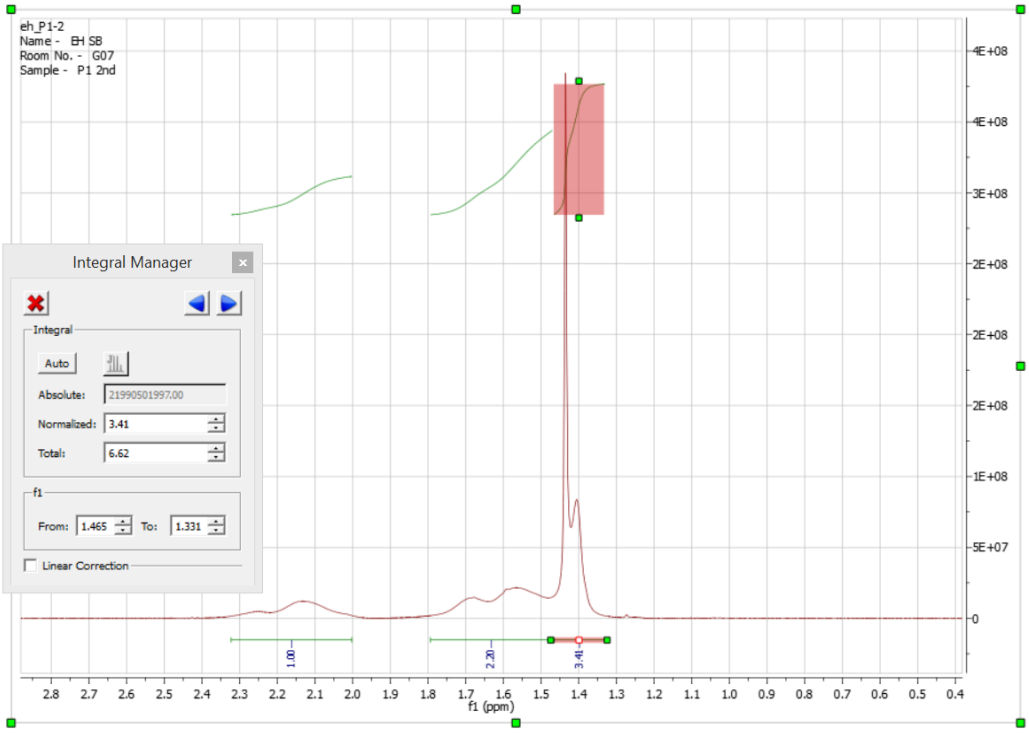

Figure 3.24: Continues.

Fig. 3.26 depicts the ATR-FTIR spectra of different co/ter-polymers and the dispersions of polymer/MWCNT. In the polymer spectra, it was observed that the adsorption peak of APSA anionic polymer containing SO_3 group appeared at 1040 cm^{-1} [287, 288]. The absorption band observed at 1037 cm^{-1} for copolymers containing APSA (samples B and D) decisively shows

the presence of anionic monomers in the structure of the copolymer, which confirms the existence of the SO_3 group stretching vibrations. The vibrations observed at 967 cm^{-1} in samples C and D are attributed to the quaternary ammonium group in the ethoxylated group of ATAC cationic polymer [289, 290]. The adsorption bands at 1649 cm^{-1} and 2930 cm^{-1} were derived from C=O bonds and C-H stretching vibration, respectively. On the other hand, the ATR-FTIR spectrum of polymer/MWCNT composites shows almost all the peaks that appear in the net polymer samples but most of the peaks become weaker. Because in ATR-FTIR, the detection depth is normally between 1 to 2μm, but it can vary depending on the materials, for instance, a black sample (e.g. MWCNTs/polymer) is highly absorbing materials which tend to have smaller sampling depths causing the signals to be weak. New peaks at around 2200 cm^{-1} are attributed to the CN stretching vibration emerging from the NH_2 group in PAM and CO in the nanocomposites. As shown in **Fig. 3.27**, different approaches such as covalent linking, complexation through the interactions and wrapping of NH-π, CH-π, π-π were proposed using polymers and functionalized MWCNTs composites [291-295]. These multi point interactions strengthen the polymer chains resulting in enhanced internal friction between the polymer chains and the molecules of the neighbouring solvents, thus improving the solution viscosity.

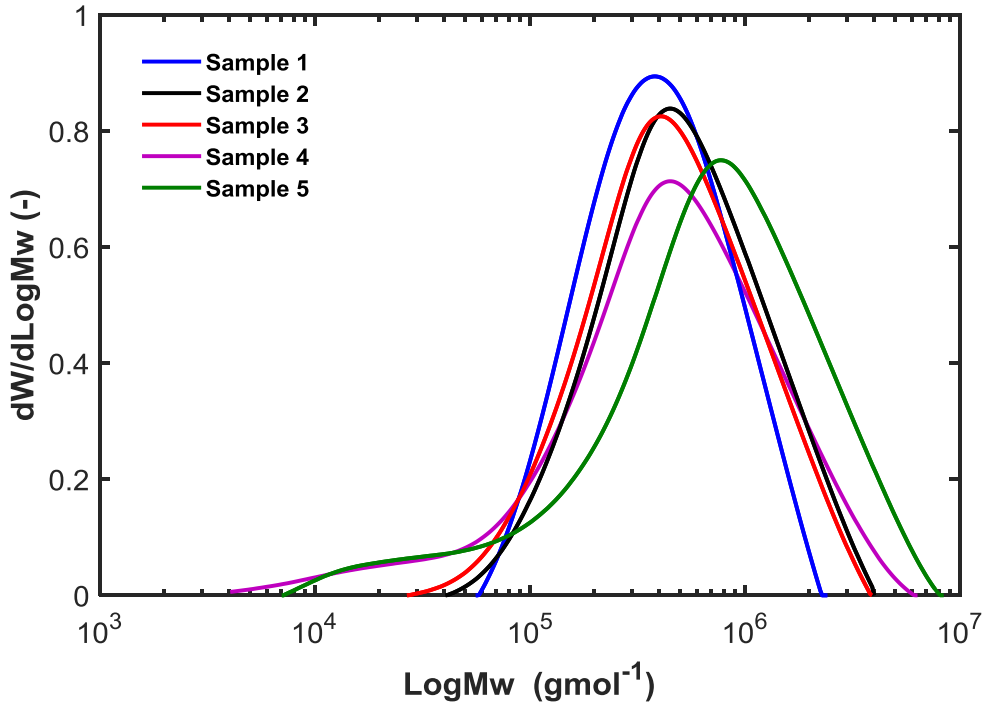

Figure 3.25. Spectra for the molecular weight distribution of polymer samples obtained from GPC.

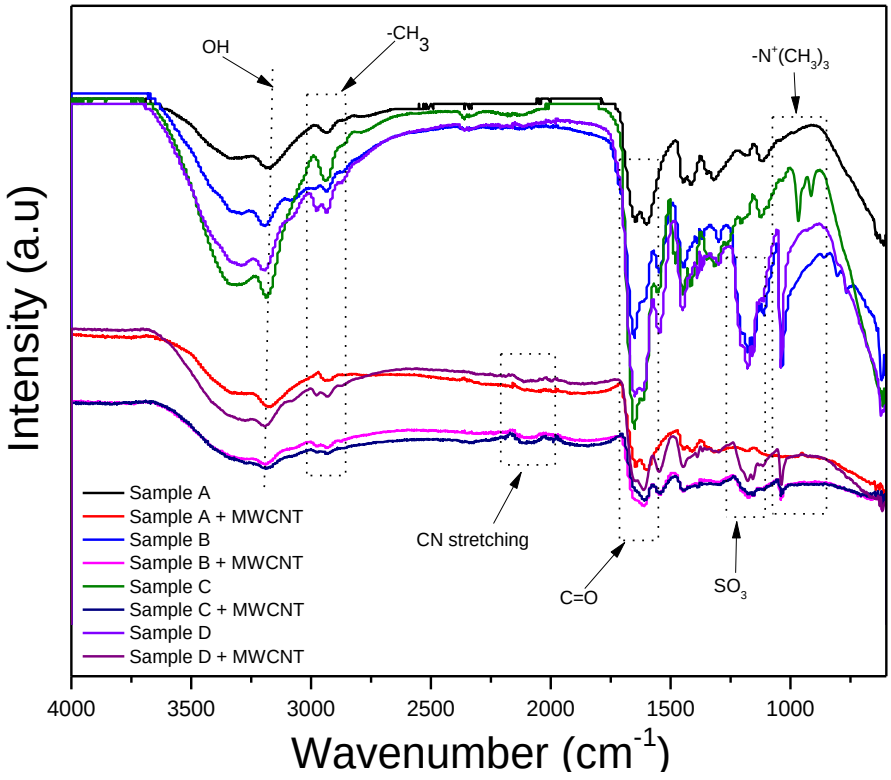

Figure 3.26. FTIR analysis of co/ter-polymers and polymer/MWCNT composites.

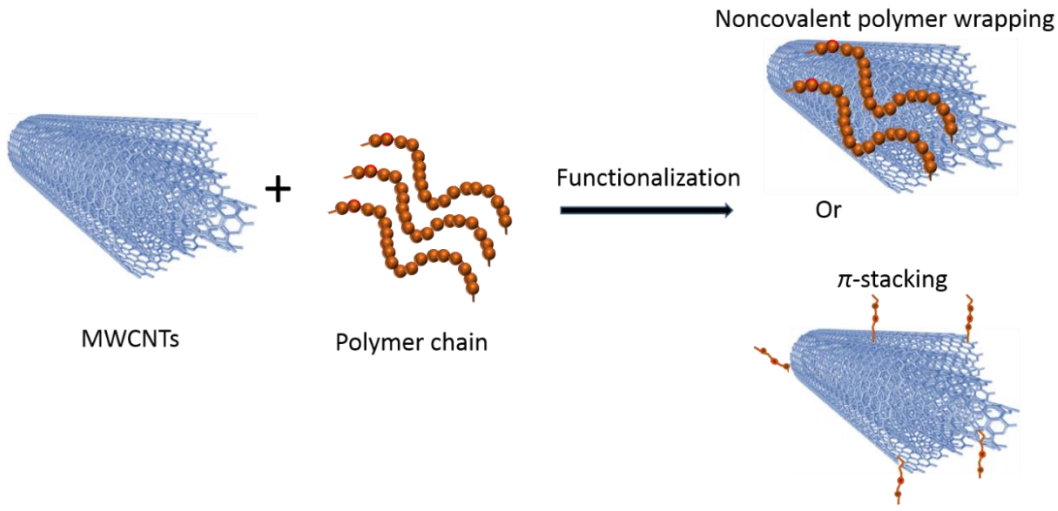

Figure 3.27. Schematic illustration for a different sequence for MWCNTs functionalization via noncovalent polymer wrapping or π-stacking

3.4.5.2. Stability analysis

Polymer/MWCNTs adsorption and stability were investigated using experimental [293, 296, 297] and MD simulation methods [298, 299]. As reported, two main factors that influence the stability of the MWCNTs in solution are the electrostatic repulsion between polymer chains when counter ions exist and the interaction of the polymer side chains with the aqueous phase. It has been reported that the flocculation of MWCNTs in the composites under severe conditions causes phase separation in an aqueous medium. The most common cations present in oil reservoirs are Na^{+}, $Ca^{2+,}$ and Mg^{2+}, which interact with the polyelectrolytes and deteriorate the polymer performance [56]. In this work, an analytical centrifugation dispersion analyser (LUMiSizer 6110) has been used to investigate the stability of the formed MWCNTs/polymer nanocomposites under harsh conditions.

Polycarbonate capillary cells were filled with 0.5 ml of MWCNTs/polymer dispersion and centrifuged at 3000 rpm for 36 min which corresponds to 1 month in actual conditions. **Fig. 3.28** shows the dispersed MWCNTs containing a negative sulfonate-functional group shows

lower stability at acidic pH. This is presumably because of the effect of a positive molecular proton (H^+) on the sulfonate groups. in contracts, the deprotonation of sulfonate groups on the copolymer was higher at alkaline pH rather than acidic pH which contributes substantially to electrostatic repulsive force between functionalized MWCNTs. Comparatively, high stability of dispersed MWCNTs/sample C was observed in positive groups of a copolymer containing quarterly ammonium side chains at acidic pH, because the polymers were protonated more effectively in low pH conditions. The effect pH variation has less significance on the stability of MWCNTs in solution. However, MWCNTs were shown to be unstable at both acidic and alkali pH in the presence of positive-negative side chains in the polyampholytic polymer structure (sample D) as shown in **Fig. 3.28 (c).** Furthermore, copolymers consisting of negative sulfonate functional groups (sample B) demonstrated outstanding stability in high temperature-high salinity conditions. This is because the copolymer containing sulfonate groups can withstand divalent ions and sustain the steric repulsive forces between polymer branches and the solubility of skeleton acrylamide at high salt contents [230, 300, 301]. Therefore, the negative sulfonate group prevented the collapse of the polymer backbone by attracting both mono and divalent ions inside API brine thereby protecting the chain's repulsion of the acrylamide chains as presented in **Fig. 3.28 (b). Fig. 3.29** shows the TEM images of the MWCNTs and sample B/MWCNTs as an example to illustrate the stable dispersion and microstructure of polymer/MWCNTs solution. MWCNTs show an array of concentric cylinders, polymer/MWCNTs displayed an excellent dispersion ability, showing polymer has been grafted to the MWCNTs, which could be used to confirm the appearance of chemical bonds between the polymer and MWCNTs. Moreover, the way the MWCNTs superimpose with polymer is evidence that the polymer-MWCNTs interaction is strong chemical adhesion and not a mere physical contact.

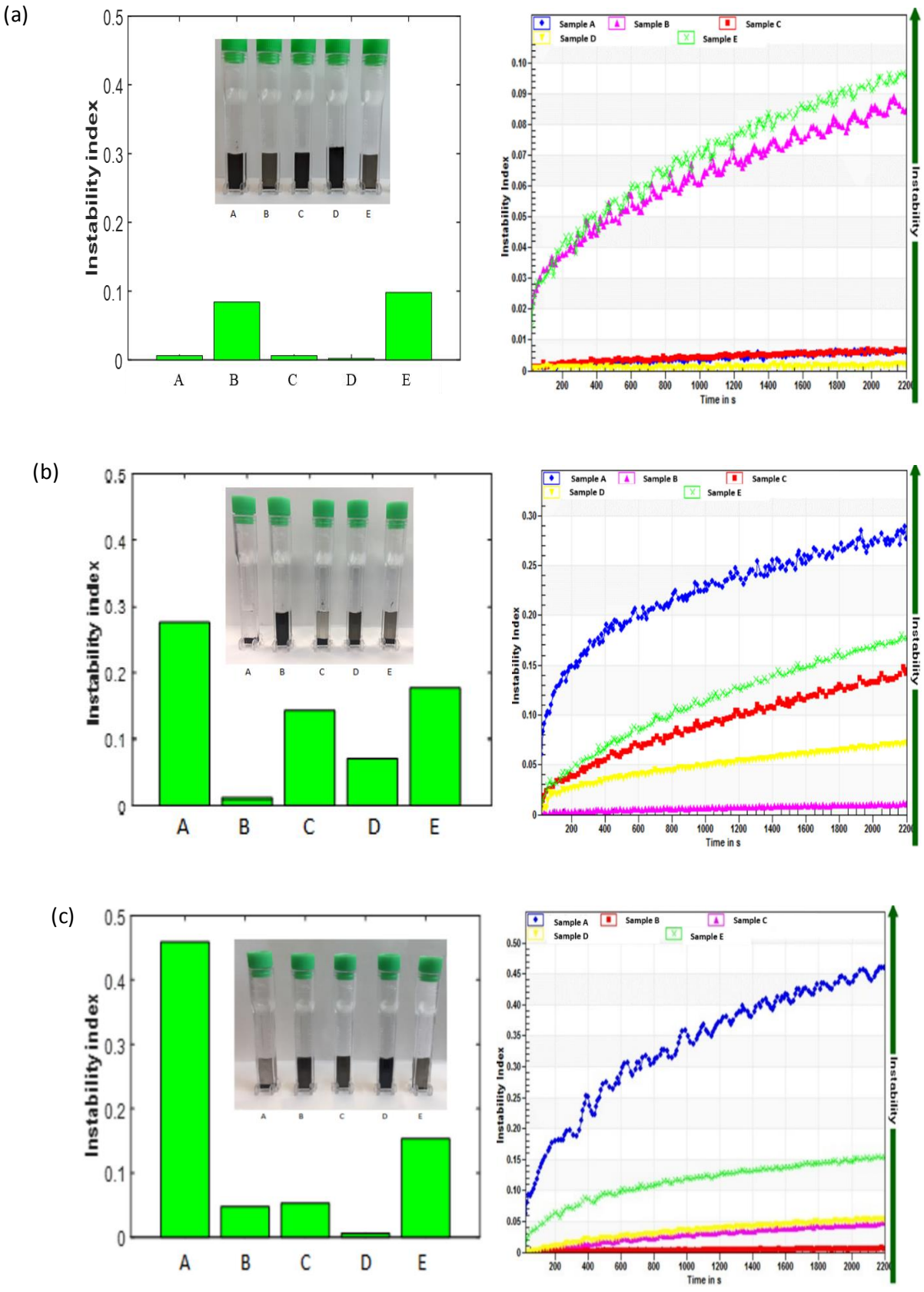

Figure 3.28. Instability index of MWCNTs (1000 ppm)/polymer (1000) at (a) normal condition, (b) API brine and (c) pH=11.

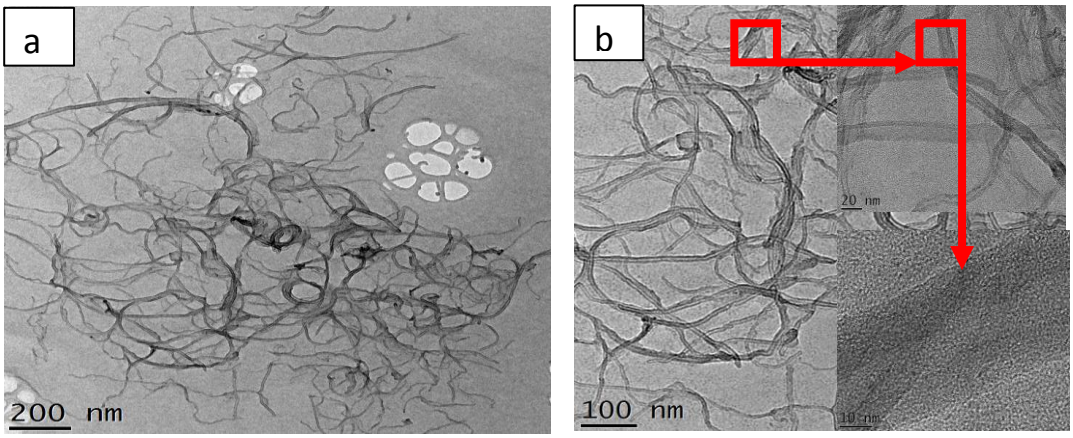

Figure 3.29. TEM photo of (a) MWCNTs and (b) MWCNTs/polymer (sample B) at different magnification.

3.5. Chapter Summary

This Chapter presented the synthesis and characterization of different polymers and polymer/NPs composites via mechanical mixing. The composites HPAM with GO and CQDs were prepared, five different modified acrylamide-based co/ter-polymers were produced via free-radical polymerization, and MWCNTs were introduced to improve the stability of the polymer under high temperature and in API and pH conditions. The synthesized materials were characterised by ^{1}H-NMR, GPC, SEM and TEM, TGA, CHNS, FT-IR, XRD and Raman analysis, etc.

The dispersion stability observed using Turbsican analysis showed that HPAM/GO and HPAM/CQDs composites exhibited excellent stability in the presence of NaCl but became unstable in API brine and complex brines. The FT-IR spectral data confirmed the formation of the covalent linkage and the electrostatic hydrogen bond between GO and HPAM functional groups, which helps to strengthen the hybrid stability. The analyses also showed the evolution

of chemical linkage between segments of HPAM and those of the GO sheets. Thus, for CQDs, the formation of strong covalent bonding is achieved in the composite material between the deaminated amine in the polymer backbone and the hydroxyl group in the CQDs.

The polydispersity of different co/ter-polymers was varied by changing various monomers during the polymerization process. The polyampholytic terpolymer and polyelectrolyte copolymer containing negative sulfonate groups showed better enhancement in the stability of MWCNTs/polymer dispersions in both alkali and API brine solution, respectively, which could be used to select proper polymers. This improvement showed that the copolymer containing sulfonate groups can withstand divalent ions and sustain the steric repulsive forces between polymer branches and the solubility of skeleton acrylamide at high salt contents, by preventing the collapse of the polymer backbone, which attracted both mono and divalent ions in the API brine solution, thereby protecting the chains repulsion of the acrylamide chains. Although, the prepared composites are not very stable in a complex brine solution, but showed a great promise for future EOR applications.

Chapter 4 *In-situ* synthesis and characterization of modified polymers and polymer nanocomposite under high ionic strength brine

4.1. Introduction

In Chapter 3, mechanical mixing was used to produce HPAM/NPs composites, which did not have good stability in complex brine solutions. In this chapter, a new approach has been explored to create the composite via *in-situ* and modification methods of polymer-nanoparticles synthesis, and characterize it spectroscopically. The first section of the Chapter involved the *in-situ* production of GO/polymer nanocomposites via covalent functionalization of polymer with the partially reduced graphene oxide (rGO), followed by further modification of the composites using 1, 3-propane sultone, to accomplish a zwitterionic character on the composites surface to get material with excellent temperature stability and dispersibility in the presence of high ionic strength brines. The second section focusses on the *in-situ* synthesis of modified SiO_2/polymer composites using (3-aminopropyl) triethoxysilane (M_SiO_2) to create positively charged active groups that promote stronger interaction with polymer functional groups, leading to high dispersion stability in complex brine solutions.

4.2. Synthesis and characterizations of zwitterionic-polyacrylamide graphene oxide nanocomposites in HT-HS Brines

4.2.1. Overview

This section aimed to address the stability challenges of graphene oxide/polyacrylamide nanocomposites in harsh conditions, by proposing a novel stabilization approach via surface modification of the COPAM and rGO using 1, 3-propane sultone to accomplish a zwitterionic character on the material surface. It has been reported that zwitterion molecules possess

outstanding solubility and stability in the presence of brines because of their antipolyelectrolyte effect [302, 303]. Resulting in the chain expansion when electrolyte materials are added and later promote stabilization and de-agglomeration via electrostatic chemistry (steric effects) [304]. Zwitterion molecules have been applied as antifouling coatings in seawater [305] and suggested to used potentially in enhanced oil recovery [306]. Recently, the zwitterionic rGO/Poly(Vinylimidazole)-co-poly(aminostyrene) composite was reported to be stable at high temperatures under the influence of high ionic strength brines for 90 days [303].

Therefore, a successful GO-COPAM composite is synthesized by covalently attaching the copolymer of acrylamide (AA, 99%) and 2-acrylamido-(3-acrylamidopropyl) trimethylammonium chloride (ATAC) monomers onto the partially reduced graphene oxide (rGO) sheets. The resulting rGO-COPAM composites were further exposed to post-functionalization chemistry using 1, 3-propane sultone to create zwitterion groups (species with functional groups, of which at least one has a positive and one has a negative electrical charge). This approach has an advantage including chemical reactivity between the polymer and large surface area of the GO basal plane [307, 308], which further promotes the functionalization and ability of the adsorbed nanomaterials to be used in the area of interest [309-312]. The synthesized zwitterionic-rGO-COPAM composites were dispersed in APIB and FB, their long-term temperature stability was monitored both spectroscopically and visually upon standing for 120 days at 80 °C. The dispersed zwitterionic-rGO-COPAM solution demonstrated excellent dispersion ability in both APIB and FB.

4.2.2. Materials

Graphite powder ≈20 μm in size, acrylamide (AA, 99%) and 2-acrylamido-(3-acrylamidopropyl) trimethylammonium chloride (ATAC) monomers, 4-4'-azo-bis-4-cyanopentanoic acid (ACPA), hydrogen peroxide (H_2O_2, 36%), potassium permanganate

($KMnO_4$, 99%), 1,3-propane sultone, sodium nitrite, ascorbic acid, and all salt component were ordered from Sigma Aldrich, sulphuric acid (H_2SO_4, 95%) and Nitric acid (HNO_3, 69%) were obtained from VWR chemicals. No further purification was done on the chemicals before use.

4.2.3. Synthesis of the copolymer of acrylamide

GO was synthesized via modified Hummers methods as described in **Section 3.3.2.** The copolymer of AA and ATAC (COPAM) were synthesised via free-radical polymerisation [167, 221]. The polymerization was carried in a three-neck bottom reactor, equipped with a reflux condenser, nitrogen inlet gas, and mechanical stirrer as shown in **Fig. 4.1**. Initially, the reactor was charged with a dissolved mixture of AA and ATAC monomers in 80 mL degassed and distilled water. An oil bath was prepared, and the reactor was placed inside. The solution was sprinkled under an inert atmosphere for 30 min while stirring. 10 mg of water-soluble ACPA initiator was added to the reactor to trigger the reaction. The mixture undergoes 6 h heating at 80 °C while string and then cool down at room temperature to afford the clear and viscous product. The solution was precipitated into acetone and allow to dry overnight under *vacuo* at 60 °C.

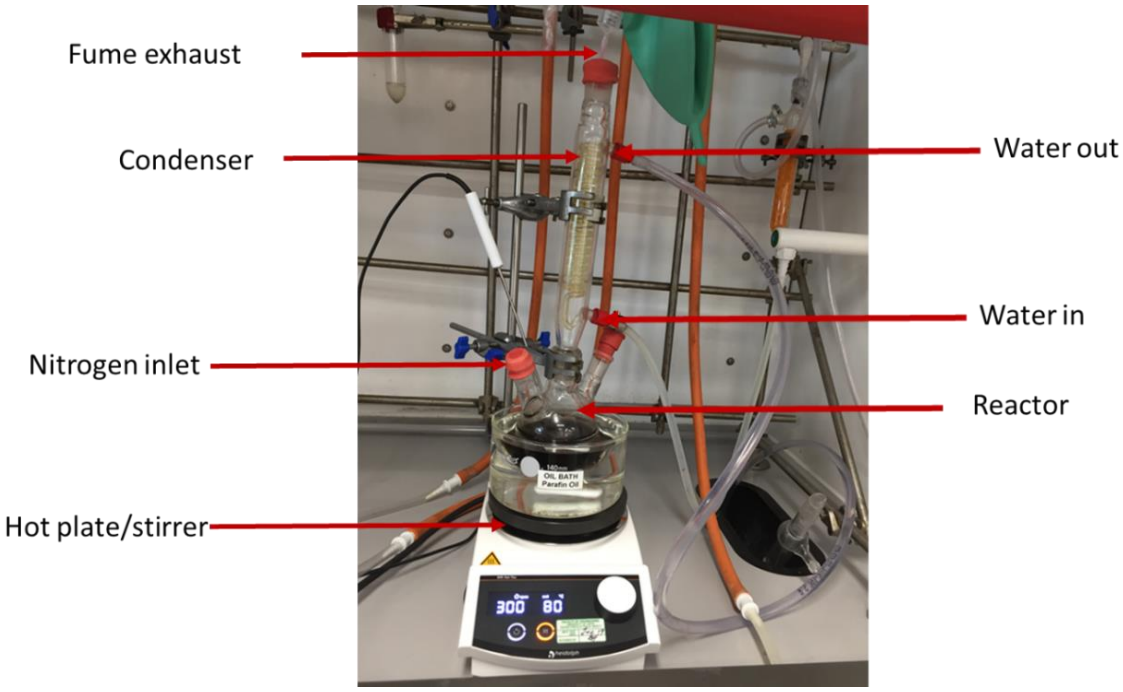

Figure 4.1. Experimental set up for polymerisation process.

4.2.4. Synthesis (preparation) of graphene oxide polymer composites

Graphene oxide was dispersed in distilled water to obtain 1 mg/mL with up to 30 mL total solution. In order to obtain partially reduced GO (rGO), 15.1 mg of L-Ascorbic acid was included in the solution followed by 1 h gentle stirring at 60 °C, the solution was cool down and used immediately in the next stage. In a separate container, 3 mg/mL of COPAM was dissolved in 50 mL water while stirring for 5 min under sonication and allowed to cool down. The cooled rGO dispersion was then slowly added to the COPAM solution followed by 30 min stirring. The mixture of rGO-COPAM was sonicated for 30 min followed by overnight stirring at 60 °C and later reduced *in vacuo* (concentrated). Subsequently, the solution was centrifuged for 15 min at 5000 rpm to induce flocculation after acetone was added. The product was freeze-dried to obtain a solid rGO-COPAM composite.

4.2.5. Synthesis of zwitterionic polymer composites

The zwitterionic-rGO-COPAM composites were prepared by modification using 1, 3 propane sultone following the procedure published in the previous literature [303]. The amount of 1, 3 propane sultone was experimentally decided after conducting many experiments to determine the effect of different 1, 3 propane sultone concentrations in COPAM solubility and viscosity. Different concentration of 1, 3 propane sultone (0.05 wt.%, 0.15 wt.%, 0.25 wt.%, 0.35 wt.%, 0.45 wt.%, and 0.55 wt. % was dispersed into the COPAM solution followed by gentle stirring at room temperature and observed their changes in solubility overnight, also, their viscosity was subsequently measured. However, both the solubility and viscosity remain the same in all the concentrations as shown in **Fig 4.2**. Therefore, the amount of 1, 3 propane sultone was selected based on the previously published procedure [303]. The rGO-COPAM was dispersed in 100 mL water under sonication at room temperature, followed by the addition of 350.2 mg of 1, 3-propane sultone [303]. The above combination was then transferred into a three-neck bottom flask and refluxed overnight under an inert atmosphere (nitrogen gas with low reactivity). The mixture undergoes 15 min centrifugation at the speed of 2500 rpm and then the supernatant was decanted. The resulting solution was then cleaned with methanol and distilled water (1:9). The obtained zwitterionic-rGO-COPAM composite was sealed and stored in a clean container after removing the methanol *in vacuo*.

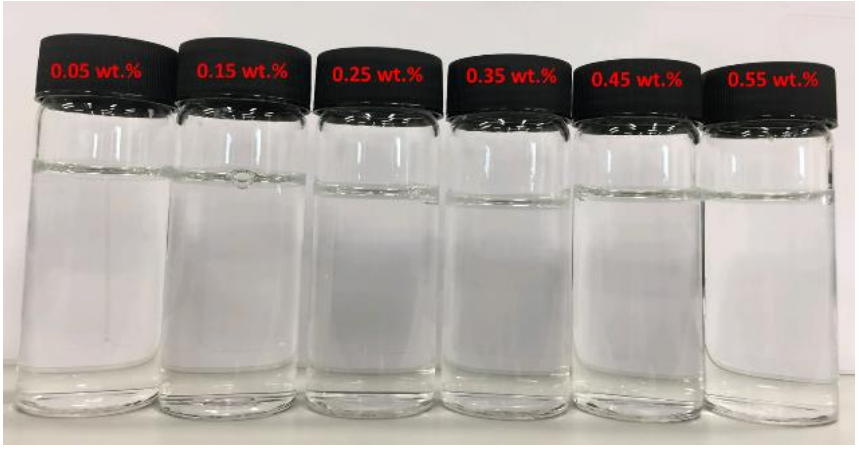

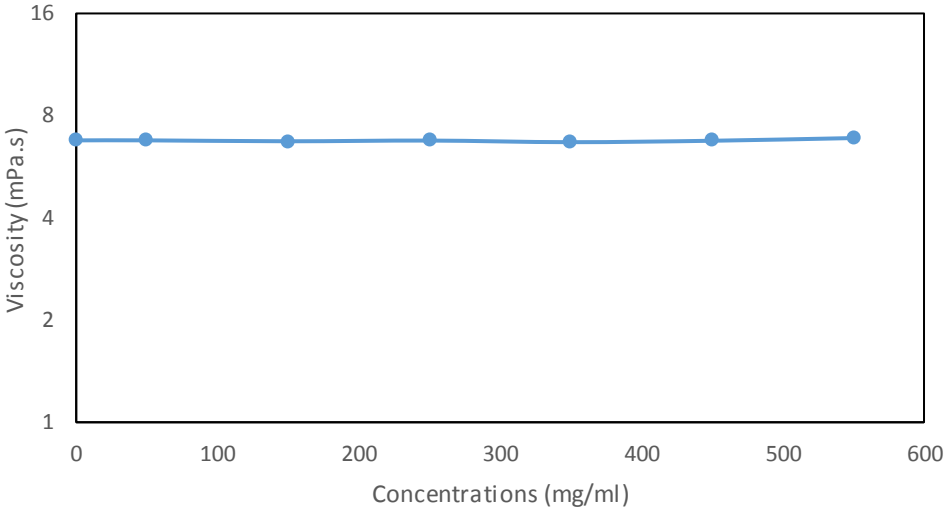

Figure 4.2. (a) Pure COPAM solutions with different concentrations of 1, 3 Propane sultone, (b) Viscosity of pure COPAM with different concentrations of 1, 3 Propane sultone.

4.2.6. Preparation of brine solutions

American Petroleum Institute brine (APIB) was obtained by dissolving 5.0 g calcium chloride dihydrate and 20.0 g of sodium chloride in 225 mL distilled water. Formation brine (FB) was achieved by dissolving 24.9 g calcium chloride dehydrate, 37.3 g Sodium chloride, 0.26 g sodium bicarbonate, 0.3 g sodium sulfate, 6.6 g magnesium chloride hexahydrate and 5 mg barium chloride, in 500 mL distilled water. The percentage of individual salts are shown in **Table 4.1**.

Table 4.1. Variation in the salt's components of brine's mixtures

Salt components	FB (%)	APIB (%)
$MgCl_2.6H_2O$	1.3	
NaCl	7.5	8
$Na_2.SO_4$	0.006	
$NaHCO_4$	0.005	
$BaCl_2$	0.001	
$CaCl_2.2H_2O$	5.0	2

4.2.7. Stability of zwitterionic-rGO-COPAM in brine's solutions

Firstly, 90 mL of the respective brine solutions were added into each of the two separate capped containers labeled APIB and FB containing 10 mL of the zwitterionic-rGO-COPAM composite to obtained 9:1 ratio. After 5 min sonication of the solutions, it was then stored at 80 °C uninterrupted in an oven. A portion of each sample was taken for characterization before the storage and after 24 h (1 day), then subsequently after the intervals of 10, 30, 60, 90, and 120 days, respectively. Photos of the extracted solutions were taken on those days for comparison as shown in **Fig. 4.9.**

4.2.8. Characterization

The proton NMR of the polymer was evaluated on a JEOL-600 NMR spectrometer. Deuterium oxide (D_2O) solvent was used for field-frequency lock, and the observed proton chemical shifts are reported in parts per million (ppm). The Agilent Technologies Infinity gel permeation chromatography (1260 MDS, GPC) was applied for determining the molecular weight of the polymer. 0.1 M $NaNO_3$ was used as a mobile phase for the molecular weight and polydispersity analysis. The samples were filtered by 0.22 μm pore size GVWP hydrophilic membrane before injection. The functionality of the samples was measured by attenuated total reflection (ATR)-

Fourier transform infrared (FTIR, Nicolet iS10). The data were recorded within the frequency range of 4000-400 cm^{-1} at a spectral resolution of 4 cm^{-1}. The percentage of chemical composition was determined on elemental (CHNS-O) analyser (CHNS-O Analyser, Thermo Scientific FLASH 2000). X-ray photoelectron spectroscopy (XPS) spectroscopy was also used to evaluate the elemental analysis for prepared composites. The thermal degradation analysis was performed using DSC-3/ TGA/ (Mettler Toledo) star^{e} system. It was operated under nitrogen gas at 50 mL/min flow rate and heating range between 35 to 900 °C with an interval of 10 °C/min. A scanning electron microscopy with high-performance cold-field emission (CFE-SEM, SU8230 Hitachi, Leeds Electron Microscopy and Spectroscopy Centre, UK) operated at 2 kV and transmission electron microscopy operated at 300 (TEM, FEI Titan Themis Cubed 300, Leeds Electron Microscopy and Spectroscopy Centre, UK) were used to observe the surface morphology. Energy-Dispersive X-ray spectroscopy (EDX, Oxford INCA 350) attached to the SEM was used to identify the elemental compositions and location of the element. The sedimentation behaviour of both GO-COPAM and zwitterionic-rGO-COPAM composites were evaluated after the initial preparation stage in APIB and FB using Turbiscan, a vertical scan analyser (MA 2000, Toulouse, France), using the procedure reported in the literature [256]. Percent transmittance (%T) spectra of the zwitterionic-rGO-COPAM solution in both APIB and FB samples was observed using Varian Cary 6000i UV-vis spectroscopy in quartz cuvettes. The zeta potential together with the particle size distribution was measured by dynamic light scatting (DLS) technique using a Malvern Nanosizer. The dispersion stability of the zwitterionic-rGO-COPAM composite was observed to investigate the sedimentation and flocculation behaviour by measuring the transmission of near-infrared (NIR) light under the influence of centrifugal force using (LUMiSizer, Lum GmbH, Germany), a dispersion analyser centrifuge. The measurement was conducted by pipetting 400 µl of the sample into a polycarbonate tube cell. The tube was then inserted into equipment to measure the

sedimentation profiles along the sample length during the centrifugation. The software attached to the system recorded the real-time transmission profiles at certain intervals.

4.2.9. Results and Discussion

4.2.9.1. Characterizations

The polydispersity index (PDI), the weight and number average molecular weight (M_w and M_n) of the polymer observed using GPC are shown in **Table 4.2**. The ^{1}H-NMR spectra of the COPAM were recorded after the sample was dissolved in D_2O as shown in **Fig. 4.4**. The peak at 1.4 ppm and around 3.1-3.7 ppm showed the presence of the methyl and ethylene protons in the polymer units. The peaks between 2.0-2.4 ppm indicate the existence of methane ($–CH_3$) in the polymer backbone. $R–CO–NH_2$ and C–H absorption peaks were observed at 7.6 and 6.9 ppm, revealing the formation of major polyacrylamide functional groups in the polymer spectrum [286]. The XPS **(Fig. 4.5)** and CHNS-O **(Table 4.3)** analysis of the dried samples confirmed that C, N, O are presence in both GO-COPAM and zwitterionic-rGO-COPAM composites, with the addition of sulfur in zwitterionic-rGO-COPAM sample, which confirmed the successful functionalization of the material using 1, 3-propane sultone.

Table 4.2. Properties and elemental compositions of the polymer.

Properties	M_w (g/mol)	M_n (g/mol)	PDI	Elemental compositions (%)				
				C	N	H	O	S
COPAM	343140	297457	2.14	47.96	15.63	8.66	26.73	0
zwitterionic-rGO-COPAM	/	/	/	37.36	10.77	5.88	44.56	1.43

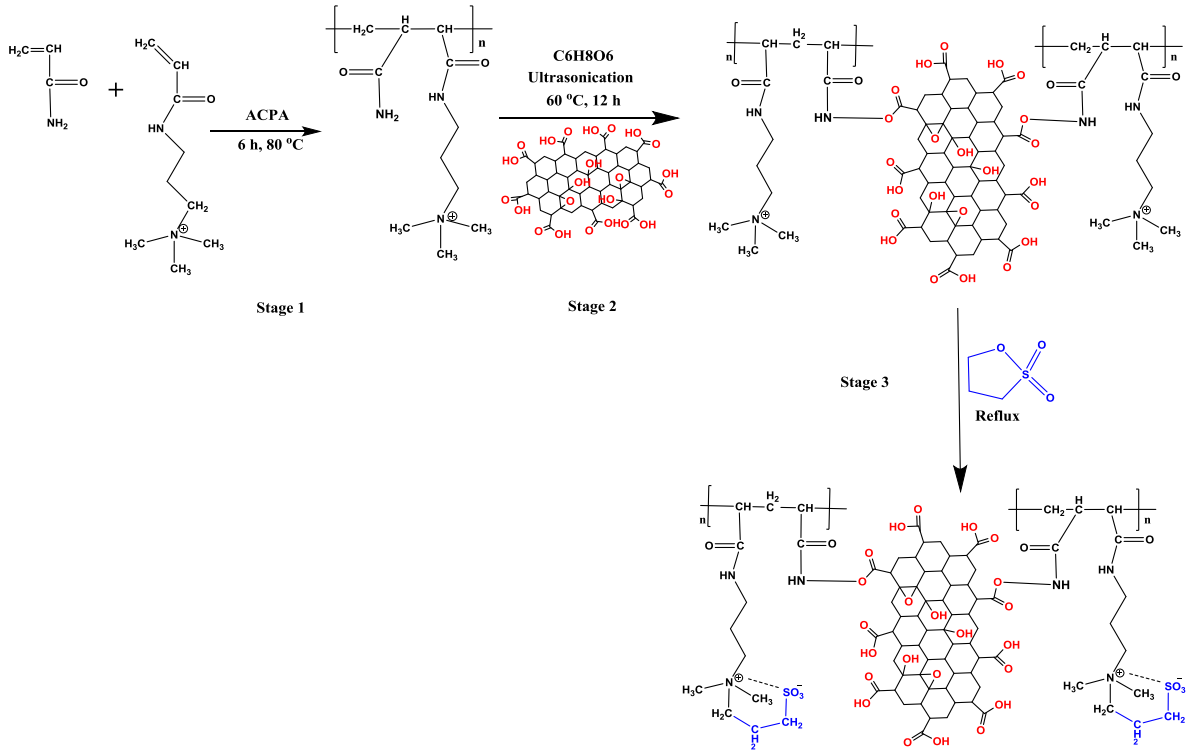

Figure 4.3. Schematic of synthesis methods of COPAM, GO-COPAM, and zwitterionic-rGO-COPAM composites. Stage 1 represents the COPAM synthesis stage, stage 2 showed the reduction of GO to rGO followed by the inclusion in the polymer solution, stage 3 showed how 1,3-propane sultone was added to create a zwitterionic character on the composite surface.

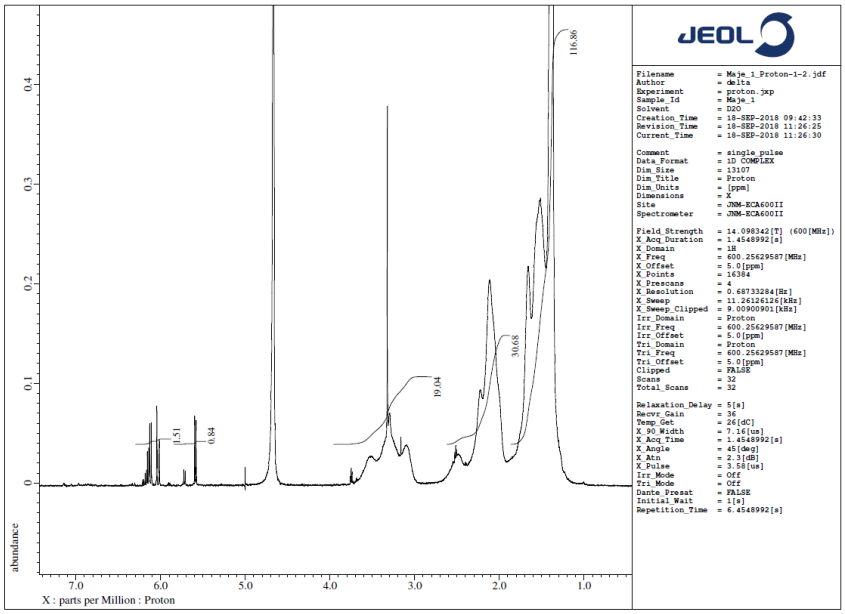

Figure 4.4. The NMR analysis of copolymer of acrylamide synthesized via free radical polymerisation.

(a)

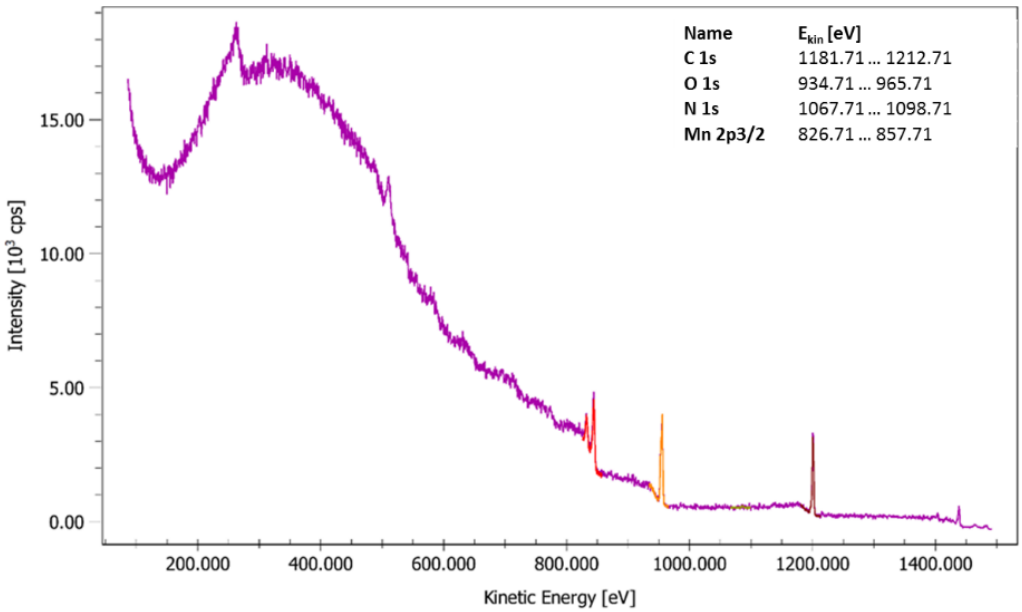

(b)

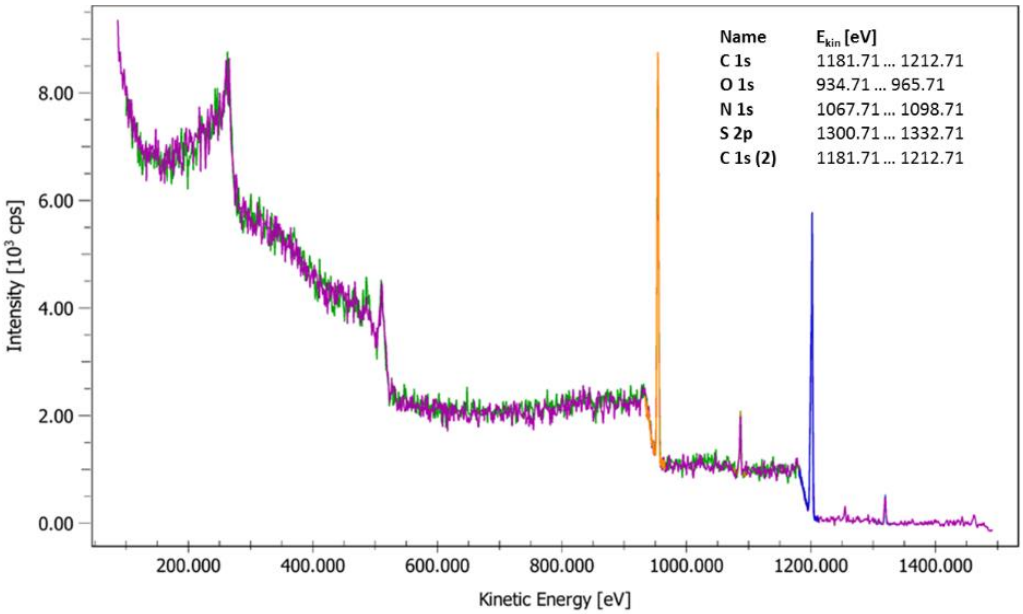

Figure 4.5. XPS spectrum of (a) GO-COPAM showing the presence of nitrogen, oxygen, and carbon and (b) zwitterionic-rGO-COPAM composites illustrating the presence of sulfur, nitrogen, oxygen, and carbon. The presence of the Mn peak in the GO-COPAM spectrum is presumed to emerge.

Fig. 4.6 depicted the ATR-FTIR spectra of GO, COPAM, and zwitterionic-rGO-COPAM composites. The spectrum of GO sheets displayed the bands at 1069.7, 1395.5, and 3420 cm^{-1} representing C-O stretching, O-H bending, and O-H asymmetric/symmetric vibrations of the GO epoxide group [271, 272]. In the COPAM spectrum, it was observed that the vibrations peak at 967 cm^{-1} is representing the quaternary ethoxylated group of ammonium molecules in ATAC cationic monomer [289, 290]. The peaks at 1649 cm^{-1} and 1117 cm^{-1} denoted the adsorption bands of C-O-C bonds and C-H stretching vibrations, the 3321 and 1700 cm^{-1} peaks corresponds to the carbonyl (C=O) functionalities while the amide vibrational bands emerged around 2923 and 1548 cm^{-1} respectively [270]. Contrarily, the spectrum of zwitterionic-rGO-COPAM samples showed the combination of peaks found in GO and COPAM samples. Although in the GO spectrum, the peak at 1069.7 cm^{-1} became weaker and peak at 1395.5 cm^{-1} shifted to the higher wavenumber, these might be due to the hydrolysable covalent cross-links formed between COPAM and GO [108, 273]. Similarly, the peaks observed at 2923 and 3321 cm^{-1} in the COPAM spectra were also seen in the composites while shifted slightly to lower wavelength (2859 and 3302 cm^{-1}), elucidating the formation of hydrogen bonds. The additional absorption peak at 1040 cm^{-1} on the composites materials corresponds to the SO_3 group from 1,3-propane sultone leading to the formation of the anionic character of the zwitterionic-rGO-COPAM structure that promotes the dispersion stability in the presence of high ionic strength brines [287, 288, 303]. TGA analysis was carried out between 25 to 900 °C heating, the TGA curves of COPAM, GO-COPAM, and zwitterionic-rGO-COPAM samples are shown in **Fig. 4.7**. The TGA analysis demonstrated that between 50 °C to 150 °C all three samples displayed a negligible weight loss, as a result of the surface desorption of water molecules. It can also be observed that, compared to COPAM and GO-COPAM samples, the zwitterionic-rGO-COPAM composites show smaller weight loss overall, indicating a highly stable material at the harsh conditions which are due to the presence of SO_3 group of the zwitterion character. However,

the weight lost on COPAM is roughly divided into three stages, at around 400 °C, almost 20% of the sample weight was lost, at around 700 °C almost 12% loss was observed, and more than 3% weight loss was observed after heating up to 900 °C, corresponding to the minor disintegration of the surface components on the polymer. Contrarily, the neat polymer showed significant loss of weight (~45%) until 350 °C, probably because of the polymer decompositions at elevated temperature, more weight loss followed on the same material to around 80% from 450 °C and above which is because of ammonia evolution and chain scission of the polymer at high temperature [313-315]. Overall, the zwitterionic-rGO-COPAM composites have high temperature durability because of the covalent functionalization that occurred between the COPAM and rGO.

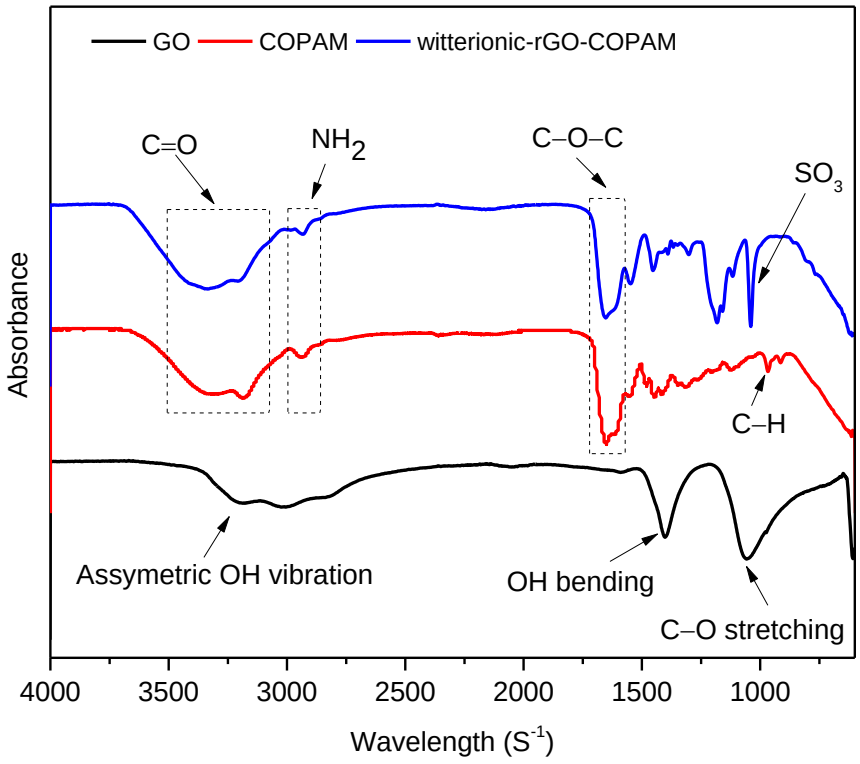

Figure 4.6. FTIR spectra of GO, COPAM, and zwitterionic-rGO-COPAM nanocomposites.

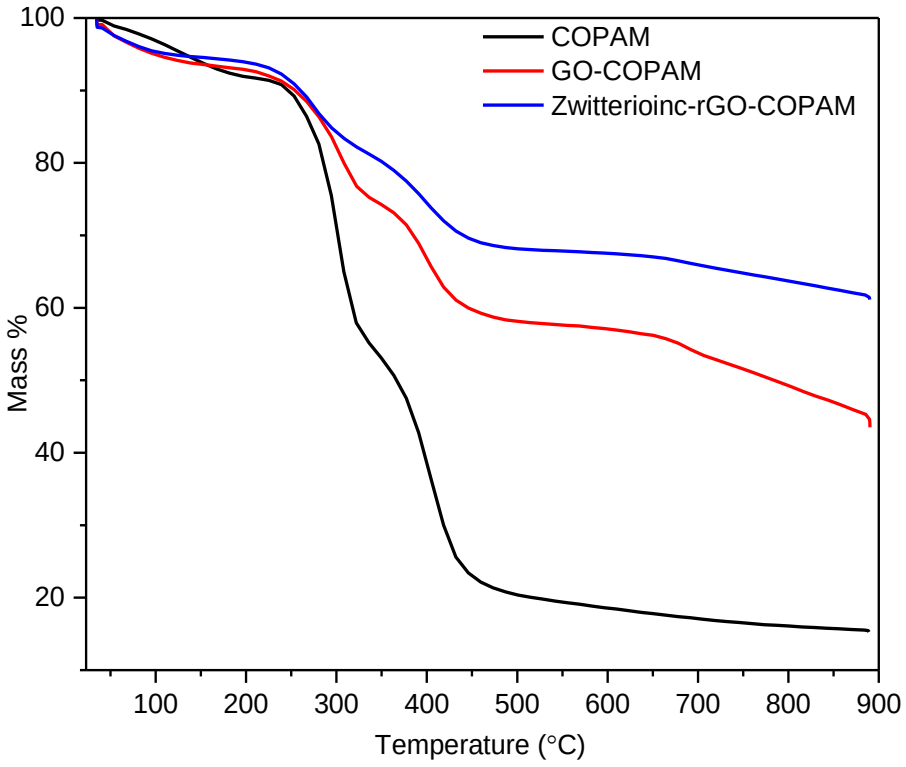

Figure 4.7. TGA profiles of COPAM and zwitterionic-rGO-COPAM nanocomposites.

The TEM and SEM images of the GO nanosheets are shown in **Fig. 4.8a and b**, the TEM images show exemplary crumble and wrinkles-like nature of GO. The SEM image described the smooth surface of GO, confirming that the sheets in the GO are linked to one another. **Fig. 4.8c and d** showed stable dispersion of the freeze-dried zwitterionic-rGO-COPAM composites via SEM analysis, the microstructure of the materials composites material indicated that the polymer has been grafted to the GO sheets, supporting the appearance of chemical bonds in the composites. More so, the superimposition of GO with the COPAM proof that the zwitterionic-rGO-COPAM interaction is not only physical contact rather a strong chemical adhesion [303, 316]. The SEM-EDX reaffirms the existence of C, N, O, and S in the composites material as illustrated in **Fig. 4.8e**. The presence of C, O, N, and S is also confirmed by elemental analysis and the percentage of each element is shown in **Table 4.2**. Interestingly, the appearance of S in the EDS mapping and elemental analysis of the zwitterionic-rGO-COPAM proposed that

some functionalization of the sample has successfully occurred together with the polymer chain alkylation which results after reacting with 1,3-propane sultone. The concentration of zwitterionic-rGO-COPAM in aqueous dispersion was obtained when the known volume of the sample was dried *in a vacuo*.

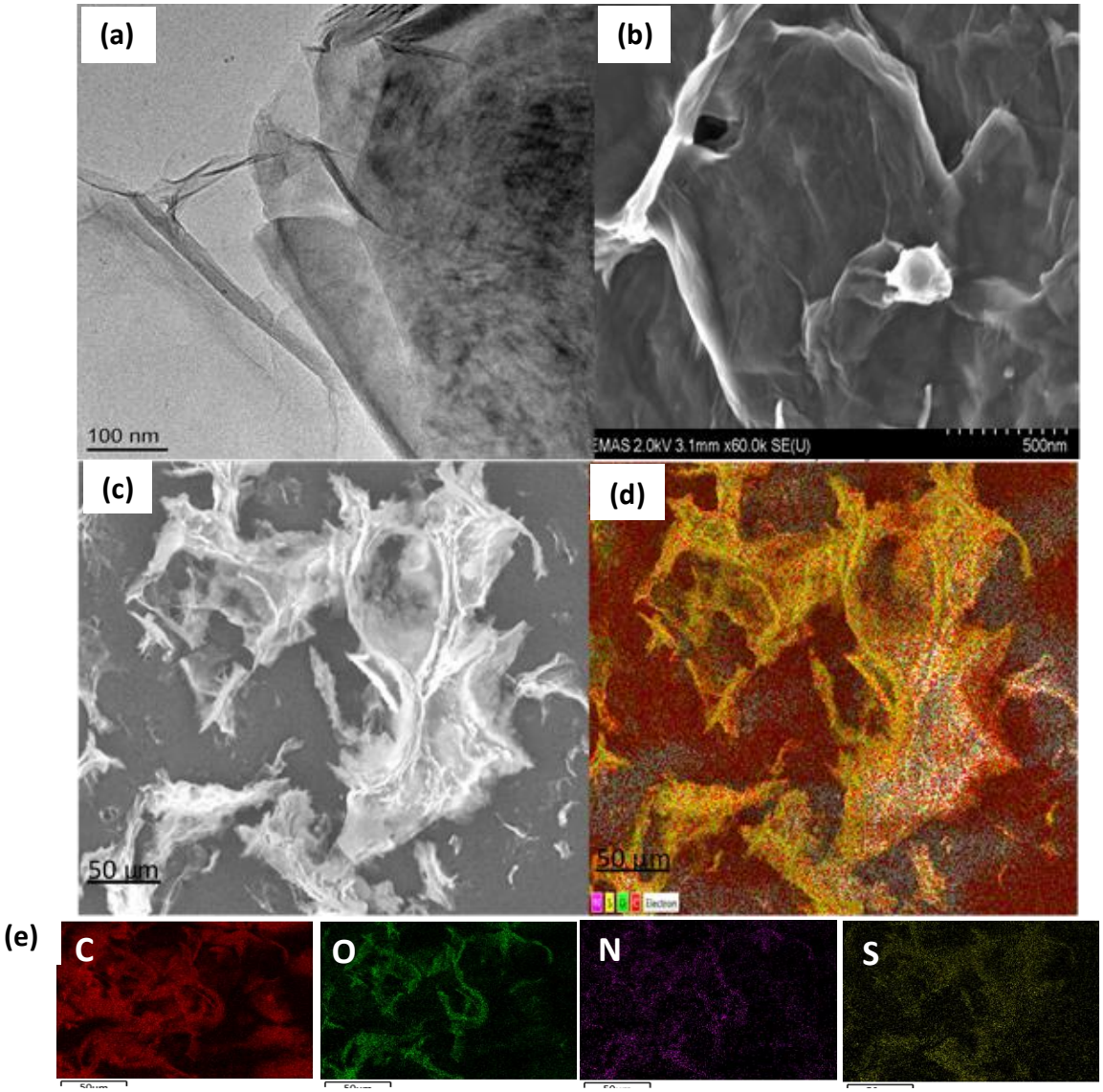

Figure 4.8. (a) TEM and (b) SEM images of graphene oxide nanosheets synthesized via modified Hummer's methods, (c) SEM image of zwitterionic-rGO-COPAM nanocomposites, (d) SEM mapping of zwitterionic-rGO-polyacrylamide sample, where the elements are represented by different colours (pink; Nitrogen, yellow; Sulfur, green; Oxygen and red; carbon), and (e) elemental analysis of zwitterionic-rGO-COPAM extracted from SEM mapping.

Firstly, in the preliminary evaluation, I pursue to select polyacrylamide and graphene oxide nanosheets as a nanocomposite of interest to produce a modified composite that stabilizes under high ionic strength to build on the stabilization issue has been encountered on HPAM/GO composites preparation via direct mixing as shown in **Fig 3.9**. To establish the guideline for stability and dispersion, two testing brine were selected: (1) APIB and (2) FB: which is normally discovered predominantly in deep oil reservoirs. The composition and relative weight percentage of salts are shown in **Table 4.1**. In comparison to APIB, the FB possess a much complex variety of salt and an unquestionably greater number of divalent ions. A preliminary study was initiated on the synthesized composite (GO-COPAM), these studies reveal that the composites were unstable in both mixtures of APIB and FB after sample preparation stage and one day aging at 80 °C as illustrated in **Fig. 4.9**. This happened because of the electrostatic cross-linking between GO sheets causes by divalent ion and consequently led to the destabilization of the solution.

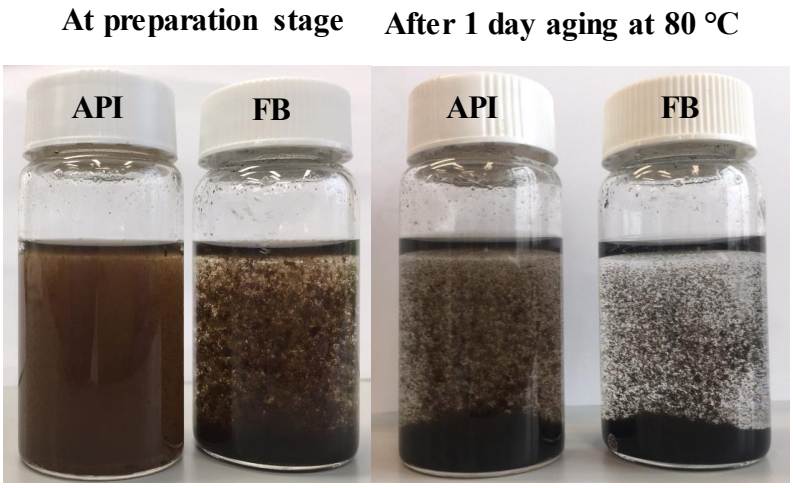

Figure 4.9. GO-COPAM dispersion in APIB and FB showing unstable mixture after the preparation stage and one day aging at 80 °C.

As disused in the introduction section, zwitterionic species and poly-zwitterions provide good dispersibility in harsh conditions such as high ionic strength brines because they exhibit the antipolyelectrolyte effect [302]. Therefore, a copolymer containing sulfobetaine zwitterionic groups was developed in this project. In the first instance, a copolymer of acrylamide and 2-acrylamido-(3-acrylamidopropyl) trimethylammonium chloride was prepared via free radical polymerization at 80 °C for 6 h using ACPA as initiator as shown in **Fig. 4.3** (**stage 1**). The interaction between COPAM and GO sheets occurred through hydrogen bonding and covalent functionalization of amino groups in the polymer chain producing a covalent attachment with graphene basal plane as depicted by FTIR analysis as shown in **Fig. 4.6.**

In the first place, the GO was partially reduced through the interaction of L-ascorbic acid to enhance the GO graphitic domains that improve the stability and enable interaction with the polymer chains. The cooled solution of partially reduced GO (rGO) was later added to the COPAM solution as illustrated in **Fig. 4.3 (stage 2).** The obtained rGO-COPAM was separated by precipitation, cleaned, as well as further consequent reaction with 1,3-propane sultone which leads to the formation of zwitterionic character on the rGO-COPAM composites (zwitterionic-rGO-COPAM) as seen from **Fig. 4.3 (stage 3).** It would be expected for the purely zwitterionic polymer to be charge-free, but this new zwitterionic-rGO-COPAM probably has anionic groups arising from the sheets of rGO enabling materials stabilization. In our finding the zeta potential **(Fig. 4.14b)** showed that the surface charge of the prepared material is anionic (negative charge), which is due to the ionization of phenolic and carboxylic acid groups in the solution [317-319]. Confirming that the formation of a stable GO-COPAM solution should be promoted not just by the hydrophilicity of the GO but the electrostatic repulsion.

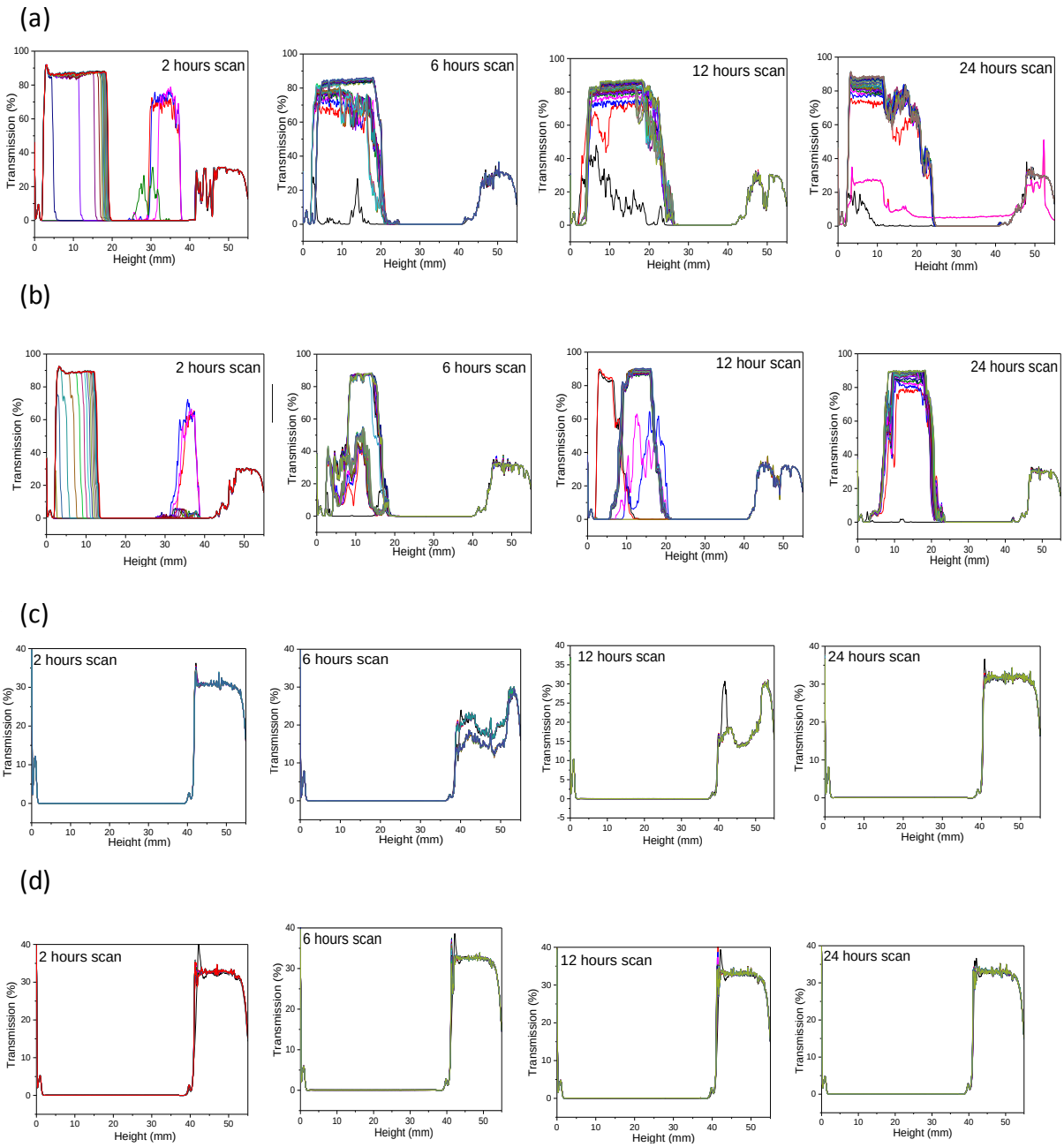

Figure 4.10. Initial stability test observed using Turbiscan analyser to understanding the extent of sedimentation of the GO-COPAM in (a) APIB and (b) FB and zwitterionic-rGO-COPAM in (c) APIB and (d) FB after preparation, with scan every 5 minutes for the duration.

American Petroleum Institute-Brine

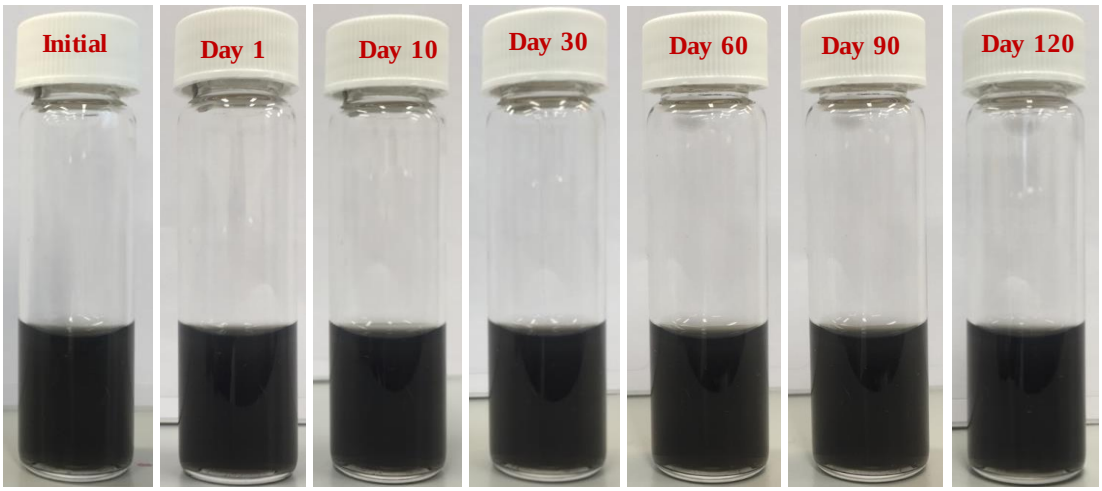

Formation brine

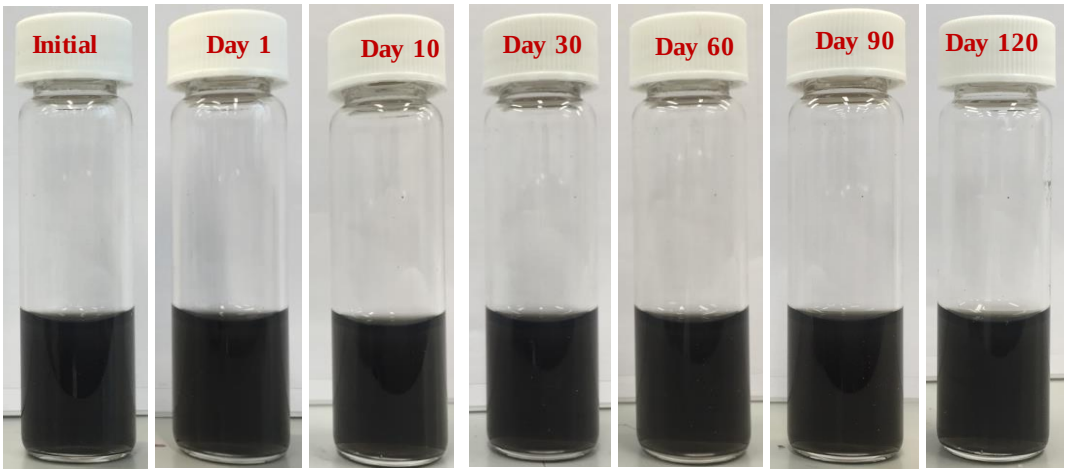

Figure 4.11. Image of the portion of stable composite dispersions taken after storage at 80 °C for 0, 1, 10, 30, 60, 90 and 120 days in the presence of APIB (top) and FB (bottom).

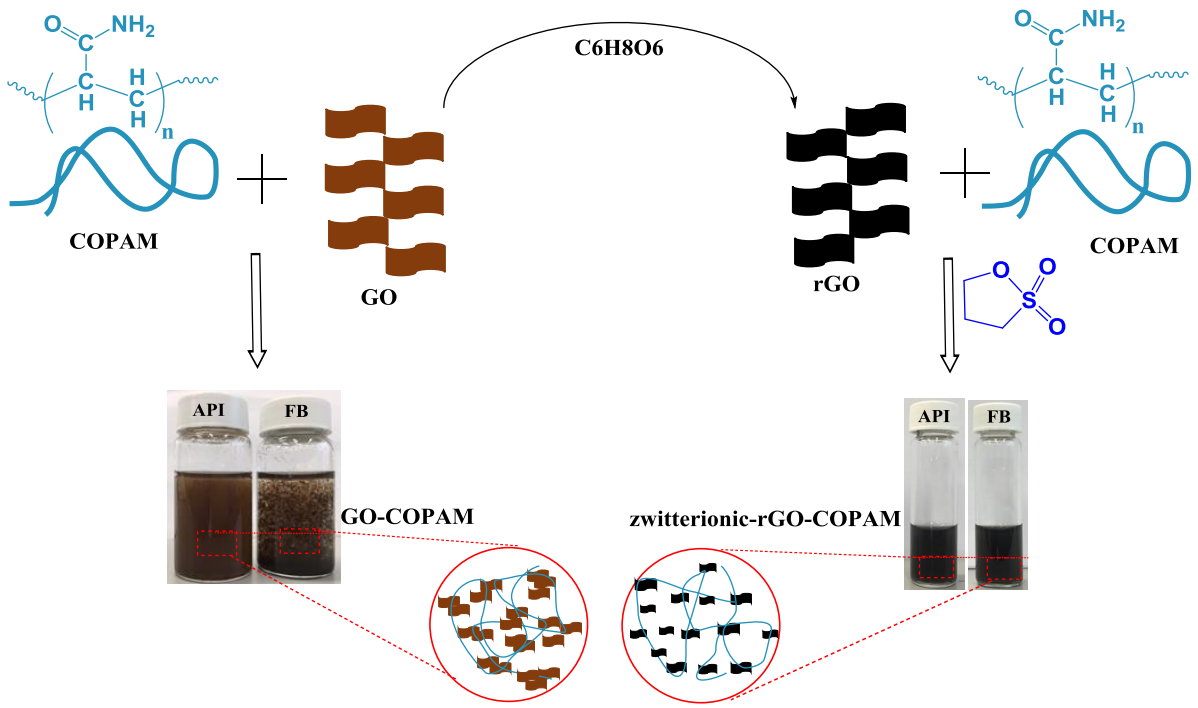

Figure 4.12. Schematic illustration showing the trends of stable and unstable composites solutions.

The long-term thermal stability and dispersibility of the aqueous zwitterionic-rGO-COPAM mixture in APIB and FB at 80 °C was investigated. 10 mL of the composites was added to 90 mL of each of the individual brine solution to obtain 100 mL mixture. 5 min sonication of the mixture was conducted to obtain a homogeneous dispersion which is aggregates free after visual inspection. Before aging the samples, both GO-COPAM and zwitterionic-rGO-COPAM composites undergoes initial stability testing using a Turbiscan analyser to monitor the sedimentation behaviour by the transmission or backscattering profile against the sample height with scan every five minutes for different time intervals (2h, 6h, 12h, and 24h) as shown in **Fig. 4.10**. The transmission/backscattering profiles use the light rays to capture the changes in the particle sedimentation within the measuring cell. At a certain interval of time, when sedimentation occurs, the changes in transmission or backscattering varies with the sample height. In this work, the GO-COPAM sample showed significant sedimentation in both APIB and FB after 24 hr scan as shown in **Fig 10a and b**, whereas, the zwitterionic-rGO-COPAM

composites displayed excellent stability in both APIB and FB throughout the scanning period as can be seen in figure **Fig 4.10c and d**.

To under the long-term stability of zwitterionic-rGO-COPAM composites, the solution was stored and left undisturbed at 80 °C for 120 days. A small portion of each of the prepared dispersion was taken for spectroscopic analysis at the initial preparation stage and after 1 day (24 h) followed by 10, 30, 60, 90, and 120 days for characterization. Photos of the aliquots are taken for visual stability test and no notable indication of settling, sedimentation, or instability of the zwitterionic-rGO-COPAM dispersion was observed in each of APIB or FB as shown in **Fig. 4.11**. However, for quantitative analysis, the dispersion stability was first examined by measuring the UV-vis spectroscopy of the samples. As can be seen in **Fig. 4.13** the results at preparation stage and after aging until 120 days at 80 °C showed a slight difference in the APIB solution, but changes were observed in FB dispersion especially at 120 days of storage, showing superimposable character were the peak of GO dispersion-shifted from >230, and the absorption in the whole spectral region increase with time, proving that the composite stability in the FB reduces at 120 days.

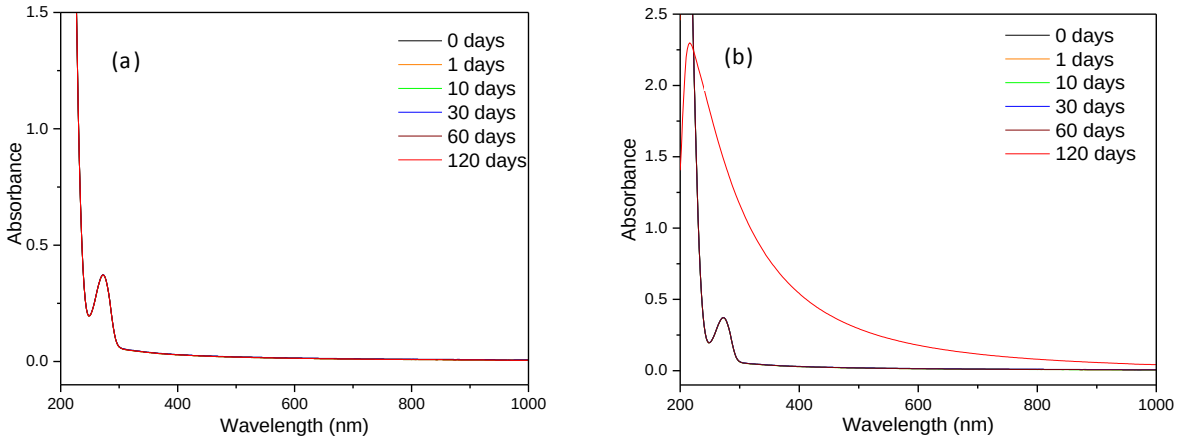

Figure 4.13. UV-vis spectra of zwitterionic-rGO-COPAM solution after 1, 10, 30, 60, 90 and 120 days aging at 80 °C in APIB (a) and FB (b).

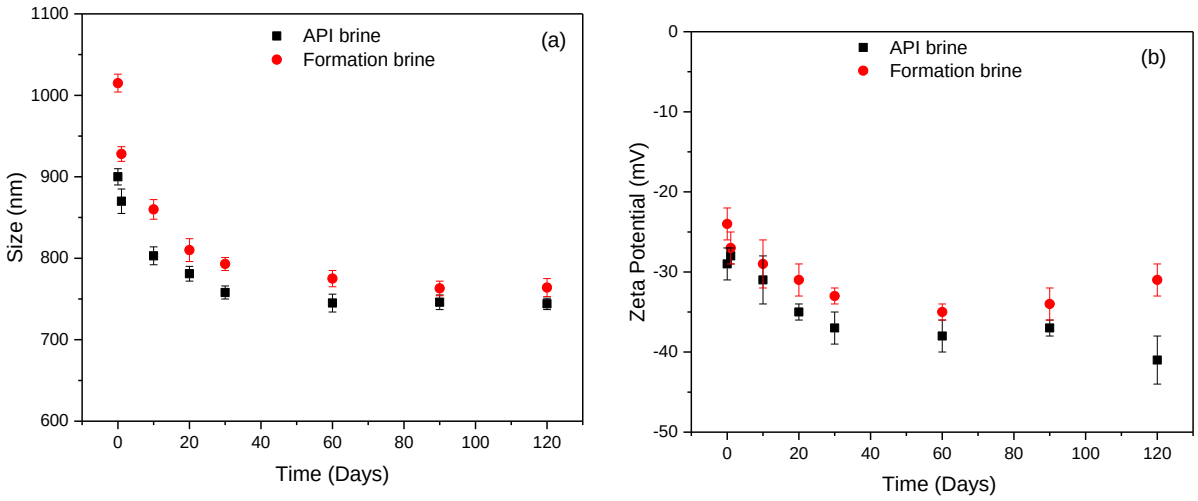

Figure 4.14. Hydrodynamic size (a) and zeta potential analysis (b) of the zwitterionic-rGO-COPAM solution after 0, 1, 10, 30, 60, 90, and 120 days aging at 80 °C in APIB and FB.

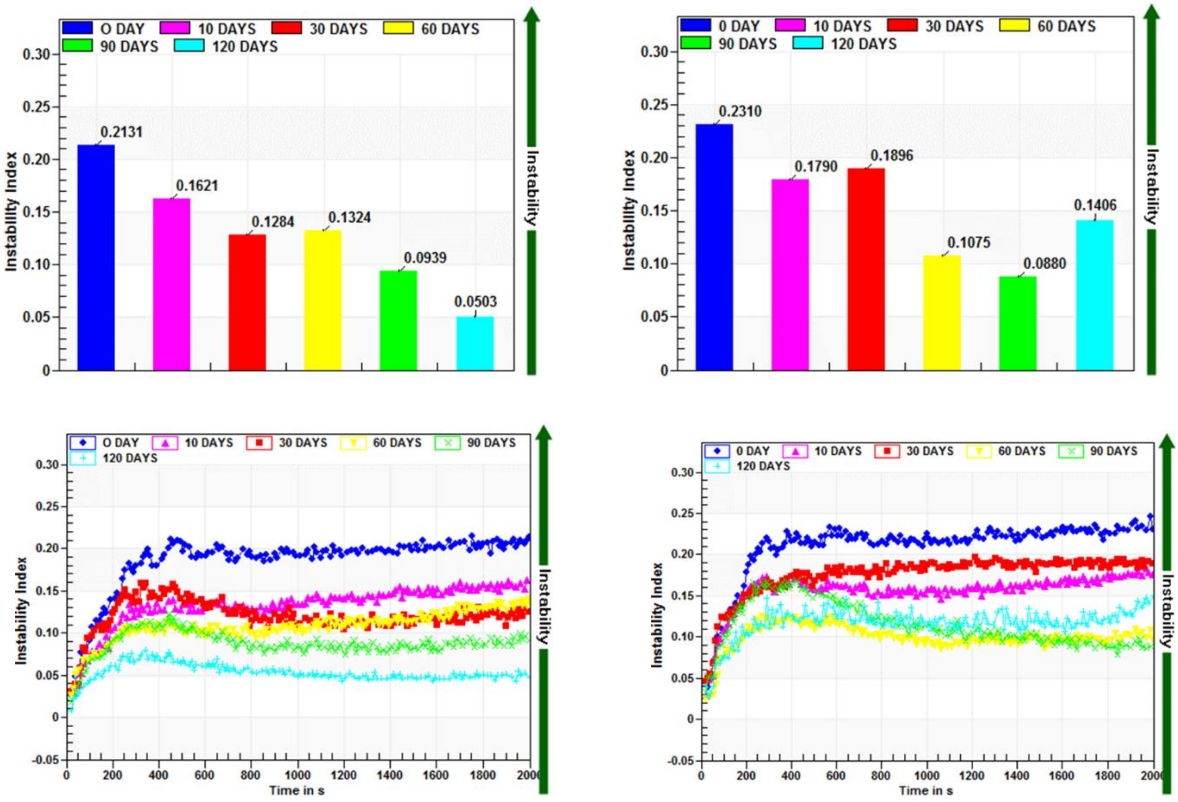

Figure 4.15. Trends of instability index versus time for zwitterionic-rGO-COPAM dispersion in the presence of APIB (left) and FB (right) after 0, 10, 30, 60, 90 and 120 days aging at 80 °C.

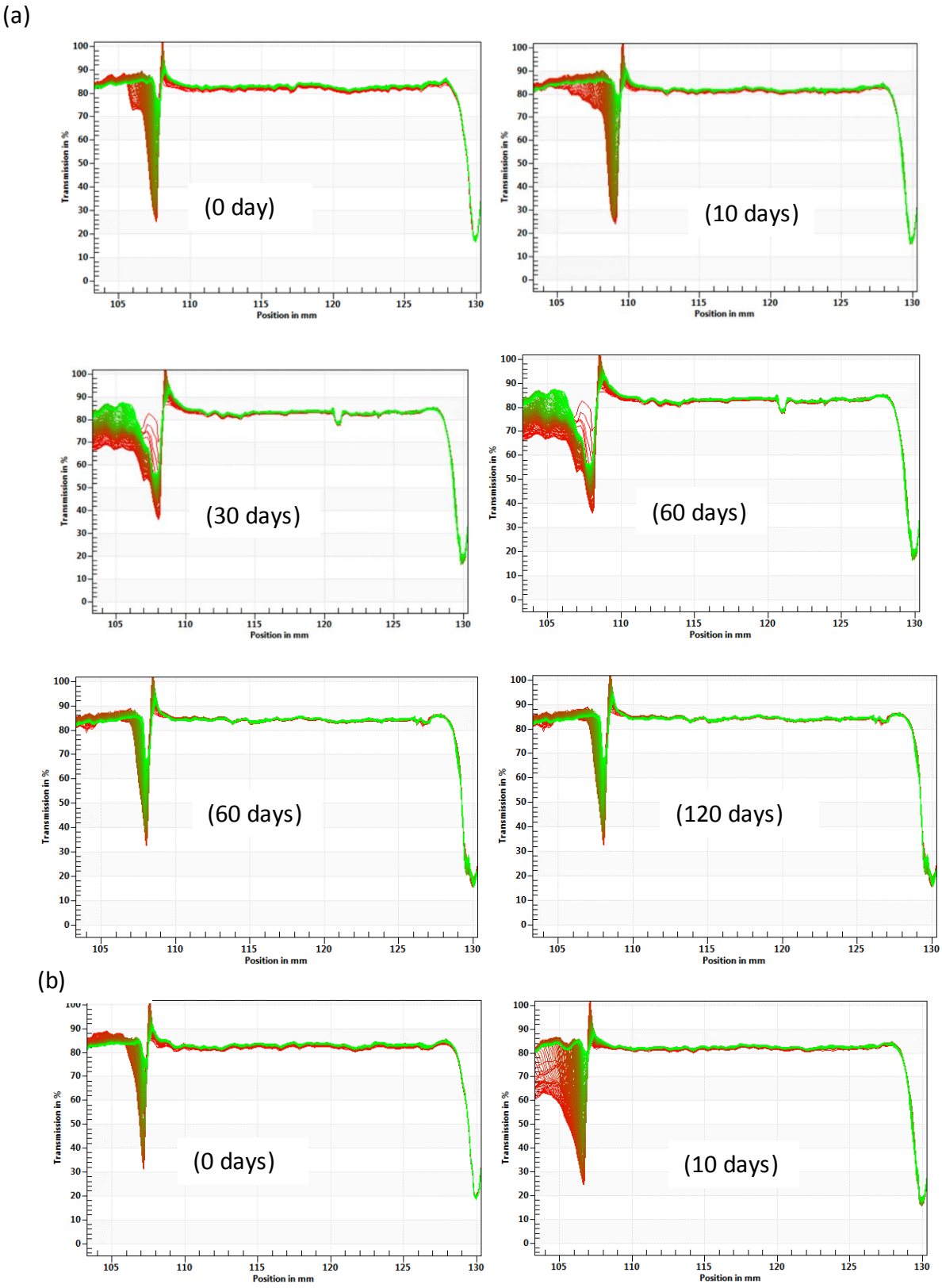

Figure 4.16. Styles of light transmission across the test tube for zwitterionic-rGO-COPAM dispersion in the presence of APIB (a) and FB (b) after 0, 10, 30, 60, 90 and 120 days aging at 80 °C.

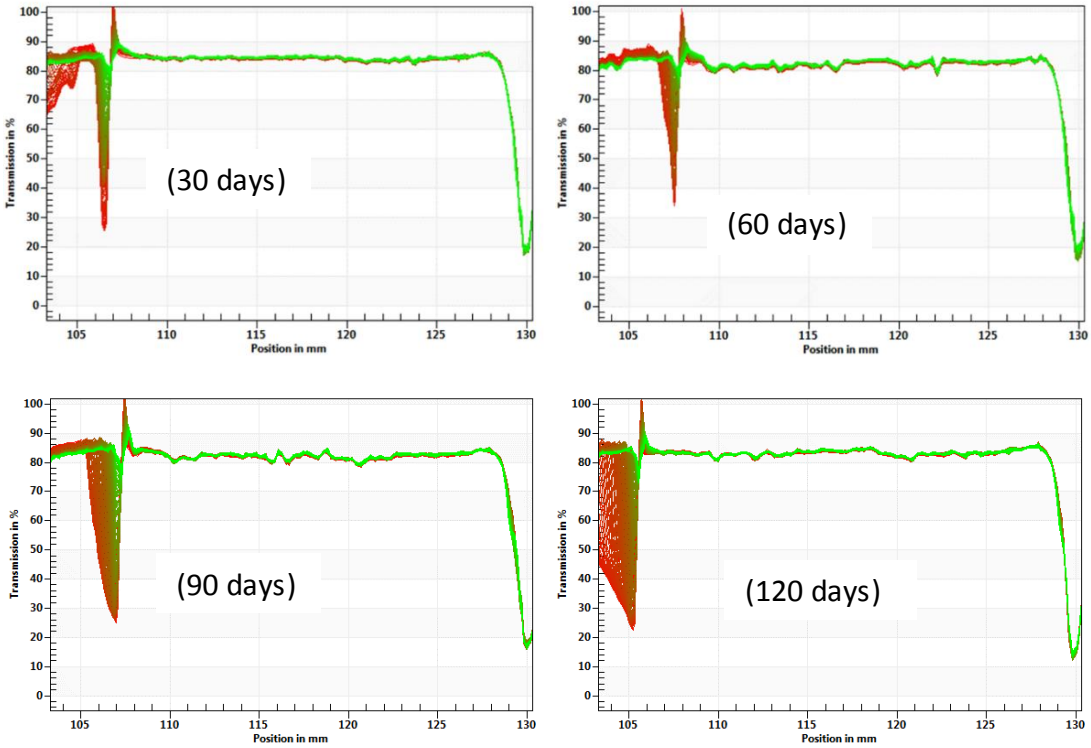

Figure 4.16. Continues.

The stability of the zwitterionic-rGO-COPAM composite at high temperature in the brines was further confirmed by the changes in hydrodynamic diameter (HD) or size and zeta potential using the DLS technique as shown in **Fig. 4.14**. The DLS results revealed that the average HD of the pure GO sheet in water was 701 ± 80 nm. At the initial preparation stage of the composite, the average HD was found to be 900 ± 10 nm and 1015 ± 11 nm in the API and FB brine solution, respectively. However, the diameters reduce to 870 and 928 after one day of aging displaying good stability with time, showing a diameter of approximately 750 nm over the storage period in both APIB and FB. Zeta potential analysis also showed the improvement in stability with zwitterionic-rGO-COPAM composite at both APIB and FB over the storage time, it was observed that the zeta potential value of the particles starts to improve after aging at 80 °C compared to that of the initial preparation, it became approximately -38 ± 3 mV in APIB and -32 ± 2 in FB. Although, in FB after 120 days aging the zeta potential decreases to around -24 ± 2 mV, which is inconsistent with the obtained UV-vis spectroscopy analysis. The

composite dispersion in brine was assumed to agree with the behaviour of pseudo-spherical nanoparticles where the rGO nanosheets wrapped by the chains of zwitterionic-COPAM. At high ionic strength brines, the presence of electrolyte ions can enhance the interactions of the ionic groups in the zwitterionic sulfobetaine polymers, creating the chain's expansion by providing adequate steric repulsion thereby preventing the flocculation/aggregation of the composite materials [302, 304].

The dispersion stability of zwitterionic-rGO-COPAM was also investigated using LUMiSizer-6110 to understand the sedimentation behaviour as described in the literature [320, 321]. As can be seen from **Fig. 15 and Fig. 4.16**, the stability of the dispersion becomes more obvious with aging in both APIB and FB, although after 120 days in FB, the instability index starts to increase which is also supporting the observation made in UV-vis and zeta potential analysis. This is probably because the GO nanosheets start to agglomerate after 120 days due to the presence of complex salt thereby creating a higher open particle bed structure which aggregated more by the applied centrifugal force. Overall, based on visual and spectroscopic analysis, the zwitterionic-rGO-COPAM displayed outstanding and promising stability in the presence of high ionic strength brines including $CaCl_2$ and $MgCl_2$, because there is no observable flocculation or precipitation and only negligible differences were observed over time in the monitored transmittance. Therefore, it could be revealed that the relative stability of the composite's dispersion may likely be prolonged above 120 days in APIB [303] because up to the storage period spent in this experiment there was a negligible formation in destabilisation of the formed materials, but no longer than 90 days in complex formation brine.

4.3. Synthesis and characterization of polyacrylamide-amino functionalized nanosilica composites at the harsh condition

4.3.1. Overview

Stability of SiO_2/polymer is challenging in high ionic strength of brine, due to NPs agglomeration which causes large numbers of silanol groups that shelter the SiO_2 surface to aggregates. The lack of good SiO_2 dispersion was also considered to be a result of their preferred face-to-face stacking in agglomerated/aggregated tactoids [233], which leads to severe agglomeration and sedimentation in a harsh environment [234]. In addition, when SiO_2 NPs and a polymer are mixed, it takes a long time to form a well-dispersed mixture, which greatly decreases the potential field application of NP-based systems [48]. It has been shown that the hydrophilic nature of SiO_2 NPs decreased the physical strength to interact with the polymer matrix that has a hydrophobic structure, making the dispersion more difficult [235, 236].

Aiming to address these two challenges facing SiO_2/HPAM dispersion, this section proposed a novel surface modification approach to produce a well-dispersed SiO_2 mixture, and use them for *in-situ* synthesis of COPAM to form a stable nanocomposite. SiO_2 NPs were modified by functionalizing the surface with (3-aminopropyl) triethoxysilane (M_SiO_2) to create positively charged active sites to produce monodispersed particles. In addition to conventional hydrogen bonds, positively charged surfaces allow strong coordination bonds with the COPAM's negative charged side chain, reinforcing its stability under HS conditions.

4.3.2. Materials

2-Acrylamido-2-methyl-1-propanesulfonic acid (APSA, 99%), acrylamide (AA, 99%), 4-4'-azo-bis-4-cyanopentanoic acid (ACPA) monomers and SiO_2 NPs (12 nm, ≥99.0% purity) were

obtained from Sigma-Aldrich. Polydimethylsiloxane, (3-aminopropyl) triethoxysilane (APTES, 99%), trimethylsiloxy terminated, high viscous silicon oil (M.Wt. 9000) were obtained from Alfa Aesar and triethylamine (TEA, 99%) was acquired from VWR International. The obtained reagents and chemicals were employed directly without any extra purification.

4.3.3. Synthesis methodologies

4.3.3.1. Synthesis of amino-functionalised nanosilica

Modified SiO_2 (M_SiO_2) was obtained by functionalising SiO_2 NPs with APTES. Firstly, 6.0 g of SiO_2 was put in a clean container followed by the addition of 100 ml ethanol and then stirred at ambient temperature for 2 h. Different APTES concentrations (see **Table 4.3**) was dissolved in 100 ml (90/10, v/v) of ethanol/water. Subsequently, the dispersion of SiO_2 and solution of APTES were introduced into a container, 2.5 ml TEA was added to the mixture and stirred for 4 h at 80 °C to achieve the modification. The resulting material was separated using a centrifuge and then rigorous washing was performed using ethanol. The dried product was obtained in a *vacuo* after 24 h at 80 °C and the M_SiO_2 suspension was obtained and sealed in a clean container. **Table 4.3** shows five different synthesised M_SiO_2 samples. Elemental compositions for all samples were measured using CHNS-O analyser while % of amino groups in all samples were quantified from TGA curves.

Table 4.3. Properties of SiO2 and M_SiO2 samples.

Sample code	NP (g)	APTES (g)	Elemental compositions (wt. %)			Amino group content (%)	Zeta potential (mV)
			N	C	H		
SiO_2	6.0	0	0.00	0.00	0.00	0	-20.2
$MSiO_2$-1	6.0	0.4	1.64	4.88	1.22	4.6	-24.7
$MSiO_2$-2	6.0	0.8	1.70	5.15	1.25	4.8	-32.4
$MSiO_2$-3	6.0	1.6	1.77	5.61	1.31	5.8	-34.8
$MSiO_2$-4	6.0	2.4	1.85	6.09	1.40	6.4	-37.3
$MSiO_2$-5	6.0	3.2	2.07	6.20	1.41	7.3	-44.7

3.3.3.2. Synthesis of polymer and NPs/polymer composites

The polymer and NPs/polymer composites were prepared *in-situ* through a free-radical polymerisation. The mixture of AA and APSA monomers, with the amount in gram as shown in **Table 4.4** was dissolved in 80 ml deionised water. The NPs dispersion was obtained by dispersing 0.6 g of either SiO_2 or M_SiO_2 NPs in 40 ml of deionised water and sonicated at ambient temperature for 30 min. The monomer solution along with NPs dispersion was poured into a three-neck bottom glass container and followed by 30 min stirring under an inert atmosphere using a magnetic stirrer at 200 RPM. ACPA was added (10 mg) as an initiator to trigger the free-radical polymerisation reaction and the reaction was then gently mixed, using a magnetic stirrer, for 6 h at 80 °C under reflux. The polymerisation reaction was performed under nitrogen gas. For the investigation, one NP-free PAM was synthesised similarly as a contrast sample as shown in **Table 4.4**.

Table 4.4. Properties of polymer and polymer nanocomposite.

Sample	Monomers (g)		NPs type/ amount (g)	$M_{wt,GPC}$ (g/mol)	Elemental compositions (wt. %)					Zeta potential (mV)
	AA	APSA			N	C	H	S	O	
NP-free COPAM	3.75	3.75	---	696575	11.91	41.82	6.31	5.93	34.03	-28.7
SiO_2/COPAM	3.75	3.75	SiO_2/0.6	---	12.07	40.98	7.11	7.22	32.62	-29.9
M_SiO_2/COPAM	3.75	3.75	M_SiO_2/0.6	---	11.91	40.65	6.19	6.94	34.31	-49.6

4.3.4. Characterisation of nanoparticles and hybrid systems

Chemical composition was determined on elemental (CHNS-O) analyser (Thermo Scientific FLASH 2000 CHNS-O Analyser). The particle size distribution (PSD) and zeta potential were measured by Malvern Nanosizer based on the dynamic light scatting (DLS) method. The stability of M_SiO_2 over sedimentation and flocculation behaviour was performed using a dispersion analyser centrifuge (LUMiSizer, Lum GmbH, Germany) to record the near-infrared (NIR) light transmission during the centrifugation processes. This multi-sampler analytical centrifuge can reveal instantaneously the differences in the particle concentration by transmitting NIR-light through the sample length and allow the measurement of the extinction profiles during centrifugation. The NMR analysis of polymer was evaluated on a JEOL-600 NMR spectrometer using D_2O as a solvent. The TGA/DSC-3 Mettler Toledo star^e system was used for the thermal degradation analysis. The system was programmed to heat between the ranges of 35 to 900 °C with an interval of 10 °C/min, the system was operated under a constant flow rate of nitrogen gas at 50 ml/min. The amount of the APTES loaded on the NPs was calculated from the data obtained on the TGA weight loss ranging between 400 and 650 °C. The functionality of the samples was analysed by attenuated total reflection-Fourier transform infrared (ATR-FTIR, Nicolet iS10). The data was collected within the range of wavenumber between 4000 and 400 cm^{-1} at a spectral resolution of 4 cm^{-1}. A cold-field emission scanning

electron microscope (CFE-SEM, SU8230 Hitachi, Leeds Electron Microscopy and Spectroscopy Centre, UK) operated at 2 kV for imaging and 15 kV for spectroscopy and transmission electron microscope operated at 300 kV (TEM, FEI Titan Themis^3 300 with a Gatan OneView, LEMAS Centre, UK) was used to observe the surface morphology. The SEM was coupled with an energy dispersive X-ray spectrometer (EDX, Oxford Aztec 80 mm^2 X-Max SDD detector) was used to identify the elemental compositions and locations. The samples for TEM were prepared via the method of Hondow *et al.* [322] to ensure that the nanoparticle dispersion state was captured. Gel permeation chromatography (Agilent Technologies Infinity 1260 MDS, GPC) was employed for polymer molecular weight determination. 0.1 M $NaNO_3$ was used as a liquid phase for analysing the molecular weight and polydispersity of the polymer. A 0.22 μm pore size hydrophilic GVWP membrane was used to filter the sample before injection.

4.3.5. Results and discussion

4.3.5.1. Characterisation of M_SiO_2

Six different samples are shown in **Table 4.3,** one pure SiO_2, and five M_SiO_2 with various APTES concentrations. The elemental analysis results demonstrated an increase in the amino groups on the M_SiO_2 surface after the addition of different APTES content from M_SiO_2-1 to M_SiO_2-5. At the highest amount of APTES (3.2 g), the highest nitrogen content and percentage of amino groups is observed (7.2 wt. %). This could be due to the condensation reaction occurred on the surface of the M_SiO_2 causes by the presence of various APTES molecules as reported in the literature [323]. Similarly, the arrangement of some particular APTES molecules on the surface of M_SiO_2 could enhance the content of the functionalisation, which could at the same time promote the interaction between the polymer and NPs. Zeta potential of pure SiO_2 and series of modified particles was recorded in **Table 4.3**, the outcome

shows that the higher the APTES content the higher the value of zeta potential, indicating that more APTES present with the particle promotes the particle stability by showing better dispersion properties. The hydrodynamic particle size distribution for pure SiO_2 and M_SiO_2-5 were measured by DLS following the particles dispersing in water as shown in **Fig. 4.17**. The pure SiO_2 shows two peaks at around 44 and 335 nm, whereas M_SiO_2-5 displays only one peak at around 177 nm. This confirms that M_SiO_2 possesses better dispersion equity than the pure SiO_2 suspension. The aforementioned finding was also confirmed by investigating the morphology of the pure SiO_2 and M_SiO_2 using SEM and TEM analysis, where it shows clearly in **Fig. 4.18** that pure SiO_2 has different size particles (bigger size labelled in red as shown in **Fig. 4.18**), while M_SiO_2 shows homogenous mixture**.**

ATR-FTIR spectroscopy was employed for pure SiO_2 and the series of M_SiO_2 samples to analyse the behaviour of the chemical bonding as shown in **Fig. 4.19**. The bands appearing at 3200 and 3583 cm^{-1} in M_SiO_2 represent the stretching vibration of N–H and O–H, respectively. The modified samples compared to pure SiO_2 shows extra new peaks at 1528 and 2931 cm^{-1} which are assigned to the N–H bending vibration and C–H stretching vibration, respectively. The peak at 1636 cm^{-1} represents the Si–O–H vibrations proving the existence of hydrogen bonding between the O molecule in SiO_2 and H atoms from the incorporated organic components [108]. The FTIR spectra for all samples exhibit a deep Si–O–Si stretching vibration near 1078 cm^{-1} along with a bending shift between 470 to 800 cm^{-1} [324].

The TGA analysis of pure SiO_2 and M_SiO_2 with various APTES contents was performed with the heating range from 25 to 900 °C as shown in **Fig. 4.20**, displaying similar results as reported in the literature [325-327]. The TGA curves demonstrated that SiO_2 displayed a small weight loss until 200 °C, which is related to desorption/evaporation of water molecules. Compared to the pure SiO_2 sample there are two stages of weight loss in M_SiO_2 samples, there was an initial weight loss at 450 °C confirming the attachment of APTES molecules on the surface of

SiO_2, with the second stage of weight loss observed from 450 to 650 °C which is attributed to the decomposition of APTES molecules to form release of NH_3. The results were used to calculate the percentage of amine content in the NPs and showed that the higher the APTES concentration the greater the amine contents present with the particle.

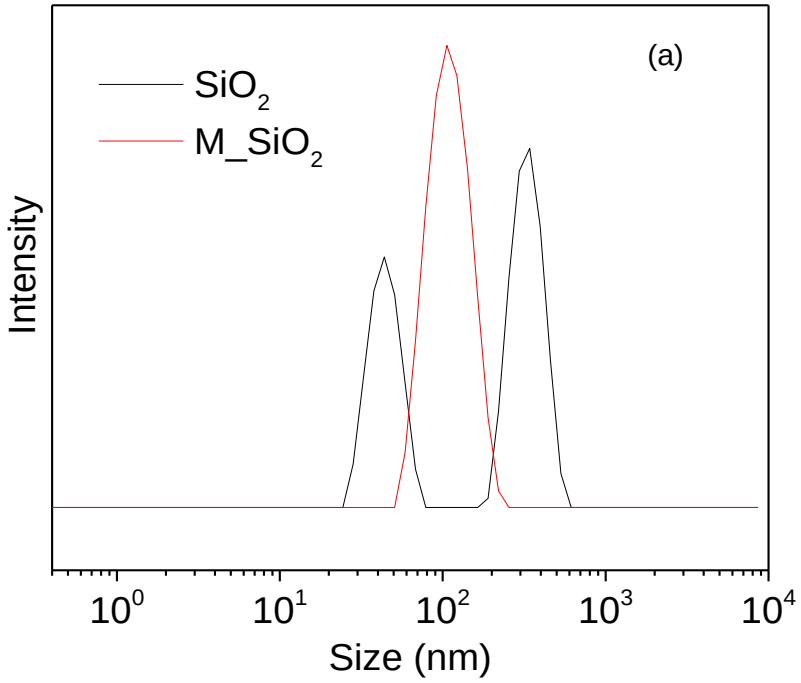

Figure 4.17. DLS particle size distributions showing the difference in dispersion state after modification of the pure SiO_2 NPs.

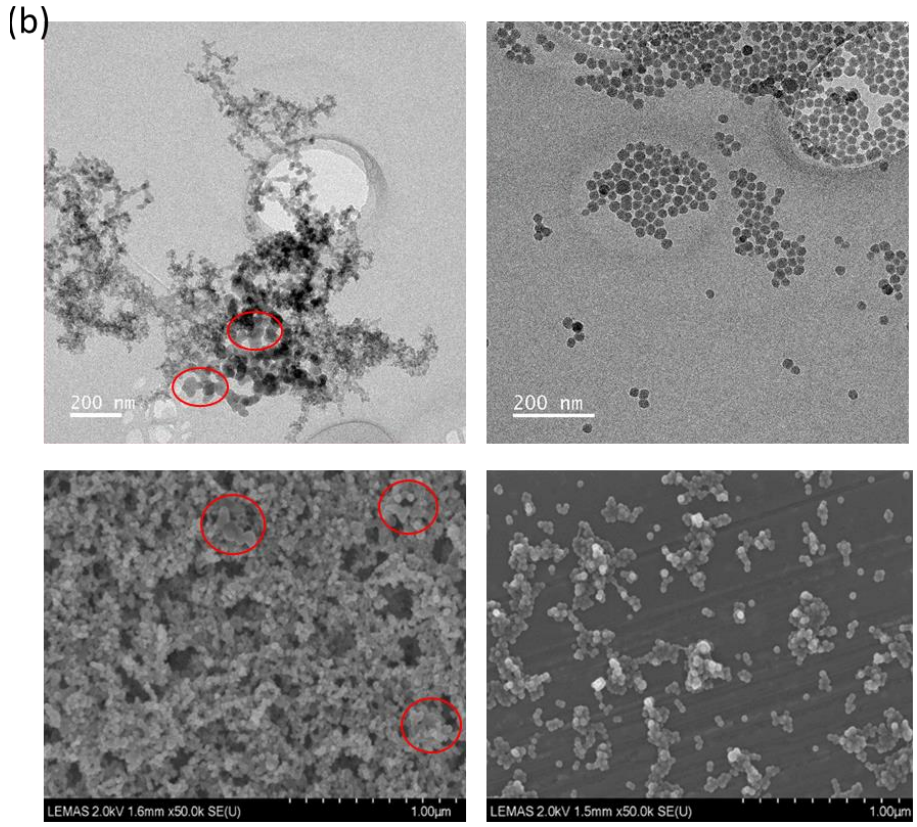

Figure 4.18. TEM (top) / SEM (bottom) images of pure SiO_2 (left) and M_SiO_2 (right), with larger particles highlighted by red circles.

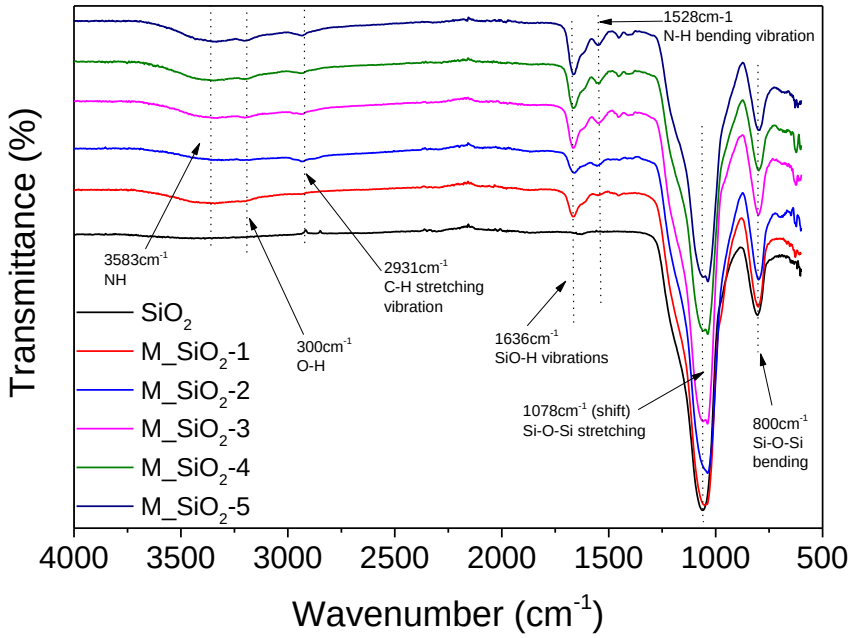

Figure 4.19. (a) FTIR spectra of pure SiO_2, M_SiO_2-1, M_SiO_2-2, M_SiO_2-3, M_SiO_2-4 and M_SiO_2-5.

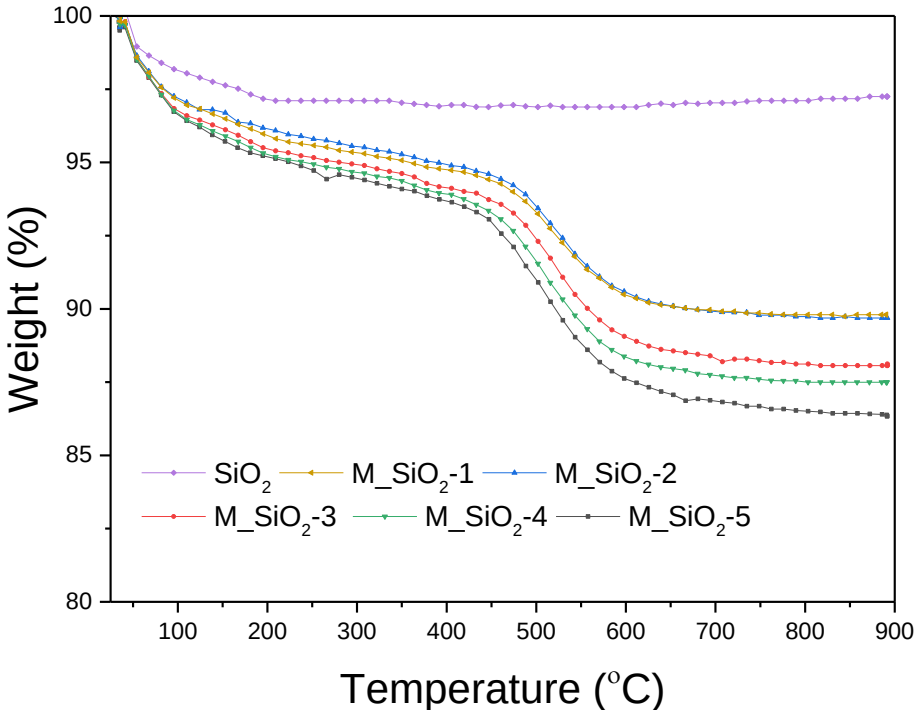

Figure 4.20. TGA profiles of pure SiO_2 and M_SiO_2 with different APTES contents

4.3.6.2. Determining the best particle sample for making the composite.

The dispersion stability of the five modified silica's (M_SiO_2-1, M_SiO_2-2, M_SiO_2-3, M_SiO_2-4, and M_SiO_2-5) and pure SiO_2 was investigated to observe the sedimentation using LUMiSizer [320, 321]. The stability behaviour of pure SiO_2 and M_SiO_2 silica can be explained schematically as shown in **Fig 4.21**. For example, the pure SiO_2 NPs tend to aggregate into larger structures and settled down over a short time. However, this makes pure SiO_2 create a higher open particle bed structure which aggregated more by the applied centrifugal force. In contrast, M_SiO_2 is less likely to sediment because they are well dispersed as proved by DLS size distribution, TEM, and SEM. Consequently, the larger mass aggregates tend to sediment quickly when compared to well-dispersed individual particles, which have longer sediment bed formation time. The examined particle packing behaviour in relation to applied centrifugal force is similar to the observation made by other researches [328-330], where the pressure-insensitive packed bed is formed by the NPs with the stable dispersion while a pressure-dependent network is created by aggregate NPs dispersion [330].

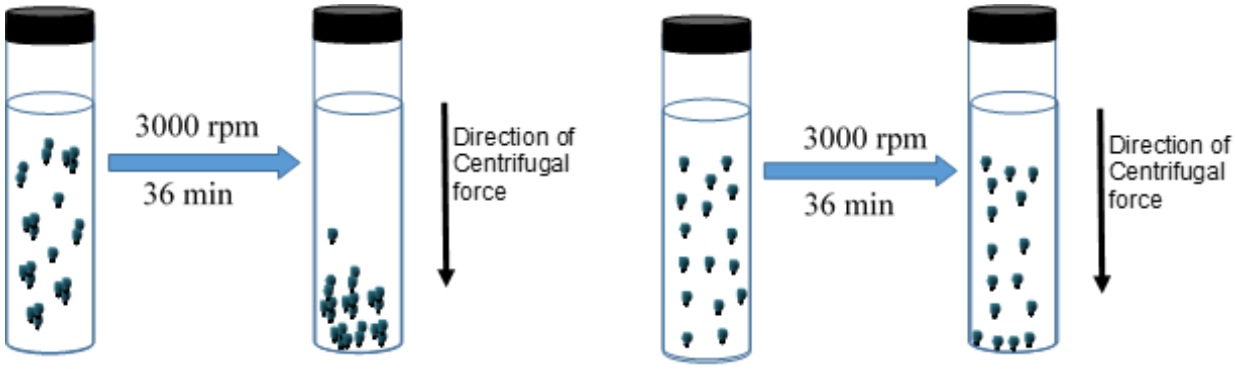

Figure 4.21. Schematic illustration showing the effect of centrifugal force on the nature of sedimentation of (left) aggregated and precipitated pure SiO_2 and (right) Stable and well-dispersed M_SiO_2.

To enable us to evaluate the effects of functionalisation on SiO_2 stability using Lumisizer, about 0.5 ml of each particle dispersion was added to a polycarbonate capillary cell and centrifuged for 36 min duration at 3000 rpm (equivalent to 1 month in real conditions) [167]. The effect of different amounts of APTES on SiO_2 was used to observe the stability of NPs dispersion. **Fig. 4.22** shows the instability index of M_SiO_2 and pure SiO_2 containing APTES dispersion with different concentrations. The results displayed that increasing the APTES contents make the stability of the suspension to increase, which is presumably occur as a result of the presence of positive charge (H^+) proton on the surface of M-SiO_2, thus providing a strong electrostatic repulsive force between functionalised particles and therefore leading to better stability. **Fig. 4.23** shows the style at which the light is passing or transmitted across the test tube indicating that the M_SiO_2 has better stability compared to pure SiO_2 NPs. **Fig. 4.23a** indicates that pure SiO_2 shows higher bed sediment to around 65% transmission profile (red colour) illustrating a quick and faster settling of the particle to form an aggregate of larger structures, however, the bed sediment starts to decrease to 58% transmission for M_SiO_2-1 as showing in **Fig. 4.23b**. The more obvious decrease in sedimentation profile was observed in M_SiO_2-5 as illustrated in **Fig. 4.20f.** This effect of dispersion stability was confirmed by zeta potential, particle size distribution, and SEM/TEM analysis as discussed in **Section 3.1**. Moreover, prior to the

analysis, the influence of NP type on the apparent viscosity (APV) was investigated using 0.1 wt. % of pure SiO_2 and M_SiO_2-5. The results show an increase in APV with the addition of APTES content from pure SiO_2 to M_SiO_2-5 (**Fig. 4.24a),** which is consistent with an increase in amino groups on the NP surface. Due to the high APV of M_SiO_2-5, different concentrations of both pure SiO_2 and M_SiO_2-5 were selected to examine the effect of particle concentrations, with the finding showing an increase in APV with increasing pure SiO_2 or M_SiO_2-5 concentration (**Fig. 4.24b**).

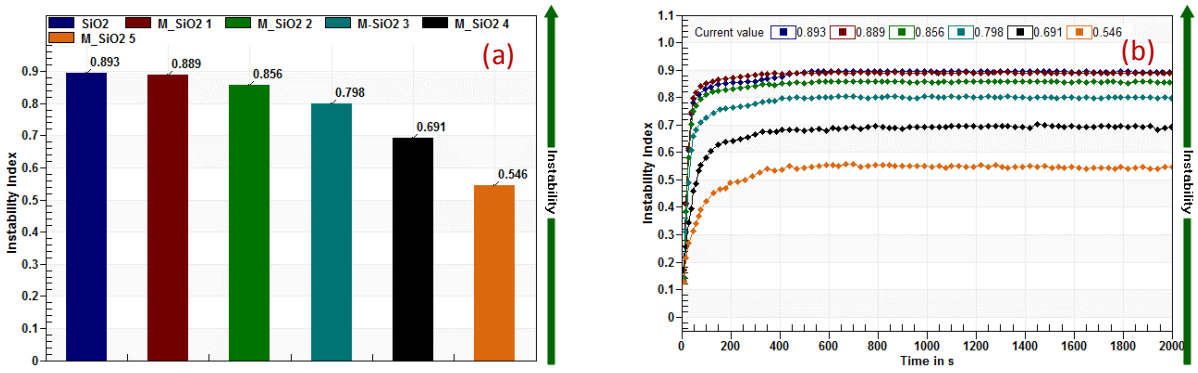

Figure 4.22. Instability index of SiO_2 and M_SiO_2 with different APTES (a) trend of centrifuge dispersion analyser for pure SiO_2 and M_SiO_2 with different APTES contents (b) stable immobile dispersions of pure SiO_2 and M_SiO_2 after 30 days at 85 °C.

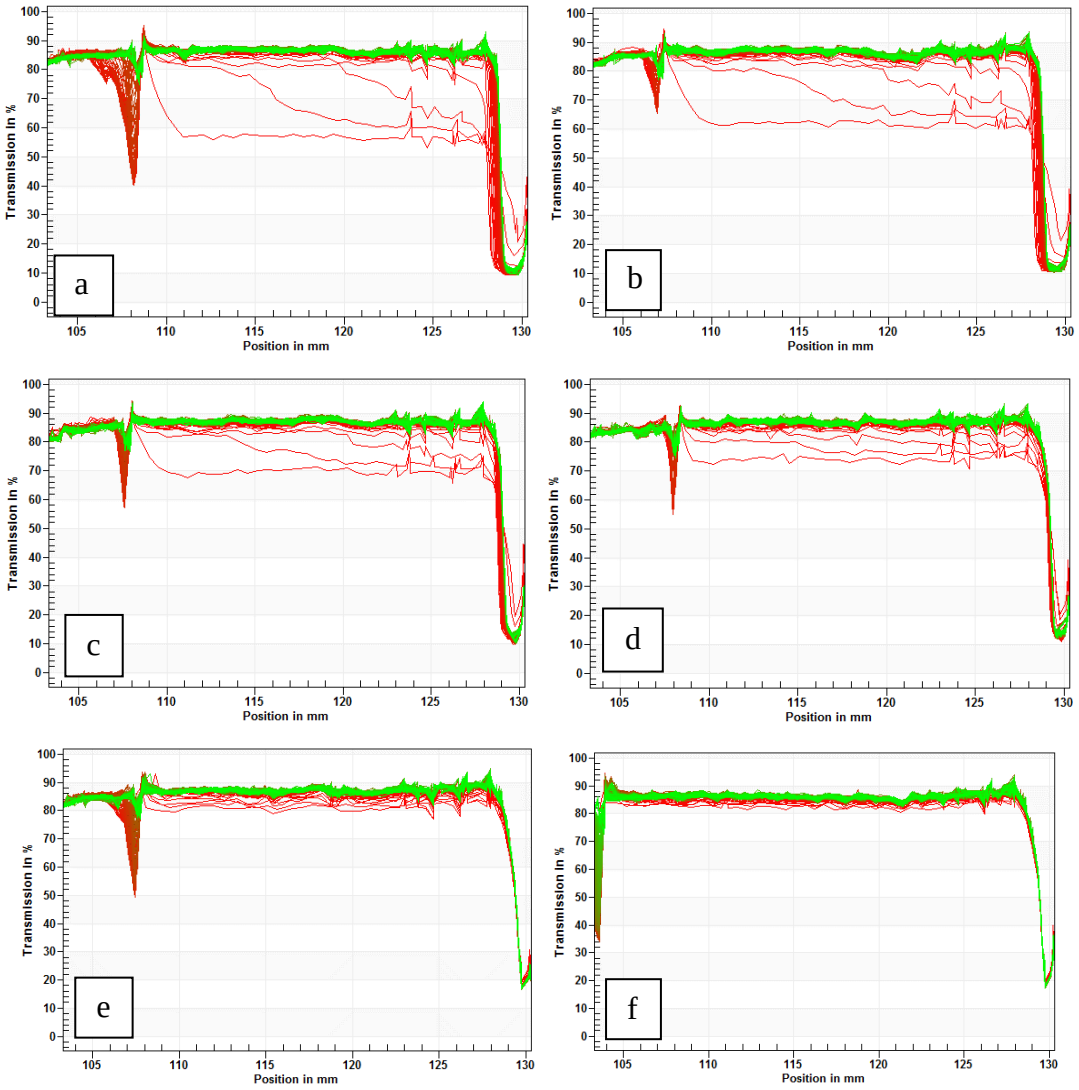

Figure 4.23. Styles of light transmission across the test tube for (a) pure SiO_2, (b) M_SiO_2-1, (c) M_SiO_2-2, (d) M_SiO_2-3, (e) M_SiO_2-4, (f) M_SiO_2-5 at the end of centrifuge process.

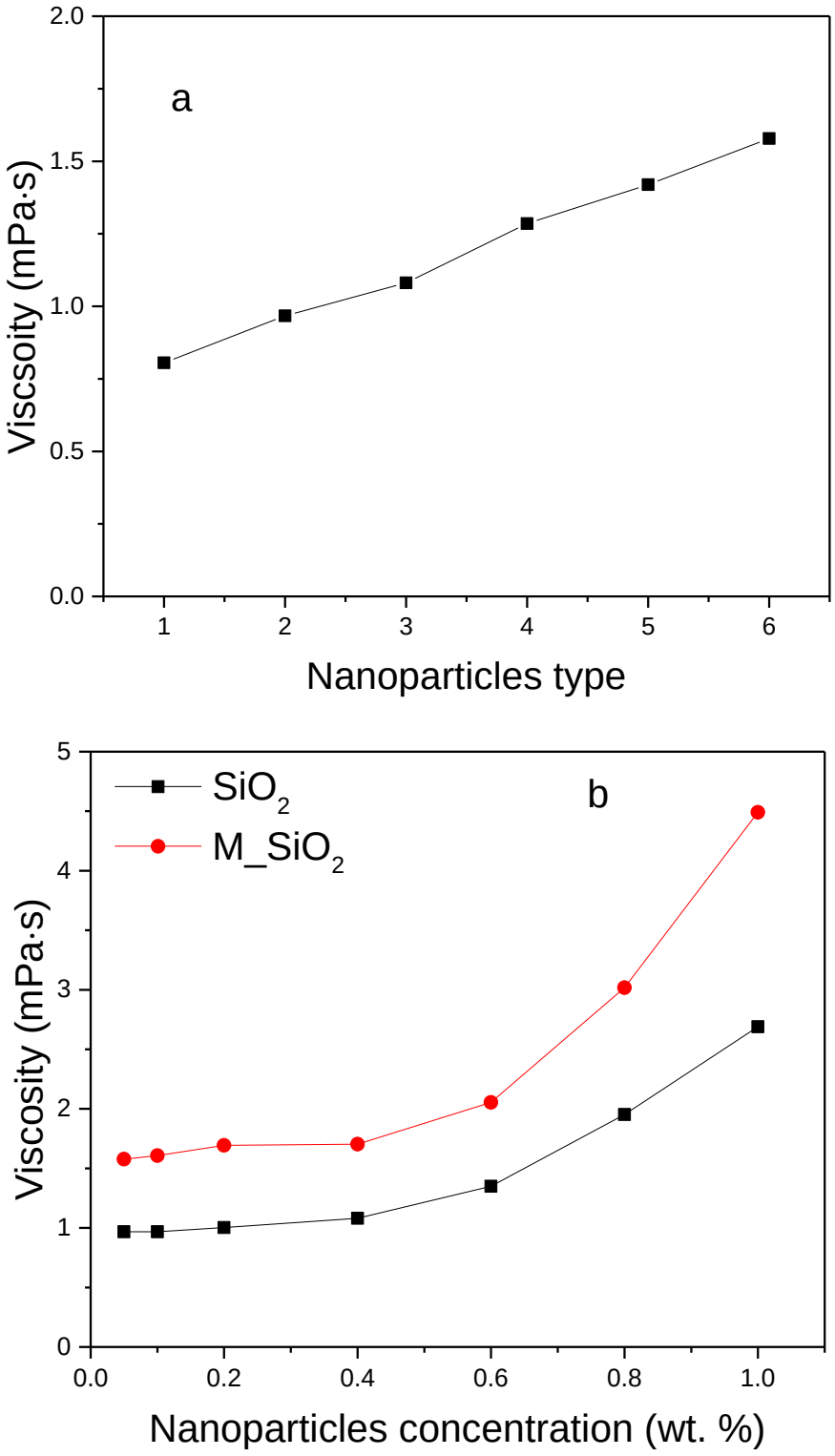

Figure 4.24. (a) Effect of NP type on the apparent viscosity and RV, and (b) viscosity as a function of pure SiO_2 and M_SiO_2-5 concentration (shear rate 1000 s^{-1} and T = 85 °C).

4.3.6.3. Characterisation of COPAM and COPAM/NPs composites

Considering higher stability and high APV of M_SiO_2-5, it was selected as an inorganic constituent for the fabrication of NPs/COPAM composites. Three samples were synthesised (NP-free COPAM, SiO_2/COPAM, and M_SiO_2/COPAM) via free radical polymerization to evaluate the effect of thermal stability. The formation of these synthesized polymers was examined by freeze-dried SEM, elemental analysis, TGA, ATR-FTIR, and ^{1}H-NMR. The morphology of the freeze-dried polymer and polymer NPs dispersion was examined using SEM analysis. The results show the sponge-like structure of the NP-free COPAM exhibiting a thick block with sparse pores as shown in **Fig. 4.25a,** pure SiO_2 NPs addition shows there is a clear particle aggregation in the polymer which results in flocculation and lack of proper dispersion and hence reduces the chances of obtaining highly stable material (**Fig. 4.25b**). Contrarily, the M_SiO_2/COPAM shows characteristics filamentous structures with interconnecting pores promoting better dispersion stability where the APTES molecules induce an energetically favoured layer-by-layer to form a stable composite with a 3D porous network having no obvious aggregation of the particles (**Fig. 4.25c**). It is interesting to know that the M_SiO_2/COPAM composite creates a denser structure of the hybrid system; this is attributed to the formation of much stronger hydrogen bond interaction between the polar function group of COPAM side chains and oxygen-containing groups of the M_SiO_2. However, this could be also due to the increasing amount of amino groups in the COPAM following the addition of M_SiO_2. It can be observed that from the EDX maps (**Fig. 4.25b and c**) a more homogenous mixture of the elements (Si, C, N, O, and S) is present in M_SiO_2/COPAM compared to SiO_2/COPAM, which reaffirms the formation of stable composite material. The ^{1}H-NMR of the polymers is displayed in **4.26**. The peak at 1.4 ppm is the methyl proton of the APSA unit, while that of methylene proton appears around 3.1-3.7 ppm. The peaks between 2.0-2.4 ppm indicate the existence of methane (–CH_3) protons in the polymer backbone. The peaks at 6.9

and 7.6 ppm attributed to the protons of C–H and R–CO–NH_2, respectively, revealing the formation of major polyacrylamide functional groups in the spectrum.

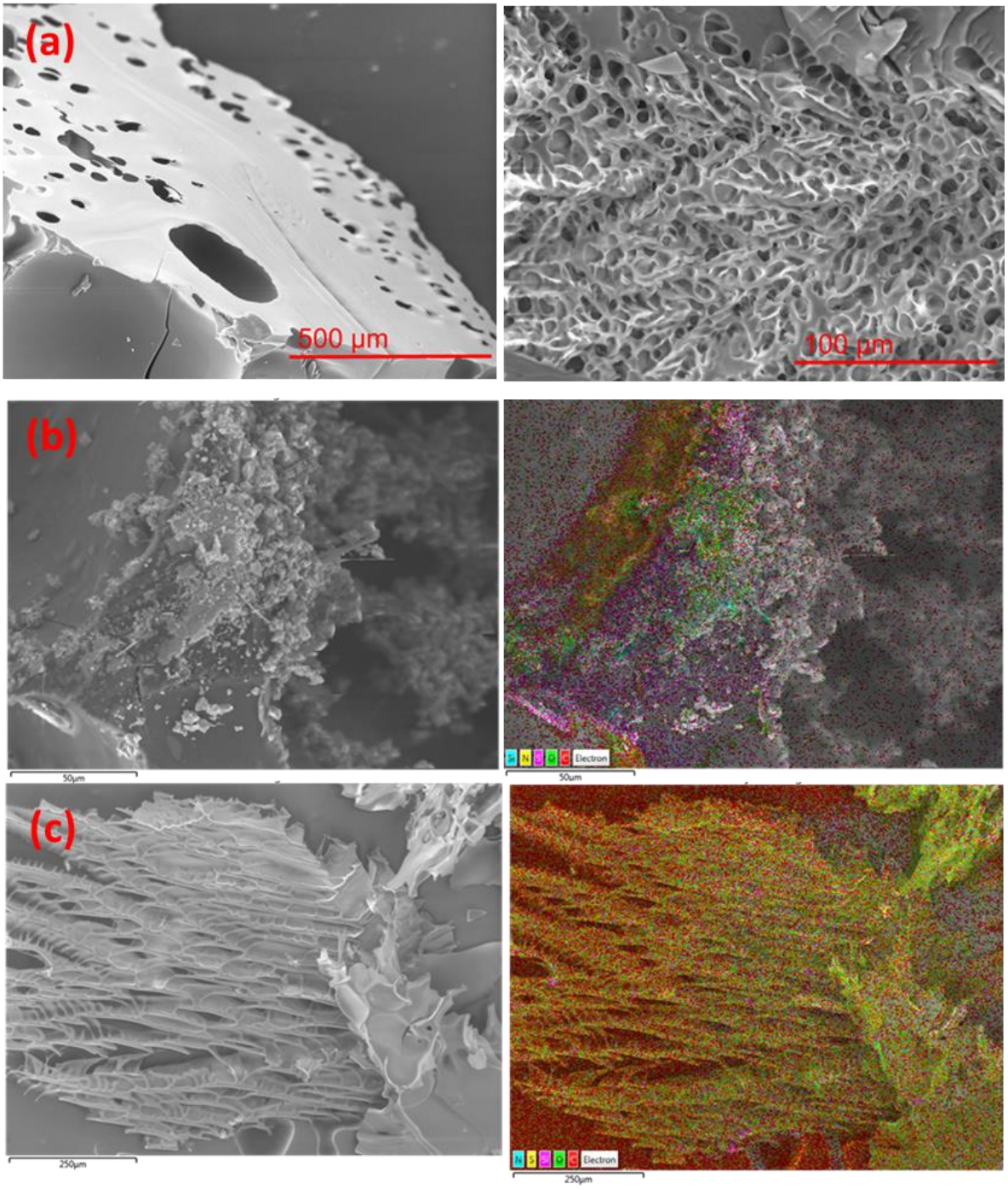

Figure 4.25. SEM images of the freeze-dried (a) NP-free COPAM (b) SiO_2/COPAM and (c) M_SiO_2/COPAM.

a

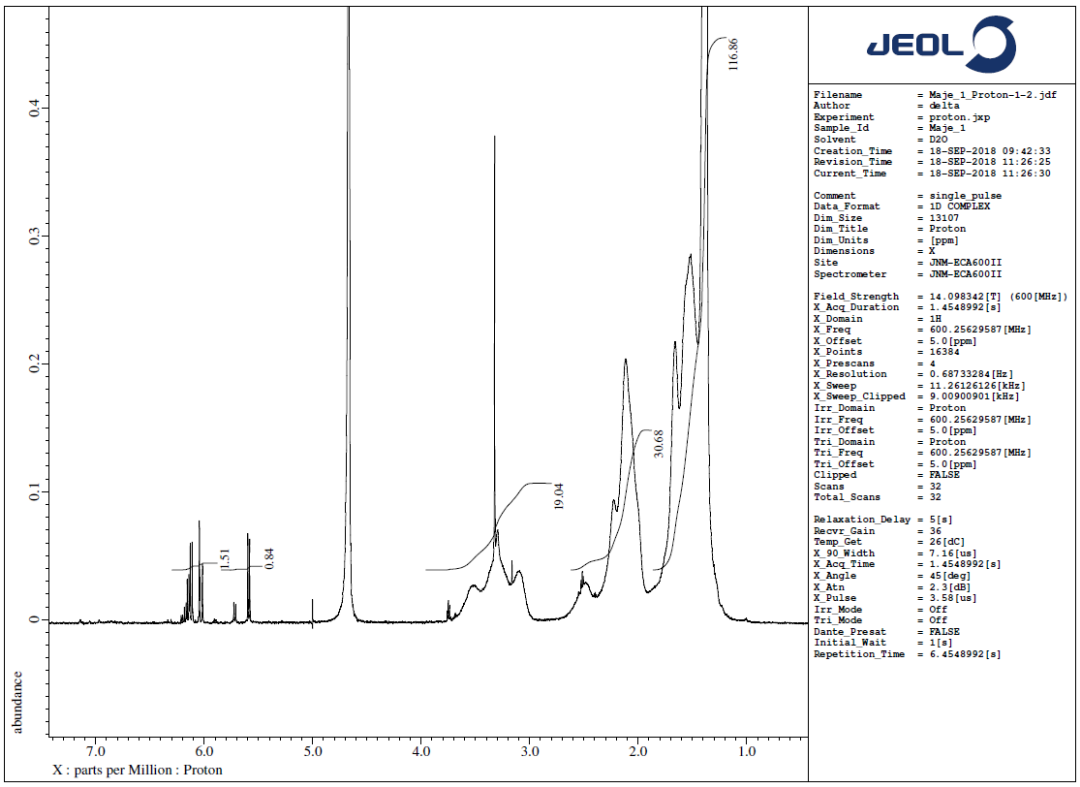

b

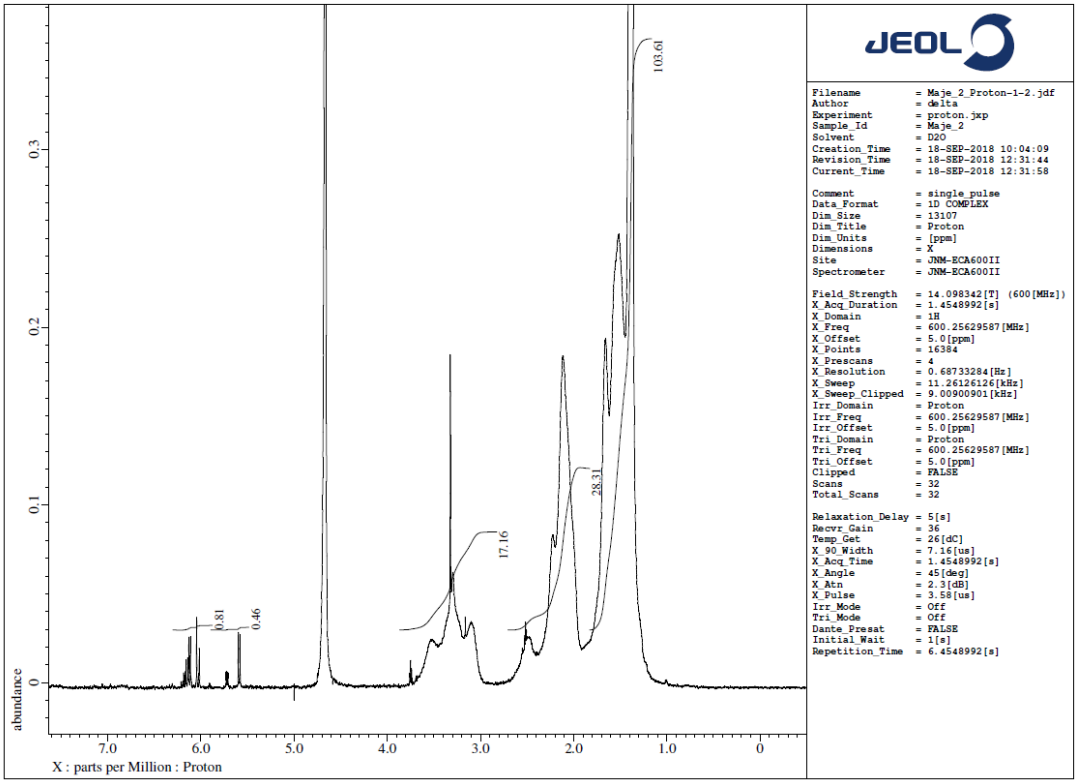

Figure 4.26. ^{1}H-NMR of (a) COPAM, (b) SiO_2/COPAM and (c) M_SiO_2/COPAM solutions.

c

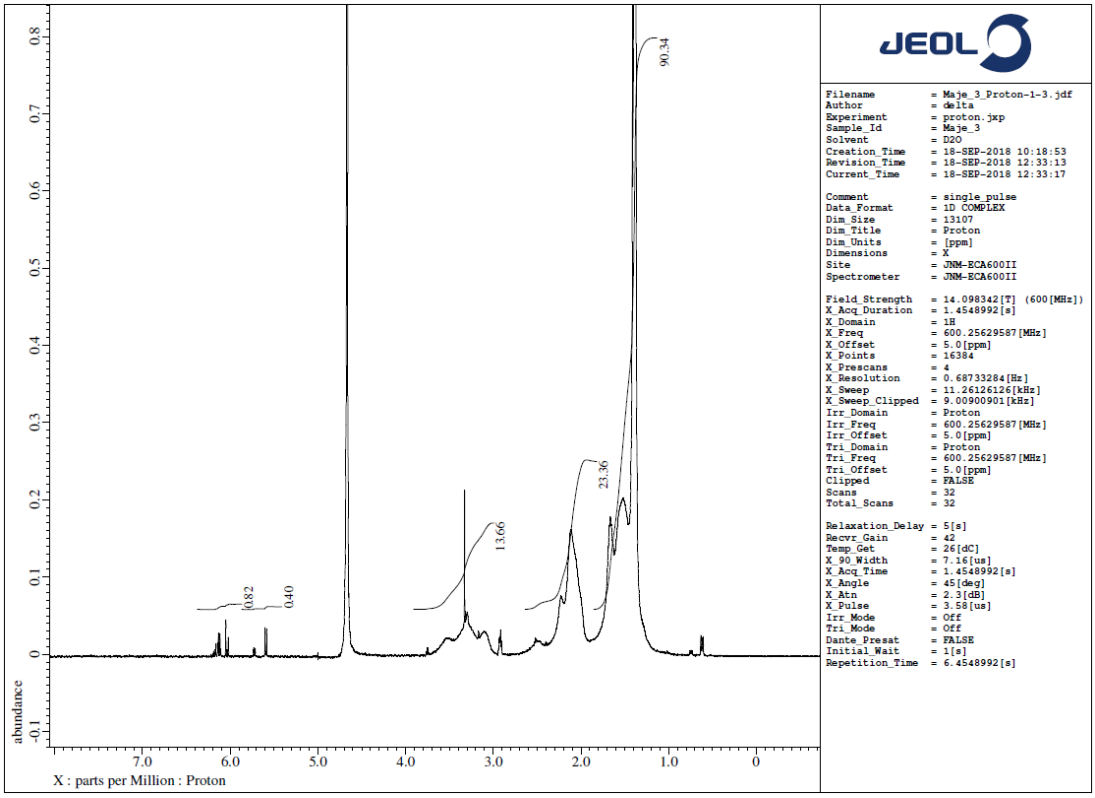

Figure 4.26 Continues.

As illustrated in **Fig. 4.27a**, the chemical bonding between the NP-free COPAM, SiO_2/COPAM, and M_SiO_2/COPAM was investigated using ATR-FTIR spectroscopy to understand the formation mechanisms of the added NPs. The peaks at 2923, 2953, and 3321 cm^{-1} are attributed to the ring structure vibration of C–H stretching, O-H group and N-H group of the COPAM amide chains, and the peak appeared at 1700 cm^{-1} is attributed to the C=O (carbonyl) functional groups of the polymer amides chain [108]. Correspondingly, the peak representing the SO_3 group initiated from APSA monomer appeared at 1040 cm^{-1} [287, 288]. The peaks at 1480 and 1078 cm^{-1} in the M_SiO_2/COPAM and SiO_2/COPAM spectra represent Si–O–Si asymmetric bending and stretching vibrations, respectively, supporting the existence of hydrogen bond between the incorporated NPs and the COPAM molecules [108]. However, in comparison to SiO_2/COPAM, there is new broader peak appears between 2000 to 2500 cm^{-1} in M_SiO_2/COPAM spectra, indicating the formation of the new electrostatic chemistry that

occurs when the additional proton (H^+) from the amino group of M_SiO_2 react with the polymer ionic charges, reinforced the ability of polymer molecules to be adsorbed onto the M_SiO_2 NPs surface by ionic linkage as illustrated in **Fig. 4.27.**

TGA was carried out using a heating range from 25 to 900 °C, with the TGA curves of the NP-free COPAM, SiO_2/COPAM, and M_SiO_2/COPAM shown in **Fig. 4.27b**. The TGA analysis demonstrated that M_SiO_2/COPAM displayed a slight weight loss betwixt 50 to 150 °C, which is attributed to the decomposition of attached APTES and desorption of water molecules from the surface. It can also be observed that, compared to NP-free COPAM and SiO_2/COPAM samples, the M_SiO_2/COPAM composites show a small weight loss (~10%), indicating how fairly stable the M_SiO_2 NPs on the COPAM surface, although the weight remains almost constant until 900 °C. However, the weight lost on SiO_2/COPAM composites is roughly divided into three stages, at around 400 °C, almost 20% of the sample weight was lost, at around 700 °C around 12% loss was observed, and more than 3% weight loss was observed after heating up to 900 °C, which is attributed to the decomposition of surface-modified components on the polymer surface. Contrarily, the NP-free COPAM shows significant loss of weight (~45%) until 350 °C, probably because of the loss of adsorbed water and slowly polymer decompositions, more weight loss followed on the same material to around 80% from 450 °C and above which is because of ammonia evolution and chain scission of the polymer at high temperature. This finding is in agreement with the literature [331, 332]. However, the M_SiO_2/COPAM composites have high-temperature durability because they possess additional covalent bonds and stronger coordination bonds between the COPAM backbone and the M_SiO_2, compared to SiO_2/COPAM which only has hydrogen bonding on the surface, this makes M_SiO_2/COPAM more temperature resistance than the other samples.

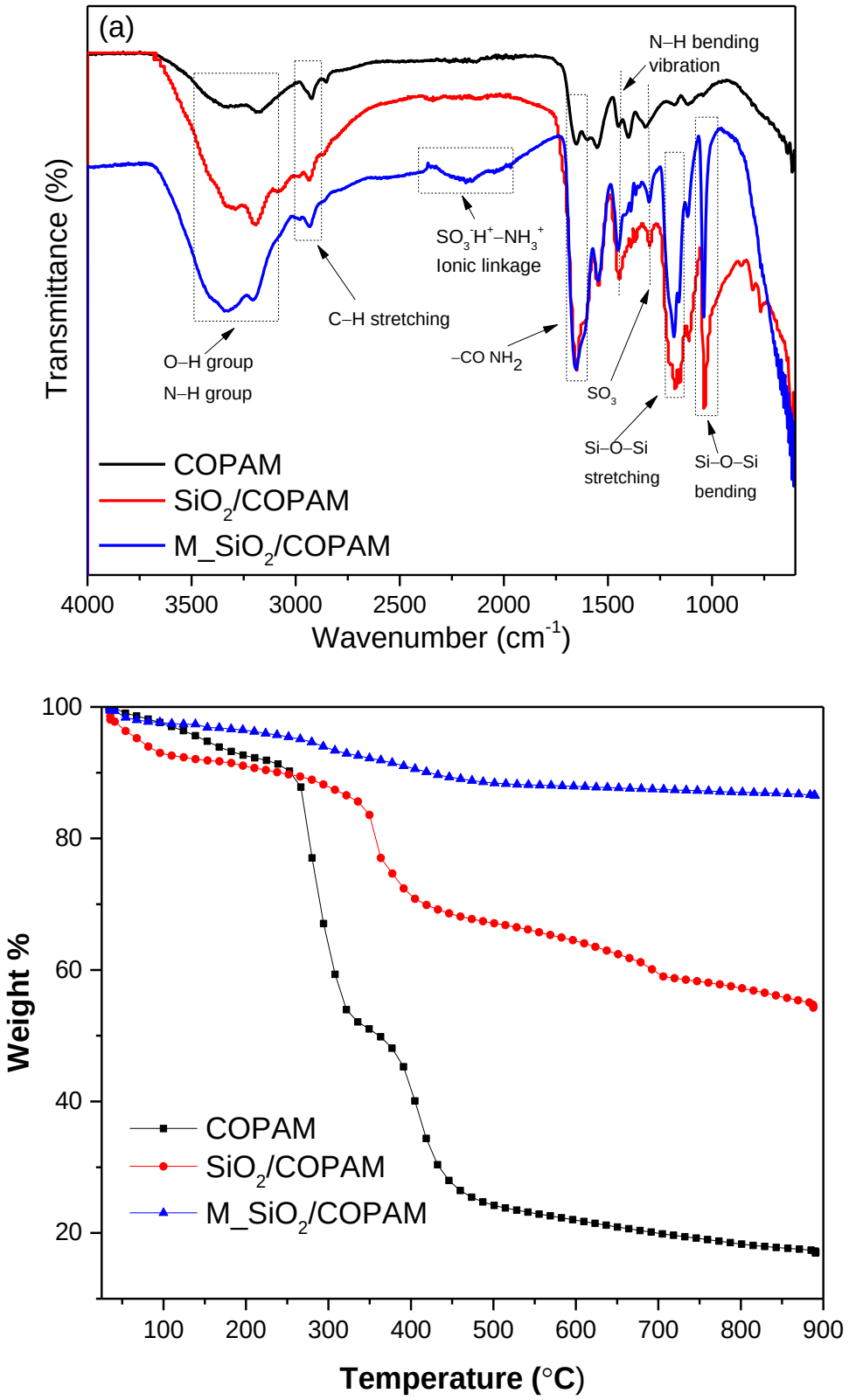

Figure 4.27. (a) ATR-FTIR spectra of NP-free COPAM, SiO_2/COPAM, and M_SiO_2/COPAM (b) TGA profiles of NP-free COPAM, SiO_2/COPAM, and M_SiO_2/COPAM nanocomposites.

4.4. Chapter Summary

The stabilization of polymer nanocomposites in high-ionic-strength brines is a challenging issue. However, for EOR applications, the stability of the nanocomposites have to be examined under high temperature and high saline conditions. According to the finding in Chapter 3, the prepared composite material was not stable in a complex brine solution, and NPs tended to agglomerate and aggregates. Therefore, in this Chapter, a novel synthesis approach was used to provide the *in-situ* synthesis and modifications of polymer nanocomposites under the influence of high ionic strength brine. The Chapter is divided into two sections, and the results of each section were conclusively summarized below.

In the first section, a novel way to enhance the stability of GO polyacrylamide nanocomposites at high-temperature and high-ionic-strength brines was developed. COPAM was covalently attached to the partial rGO via free-radical polymerization and reacted further with 1,3-propane sultone to accomplish zwitterionic groups. Compared to GO−COPAM, zwitterionic rGO−COPAM dispersions showed no noticeable sedimentation or flocculation, the particle size measured was smaller with large zeta potentials, and the instability index derived from LUMiSizer was smaller over a storage of 120 days at 80 °C under both APIB and FB conditions. It also showed that the dispersion stability was better in APIB than in FB, where the GO-sheet conjugated structure may have been altered after 90 days in the FB. FTIR and other chemical analysis suggested that the formation of zwitterionic character on the rGO−COPAM composites was responsible for the excellent temperature stability and dispersibility in the presence of high salinity and high temperature. Such results suggest that the zwitterionic molecules could be used as a stability enhancer for different particles, and the zwitterionic polyacrylamide−GO systems possess greater potential for future enhanced oil recovery applications.

In the second section, SiO_2 NPs were successfully functionalised with (3-aminopropyl) triethoxysilane to create positively charged active sites on the surface to form a stable NP dispersion, which facilitated the formation of strong coordination bond with the negatively charged COPAM chain. Three samples including M_SiO_2/COPAM, SiO_2/COPAM, and NP-free COPAM were synthesised *in-situ* via free radical polymerisation, and their thermal degradation, variations of apparent viscosity and effect of the aging time were investigated. The outcome of the finding revealed that M_SiO_2 could inhibit HT-HS degradation of the polymer and safeguard its backbone to prevent the polymer molecule from rupture. These improved properties of M_SiO_2/COPAM were generated due to the incorporation of amino functional groups on the surface of the SiO_2 NPs, which resulted in the formation of electrostatic attraction that reinforced the bonding of COPAM molecules with M_SiO_2.

Chapter 5 Investigation of rheological properties of produced polymers and polymer nanocomposites

5.1. Introduction

This Chapter investigates the rheological properties of different formulated materials synthesized in Chapters 3 and 4. The rheological investigation of the HPAM seeded with GO and CQDs were investigated. The impact of various nanoparticle concentrations, temperatures, and electrolyte concentrations on the long-term thermal stability and rheological behaviour were being investigated. In addition, the investigation of the influence of MWCNTs on the rheological properties (viscosity and viscoelasticity) of five polymers synthesised via free radical polymerization, was conducted and appropriate polymers were identified for EOR at API brine and alkaline pH conditions. The effects of modified rGO and modified SiO_2 on the polymer rheological properties were also observed.

5.1.3. Rheometers used for rheology analysis

Anton Paar 'Physica MCR 301 **Fig 5.1**, and Discovery hybrid rheometer (DHR 3) **Fig. 5.2**, from TA instrument, were used to measure both steady and dynamic rheology. Before the measurement, the rheometer was calibrated with standard substances at low and high temperature respectively. This was done to guarantee both the instrument and its setup applied were calibrated and provide accurate results as shown in **Fig. 5.5**.

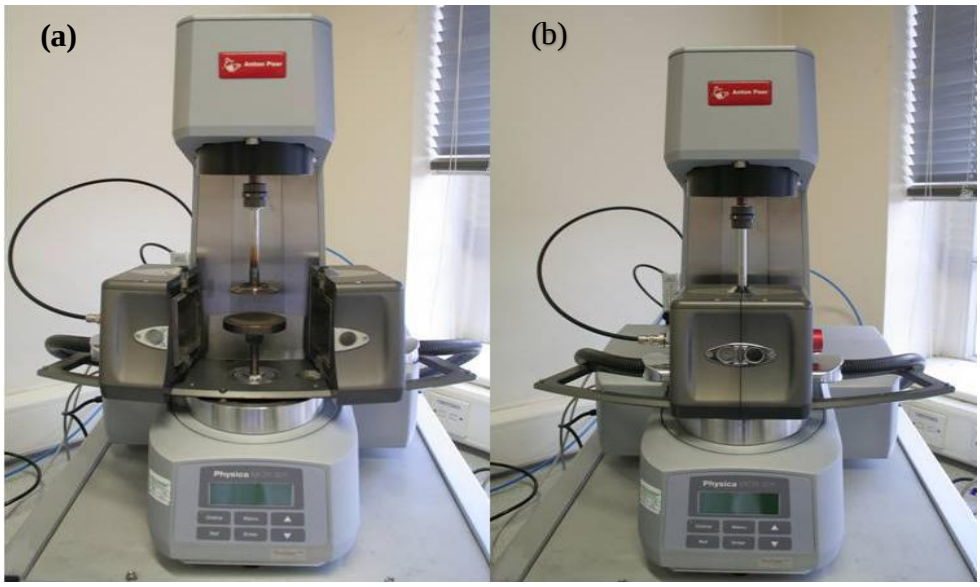

Figure 5.1. Anton Paar Rheometer.

- (a) Displayed open furnace, with diameter stainless steel plate (65mm or 50mm) in the middle on to which the sample is placed and an overhanging stainless steel cone of 50mm diameter, and 1° angle.
- (b) The setup of the rheometer ready for measurement after the furnace is closed.

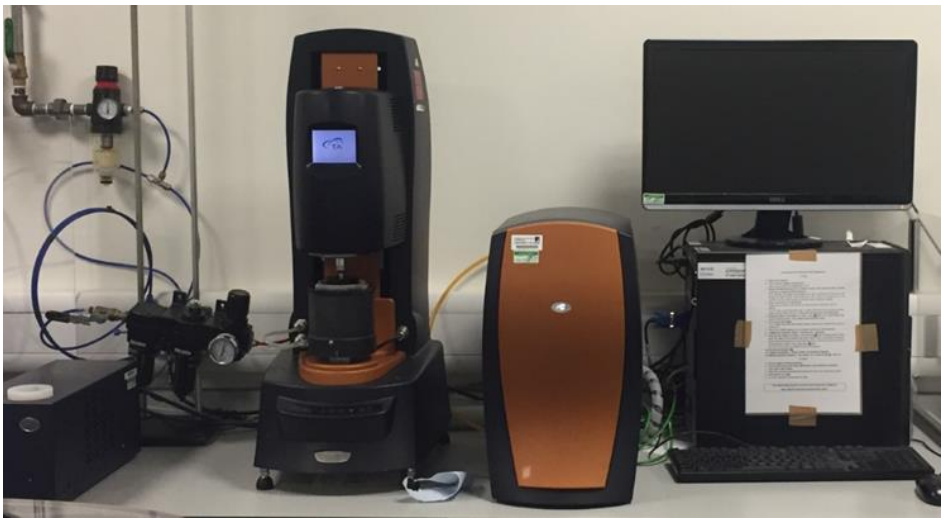

Figure 5.2. DHR Rheometer

5.1.4. Rheometer calibration test

The calibration test with Rheotek oil was conducted at different temperatures, (25, 40, 50, 60, and 100), and it repeated many times and recorded the average data. **Fig. 5.3** shows the viscosity vs shear rate; it was observed that the shear rate demonstrated the Newtonian and thinning behaviour. **Fig. 5.4** the effect of temperature on viscosity of the rheotek oil; it can be seen that increasing temperature decreases the viscosity, and by comparing the experimental data obtained with standard data of Rheotek oil, both experimental and standard results showed a decrease in viscosity as temperature increases, and their difference is approximately 3%. These results indicate the results close to accuracy when using the Anton Paar 'Physica MCR 300 Trugap' rheometer. Deionized water and standard oil were used to check the accuracy of the rheometers to ensure that before any of the tests started, the rheometer was calibrated. After setting up the cone and plate geometry, space was pre-set at 0.098mm between the flat tip of the cone and plate. Having a precise amount of liquid solution in the gap to achieve an accurate test is highly important, making sure the whole cone area is utilized. However, too little or too much liquid would provide a smaller or greater contact area (**Fig. 5.5**). 0.57ml, which is equivalent to $0.57cm^3$, is the pre-set volume required, providing the density is $1.00g/cm^3$. Notwithstanding, when the fluid density is known, calculating it required amount is possible. The calibration test with the above volume of deionized water and standard oil will provide assurance that the amount/volume used was right.

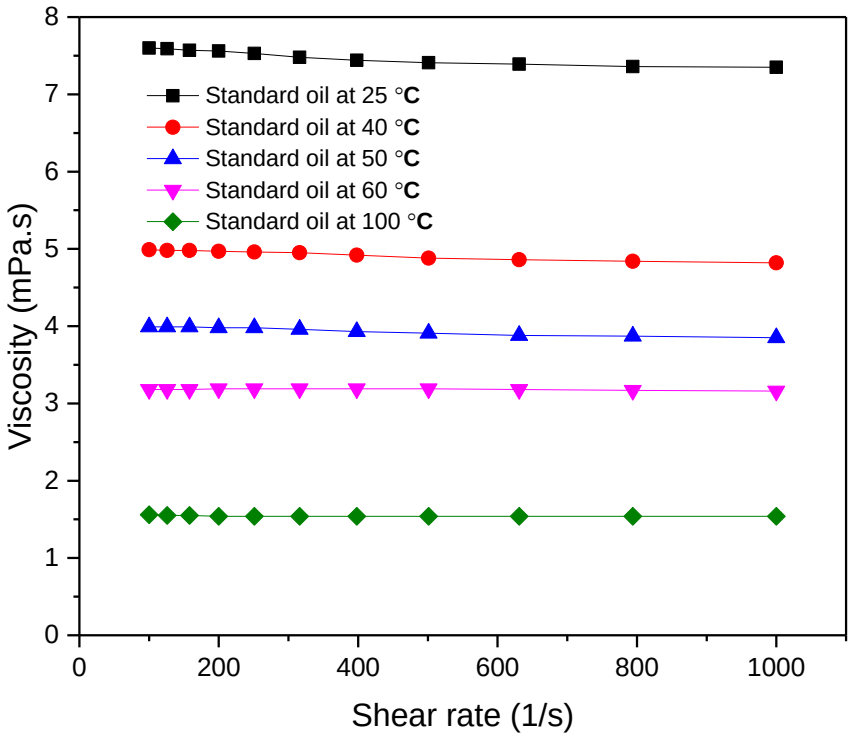

Figure 5.3. Viscosity versus shear rate demonstrated the Newtonian character of calibration oil.

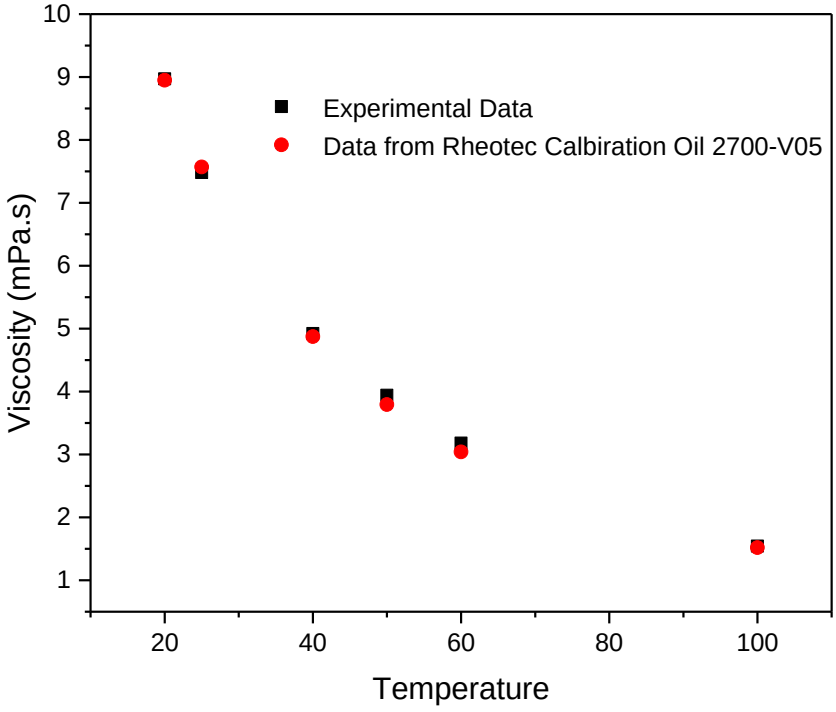

Figure 5.4. Calibration of Rheometer using Rheotec Calibration oil 2700-V05. The obtained values were within 3%.

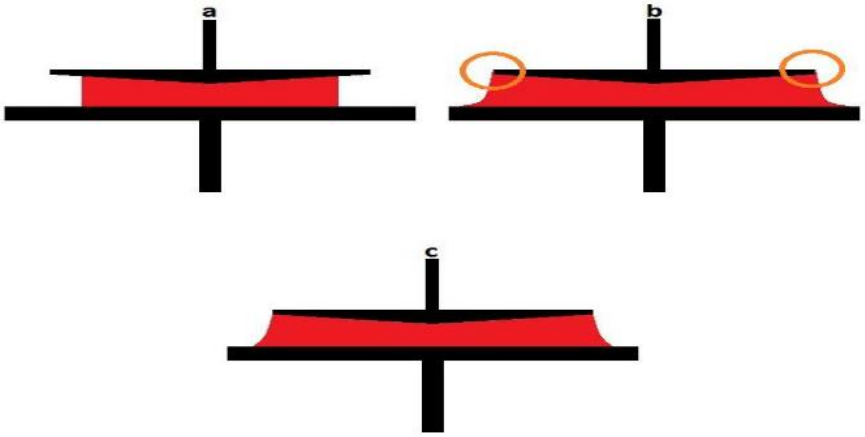

Figure 5.5. Schematic illustration of the contact area between the cone & plate geometry and the liquid sample [67].

a) Has no enough sample between the cone and the plate.

b) It has too much sample between the cone and plate, as such the cone is taken into consideration (indicated using orange circles).

c) Almost right, and this would provide more accurate values because only the underside of the cone is been used and covered by the sample during the measurements**.**

5.2. Rheology Measurement

All rheological measurements were carried out on a Physica MCR301 (Anton-Paar) Rheometer and Discovery Hybrid Rheometer (DHR-2). The rheometers are equipped with a convection oven and a 'TC30' temperature controller unit, which can stabilize the sample temperature from 0 to +1000 °C with an accuracy of 0.1 °C. Temperature bath and Rheometer controllers were turned on before the experiment to warm up the system. Minor adjustments were made if necessary to centre bob with adjustment knob until the output reading was ± 0.02 in range. A cone-and-plate geometry was selected for the rheological measurement, the gap is pre-set to the standard (0.098 mm for MCR301 and 0.52µm for DHR-2) as determined by the manufacturer. The system only requires a small amount of sample (maximum 0.7 ml) for each

test and is easy to clean [108]. Before any measurement, the rheometer was tested with a standard oil and pure water at different temperatures to ensure that both the instrument and this particular setup were calibrated, yielding reliable data. The measurement was then performed over the range of shear rates. The digital output often fluctuated greatly, but usually, fluctuation decreased with time and an average or range observed values were recorded. The rheological behaviour of different prepared solutions was determined under both oscillatory and steady shear to obtain the dynamic and steady viscoelastic properties. The experiment was conducted at 25 °C and 85 °C, or different temperature range (temperature ramp), the temperature was controlled by a Peltier system that provides fast and precise temperature adjustment during heating. Throughout the experiment, a solvent trap was used to avoid solvents evaporation while measurement. The above procedure was repeated at least 3 times for each sample.

5.2.1. Long-term thermal stability

In a polymer flooding process, injection fluid stays for a long period of time in the reservoir under severe conditions before reaching the oil, therefore it is imperative to consider the effect of aging as a benchmark of understanding the capability of displacing fluid. In this work, the sample of fixed HPAM cross-linked by fixed NP solution was selected for the long-term thermal stability test, while a particle-free sample with the same polymer concentration was selected as the reference. The samples were stored in glass bottles covered by screw-caps with promoted sealing by a sealing tape and were placed into an oven at 80 °C. The viscosities of those samples were measured at 85 °C at different time intervals [108].

The relative viscosity (RV) was then calculated from Eqn. 5.3.

$$RV = \eta_t/\eta_0 \times 100\% \ldots\ldots\ldots 5.3$$

Where η_t represent apparent viscosity of the aged sample (mPa·s) (at particular day) and η_0 is the apparent viscosity at zero-day aging.

5.3. Results and discussion

The rheological investigation is a key factor in the polymer flooding process. In order to achieve an optimum oil recovery, an accurate viscosity of the polymer is required to obtain favourable mobility ratio between the oil and displacing fluid. However, the polymer viscosity is affected by the temperature and salinity present in the oil reservoirs [56, 333-335]. Both salinity and temperature cause different mechanisms for HPAM viscosity reduction. Higher temperature results in the diminishing of the copolymer hydrophobic effect between the polymer chains and speed up polymer solubility, and hence decreases its viscosity [56, 334]. Whereas, in the presence of salinity, the ionic shielding on the amide groups ($CONH_2$) in the chemical structure of PAM reduces the chains' repulsion of the PAM backbone which results in the collapse of polymeric coils and reduction in polymer size and hence more viscosity reduction [334, 335]. However, the addition of nanoparticles into the polymer backbone enhances its rheological behaviour at high salinity and high-temperature conditions.

5.3.2. Effect of GO on the rheological properties of HPAM.

5.3.2.1. Critical association concentration

Polymer molecules can develop concentration-dependent association, which can occur mostly when mixing with other substances like surfactants and nanoparticles [108, 336]. This association can be apparent at the concentration of the first break, often termed the critical association concentration (CAC), where polymer molecules and other substances begin to associate. It is significant to know the CAC value to achieve required morphological features or specific modification of the polymer solution such as in a polymer/nanoparticle hybrid. However, the CAC value can be obtained using other approaches such as light scattering determination, variable view cell apparatus [336], and the changes in fluorescence characters when micellisation occurs [337].

Notwithstanding, HPAM solution rheological investigation at 25 °C was used, in this work, to determine the CAC. **Fig. 5.6** illustrates the 1000 shear viscosity versus HPAM concentration, and it can be observed that the curve is split into two parts, below 0.06 wt. % HPAM concentration, the viscosity patterns show slight differences with the increase in polymer concentration. For the concentration equal to and above 0.06 wt. %, the viscosity was sharply increased as HPAM concentration increases. This trend suggests that 0.06 wt. % is the HPAM CAC used in this study. As the polymer concentration increased, the number of molecules increased within the solution resulting in a more significant interaction between the polymer chains, leading to greater frictional effect and subsequently alter the stability of the composite.

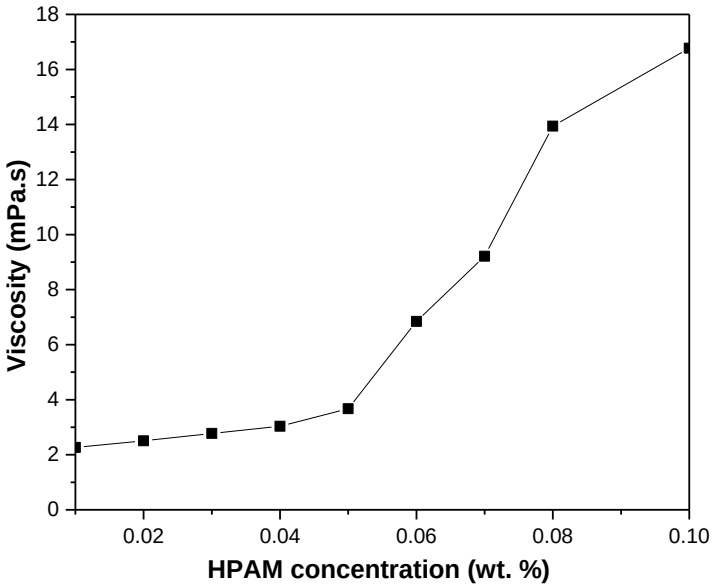

Figure 5.6. Viscosity as a function of HPAM concentration (25 °C and shear rate 1000 s^{-1}).

5.3.1.1. Effect of nanoparticle concentration

As mention earlier, the intramolecular hydrophobic association can play a significant role when making polymer-nanoparticle hybrids because of the CAC of the polymer. In this section, 0.05 wt. %, which was immediately below the CAC level, was used for investigating the impact of GO nanoparticle on the rheological properties of HPAM. Different GO concentration 0.01,

0.02, 0.04, 0.06, 0.08 and 0.1 wt. % was added into the solution containing 0.05 wt. % HPAM and their rheological behaviour were studied. **Fig. 5.7a and b** illustrate the dependence of the solution viscosity on the shear rate for the HPAM/GO hybrids at 25 and 85 °C, respectively. It can be seen from the graphs, the apparent viscosity decreases sharply with increasing shear rate from 100 to 1000 s^{-1} indicating a shear-thinning behaviour for the entire system. Compared to the HPAM and low GO loading, the solution with the high GO concentration shows better resistance to shear rate with less viscosity reduction as the shear rate increases. The decrease in viscosity with shear rate may result from the slippage of HPAM chain on to the GO sheets platelets. The results show that the low viscosity of the solution at a high shear rate is due to the extension of the average distance from end to end, and as a result of the disentanglement process of the polymeric chain when shearing. It can be viewed that, the shear-thinning behaviour of the hybrids depends on the viscoelastic characteristics of the polymer matrix, which may emerge from the disintegration of HPAM/GO bridged at shear fields.

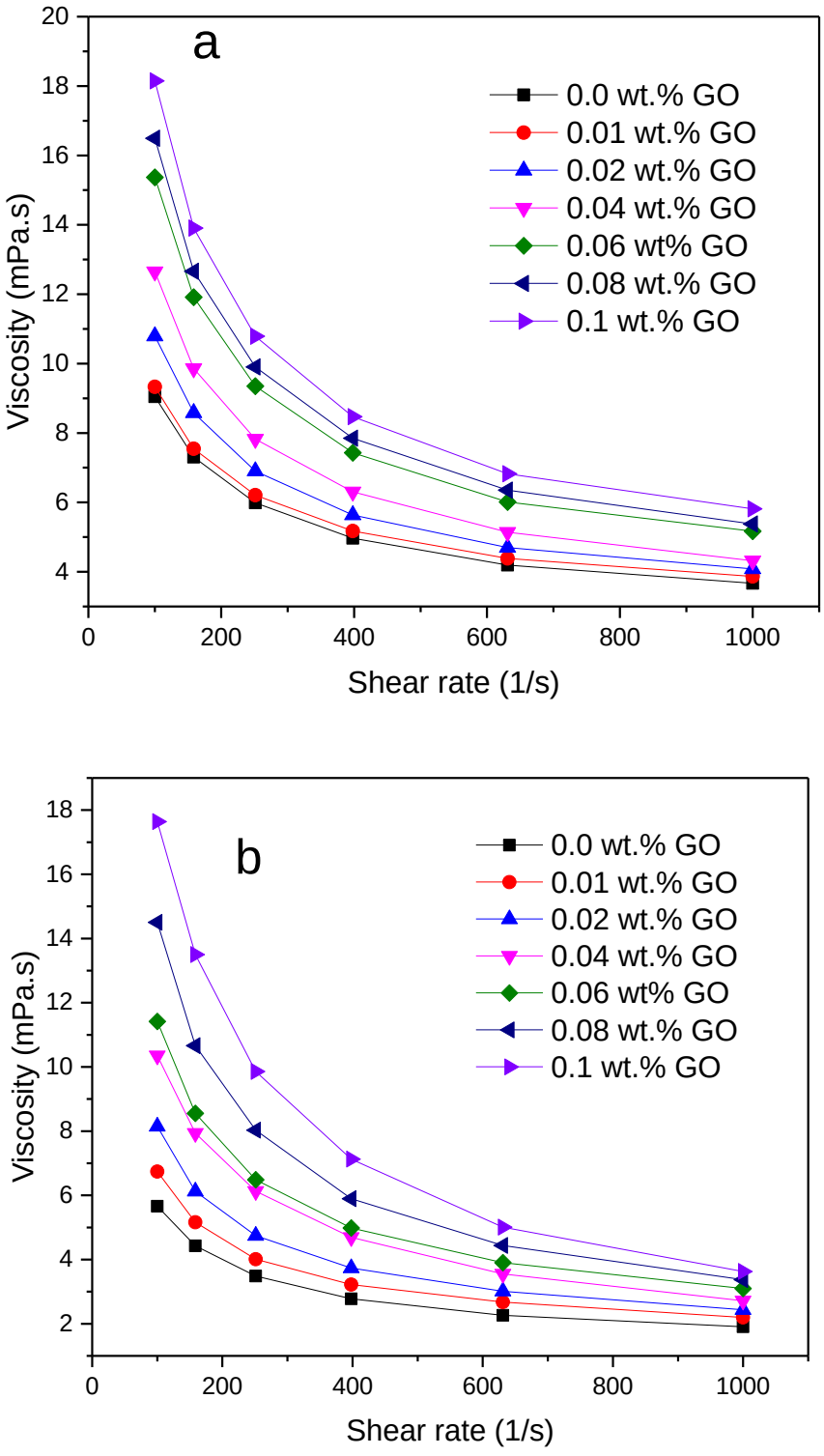

Figure 5.7. The dependence of viscosity for HPAM/GO nanocomposites on the shear rate with different GO loading ((a) T= 25 °C (b) T= 85 °C and shear rate 100-1000 s^{-1}).

On the other hand, **Fig. 5.8** shows viscosity as a function of GO concentration for both 25 °C and 85 ^{0}C respectively. It is evident that the thickness of the hybrid increases with the increase in GO concentration. This result behaves the same trends with adding HPAM concentration, which shows the rapid growth in the viscosity as the concentration was increased. It can be observed that with the addition of 0.01 wt. % GO at 85 °C, the apparent viscosity of the HPAM increases by 13 % and correspondingly increases by 47% with the addition of 0.1 wt. % GO. While at 25 °C, the HPAM viscosity increases by 5% after adding 0.01 wt. % GO and then 36 % increases were observed following the addition of 0.1 wt. % GO. The same concentration of GO was also dispersed in water, after measuring the viscosity, it was seen that with the addition of GO suspension in the water there are slight changes in the viscosity at both 25 and 85 °C respectively. These may be interpreted by the high water polarity such that when the GO nanoparticles are dispersed in water, the molecules of water covered the surface of the particles, and thus cause the suspension to retain most of its viscosity. The higher viscosity of HPAM/GO composites could arise as a result of the strengthened the polymer molecular weight, ductility, and embrittlement due to the formation of covalent linkages and electrostatic hydrogen bonding between the GO and the HPAM functional groups, leading to enhanced material stability and hence more viscosity enhancement as demonstrated by the FT-IR results. This increase in viscosity of HPAM with GO loading could be attributed to the large surface area of two-dimensional (2D) layer of the GO particle, this peculiarity leads to significant improvements of different properties such as thermal stability of the polymer matrix following the insertion of a very small content of the GO. Similar results were reported for graphene-based poly(vinyl alcohol) composite [338], and PAM/GO composites with the enhanced mechanical strength [339]. Moreover, Hu *et al.* [108] observed similar viscosity increase with the addition of SiO_2 nanoparticle in HPAM but with lower viscosity increase at an equivalent particle concentration.

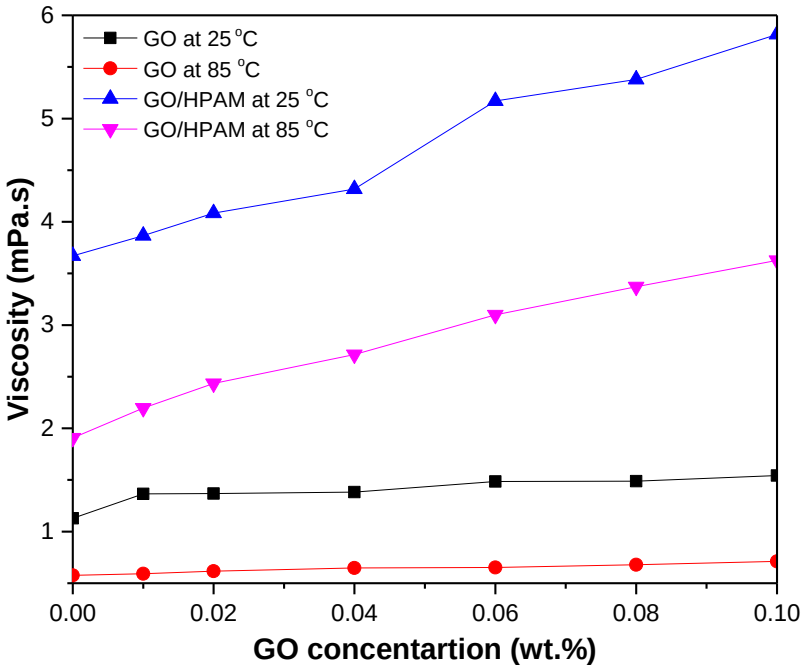

Figure 5.8. Viscosities of 0.05 wt. % HPAM with different GO loadings (T= 85 °C and 25 °C, and shear rate 1000 s^{-1}). Under the same experimental conditions, the viscosity for the neat 0.05 wt% HPAM was measured as 1.90759 mPa·s at 85 °C and 3.67055 mPa·s at 25 °C.

5.3.2.2. Effect of temperature on viscosity of HPAM/GO composites

Water-soluble polymers are susceptible to temperature. As heat is applied, the polymer chains can undergo chemical or physical changes, which can result in unwanted changes to the significant properties of the polymer, leading to polymer degradation. In many cases, molecular degradation often called thermal degradation occurs due to overheating, especially when the polymer is subjected to high temperature. The long-chain molecular component of the polymer backbone begins to separate at a high temperature which can eventually cause molecular scission. Typically at a specific temperature, the strength of the bonds deteriorates and causes the attached elements on the polymer to be detached. Because of this, the influence of GO NPs polymer stability will be investigated at a different temperature, ranging from 25 to 85 °C. **Fig. 5.9** describes the apparent viscosity as a function of temperature for the composites containing

0.05 wt. % HPAM/0.02 wt. % GO, the corresponding concentration of both pure HPAM and GO were also investigated. It shows that the viscosity of all the three samples decreased drastically with increasing temperature. This effect can also be seen when the viscosity curves of the pure HPAM and that of the HPAM/GO are compared such that a sharper in viscosity decrease is observed as the temperature rises indicating less tolerance to temperature. For a pure HPAM, the higher temperature would necessarily continue to break down intermolecular hydrophobic associations changing the HPAM backbone and then hydrolyse its acrylamide group into acrylate groups. Hence more viscosity reduction for HPAM solutions. It can also be seen in **Fig. 5.9** that, in the case of the pure GO, increasing the temperature the decrease in viscosity is not as much as pure that HPAM. This could be the reason why HPAM/GO composites acquired more viscosity than sole HPAM because of the strong thermal stability of GO, and probably due to the coupling of the network linkage between GO to HPAM.

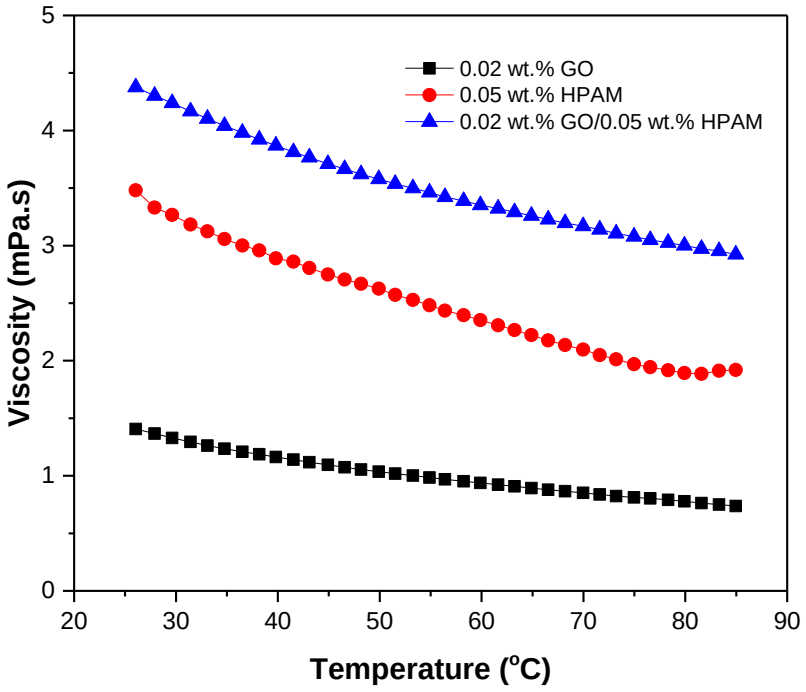

Figure 5.9. Comparison of the temperature effect on effective viscosities at a different temperature.

5.3.2.3. Long-term thermal stability of HPAM/GO composites

In industrial PF processes, the polymer is required to undergo long-term treatment under harsh conditions in the reservoir. Persistent aging of the polymer under severe circumstances would cause viscosity reduction and hence drawbacks to the oil recovery [53]. The only available viscosity will serve as a primary benchmark for the injected polymer to reach the oil in the unfavourable environment. Here, the influence of GO on aging time is investigated. 0.05 wt. % HPAM and 0.0 5wt. % HPAM/0.1 wt. %GO Composites were examined at 80 °C, as illustrated in **Fig. 5.10**. The results indicate that the pure HPAM solution displayed less tolerance to aging under harsh conditions, while the composites containing HPAM/GO exhibited a strong affinity to stay longer at the reservoir-like condition. It can be seen that the HPAM drops sharply after the five days showing less strength to withstand high temperature. Unlike pure HPAM, the viscosity of HPAM/GO composites dropped by only 4 % after the five days of aging, and 6% after 30 days, whereas, HPAM viscosity reduction were up to 35 % after five days and almost 60% decrease was observed after 30 days. Such results are quite different from what was reported in the literature [48, 63], but similar to what was observed previously by using SiO_2/HPAM hybrid [108]. Both works showed that the nanocomposites have a strong ability to work under the harsh environmental condition, and could improve the HPAM stability while aging. It is still unclear on the exact mechanism of stability reinforcement, which could be a result of inter-place among strengthened polymer molecular weight, ductility, and embrittlement due to the formation of covalent linkages and electrostatic hydrogen bonding between the GO and the HPAM functional groups, leading to enhanced material stability and hence more viscosity enhancement.

Fig. 5.11 showed a comparison between HPAM/GO prepared via direct mixing in 8wt.% NaCl, and zwitterionic-rGO-COPAM composites synthesised via *in-situ* free-radical polymerization

in the presence of APIB and FB, respectively. The viscosity of each sample was measured before and after 60 days of storage at 80 °C to understand the influence of modification on long-term temperature and salinity stability. As explained in **Section 3.3.4**, the HPAM/GO hybrid was not properly dispersed in a complex brine solution. As can be seen, the HPAM/GO hybrid in 8 wt.% NaCl has the lowest viscosity compared to zwitterionic-rGO-COPAM in APIB and FB. After 60 days of aging HPAM/GO solution lost almost 18% of its viscosity while zwitterionic-rGO-COPAM lost 1.6% in APIB and 3.5% in FB, respectively. Even though HPAM/GO showed good thermal stability compared to pure HPAM after 30 days storage as showing in **Fig. 5.11,** but the finding also showed that the modified zwitterionic-rGO-COPAM solution displayed much better salinity and temperature tolerance, this can be due to excellent dispersion stability displayed by the composite in brines which is assumed to agree with the behaviour of pseudo-spherical nanoparticles where the rGO nanosheets wrapped by the chains of zwitterionic-COPAM. At high ionic strength brines, presence of electrolyte ions can enhance the interactions of the ionic groups in the zwitterionic sulfobetaine polymers, creating the chain's expansion by providing adequate steric repulsion thereby preventing the flocculation/aggregation of the composite materials, and hence prevent much degradation at high-temperature condition [302, 304].

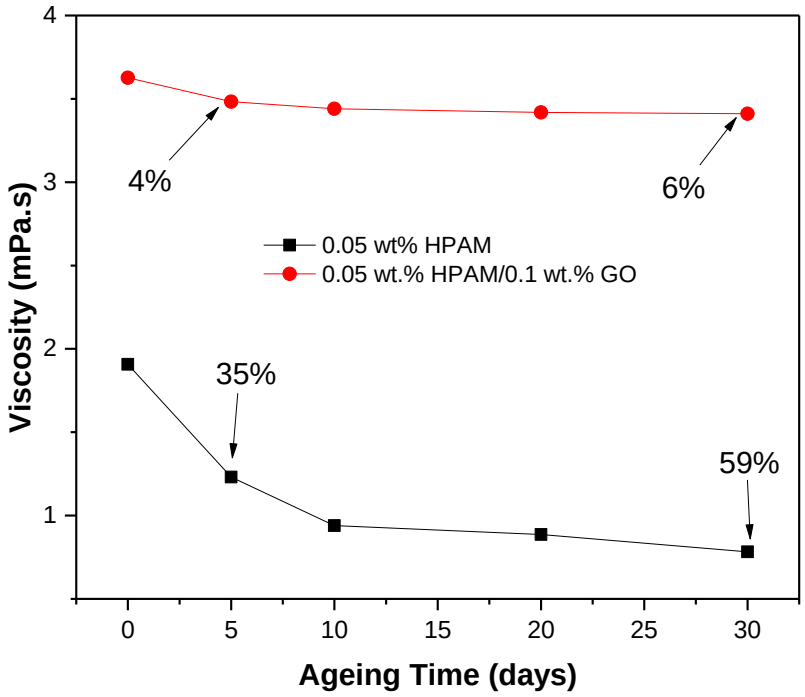

Figure 5.10. Long-term thermal stability to investigating the effect of aging time (T=85 °C and shear rate 1000 s^{-1}) for 30 days.

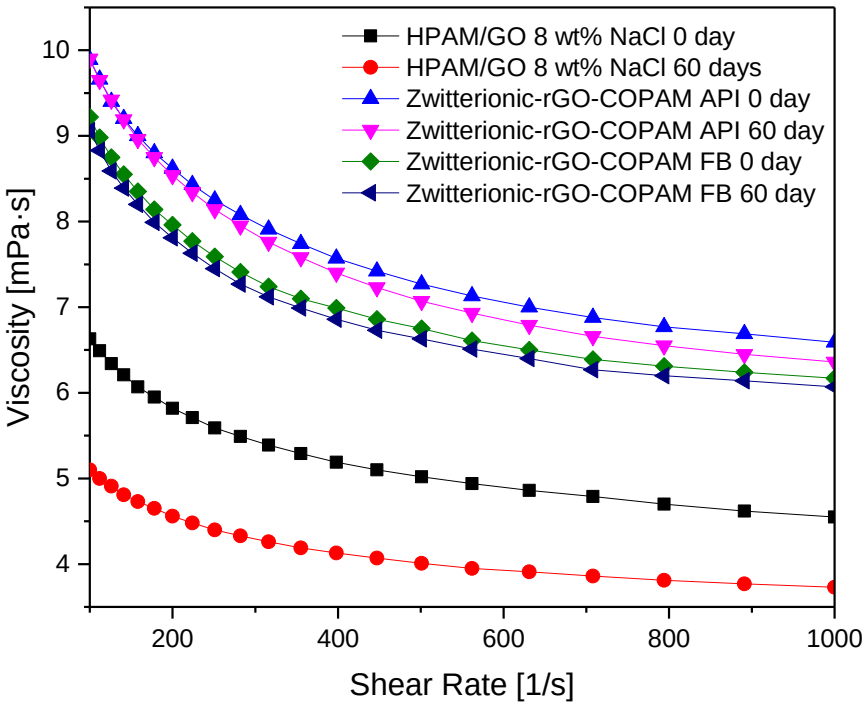

Figure 5.11. Comparison of the effect of long-term thermal stability of HPAM/GO in 8wt.% NaCl, and Zwitterionic-rGO-COPAM composites in APIB and FB, respectively. The viscosity of each sample was measured before aging and after 60 days of aging.

5.3.2.4. Effect of electrolyte on the viscosity of HPAM/GO composites

Salinity tolerance is a significant factor in deteriorating the application of polymers in EOR processes. Since HPAM is regarded as a polyelectrolyte, its viscosity and hydrodynamic size are responsive to the electrolyte concentration. In this study, the effect of electrolyte on the apparent viscosity of HPAM and the composite of HPAM/GO was investigated at 85 °C. It was observed from **Fig. 5.12** that for both HPAM and HPAM/GO composites, the addition of the NaCl from 1 to 8 wt. % decreases the viscosity, which is opposite to what was found in the literature [108, 340]. This is because when salt is added to the solution, the Na^+ can neutralise the negative charges of HPAM $-COO^-$ groups, reducing the polymer chains electrostatic repulsion, and therefore causing a conformational transition of the polymer to change from stretch to coiled or shrinkable state. Consequently, these lead to a reduction in the hydraulic radius and degree of entanglement of the polymer chain, which eventually decreases the viscosity. Furthermore, when HPAM is dissolved in water, the $-COO^-$ groups in the polymer chain repel each other causing its structure to remain extended, leading to high hydrodynamic volume to the molecular chain which increases the solution viscosity. It is, however, in a good agreement with the literature [46, 48] where a decrease in viscosity was observed at high salinities. For the HPAM solution, it can also be seen that the viscosity continued to decrease until it reached a critical salinity threshold (CST) (i.e., above which the salinity has less or no effects on the viscosity). On the other hand, the HPAM/GO composites viscosities start to increase after it reaches CST. This is because the number of molecules to be shielded by the NaCl cations were limited. In this study, the critical salinity was found to be approximately 4 wt. % as shown in **Fig. 5.12.** This observation agrees with reports by Levitt *et al.* [341] which indicated that above 3 wt. % NaCl concentration any variations in the HPAM viscosity are insignificant. Additionally, the minor change at high salt concentration results due to the corresponding increase in the polarity of the solvents, which reinforced the intermolecular

association of the hydrophobic groups, making the viscosity to remain stable. Also, in the presence of GO, the insignificant influence of salt at high concentration can arise because most molecules of NaCl are already shrunk by the high proton concentration at a low NaCl content, therefore, after interacting with GO, the change in CST value is observed. It can be concluded that addition of the salt concentration into the polymer affects the viscosity of HPAM significantly, HPAM/GO hybrid shows better capability of changing the CST, which could make the composites to be considered useful at high salt content compared to pure HPAM although the exact mechanism remains unclear.

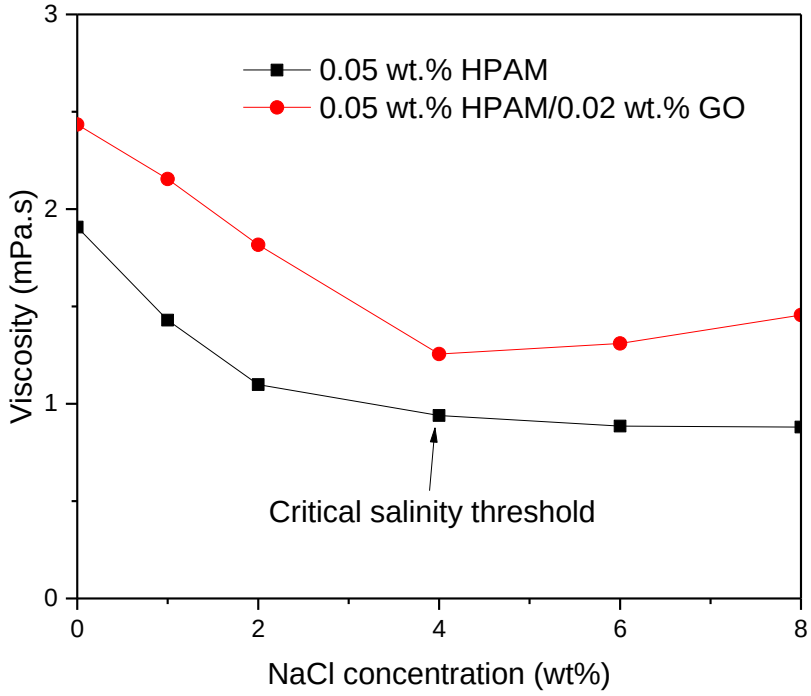

Figure 5.12. Influence of ionic strength on the average viscosity of HPAM and HPAM/GO composites (T=85 °C, shear rate 1000 s^{-1}).

5.3.2.5. Viscoelastic properties of HPAM/GO composites

The viscoelastic properties are mostly used to achieve a better perception of the deformation and molecular structure of the polymer(s), as their role in the EOR process is imperative [47, 342-344]. Oscillatory tests were conducted in this work for pure HPAM and HPAM/GO

composites. The results obtained for storage modulus (G') and loss modulus (G'') versus angular frequency (ω) are plotted. **Fig. 5.13a** shows the outcomes of dependency of loss factor on frequency (tan δ = G''/G') for both plain HPAM and the GO/HPAM nanocomposites. Precisely, with the addition of GO loading, a diminishing trend of tan δ was observed in the nanocomposite dispersions, indicating that when GO is incorporated into HPAM, it enhances elastic properties. Moreover, at the highest GO content (0.1 wt. %) the value of tan δ was further decrease, and also shows a Newtonian character at a lower angular frequency of 1–10 ($rads^{-1}$) and displaying behaviour relatively independent of frequency. The results in **Fig. 5.13b** shows a gradual increase in both elastic and loss modulus with the increasing angular frequency with the addition of GO, and continue to become more elastically dominant at the highest GO concentration. Such trends are similar to what was reported in the literature [345]; some work also showed that GO improved the elasticity of polyacrylamide for dye adsorption capacity [346, 347]. At low-frequency region, the plateau of G' indicates a more obvious nature of an elastic material demonstrating solid-like character and gel network behaviour of nanofillers in polymer composites and colloidal gels [348-350]. Moreover, the results indicate that compared to the pure HPAM, the composites solutions possesses long-term relaxing time as a result of sufficient links and network structure between macromolecules. It can be concluded that the hybrids of HPAM/GO exhibit better viscoelastic strength. These indicate that the hybrid could have more ability to improve oil recovery under harsh reservoir conditions. The samples showed less frequency dependence behaviour in both G' and G'' indicating more solid-like than liquid-like viscoelastic nature particularly at high GO concentration. Therefore, the material with high GO loading displayed good behaviour, suggesting that the GO reduced the relaxation of the HPAM macromolecular chain, and hence the effect of the liberation of the solution became less obvious, for example, at 0.1 wt. % GO, the G' increases by 59% and G" increases by 63% respectively as compared to that of pure HPAM. This viscoelastic behaviour

is similar to what was found in the studies about LDH/PAM and clay/polymer nanocomposites [345, 351].

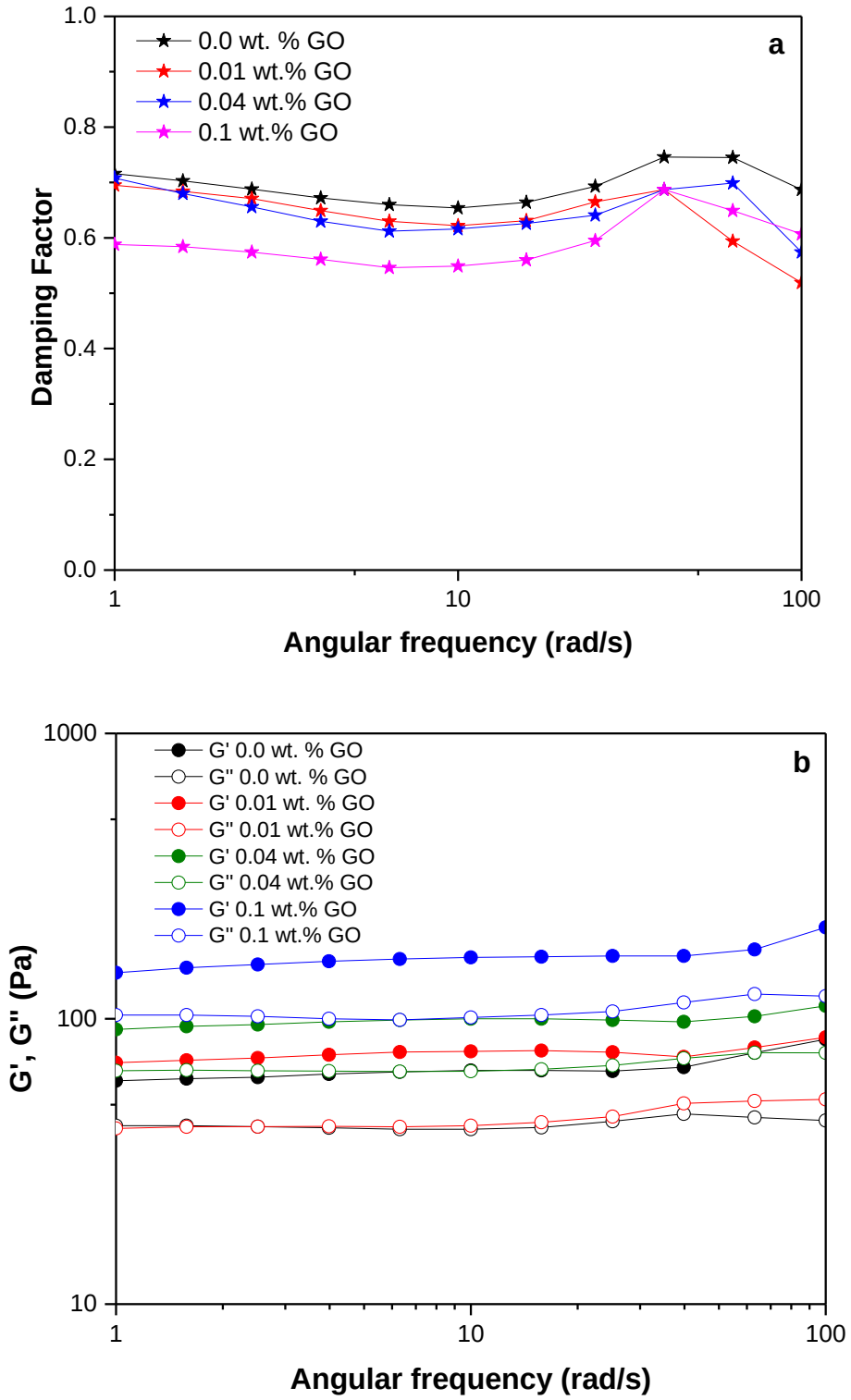

Figure 5.13. Damping factor and (b) Storage modulus (G') and loss modulus (G") for HPAM and HPAM with different GO concentrations as a function of angular frequency (ω).

5.3.3. Effect of CQDs on the viscosity reduction of HPAM solution

5.3.3.1. Effect of CQDs concentrations on viscosity reduction

Different CQDs concentrations were used to investigate the influence of the CQDs on the viscosity reduction of the PAM polymer. Both the HPAM and the HPAM/CQDs composites showed shear-thinning behaviours with an increase in shear rate, as shown in **Fig. 5.14**. **Fig. 15a** shows 1000 s^{-1} shear viscosity as a function of the CQDs concentration for 25 and 85 °C, respectively. It can be seen that with the addition of the CQDs, the effective viscosities decreased significantly at both temperatures. The higher the CQDs concentration, the lower was the effective viscosity. A nearly linear relationship in viscosity reduction was observed at 25 °C, corresponding to a change from 3.3 to 57.2% as the CQDs concentration was increased from 0.05 to 0.5 wt.%. As expected, a much lower effective viscosity is found at 85 °C. However, the effect of the addition of the CQDs is more pronounced, especially at the CQDs concentrations < 0.4 wt.%. A sharp decrease in the effective viscosity by 27.7% was observed at 0.05 wt. % and the reduction continued, reaching 85.2% at 0.5 wt. % loading of the CQDs. Similar viscosity reduction was reported by Yasufumi *et al.* [352] for some PAM/silica nanoparticle suspensions. Such reduction was ascribed to the PAM adsorption on the surface of silica particles, resulting in a decrease in the amount of polymer in the mixture, and hence a reduction of the effective viscosity. We found that such a reduction is possible due to the dissociation of the HPAM. This is discussed in detail in **Section 3.3.2.2**. In contrast, aqueous solutions of typical HPAMs show Newtonian behaviour, with their effective viscosities slightly increasing with an increase in the concentration of CQDs. This is consistent with conventional thought. It is expected that when the CQDs are dispersed in water, water molecules are likely bonded onto the surface of the particles due to its high polarity (hydroxyl O–H, carbonyl C=O and carboxylic –CO–OH groups), thereby causing the suspension viscosity to remain unchanged.

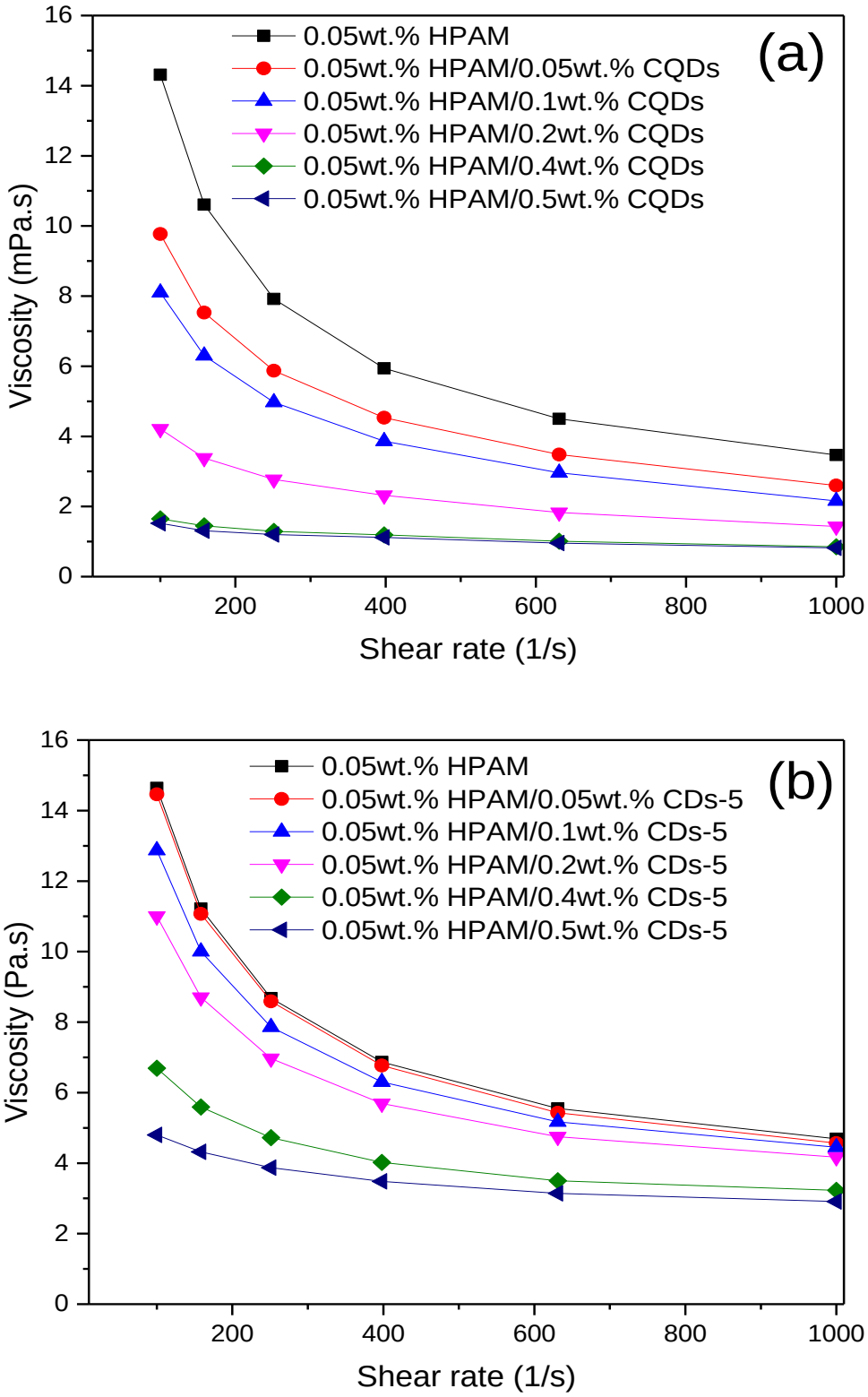

Figure 5.14. The dependence of viscosity for HPAM/CQDs composite on shear rate with different loadings of the CQDs (a) T= 85 °C (b) T= 25 °C (shear rate 100-1000 s^{-1}).

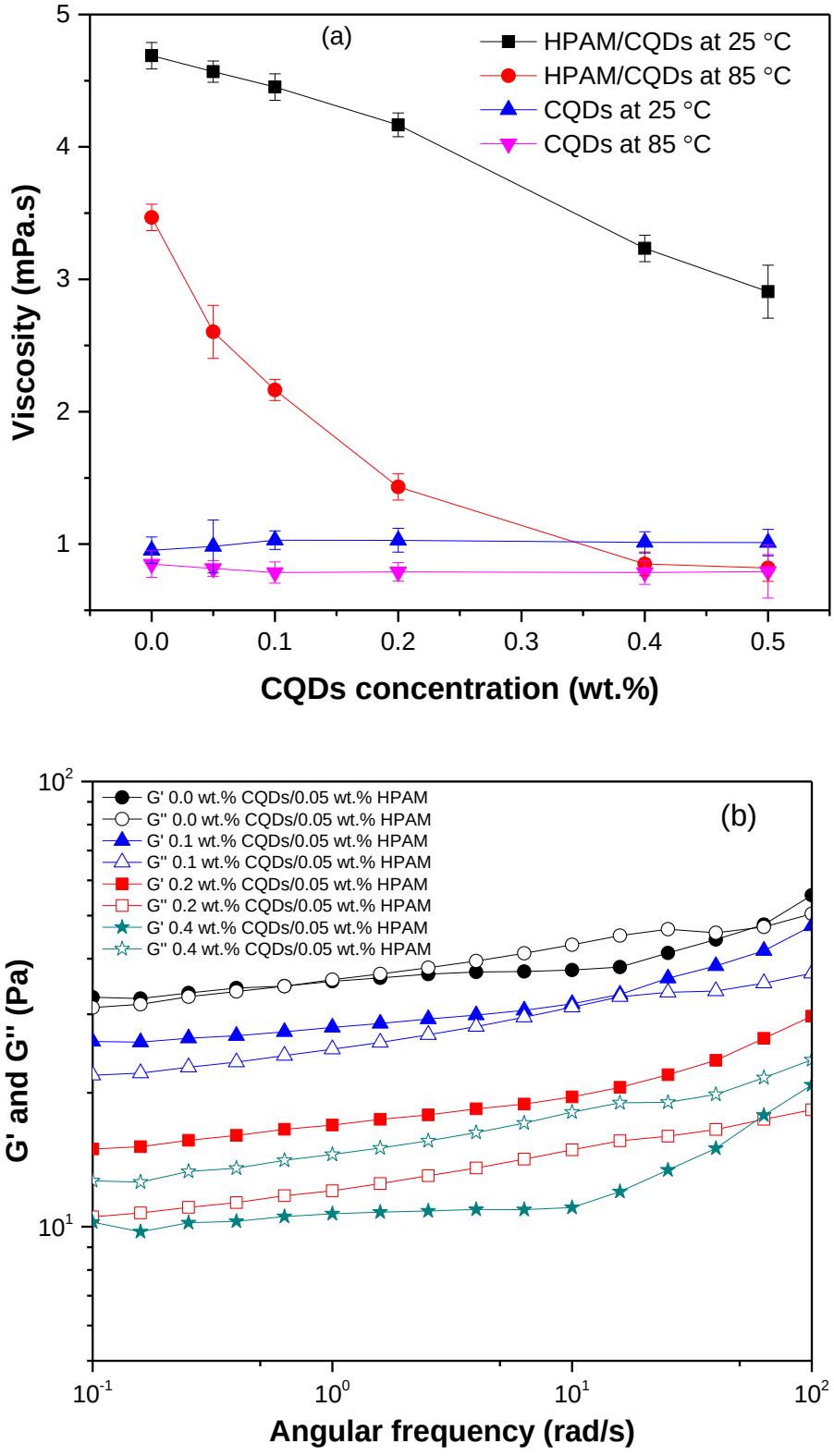

Figure 5.15. (a) Viscosities of 0.05 wt.% HPAM with different concentrations of the CQDs, T= 85 and 25 °C, shear rate 1000 s^{-1}), (b) Storage modulus (G') and loss modulus (G").

The effect of the addition of the CQDs on the viscoelastic properties of the HPAM was examined by a linear oscillatory frequency sweep test. The results obtained for the storage modulus (G') and the loss modulus (G'') are plotted against angular frequency (ω) (**Fig. 15b**). The results showed a decrease in both G' and G'' with the addition of the CQDs into the composite. This indicates that the composite material becomes less elastically dominant.

As shown in **Fig. 5.16,** the damping factor (tan δ) increases with the CQDs addition in the solution. Generally, a value of tan $\delta > 0.1$ accompanied by its comparatively small dependence on frequency is agreed to be the symptomatic character of a so-called weakened gel solution [353]. Here, it was observed that when the concentration of the CQDs was increased, the value of tan δ also increased. Therefore, it can be deduced that the addition of the CQDs into the PAM matrix formed elastically weaker material compared to the pure HPAM. Furthermore, compared to the aqueous suspension of the HPAM/CQDs material, pure HPAM displayed less frequency dependence behaviour for both G' and G'', showing a good tendency of transition from liquid-like to solid-like viscoelastic state. The complex viscosity μ^* of the HPAM and the HPAM/CQDs composite obeys similar changing trends as observed for (G') and (G''), as a function of (ω) (**Fig. 5.17a)**. The complex viscosity (μ^*) of the HPAM/CQDs composite (containing 0.05 wt. % CQDs) was lower than that of the pure HPAM. This could not be explained by the Einstein–Batchelor law for the viscosity of a particle suspension [219]. As the concentration of the CQDs in the composite was increased to 0.5 wt.%, the μ^* continued to decrease. It was found that the value of μ^* for the HPAM/CQDs composite was lower than that of the pure HPAM solution.

To support the above findings, the continuous relaxation spectra of the solutions were also calculated from the results of G' and G''. The TRIOS software available with the HDR-2 rheometer was used to calculate the continuous relaxation spectra, using the analysed G' and G" data, respectively. The continuous relaxation time spectrum can be extracted by fitting the

following model in terms of either oscillation [G' (w), G"(w)] or relaxation [G(t)] data. The theoretical basis for the relaxation expressions is given in Eqns. 5.4 to 5.7. **Fig. 5.17b** shows the continuous relaxation spectra of the HPAM solution and that of the HPAM/CQDs composite, as a function of the relaxation time. In comparison to the relaxation behaviour of the pure HPAM solution, the relaxation time of the HPAM/CQDs composite was shorter. The solutions containing higher concentrations of the CQDs (0.2 and 0.4 wt. %) show a significant effect on the continuous relaxation spectrum of the HPAM solution, especially at a short time scale. Therefore, it can be deduced that the HPAM solution possesses long-term relaxation time as a result of sufficient links and associations between its macromolecules. This suggests that the mechanism behind the reduced viscosity behaviour of the HPAM/CQDs composites is bounded by the relaxation effect of the samples.

$$d\ ln\ \tau = \frac{d\tau}{\tau}, g(\tau) = H(ln\ \tau) \tag{5.4}$$

$$G(t) = G_e + \int_{-\infty}^{+\infty} H\ (ln\ \tau) e^{-t/x} d\ ln\ \tau \tag{5.5}$$

$$G' = \int_{-\infty}^{+\infty} H\ (ln\ \tau) \frac{\omega^2 \tau^2}{1 + \omega^2 \tau^2} d\ ln\ \tau \tag{5.6}$$

$$G'' = \int_{-\infty}^{+\infty} H\ (ln\ \tau) \frac{\omega \tau}{1 + \omega^2 \tau^2} d\ ln\ \tau \tag{5.7}$$

In Eqns. 5.4 to 5.7, H is the continues relaxation spectrum, τ is the relaxation time and G(t) is the relaxation data.

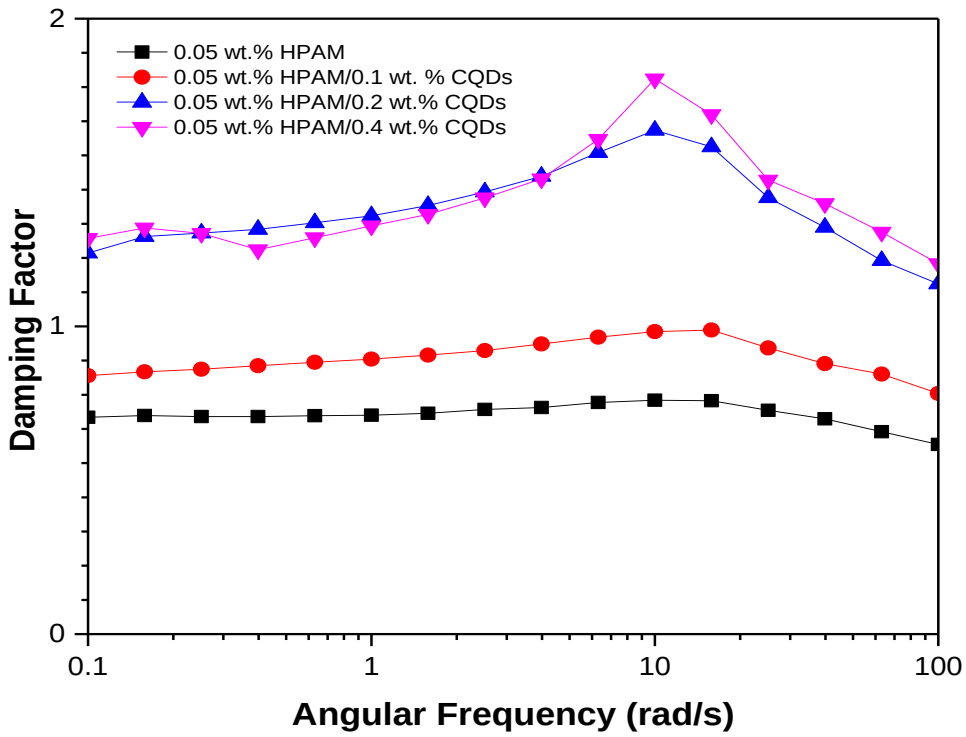

Figure 5.16. Plots of the damping factor of HPAM and HPAM, with different concentrations of the CQDs, as a function of angular frequency (ω).

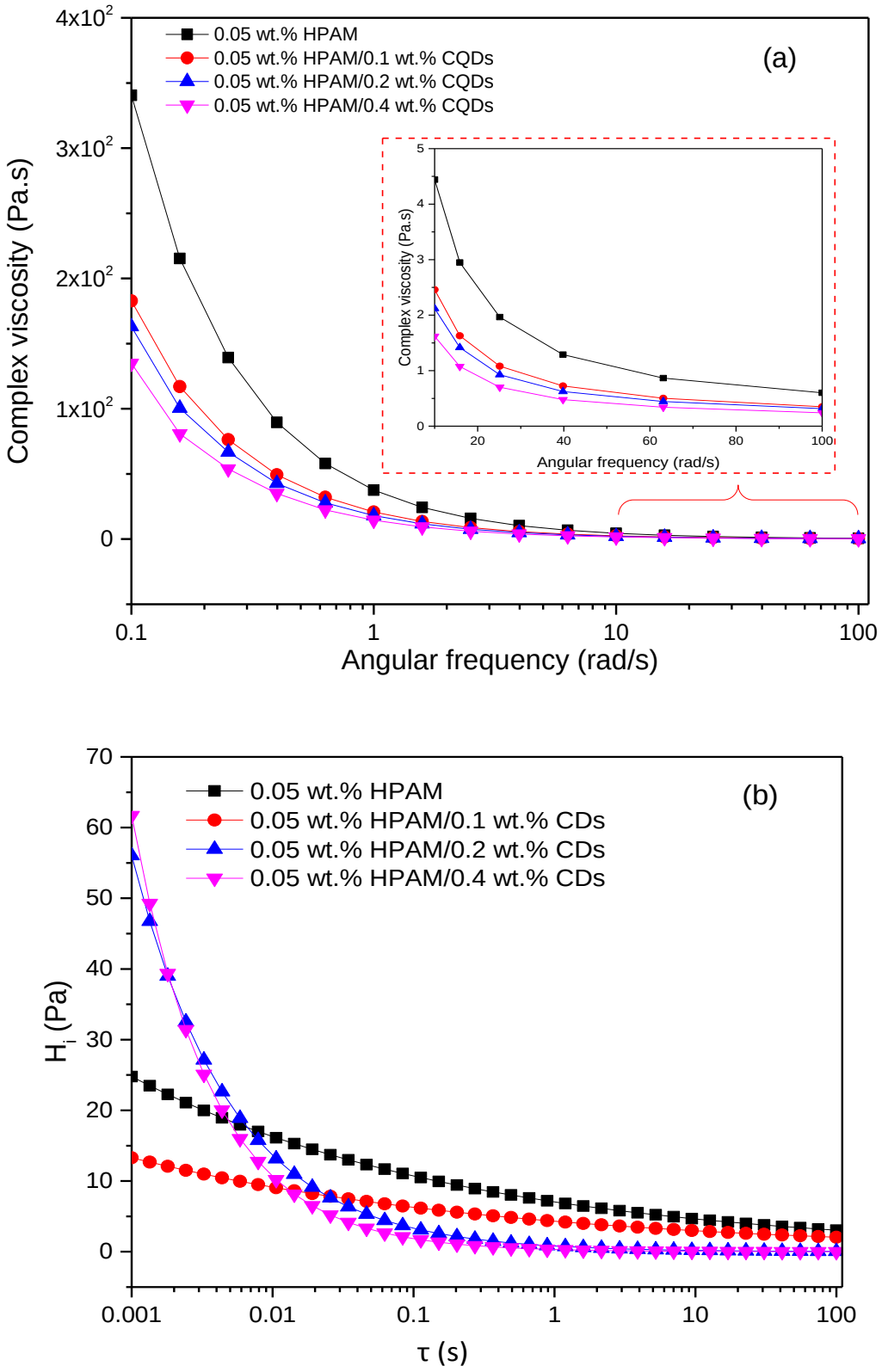

Figure 5.17. (a) Complex viscosity for HPAM and HPAM/CQDs composites, with different concentrations of the CQDs, as a function of angular frequency (b), Continues relaxation spectra of HPAM, and HPAM/CQDs composites, as a function of relaxation time.

$$k = Ae^{\frac{-Ea}{RT}} \quad \ldots\ldots\ldots\ldots\ldots\ldots (5.8)$$

$$\tau^{1/2} = \tau_0^{1/2} + \mu_\infty^{1/2}\gamma^{1/2} \quad \ldots\ldots\ldots\ldots\ldots\ldots (5.9)$$

In Eqns. 5.8 and 5.9, k is the rate constant, T is the absolute temperature, A is the pre-exponential factor, E_a is the flow activation energy, R is the universal gas constant, τ_0 is the yield stress, μ_∞ is the suspension/solution viscosity at an infinite shear rate, and $\dot{\gamma}$ is the shear rate.

The rheological results were given a kinetic treatment using the flow Arrhenius relationship (Eqn. 5.8) and the Casson-Asbeck equation (Eqn. 5.9) [354]. These relationships are widely applied to polymeric systems [355]. Thus, values were obtained for the yield point/stress (YP), the flow activation energy (FAE), and the infinite shear viscosity (ISV) for the CQDs, the HPAM, and the HPAM/CQDs composite, as shown in **Table 5.1.** The plot of ln(viscosity) vs 1/T, used in modeling the flow kinetics of HPAM, CQDs, and HPAM/CQDs is shown in **Fig. 5.18.** Differences in the yield point, the infinite shear viscosity, and the activation energy of flow can be seen. The yield stress is sensitive to shear history, as the corresponding un-sheared materials have yield values more than the sheared ones. The lower value of yield stress obtained for the HPAM/CQDs composite shows that the material has higher shear sensitivity in comparison to the corresponding HPAM material. This effect arises as a result of the rapid movement and subsequent breakdown of structural linkages that priory exists between the CQDs and the HPAM materials. According to **Table 5.1**, the HPAM/CQDs composite has the highest value of flow activation energy of 745 kJ/mol compared to the pure HPAM, indicating a high sensitivity to the influence of temperature during any potential applications.

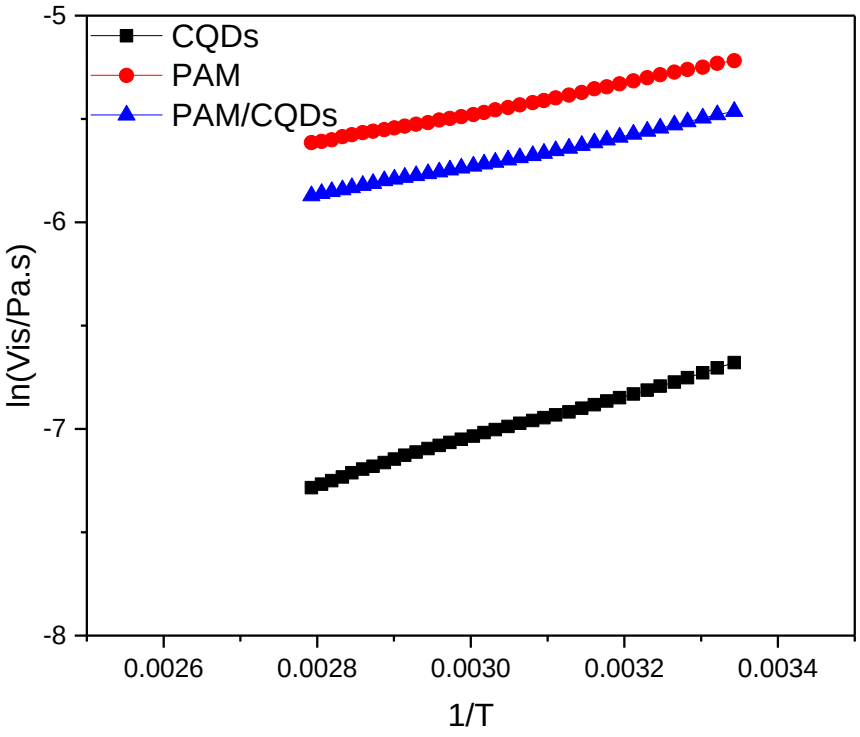

Figure 5.18. A plot of ln(Viscosity) vs 1/T, used in modeling the flow kinetics of HPAM, CQDs, and HPAM/CQDs.

Table 5.1 Data obtained from kinetic treatment of rheological plots, at 25 °C, on the basis of the flow Arrhenius equation and the Casson-Asbeck relationship.

Solutions	YP (Pa)	FAE (kJ/mol)	ISV (mPa s)
CQDs	$9.7x10^{-3}$	1100	0.47
HPAM	0.59	733	3.4
HPAM/CQDs	0.58	745	9.2

5.3.3.2. Potential mechanisms of the viscosity reduction for HPAM/CQDs composites

Clearly, the reduction of effective polymer viscosity by nanoparticle addition cannot be explained by conventional theories such as the Einstein-Batchelor relationship, which always states that the effective viscosity shall increase with an increase in particle concentrations. [356]. To account for this, two main mechanisms, including the free volume effect and particle agglomeration, have been proposed in the previous literature [207, 208, 215, 357, 358]. For the first mechanism, the viscosity reduction occurs in the polymer composites when the polymer

was entangled and the nanoparticles were spherical [9]. Mackay *et al.* [219] used the criteria of excluded free-volume around the nanoparticles to explain the decrease in the viscosity of nanoparticle-filled polymer melts. They stated that the free volume was governed by the glass transition temperature (T_g) of the materials, and the increase of T_g indicated the reduction of the free volume [359]. As shown in **Fig. 3.22b**, based on the finding, the inclusion of the CQDs did not significantly result in the change of T_g of the HPAM, and no direct relationship between the slight change in T_g and the reduction of viscosity of the HPAM/CQDs composites was observed. Thus, the concept of an increase in sample free volume, induced by the nanoparticles, cannot be considered as a plausible mechanism for the viscosity reduction of the HPAM/CQDs composites.

For the second mechanism, it was reported that particle stability and aggregation could result in changes in the melt viscosity of polymer-nanocomposites during rheological measurements [360]. The results on the behaviour of HPAM and HPAM/CQDs composites from this study were analysed using a Turbiscan to investigate their stabilities (**Fig. 3.24b**). The data showed no sedimentation for all the range of concentrations of the CQDs that were studied. Therefore, this excludes the influence of the aggregation of the CQDs and their stability as a possible reason for the observed viscosity reduction.

Clearly, the existing mechanisms cannot explain our current experimental results. It is proposed that the viscosity reduction is due to the degradation of HPAM polymer by the deamination in the repeating unit of the polymer, leading to the formation of polyacrylic acid (PAA) and ammonia (NH_3) (**Fig. 5.19**). When the CQDs were included in the composites, a large number of oxygen-containing groups in the CQDs attack the HPAM material through nucleophilic reaction, thereby forcing it to release $–NH_2$ groups from the HPAM repeating unit, leading to the formation of PAA and NH_3. These trends continue and deteriorate the polymer backbone, resulting in macromolecular degradation and the subsequent reduction of the HPAM's ductility

and embrittlement, hence the loss of viscosity. There are two proposed mechanistic pathways for the deamination and the formation of a covalent bond between the HPAM and the CQDs materials, as shown in **Fig. 5.19**. In the case of the proposed mechanism (**i**), a nucleophilic attack on the carbonyl group in the CQDs is achieved via water molecules. This is then followed by the nucleophilic addition of the CQDs onto the backbone of the HPAM, leading to the formation of an unstable transition state. This then leads to the release of NH_3 molecules. However, according to the mechanism (**ii**), the first step involves the elimination of NH_3 molecules from the HPAM repeating unit before the addition of the CQDs.

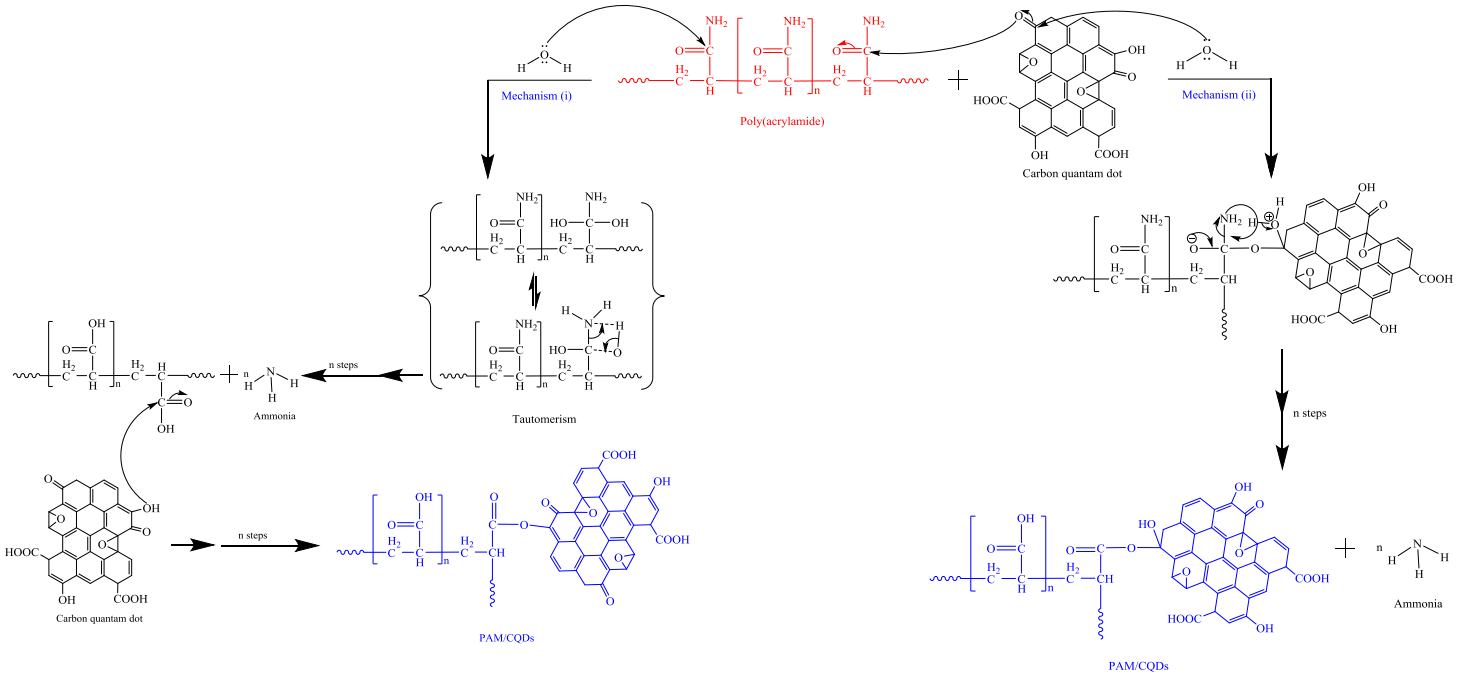

Figure 5.19. Schematic illustration of proposed mechanistic pathways leading to the reduction of viscosity in the HPAM/CQDs composites.

Additionally, the CQDs could make the HPAM transform from a stretch-state to a coil-state (**Fig. 5.20**). Since HPAM is regarded as a polyelectrolyte, its viscosity and hydrodynamic size are responsive to the presence or addition of electrolytic functionalities. However, CQDs have been reported as cationic [361-363], and due to their electrolyte nature, when added to the

HPAM solution, they can cause protonation of the HPAM's carboxylate groups into carboxyl groups ($–COO^-$ to –COOH). This then causes an increase in the acidity of the medium, being consistent with the experimental result shown in **Fig. 3.18.** This eventually causes a conformational transition of the polymer, changing from a stretch-conformation into a coiled-conformation (or shrinkable state). This then consequently leads to the reduction in the hydraulic radius and degree of entanglement of the polymer chain, eventually decreasing its viscosity.

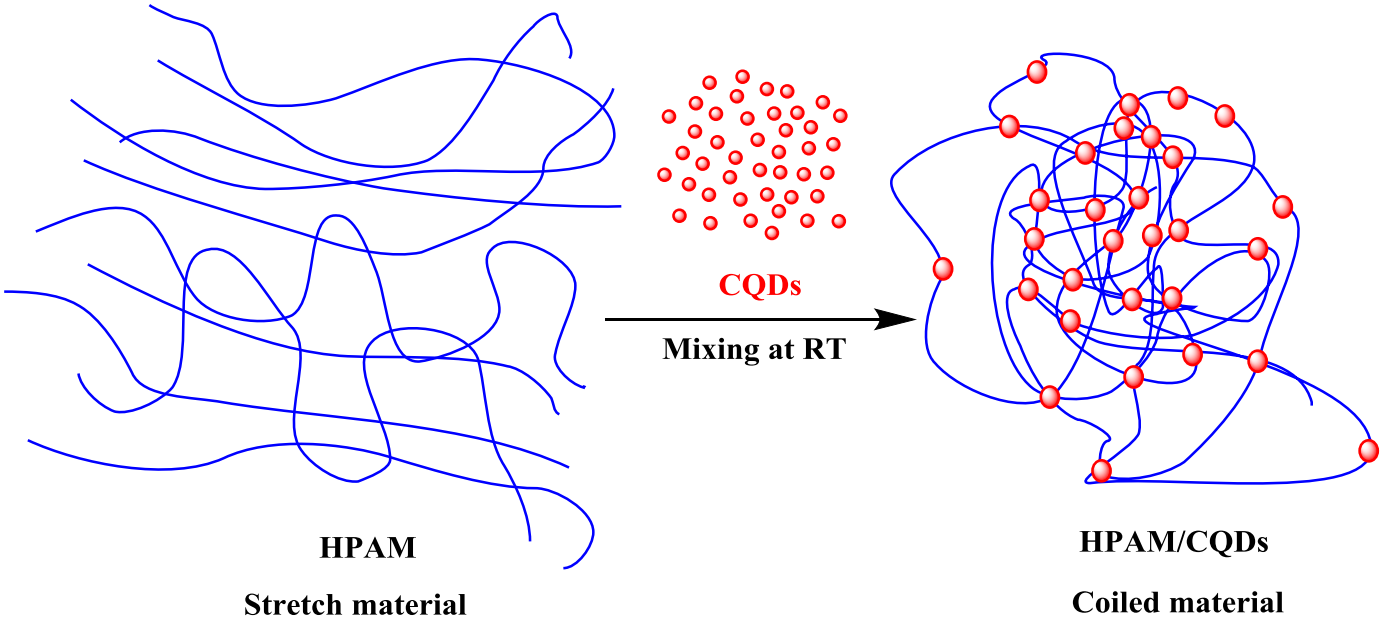

Figure 5.20. Schematic showing how the HPAM can change from a stretch-state into a coil-state.

5.3.4. Effect of surface modified SiO_2 on polymer viscosity

As shown in **Table 5.2**, when SiO_2 is added to the HPAM solution, the viscosity of the composite overruled that of pure HPAM**,** showing behaviour similar to what was reported in the literature [108]. Which is due to the hydrogen bond formation between the silanol function of silica and the amide group of HPAM [108]. The measurement was conducted under the effect of 8 wt.% NaCl, however, as previously described, when SiO_2/polymer solution is

prepared in high ionic strength of brine, it leads to agglomeration that causes a large number of molecules on the surface of the particle to create aggregates of NPs. It is also stated that a lack of good SiO_2 dispersion was likely due to their preferred face-to-face stacking in agglomerated/aggregated tactoids, which leads to sedimentation problems in a harsh environment. These reduced reduces its stability when aged at high HT-HS conditions for a longer period of time.

Notwithstanding, for EOR applications, the stability and viscosity of these nanocomposites have to be examined under temperature and high saline conditions. When HPAM is dissolved in water, their carbonyl groups repel one another, resulting in the polymer structure to extent increasing the molecular chain hydrodynamic volume to which consequently improves the solution viscosity. Whereas, the presence of excessive salinity in the water deteriorates the polymer performance in PF-EOR. The viscosity and hydrodynamic size of polyelectrolyte polymers, such as HPAM, are highly responsive to electrolyte concentration, for example, the ionic shielding on the amide group ($–CO–NH_2$) reduces the polymer chain repulsion. This causes the polymeric chains to collapse and consequently reduces the molecular coil size and hence lower down the viscosity [334, 335]. At extreme salt content with divalent ions such as Mg^{2+} and Ca^{2+}, the polymer starts to precipitate and become coiled from the elongated state as shown in **Fig. 5.21**.

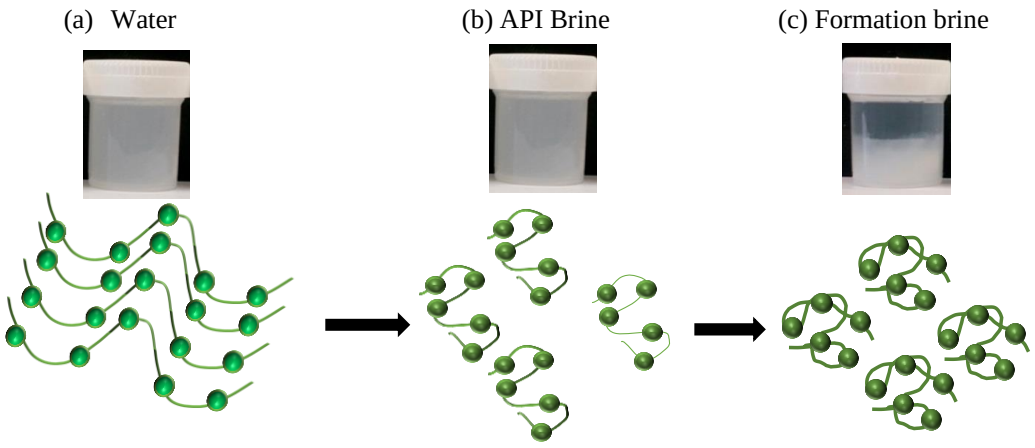

Figure 5.21. Schematic illustration of the transformation from stretch to coiled or shrinkable state in the presence of (a) pure water (b) API brine and (c) Formation brine (details provided in **Table 5.2**).

Table 5.2. Variation of the amount of salt

Salt species	Formation brine (FB) (%)	API Brine (AB) (%)
$BaCl_2$	0.001	/
$NaHCO_4$	0.005	/
Na_2SO_4	0.006	/
$MgCl_2.6H_2O$	1.3	/
$CaCl_2.2H_2O$	5.0	2
NaCl	7.5	8

In this section, the effect of electrolyte on the APV of NP-free COPAM, SiO_2/COPAM, and M_SiO_2/COPAM was investigated at 85 °C. **Fig. 5.22** presented the result of the influence of polymer type on the viscosity with brine solution, and **Table 5.3** illustrates the effect of API brine and formation brine (FB) on the viscosity decrease (percentage). The results show that the addition of salt decreases the viscosity of all the three samples, this finding is similar to that reported in the literature [46, 48] where a reduction in viscosity was seen at high salinities. It can be said that when salt is introduced into the polymer, the cationic charge can neutralise the ionic charge of the polymer $–CO–O^-$ groups, decreasing the electrostatic repulsions of the polymer chains to create a conformational transition from stretch to shrinkable or coiled state [364]. This causing the entanglement and hydrodynamic radius of the polymers to dissociate

which ultimately reduces the viscosity. M_SiO_2/COPAM exhibits much stronger salt tolerance with higher viscosity compared to NP-free COPAM and SiO_2/COPAM in the presence of both API and FB. This is because the M_SiO_2/COPAM has an additional positively charged active sites on the surface that can generate electrostatic repulsion between the polymer cationic groups.

Table 5.3. Percentage of the remaining viscosity in the presence of FB and API brine

Sample	COPAM	SiO_2/COPAM	M_SiO_2/COPAM
Pure	100 %	100 %	100 %
Formation brine	66%	72%	91%
API brine	42%	60%	80%

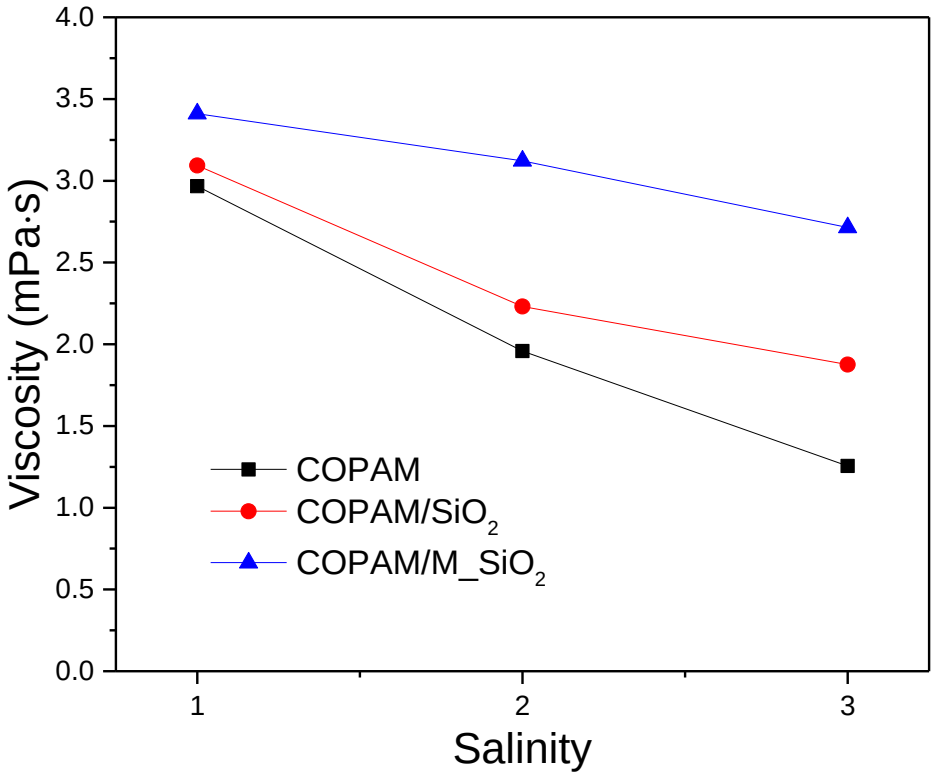

Figure 5.22. Influence of salinity (1= No salt, 2 = API brine 3 = Formation brine) on the viscosity of NP-free COPAM, SiO_2/COPAM, and M_SiO_2/COPAM to investigate the effect of polymer type.

5.3.4.1. Effect of long-term thermal stability on COPAM, COPAM/SiO_2 and COPAM/M_SiO_2 viscosity

Long-term aging under prolonged temperature results in detrimental effects in the PF-EOR, as it inhibits the overall performance of polymers by causing continuous viscosity reduction [53, 108]. Therefore, the effect of aging under HT-HS condition (80 °C and FB) has been investigated to highlight the influence of different polymers as shown in **Fig. 5.23a**. In the first instance, the results show a slight increase in the viscosity after one day of aging in both SiO_2/COPAM and M_SiO_2/COPAM. This finding could be possibly due to the hydrolysis of the amide side chain of the polymer to its carboxylate group [108]; this shows that some parts of the polymer carboxylate group could enhance the hydrodynamic volume. After 10 days aging M_SiO_2/COPAM displayed better heat endurance capacity with 7.5% viscosity reduction, NP-free COPAM, and SiO_2/COPAM with 41 and 28% reduction in viscosity, respectively. The viscosity of M_SiO_2/COPAM dropped slightly until 30 days of aging while in NP-free COPAM and SiO_2/COPAM a sharp decrease was continued to be seen within the first month of aging. However, after 30 days of high-temperature storage, the viscosity of the NP-free PAM continues to decline day by day. This is due to the effect of bridging anionic carboxylic groups of the polymer with divalent ions (Ca^{2+} and Mg^{2+}) and also polymer partial precipitation at a high degree of hydrolysis [365]. Overall, M_SiO_2/COPAM exhibits much stronger heat tolerance and stable viscosity compared to NP-free COPAM and SiO_2/COPAM over the whole period of aging, for instance, at 30 days COPAM and SiO_2/COPAM lost almost 51% and 41% of viscosity while M_SiO_2/COPAM lost only 9.5%. After 90 days of aging, the amount of viscosity lost is 10.5% for M_SiO_2/COPAM and 78.7% and 45% viscosity reduction were observed for NP-free COPAM and SiO_2/COPAM. **Fig. 5.23b** shows consistent trends after calculating the relative viscosity of NP-free COPAM, SiO_2COPAM and M_SiO_2/COPAM, respectively.

The findings prove that the introduction of SiO_2 NPs to acrylamide based polymers noticeably enhances the polymer thermal stability. Further improvement of the thermal properties was observed on M_SiO_2/COPAM. The mechanism of thermal degradation and viscosity reduction of the polymer can be explained by two structural changes in the polymer molecule, both of which are caused by extreme temperature. First, carboxyl groups form by hydrolysing the amide chain, and second, the polymer backbone scission lowers the viscosity [366]. When the carboxylic group content increases, the polymer molecules exhibit greater expansion state because of repulsion between negative charge groups, and at the same time promote the polymer molecules interaction by creating a hydrogen bond betwixt the carboxyl and amide groups. Intermolecular and intramolecular interactions occur between the polymer molecules, this is an interaction between different functional groups of the polymers which may lead to the formation of larger molecules and consequently increases the viscosity. Further interaction between functional groups of the same polymer may cause the polymer molecules to shrink and hence lowers the viscosity [367-369]. Many recent studies reported that introducing NPs in the polymer solutions could produce crosslinking networks of individual polymers and produce a solid hybrid system via the formation of hydrolysable covalent bonds and hydrogen bonds [63, 108].

The proposed mechanism showing in **Fig. 5.24**, shows a tremendous improvement in the polymer NPs interaction with the M_SiO_2 compared to pure SiO_2. This is because the M_SiO_2 surface has more functional groups, higher amino group reactivity, presence of more hydrogen in the amino groups and at the same time promote the formation of new electrostatic chemistry that occurs when the additional proton (H^+) from the amino group of M_SiO_2 react with the polymer ionic charges, reinforced the ability of polymer molecules to be adsorbed onto the M_SiO_2 NPs surface by ionic linkage as illustrated in **Fig. 5.24**. This has also led to the improved thermal stability of polymer backbone, polymer molecules, and polymer

nanocomposites network. These results show that M_SiO_2/COPAM show how M_SiO_2 could play a role in strengthened polymer molecular weight, ductility, and embrittlement, and greater efficiency to perform under harsh reservoir conditions.

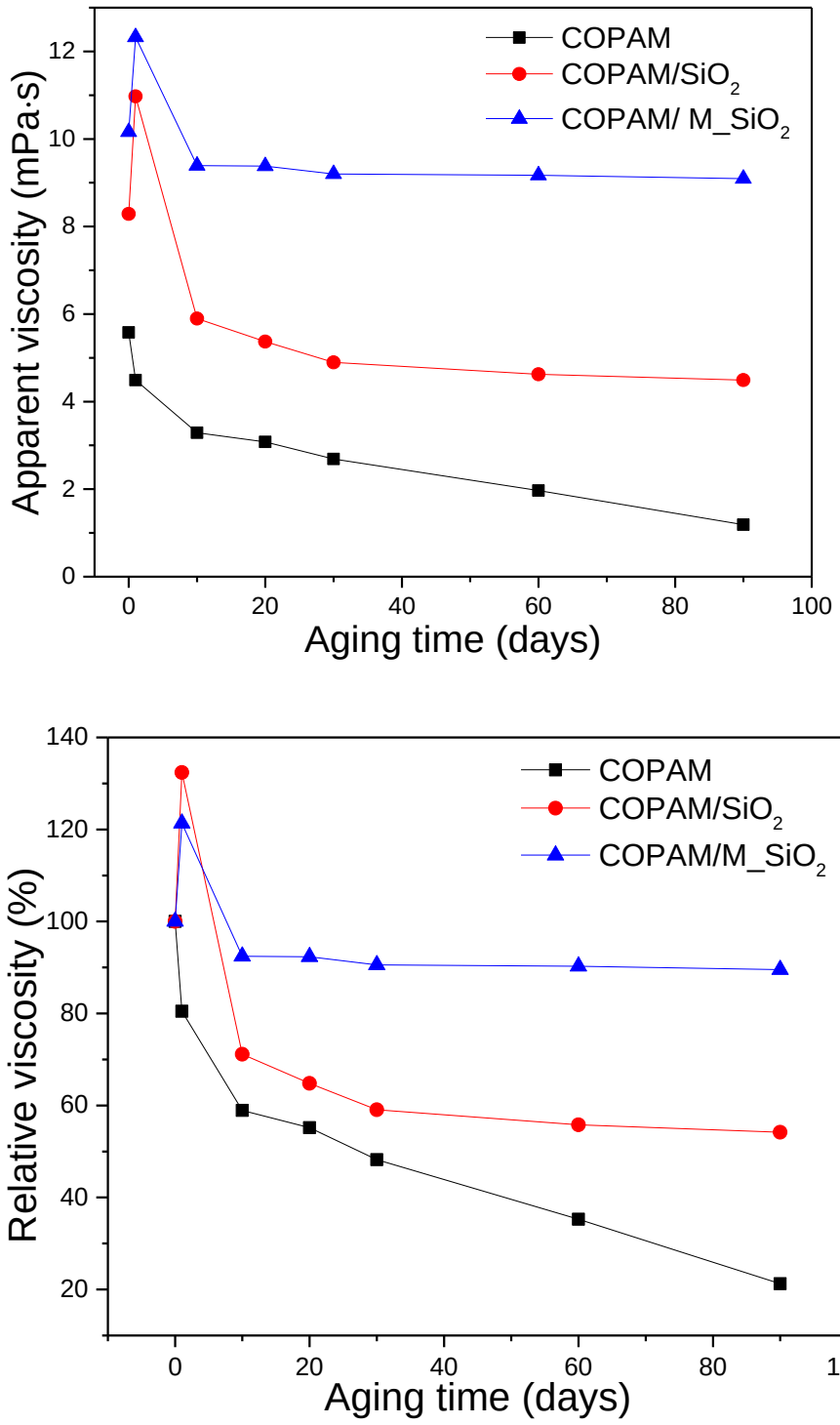

Figure 5.23. (a) Apparent viscosity (b) Relative viscosity as a function of aging the samples to investigate the effect of Long-term thermal stability after 90 days at 85 °C.

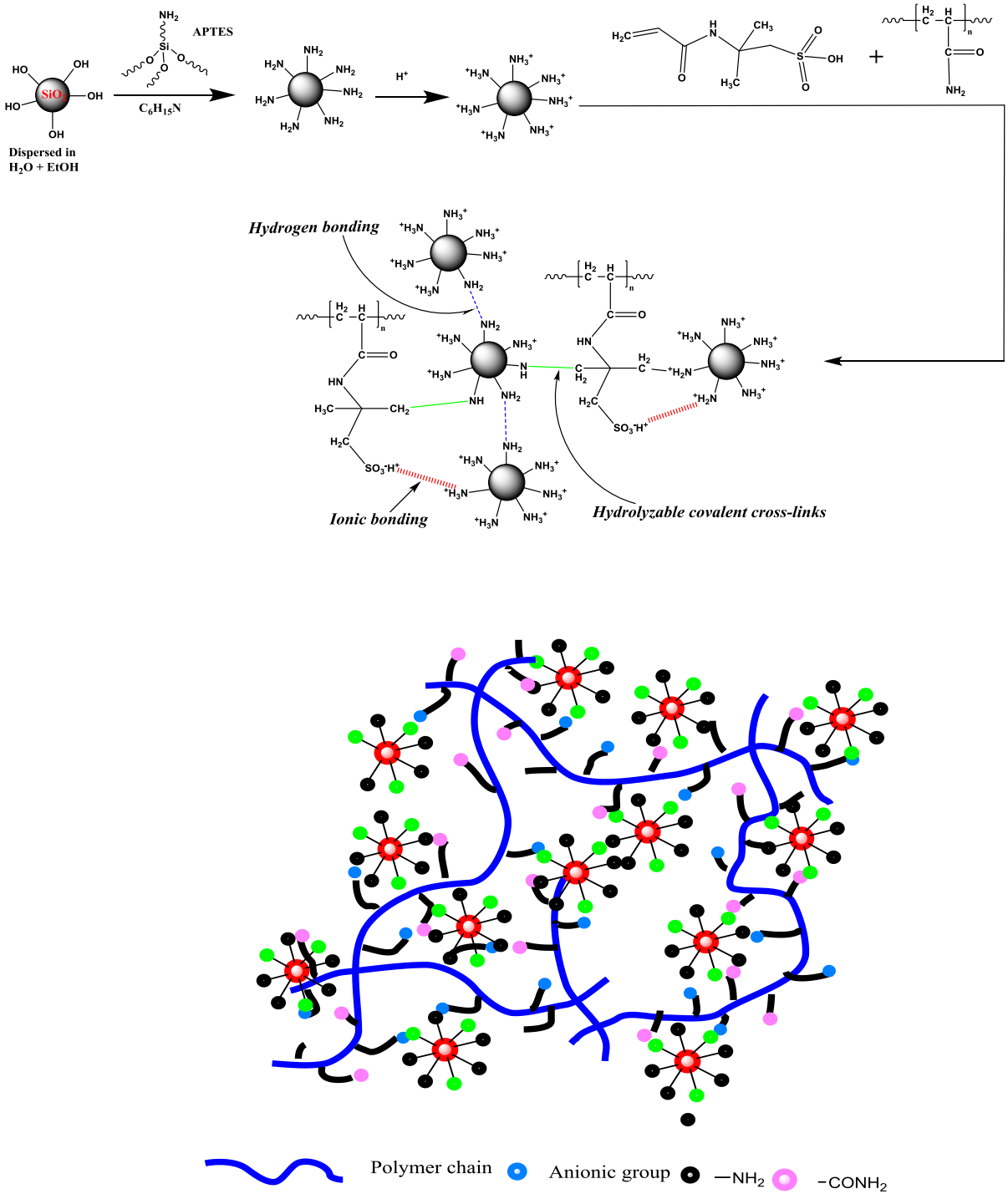

Figure 5.24. Schematic representation of preparing M_SiO_2/COPAM and potential interactions between polymer molecules and M_SiO_2 particles (top). Cartoons illustration of the composites network system of M_SiO_2/COPAM (bottom).

5.3.4.2. Effect of COPAM, COPAM/SiO_2 and COPAM/M_SiO_2 on viscoelastic properties

In the PF process, it is important to examine the viscoelastic behaviour of the fluid to have a reasonable interpretation of the deformation characteristics of the polymer structure [47, 342-344]. Here, we have investigated the oscillatory behaviour of the polymers by measuring the changes in their loss modulus (G'') and storage modulus (G') as a function of angular frequency (ω). The results in **Fig. 5.25a** shows an increase in both G' and G'' with an increasing ω in all the three samples, however, at low ω the plateau of G' and G'' indicating the obvious solid-like behaviour of an elastic material and gel network nature of nanofillers in polymer composites and colloidal gels. Precisely, it could be noted that M_SiO_2/COPAM samples show higher G' and G'' values exhibiting a better viscoelastic strength compared to SiO_2/COPAM and NP-free COPAM samples, respectively. This proves that the M_SiO_2 can reduce the relaxation of the polymer chain and change the effect of polymer liberation to become less obvious. **Fig. 5.25b** shows the effect of complex viscosity (μ^*) of the composites against ω; the results obey similar changing trends as observed for G' and G''. The μ^* of NP-free COPAM and SiO_2/COPAM is lower than that of M_SiO_2/COPAM. This finding shows the potential of using amino M_SiO_2 as a potential agent in improving the polymer performance in EOR.

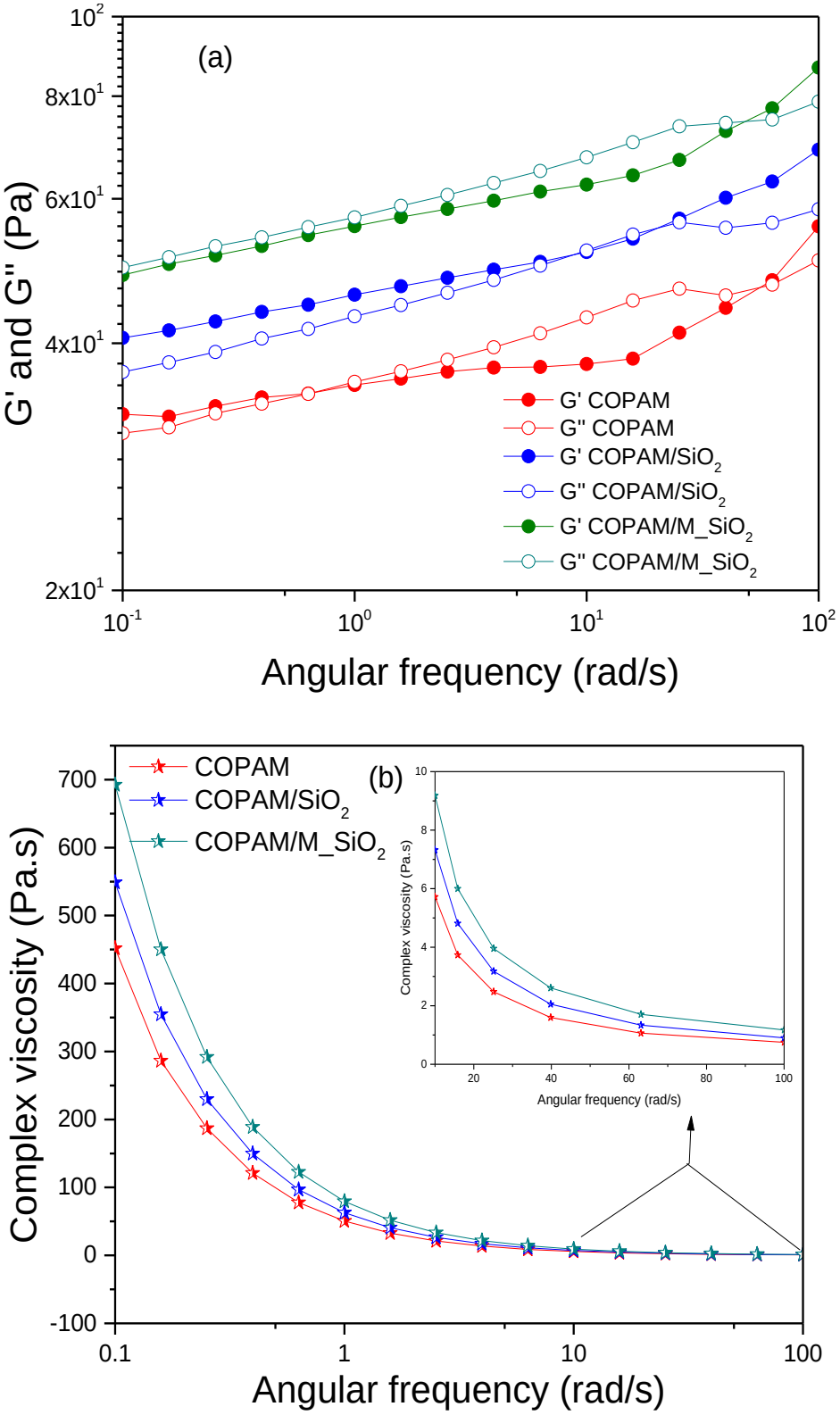

Figure 5.25. (a) Storage modulus (G') and loss modulus (G'') and (b) complex viscosity of NP-free COPAM, a SiO_2/COPAM, and M_SiO_2/COPAM versus angular frequency (ω).

5.4. Influence of MWCNTs on the rheological properties of synthesized polymers

In this section, the influence of MWCNTs on the rheological properties (viscosity and viscoelasticity) of the five polymers synthesis in **Section 3.4** was investigated. The outcome could be used to select the appropriate polymer for enhanced oil recovery analysis at API brine and alkaline pH conditions, respectively. **Fig. 5.7a** demonstrates the viscosity of 1000 ppm co/ter-polymers as a function of shear rate at 85 °C. The results indicated that after the incorporation of hydrophobic chains in pure acrylamide structure (Sample A), the viscosity of the modified samples improved, and this enhancement of viscosity would be ascribed to the intermolecular hydrophobic association of polymeric chains. However, the hydrophobic chains combined to reduce self-exposure in the aqueous medium resulting in an increase of apparent viscosity, similar to what Hussein and co-workers [34] observed in which the addition of a hydrophobic fraction improved the polymer structure and increased the viscosity.

Fig. 5.27b demonstrates the viscosity of polymer/MWCNTs at alkaline pH. Reduced value of viscosity for all polymers at pH = 11 with increasing shear rate was observed because of a high hydrolysis degree in the presence of OH- ions and these results are consistent with some early studies [333, 370, 371]. However, the decrease in viscosity was lower in samples B and D (polymer containing negative group) than the other samples. This is due to enhanced intermolecular interaction between the polymer containing negative groups and the MWCNTs in comparison to other functional groups due to the presence of sulfate group as confirmed by FTIR analysis. The interaction was found to be stronger, specifically at a higher shear rate which produced greater internal friction. Several investigations [230, 372] also reported high-temperature resistance by the polymer containing sulfate and sulfonates groups.

Fig. 5.27c highlights the influence of salinity on the viscosity of polymer/MWCNTs at 85 °C. Correspondingly, the polymer containing negative groups (sample B) showed better salinity resistance, while the cationic polymer (sample C) showed less salt tolerance. The reason is that the positive group in the polymer is compatible with monovalent and divalent ions (Na^{+}, $Mg^{2+,}$ and Ca^{2+}), which results in mutual repulsion and shields the amide negative groups in the co/ter-polymer chemical structure and therefore causes a reduction in viscosity. As shown in **Fig. 5.26**, different approaches such as covalent linking, complexation through the interactions, and wrapping of NH-π, CH-π, π-π were proposed using polymers and functionalized MWCNTs composites [291-295]. These multi-point interactions strengthen the polymer chains resulting in enhanced internal friction between the polymer chains and the molecules of the neighbouring solvents, thus improving the solution viscosity.

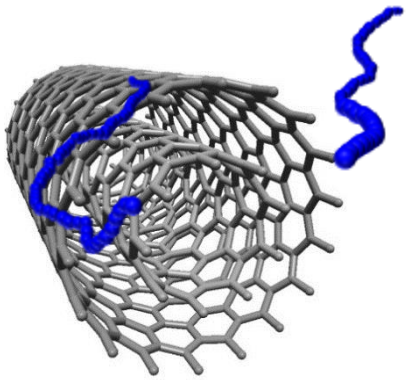

Figure 5.26. Schematic illustration for different sequence for MWCNTs functionalization via noncovalent polymer wrapping or π-stacking.

Viscoelastic behaviour of the two best samples was investigated before the EOR experiment. Both storage (G′) and loss (G″) moduli increased after the addition of MWCNTs, as shown in **Fig. 5.28**. Four different reaction mechanisms are accountable for the changes in viscoelastic properties of the polymers [373], these are (a) MWCNTs/polymer network where the polymer

shape could be entangled or adsorbed on the nanotube, (b) MWCNT-MWCNT network due to overlap of two nanotubes, (c) temporary entanglements of polymer network to form polymer matrix and (d) MWCNTs bridging by polymer. The crossover of modulus (where G′ > G″) represent characteristic relaxation times, which is in agreement with the time for a MWCNTs to circulate a distance similar to its length [374]. At low MWCNTs concentration, the relaxation could be identified across a section but it tended to increase with increasing concentrations because of the slowing of nanotube diffusion and ability of the solution to act in similarity to an elastic solid [374].

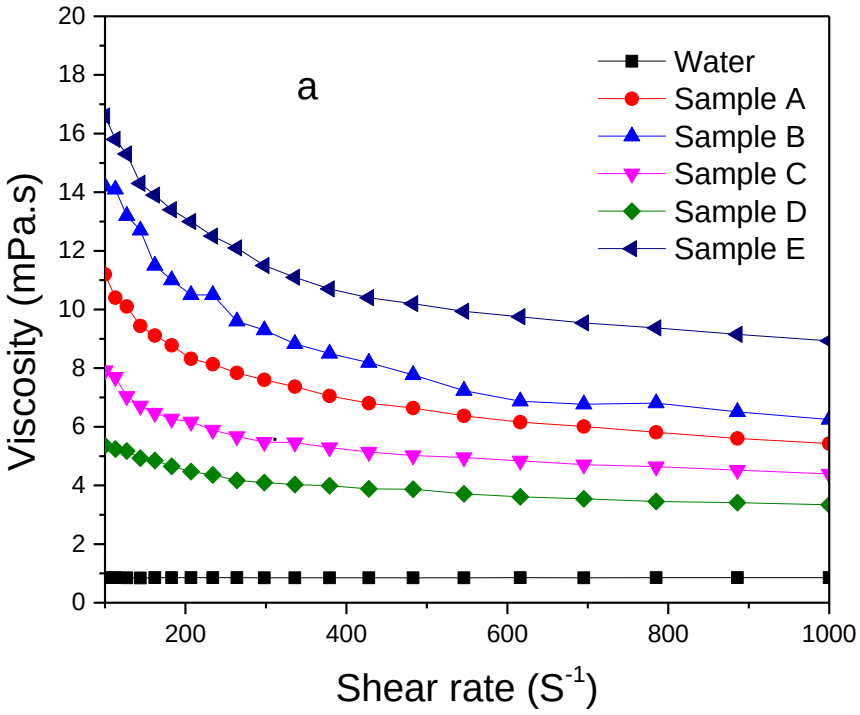

Figure 5.27. Dependent of viscosity on shear rate for (a) pure co/ter-polymers (1000 ppm) in water, (b) MWCNTs (1000ppm/1000ppm) in pH-11 and (c) polymers/MWCNTs (1000ppm/1000ppm) in API Brine, all measurement was conducted at 85 °C and shear rate 100-1000 S^{-1}.

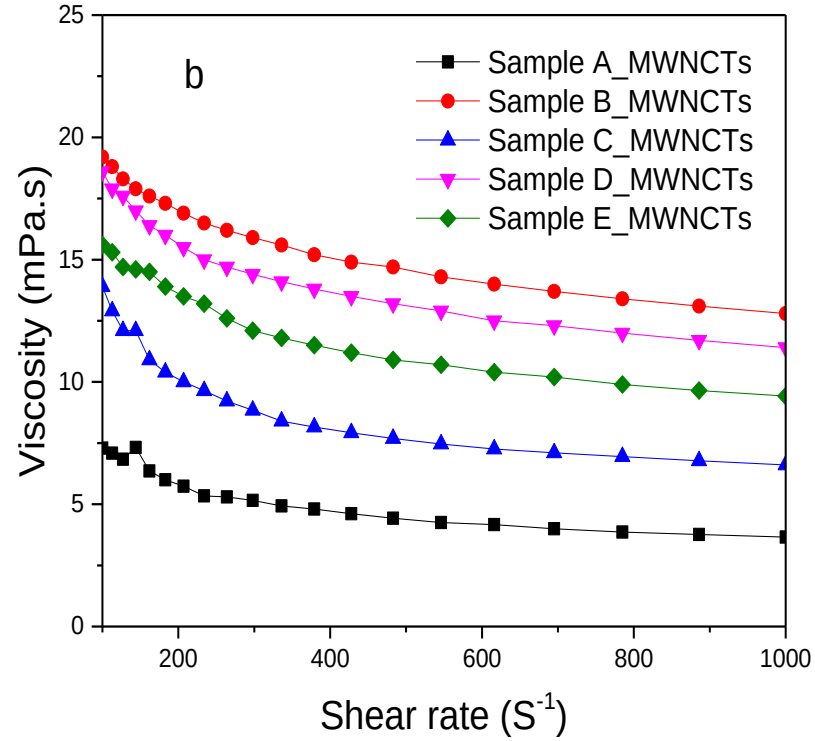

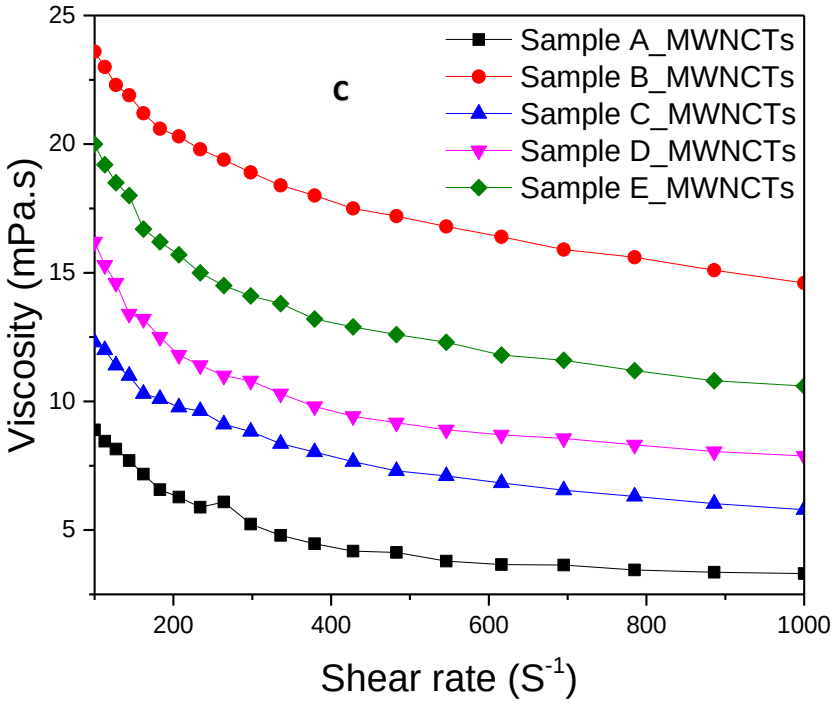

Figure 5.17: Continues

(a)

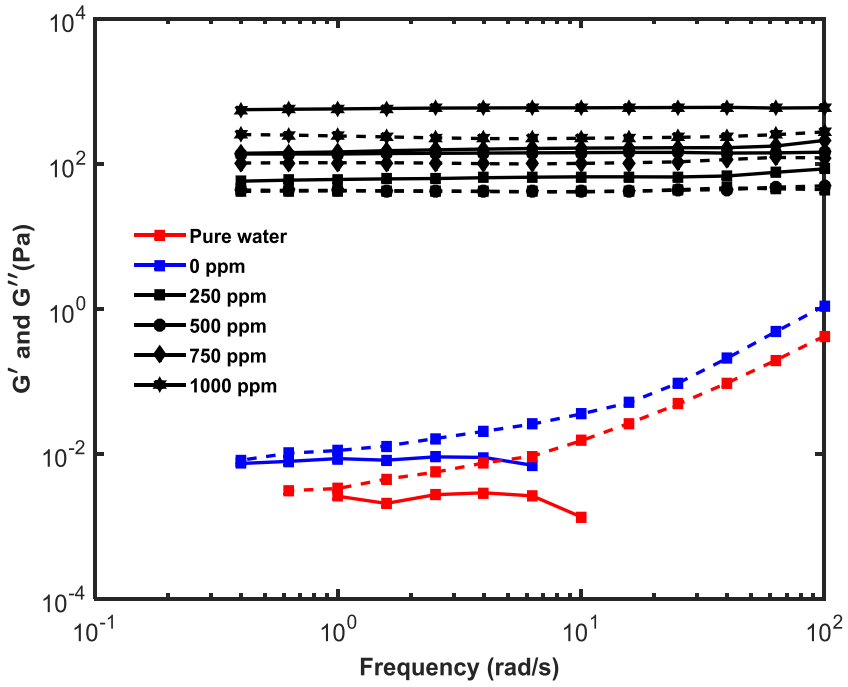

(b)

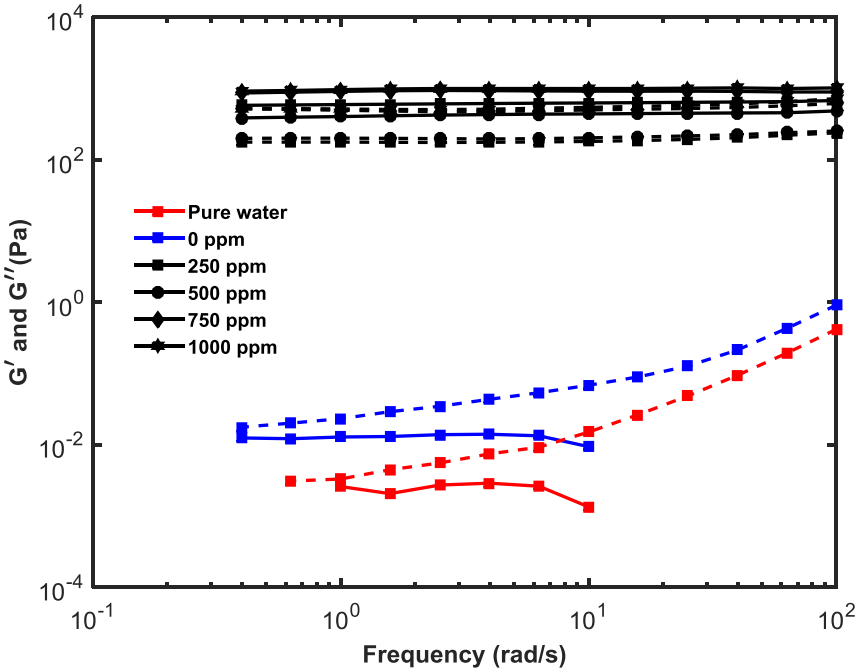

Figure 5.28. (a) Viscoelastic properties of polyampholytic terpolymer (sample D) with different MWCNTs concentrations at alkali solution (b) viscoelastic values of a copolymer containing negative sulfonate group (sample B) with different MWCNTs concentrations at API.

5.5. Chapter Summary

Understanding the mobility control between the oil and displacing fluid is paramount in EOR, which is closely related to rheological properties such as viscosity of the fluid especially at different experimental conditions. PAM, a commonly used polymer for EOR suffer common viscosity lost at high temperature and high salinity conditions. In this Chapter, the influence of the materials prepared in Chapters 3 and 4 on the rheological properties was investigated at different conditions, such as the NPs concentrations, effect temperatures, long-term thermal stability, and electrolyte effect were investigated.

The addition of different GO concentrations increased the viscosity of the suspensions significantly, and the effect is more significant. Addition of 0.1 wt. % of GO increased the viscosity by 47 % and 36 % respectively at 85^{o}C and 25 °C. The addition of GO increased long-term thermal stability significantly due to the formation of covalent linkages and electrostatic hydrogen bonding between the GO and the HPAM functional groups. After aging for 30 days at 80 °C, the viscosity of the composite's solution decreased very slightly while a 59 % reduction was observed for pure HPAM solution. Increasing the GO content increases both storage and loss modulus the HPAM solution, making them favourable for EOR applications. Though the solution viscosity decreased with an increase in NaCl concentration for both HPAM and HPAM/GO composites, the later improve the CST value showing promising performance at high salt content. Despite the improvement in long-term thermal stability and salinity tolerance of the HPAM/GO composite, the zwitterion-rGO-COPAM composite showed much better thermal and brine stability after aging. These are because at high ionic strength brines, the presence of electrolyte ions can enhance the interactions of the ionic groups in the zwitterionic sulfobetaine polymers, creating the chain's expansion by providing adequate steric repulsion thereby preventing the flocculation/aggregation of the zwitterion-rGO-COPAM and hence better stability.

Contrarily, the addition of CQDs decreased the viscosity of HPAM suspensions. Both the storage and the loss moduli are decreased with an increase in the concentration of CQDs. The flow activation energy of HPAM/CQDs composite is 745 kJ/mol, while that of pure HPAM solution is 733 kJ/mol. This indicates that the hybrid would be more sensitive to temperature, during any potential applications. The results showed that the mechanism behind the reduced viscosity behaviour of the HPAM/CQDs composites arises from the relaxation effect of the samples, with the value of the relaxation parameter shorter in the HPAM/CQDs composites, compared to that in the pure HPAM. Two possible schemes are proposed for the decreased viscosity phenomenon, which is: 1- formation of carboxylic acid groups on the HPAM backbone, giving rise to a reaction with hydroxyl groups on the CQDs and the subsequent formation of ester bonds; 2- breakage of long macromolecular chains in the HPAM into smaller chains, with the CQDs being able to protonate the carboxylate groups in the HPAM ($–COO^-$ to –COOH), which make it more acidic and eventually cause a conformational transition of the polymer to change from a stretch-state into a coiled-state.

To alleviate the problems associated with traditional SiO_2, a novel modification approach has been proposed. The M_SiO_2/COPAM showed higher viscosity and possessed excellent temperature tolerance and long-term stability than pure SiO_2/COPAM and NP-free COPAM solution at extreme salinity conditions. While SiO_2/COPAM and NP-free COPAM had 45 and 78% viscosity reduction respectively after 90 days of aging, only a 10% reduction was observed in M_SiO_2/COPAM. This improved viscosity and stability of M_SiO_2/COPAM were due to the incorporation of amino functional groups on the surface of the SiO_2 NPs, which result in the formation of electrostatic attraction that reinforced the bonding of PAM molecules with NPs.

The addition of MWCNTs into five different synthesised polymers showed improved viscosity and viscoelasticity of the polymer dispersions. The polyampholytic ter-polymer and polyelectrolyte copolymer containing negative sulfonate groups showed better enhancement in viscosity of MWCNTs/polymer dispersions in alkali and API brine solution respectively. MWCNTs were found to improve the viscosity of synthesised COPAM more than the commercial HPAM. This is due to the multi-point interactions that strengthen the polymer chains resulting in enhanced internal friction between the polymer chains and the molecules of the neighbouring solvents, thus improving the solution viscosity. Also, the negative sulfonate groups in the co/tar-polymer resulted in a strong interaction of polymer/MWCNTs system which prevented the collapse of the polymer backbone by attracting both mono and divalent ions inside API brine thereby protecting the chains repulsion of the acrylamide chains.

Chapter 6 Enhanced oil recovery using nanoparticles modified polymer solutions

6.1. Introduction

This Chapter investigates the influence of different materials prepared in Chapters 3 and 4 (polymer and polymer nanoparticle composites) on EOR using a core flooding experimental set-up. The effect of MWCNTs on the recovery enhancement of the two selected polymers are evaluated at high temperature under the influence of API brine and alkaline pH condition, respectively. Effect of different GO concentrations on the HPAM oil recovery efficiency in comparison with the modified zwitterionic-rGO-COPAM at high temperature (up 80° C) condition is investigated, the effect of M_SiO_2/COPAM in comparison with the pure SiO_2/COPAM and NP-free COPAM are also evaluated at complex salinity and high-temperature conditions.

6.2. Core flooding procedure

For the preparation of core flooding, the Ottawa sands were packed into a metallic column by conducting a sequence of rigorous procedures for wet-packing to determine relatively constant porosity and permeability values for various packing based on the procedure obtained from [375]. The resulting parameters obtained for the column are recorded in **Table 6.1**.

To evaluate the EOR potential for polymer and polymer/NPs composites, a core-flooding set up was prepared as illustrated in **Fig. 6.1**. During the flooding process, a piston pump (series I, Core-Palmer Instrument Co. Ltd) was used for brine injection. A syringe pump (KDS 410, KD Scientific Inc. USA) was employed for mineral oil injection and a new syringe was used for the injection of each sample to avoid cross-contamination of the samples. A pressure transducer (150 psi, Omega Engineering Ltd.) was applied for measuring the pressure drop while carrying out the experiments. The heating was supplied and controlled by the EZ-ZONE PM Integrated

PID Model. There are three K-type thermocouples (5TC-TT-K-36-36, a diameter of 0.13 mm and a precision of ±0.5 K, Omega) attached to both ends and the middle of the stainless steel core holder. They are parallel twisted together and feed the average temperature back to the controller as a process signal. The target temperature of the controller was set at 85 ˚C, and the output power of heating tape (SRT051-040, OMEGA) was controlled by a PID control loop based on the difference between the set temperature and the process temperature from those three parallel-twisted thermocouples. The following procedure was used for the core flooding investigation:

- The core was saturated with the brine by injecting at least 100 mL of brine into the packed column at a continuous flow rate of 2ml/min. This resulted in a thoroughly saturated column thereby allowing sufficient time for sand grain deposition.
- The column was saturated with the oil by injecting 20 mL of high viscous mineral oil at a constant flow rate of 0.5 mL/min until achieving water saturation of $S_{wi} = 25\%$.
- The secondary oil recovery stage using brine flooding was executed by injecting 3 pore volume (PV) at a constant flow rate of 0.5 mL/min.
- Tertiary flowing was performed at a similar flow rate of 0.5 mL/min using polymer or polymer/NPs samples.
- The effluent liquid was collected in a 50 ml granulated cylinder marked in 0.1 mL division to know the actual oil recovery.
- The overall oil recovery and the tertiary recovery factors were calculated by polymer or polymer/NPs flooding.
- The temperature was maintained at 85 °C during the whole process.

Table 6.1. Average value of parameters for packed sands column.

Porous media properties	Values
Bulk volume (mL)	33.7 ± 4
Pore volume (mL)	12.8 ± 0.1
Porosity (%)	38.23 ± 5
Absolute permeability (mD)	95 ± 5
Mass of dry sands (g)	53.5 ± 1
The liquid in the pore space (g)	12.8 ± 1
Temperature (˚C)	85 ± 1.5

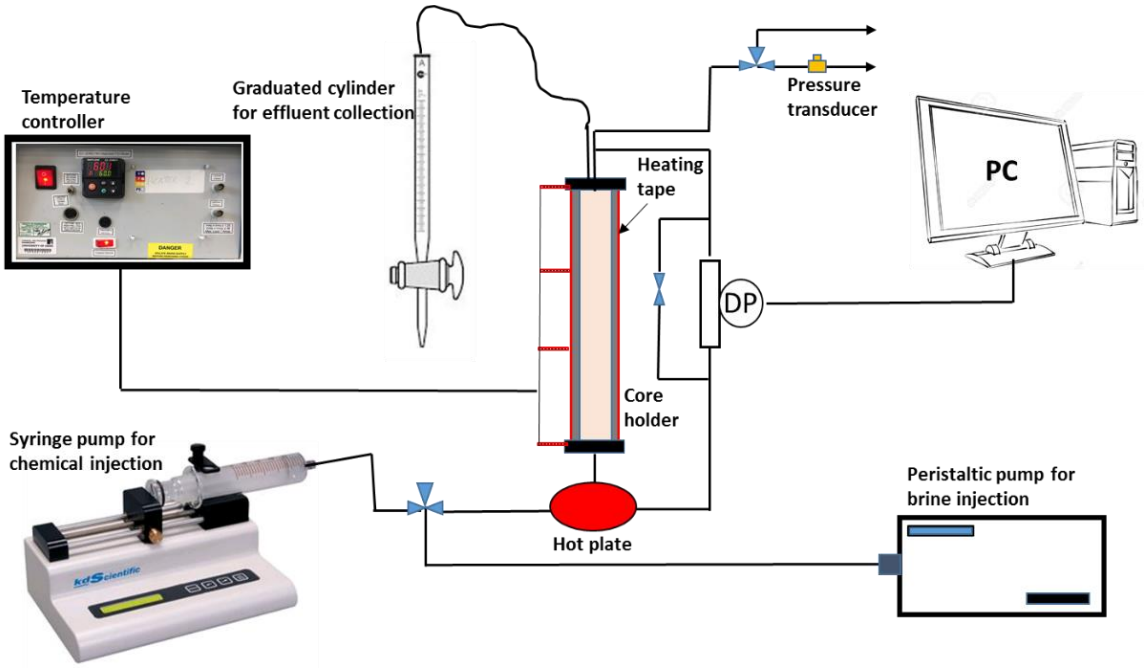

Figure 6.1. Experimental setup for core flooding and (b) Schematic illustration of the core flooding system.

6.3. Effect of MWCNTs on the EOR performance of synthesised polymers at high salinity and alkaline pH.

6.3.1. Selection of properly synthesised polymers for EOR experiment

Among the five synthesized polymers, the best polymers for core flooding investigation were selected based on the stability and rheological analysis with MWCNTs. The observations on the stability and rheological properties of these materials were conducted and recorded in **Section 3.4** and **Section 5.4**. The summary of the findings is shown in **Table 6.2** for the evaluation of different polymer/MWCNTs dispersion samples. The study indicates that the polyelectrolyte copolymer and polyampholytic ter-polymer containing the negative sulfonate group (samples B and D) improved the stability and viscosity in both saline and alkaline conditions, and are thus considered as better candidates for the core flooding experiment.

Table 6.2. Viscosity and stability evaluation of different MWCNTs/polymers.

Condition	Sample A		Sample B		Sample C		Sample D		Sample E	
	Viscosity (85 °C)	Stability (60 °C)	Viscosity (85 °C)	Stability (60 °C)	Viscosity (85 °C)	Stability (60 °C)	Viscosity (85 °C)	Stability (60 °C)	Viscosity (85 °C)	Stability (60 °C)
Water	Weak	Good	Good	Fair	Weak	Good	Fair	Good	Good	Fair
Alkaline condition	Weak	Weak	Fair	Fair	Fair	Fair	Fair	Good	Fair	Fair
API brine	Weak	Weak	Good	Good	Fair	Weak	Weak	Fair	Fair	Weak

6.3.2. Oil recovery efficiency

A series of core flooding investigations (runs 1-6) were conducted for the two best-selected polymers and their dispersion with MWCNTs, also bare co/ter-polymer was tested as a reference to examine MWCNTs effect on incremental oil recovery. The experimental conditions and the results of oil recovery efficiency with the uncertainty of 0.2% are

summarized in **Table 6.3**. Also **Fig. 6.2** shows the accumulated oil recovery efficiency by co/ter-polymer, copolymer containing negative sulfonate group (sample B) and its composites with MWCNTs at high temperature (85 °C) and high brine salinity (2 wt.% $MgCl_2$, 2 wt.% $CaCl_2$ and 8 wt.% NaCl), relative to the original oil in place (OOIP) after oil saturation for secondary and tertiary flooding, respectively. It can be seen that the polymer/MWCNTs improved the oil recovery by 14.8% OOIP (from 70.2% to 85%) in the tertiary recovery stage while the copolymer containing negative sulfonate group and bare co/ter-polymer increase the recovery by 10.6% and 7.6% respectively. The photos of recovered oil for each case can be found in **Fig**. **6.3**. On the other hand, **Fig. 6.4** demonstrates the results of accumulated recovered oil after flooding with co/ter-polymer, a copolymer containing positive-negative group (sample D), and its composites with MWCNTs at high temperature (85°C) and pH=11. Similar to the above findings, the composites of positive/MWCNTs show a higher oil recovery of 10.8 % (from 70.5% to 81.2%) whereas the copolymer containing a positive-negative group and bare co/ter-polymer increase the recovery by 8.7% and 7.0% respectively. The photos of recovered oil for each case can be found in **Fig. 6.5**.

The greater recovery factor by the polymer containing MWCNTs in both experimental conditions revealed the outstanding capability of the composites to modify the oil/water mobility ratio. However, higher oil recovery could be attributed to the high viscosity of the composites compared to other tested samples, and its ability to perform under high temperature and high salinity without losing much of its viscosity. The polymer/MWCNTs displayed greater rigidity in the porous medium due to its reasonable viscous force when it flowed in the core plug, whereas bare polymers were believed to lose a considerable viscosity fraction in the porous medium, specifically at high temperature and high saline conditions. Thus, a larger area of the core could be swept by polymer/MWCNT solution without the fingering effect and hence more oil recovery was achieved. Although the copolymer containing negative sulfonate group

has around 3% higher oil recovery compared to bare co/ter-polymer, this could be due to the greater salinity resistance exhibited by the modified sulfonate group as explained above. Generally, it can be deduced that polymer/MWCNTs flooding, could be more successful over the other samples because of its better mobility control, which has been achieved by enhancing the rheological properties of the solutions.

Table 6.2. Oil recovery efficiency by using polymer and polymer nanoparticles composites

Displacing Fluid	Efficiency after brine flooding, % OOIP	Efficiency after tertiary flooding, % OOIP	Enhance oil recovery efficiency, %
Sample A (API)	65.6	73.2	7.6
Sample B (API)	67.2	77.7	10.6
Sample B + MWCNTs (API)	70.2	85	14.8
Sample A (pH-11)	67.9	74.9	7.0
Sample D (pH-11)	68.9	77.6	8.7
Sample D + MWCNTs (pH-11)	70.5	81.2	10.8

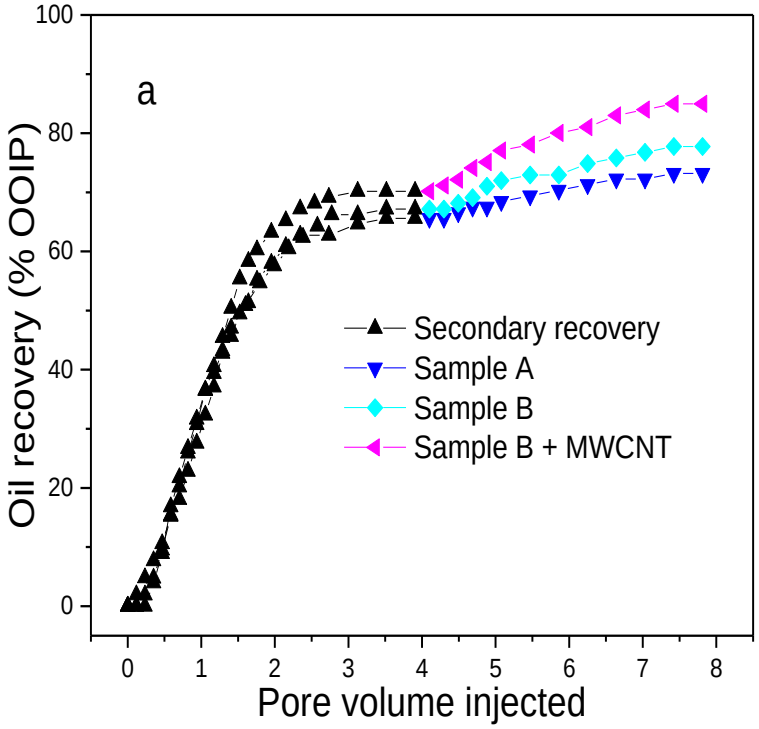

Figure 6.2. Tertiary oil recovery obtained by co/ter-polymer (sample A), a copolymer containing negative sulfonate group (sample B) and its composites (sample B + MWCNTs) at high temperature (85 °C) and high brine salinity (2 wt.% MgCl2, 2 wt.% CaCl2 and 8 wt.% NaCl.

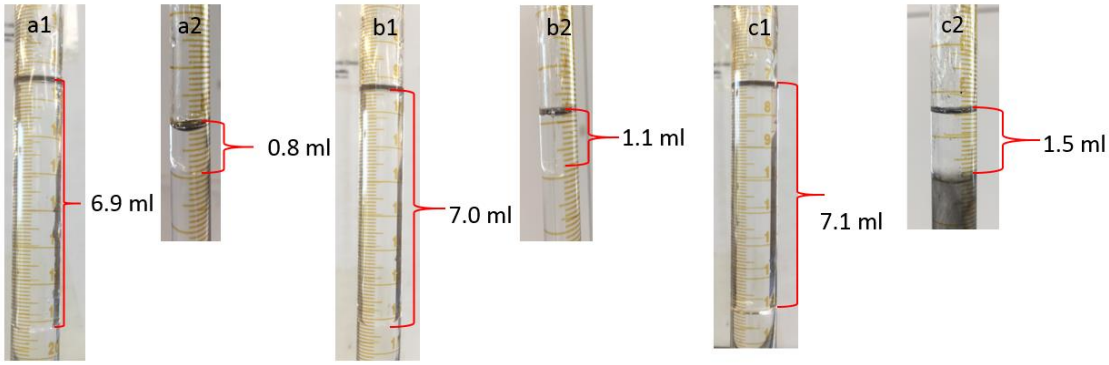

Figure 6.3. The oil recovered at the stage of secondary and tertiary flooding displaced by (a) Sample A, (b) Sample B, and (c) sample B + MWCNTs. In each case, the number 1 stand for secondary (brine flooding) while 2 stands for tertiary flooding. The amount of oil recovered by brine flooding is relatively the same in all cases indicating that the sand was stably packed into the core holder.

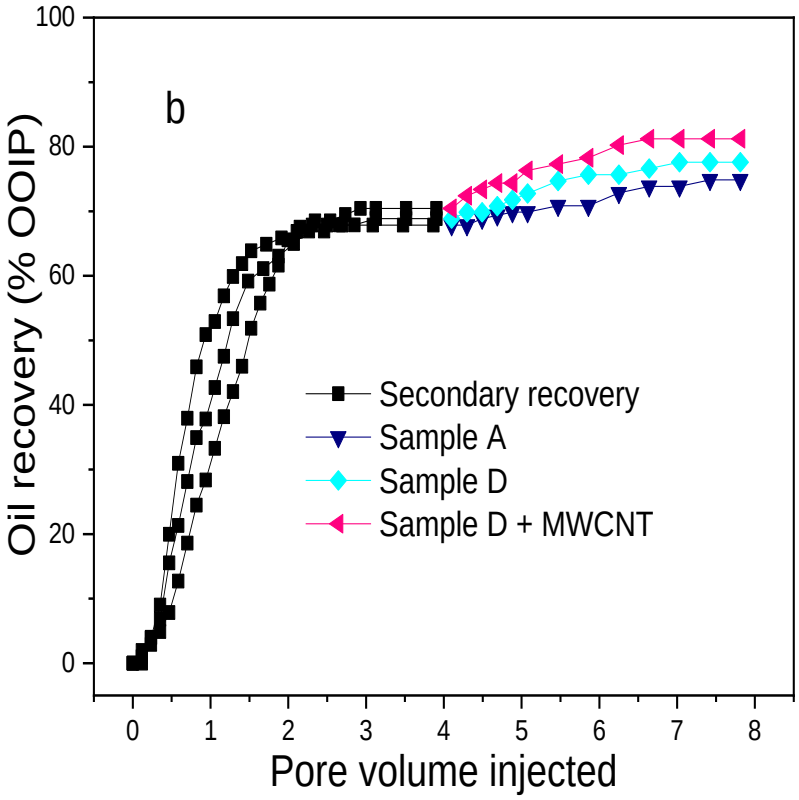

Figure 6.4. Tertiary oil recovery obtained by co/ter-polymer (sample A), ter-polymer containing positive-negative group (sample D), and its composites (sample D + MWCNTs) at high temperature (85 °C) and pH =11.

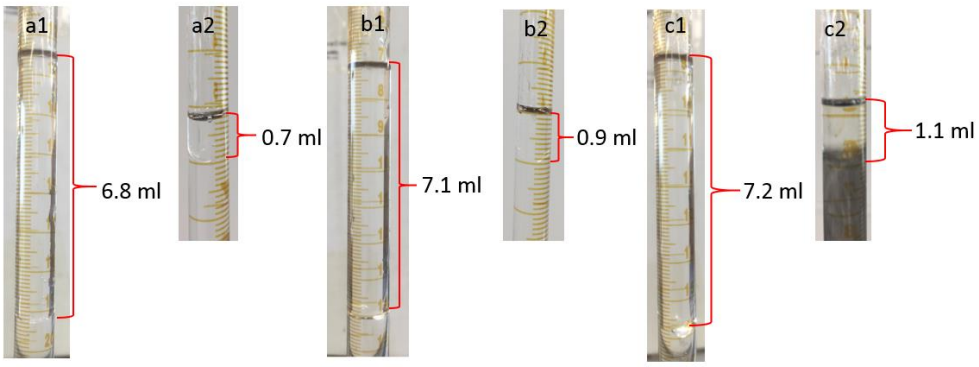

Figure 6.5. The oil recovered at the stage of secondary and tertiary flooding displaced by (a) Sample A, (b) Sample D, and (c) sample D + MWCNTs. In each case, the number 1 stand for secondary (brine flooding) while 2 stands for tertiary flooding. The amount of oil recovered by brine flooding is relatively the same in all cases indicating that the sand was stably packed into the core holder.

The results of the interfacial surface tension (IFT) and contact angle (CA) for all 6 samples are shown in **Table 6.4.** An alteration is observed for both factors with the addition of MWCNTs to the polymer solutions at high salinity and alkaline pH conditions. According to the results, the wettability was changed towards neutral-wet status with the addition of MWCNTs. The CA for pure polymer solutions was found to be between 40° to 42° in both high salinity and alkaline conditions. The results show that the addition of MWCNTs changes the CA slightly from 42° to around 36°. Similarly, the IFT values are also decreased slightly with the addition of MWCNTs into the fluids. However, two different scenarios were observed for IFT reduction, at API brine condition the fluids IFT is 34 mN/m while 55 mN/m was observed at pH=11. This may be because of the salt capability to enhance the adsorption rate at the oil-water interface which accounts for the compression of the electrical double layer [376]. The weakening of the electrical double layer enhances the molecules transfer faster from bulk-phase to oil-water interface and thus reduces the value of IFT [376]. It was also mentioned that the addition of NaCl decreases the solubility rate of the injected fluid, and makes it more ionized, and thereby it adsorbs more strongly at the oil-water interface which reduces the IFT value [377]. With the addition of MWCNTs, the IFT values for sample B reduced from 34 to 28 mN/m whereas that of sample D reduced from 55 to 47 mN/m, respectively. This IFT reduction proves the nanoparticle's capability to mobilize the oil, leading to the easy flow of targeted oil by reducing the energy required by oil droplets to flow through the pore throat.

The differential pressure recorded during oil recovery analysis for the core flooding investigation for the copolymer containing negative sulfonate group (sample B) and sample B/MWCNTs at high temperature (85 °C) and high brine salinity (2 wt.% $MgCl_2$, 2 wt.% $CaCl_2$ and 8 wt.% NaCl) are shown in **Fig. 6.6.** It can be observed in **Fig. 6.6a** that pressure drop increases after the injection of the bare polymer whereas, after injecting the solution of MWCNTs in copolymer containing negative sulfonate group we observed that the pressure

drop became lower than that after brine injection (**Fig. 6.6b**). Contrary to the conventional thought that the MWCNT dispersion has a higher viscosity than the pure polymers and would have a greater possibility to form a wedge or block the pore channel, thereby causing the pressure drop to increase, the reverse was observed. This implies that MWCNTs play a leading role in enhancing the fluidity while moving along the pores, and also have the tendency to reduce the cost associated with polymer flooding as it lowers the amount of energy required during the injection process. A similar observation was made in the case of the copolymer containing a positive-negative sulfonate group (sample D) and its composites (sample D + MWCNTs) at high temperature (85 °C) and pH=11 (the results are reported in **Fig. 6.7.** Nevertheless, the pressure drop for the MWCNTs/polymer sample is even lower than that of the brine injection.

Considering these results, it was assumed that polymer/MWCNTs dispersions altered the surface condition of the core sample to become more hydrophilic during the nanofluid injection [378, 379]. As explained, both copolymers containing negative and positive-negative groups are hydrophilic with anionic and cationic side chains, but, the addition of MWCNTs makes them more hydrophobic, promoting partial interaction between the particles and demonstrate electrostatic repulsion against the pore surface. Such partial but lengthy hydrophobic attraction of the hybrid materials would advance the formation of a favourable wedge film, created by disjoining pressure, hence causing incursion of the nanofluid to the oil-wet glass surface [379]. This wedge film easily changes the surface wettability of the oil drop against the glass surface, thus reducing the adsorption of the oil phase on the porous medium and lowering the pressure drop. This could enhance the sweep efficiency and hence more oil recovery.

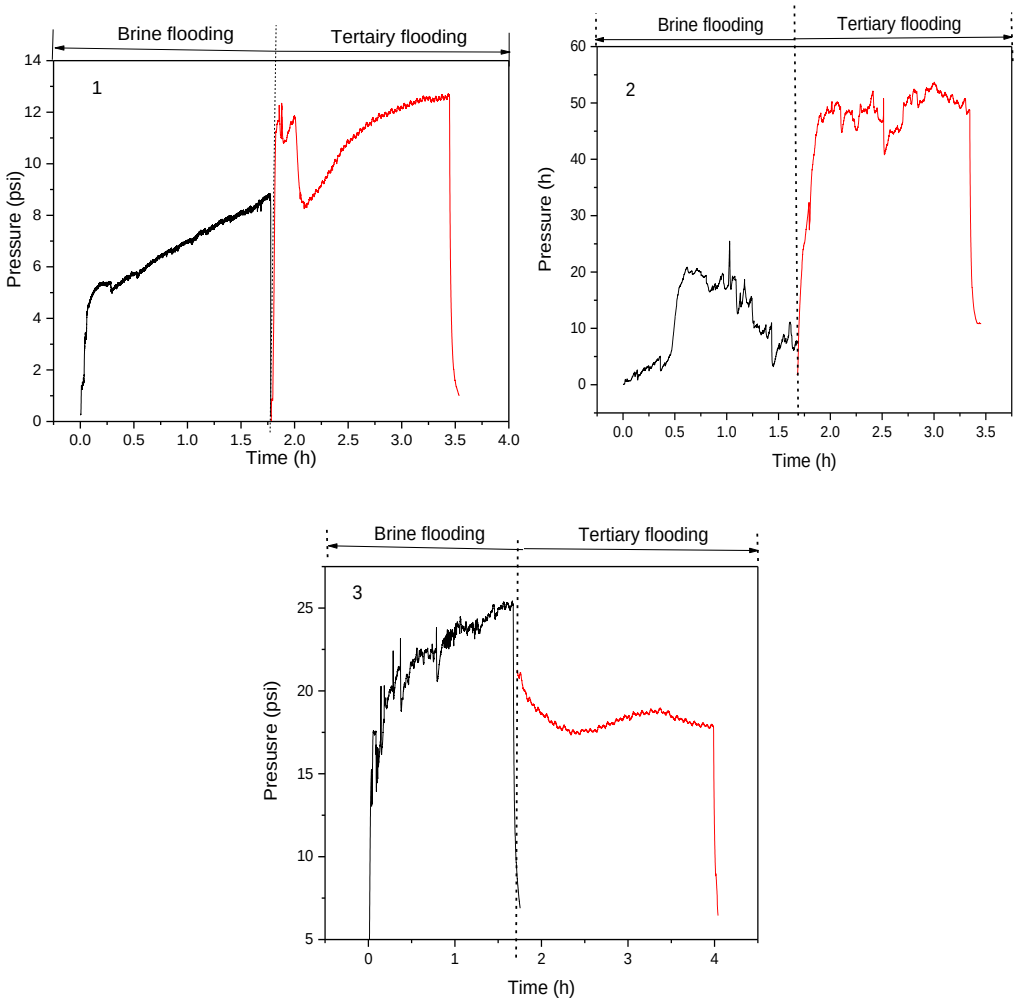

Figure 6.6. The Differential pressure for (1) co/ter-polymer (2) copolymer containing negative sulfonate group and (3) copolymer containing negative sulfonate group/MWCNT at high temperature (85°C) and high brine salinity (8 wt.% NaCl, 2 wt.% $CaCl_2$ and 2 wt.% $MgCl_2$).

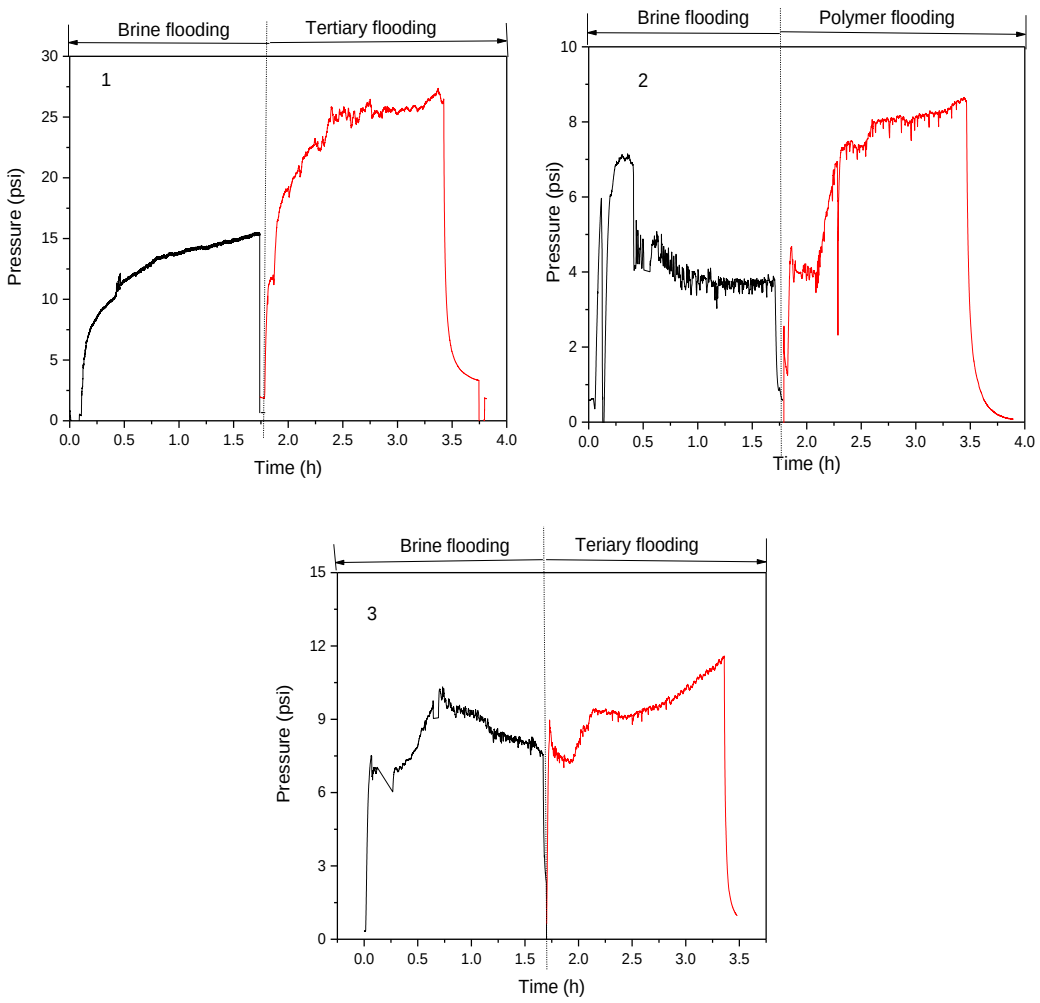

Figure 6.7. The Differential pressure for (1) co/ter-polymer (2) copolymer containing positive-negative group and (3) copolymer c containing positive-negative group/MWCNT at high temperature (85°C) and pH=11.

Three major mechanisms of oil recovery enhancement (IFT, CA and viscosity) were all investigated in this work and the contribution of those factors was evaluated using the desirability model (**Eqn. 6.1 and 6.2**) by demonstrating the relationship between the desirability of the related factor and efficiency of the recovered oil to evaluate the factor with the greater influence to the overall EOR efficiency. Both individual (d_i) and combined (D) desirability is used to observe the effect of each factor affecting the EOR. Once a good correlation is accomplished the dominant factor could be extended to predict a trend of the

potential relationship between the factors and recovery efficiency [380]. IFT, CA, and viscosity are selected to examine their influence on oil recovery efficiency. The results of selected factors for samples used in the core flooding experiment are shown in **Table 6.3** and the analysed desirable values are plotted in **Fig. 6.8**. As can be seen from **Fig. 6.8**, only viscosity desirability can imply the relationship. However, the aforementioned trends of the factor to the % recovery efficiency indicate that viscosity is the favourable mechanism playing a dominant role to recover the high viscous oil from the core, while IFT and CA show less significant changes in the relationship. After combining all three desirabilities (D) no clear correlation with the recovery efficiency was observed.

$$d_i = e^{-e^{-x_i}} \dots\dots\dots\dots\dots\dots\dots\dots Eqn.\,6.1$$

$$D = \left(\prod_{i=1}^{n} d_i\right)^{1/n} = \sqrt[n]{d_1 d_2 \dots d_n} \dots\dots\dots\dots\dots\dots Eqn.\,6.2$$

Where, d stands for the individual desirability function ((i) while n stands for the amount of the affecting factors that are designed to affect the indicator.

Table 6.3. Evaluation of affecting factor (IFT, CA, and Viscosity) with their desirability (dIFT, dΘ, and dμ) and combined desirability (D) for each fluid use in this experiment.

Fluid	EOR Mechanisms			Individual desirability (d)			Desirability (D)	% Oil recovery efficiency
	IFT(mN/m)	Θ(^{0})	μ(mPa·s)	d_{IFT}	d_Θ	d_μ		
Sample A (API)	34.27	40.18	3.01	2.89×10^{-1}	4.10×10^{-1}	1.29×10^{-2}	1.15×10^{-1}	7.6
Sample B (API)	34.15	40.87	6.88	2.84×10^{-1}	3.94×10^{-1}	2.08×10^{-1}	2.85×10^{-1}	10.6
Sample B + MWCNTs (API)	28.18	36.86	16.14	7.01×10^{-2}	4.84×10^{-1}	8.71×10^{-1}	3.09×10^{-1}	14.8
Sample A (pH =11)	55.48	41.97	3.55	9.16×10^{-1}	3.69×10^{-1}	2.28×10^{-2}	1.97×10^{-1}	7.0
Sample D (pH =11)	52.11	42.09	8.71	8.75×10^{-1}	3.66×10^{-1}	4.01×10^{-2}	2.34×10^{-1}	8.71
Sample D + WMCNTs (pH =11)	47.28	36.99	12.59	7.83×10^{-1}	4.83×10^{-1}	7.05×10^{-1}	6.43×10^{-1}	10.8

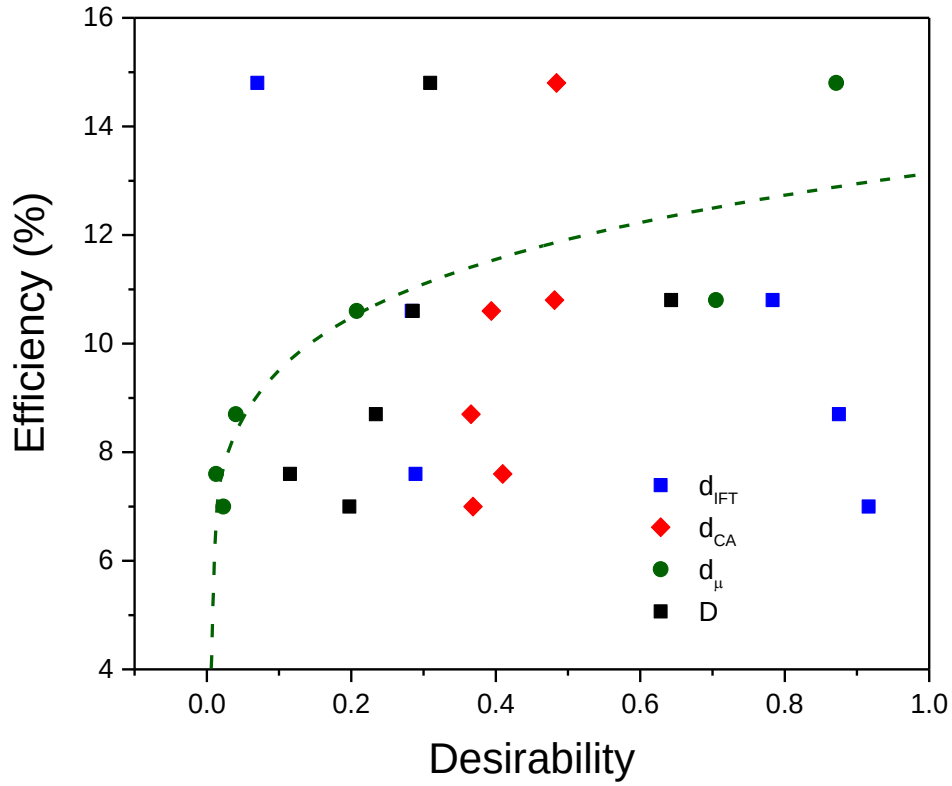

Figure 6.8. % EOR efficiency as a function of overall desirability (D) and individual desirability (d) factors for three EOR mechanism.

6.4. Effect of GO concentrations on HPAM and comparison with modified zwitterionic-rGO-COPAM on EOR performance

IFT measurement was conducted between mineral oil and different aqueous phase to examine the influence of GO in the HPAM/GO composites on the IFT variation. **Fig. 6.9b** showed the dynamic IFT when the composite with different GO concentrations was introduced while **Fig. 6.9aand Table 6.4** showed the values of equilibrium IFT as a function of GO concentrations at 1500 s. The IFT values decreased steadily with increasing GO concentration. As we can see the HPAM IFT was found to be 62.54 mN/m, with the addition of 0.01 wt.% GO into HPAM the IFT value dropped down to 54.06 mN/m and similar trends were observed with up to 22.5 mN/m reduction after adding 0.1 wt.% GO showing the total of 40.0 mN/m. When the higher

concentration of GO was added a rapid reduction in the ITF was observed showing that GO is an effective surfactant for oil/water interface. According to a report by Sun *et al.* [381] on the IFT investigation GO/diblock copolymer it was found that GO can be effectively trapped at the oil/water interface and jammed into a solid film by hydrogen bonding or electrostatic interaction with the polymer amine unit. This similar phenomenon of jamming was also reported somewhere with silica nanoparticle [382]. GO is widely known as amphiphilic, having a hydrophobic domain on its unoxidized graphite patches and hydrophilic oxygen functionalities as illustrated in **Fig. 6.9a**. Because of this amphiphilicity GO can be regarded as a class of surfactant that can stabilize oil-water interfaces, and at the same time reduced oil-water IFT [383]. Contrarily, when zwitterionic-rGO-COPAM were used the IFT value rises to around 57.12 mN/m. This is because there is no amphiphilic character on its surface since the GO used for composite preparation has been reduced to rGO.

Table 6.4. Values of equilibrium IFT at 1500 s as a function of GO concentrations, and the IFT value of zwitterionic-rGO-COPAM for comparison.

Composite solutions	Equilibrium oil-water IFT (mN/m) at 1500 s
0.05 wt.% HPAM	62.54
0.05 wt.% HPAM/0.01 wt.% GO	54.06
0.05 wt.% HPAM/0.02 wt.% GO	52.49
0.05 wt.% HPAM/0.04 wt.% GO	47.18
0.05 wt.% HPAM/0.06 wt.% GO	44.68
0.05 wt.% HPAM/0.08 wt.% GO	42.78
0.05 wt.% HPAM/0.1 wt.% GO	40.04
Zwitterionic-rGO-COPAM	57.12

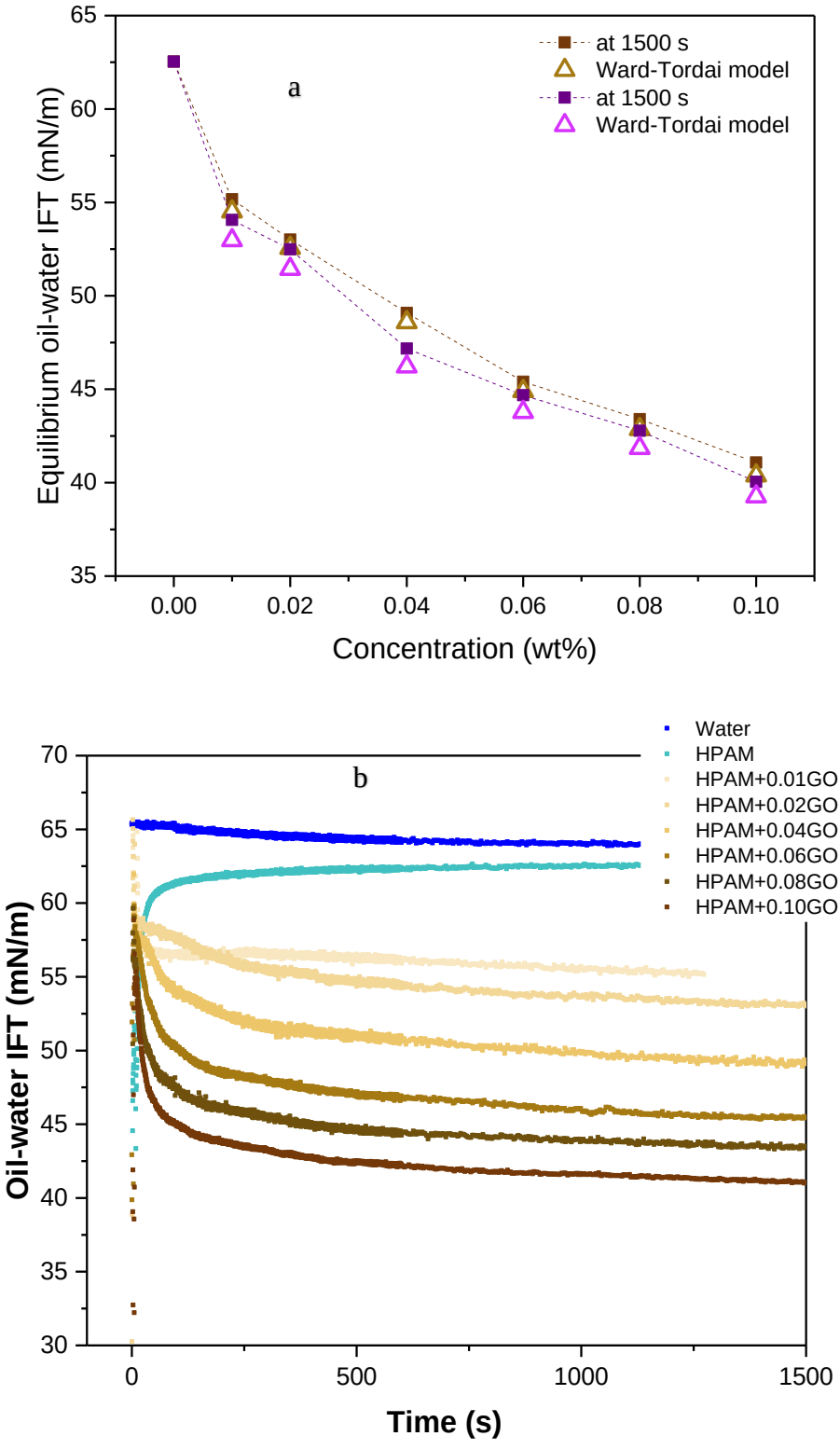

Figure 6.9. (a) dynamic IFT as a function of time (b) averaged values of equilibrium IFT as a function of GO concentrations and (c) schematic illustration showing the amphiphilic nature of GO at the oil-water interface.

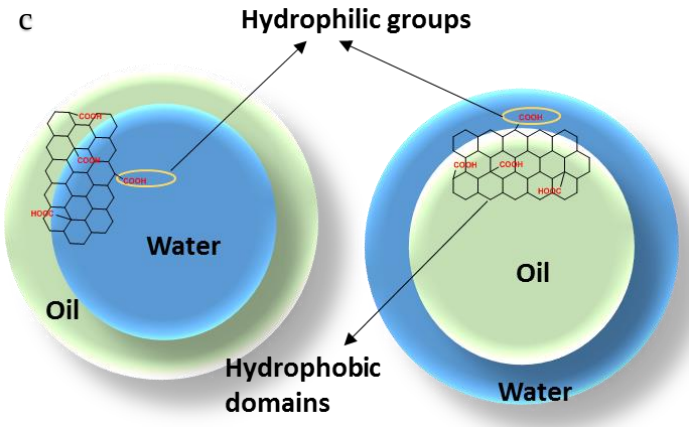

Figure 6.9. continues.

For EOR analysis, four different sets of core flooding experiment were prepared with 0.05 wt.% HPAM, 0.05 wt.% HPAM/0.01 wt.% GO, 0.05 wt.% HPAM/0.04 wt.% GO and 0.05 wt.% HPAM/0.1 wt.% GO to determine the influence of GO on the oil recovery enhancement. Also, for comparison, zwitterionic-rGO-COPAM composites prepared in both APIB and FB were subjected to core flooding investigation, aiming to determine the effect of modified material in the recovery. The obtained results are summarised in **Table 6.5**. The accumulated oil recovery efficiency is plotted in **Fig. 6.10.** As can be seen with the increasing amount of GO in the composites the percentage of recovered oil also increased slightly. Pure HPAM generates an increase of 6.52% of the oil relative to the original oil in place (OOIP) after secondary brine flooding, from 60.87 to 67.39%. With the addition of 0.01, 0.04, and 0.1 wt. % GO concentration the oil recovery increased with 6.74%, 10.98%, and 13.33%, respectively. On the other hand, the zwitterionic-rGO-COPAM composite showed more oil recovery enhancement compared to HPAM and HPAM/GO materials, generating about 16.67% in API and 15.56% FB brine solutions, respectively.

The increased recovery factor could be due to the improved mobility ratio between the oil and polymer solution. This is attributed to the increase in the viscosity of the composite compared to the neat polymer solution. This showed that the composite displayed better rigidity in the

porous medium because it has more viscous force when moving through the core flog compared to the neat polymer solution, which is prone to losing its viscosity, especially in harsh conditions. Nevertheless, in the case of HPAM/GO composite, the improvement in IFT with the inclusion of GO into the polymer, could also be the reason why there is more oil recovery. The lower IFT value may be because particles can transfer from the bulk-phase to the oil-water interface leading to IFT reduction (66). This showed the tendency of GO to mobilized the oil and move it to the targeted area. With regards to zwitterionic-rGO-COPAM composites, the higher oil recovery is also attributed to the higher viscosity and much better salinity and temperature tolerance, which is due to excellent dispersion stability displayed by the composite in brines [384], which is assumed to agree with the behaviour of pseudo-spherical nanoparticles where the rGO nanosheets wrapped by the chains of zwitterionic-rGO-COPAM. At high ionic strength brines, presence of electrolyte ions can enhance the interactions of the ionic groups in the zwitterionic sulfobetaine polymers, creating the chain's expansion by providing adequate steric repulsion thereby preventing the flocculation/aggregation of the composite materials, and hence prevent much degradation at high-temperature condition, and hence more oil recovery [302, 304].

The recorded differential pressure during the oil recovery experiment is plotted in **Fig. 6.11**. The results showed that the pressure drop increases after injecting the HPAM and three HPAM/GO composite solutions, while zwitterionic-rGO-COPAM sampled showed reduced pressure drop. This showed that even though zwitterionic-rGO-COPAM composites has the higher viscosity, but it can still control the flow of the solution by driving the oil into the area of interest with the same amount of energy required as that of polymer injection. Showing potential in future EOR application.

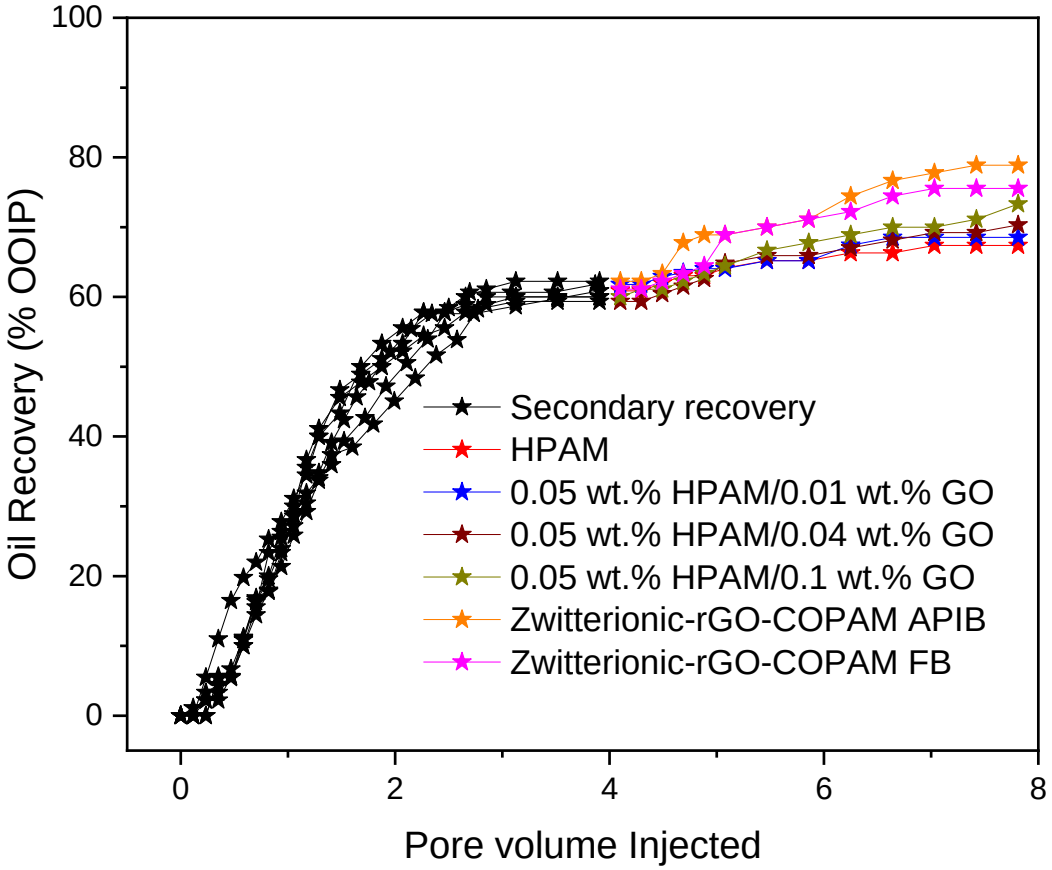

Figure 6.10. Comparison of tertiary oil recovery between HPAM, HPAM/GO with different GO concentrations (0.01, 0.04 and 0.1 wt. %) in 8 wt.% NaCl, and zwitterionic-rGO-COPAM composites in APIB and FB brine respectively.

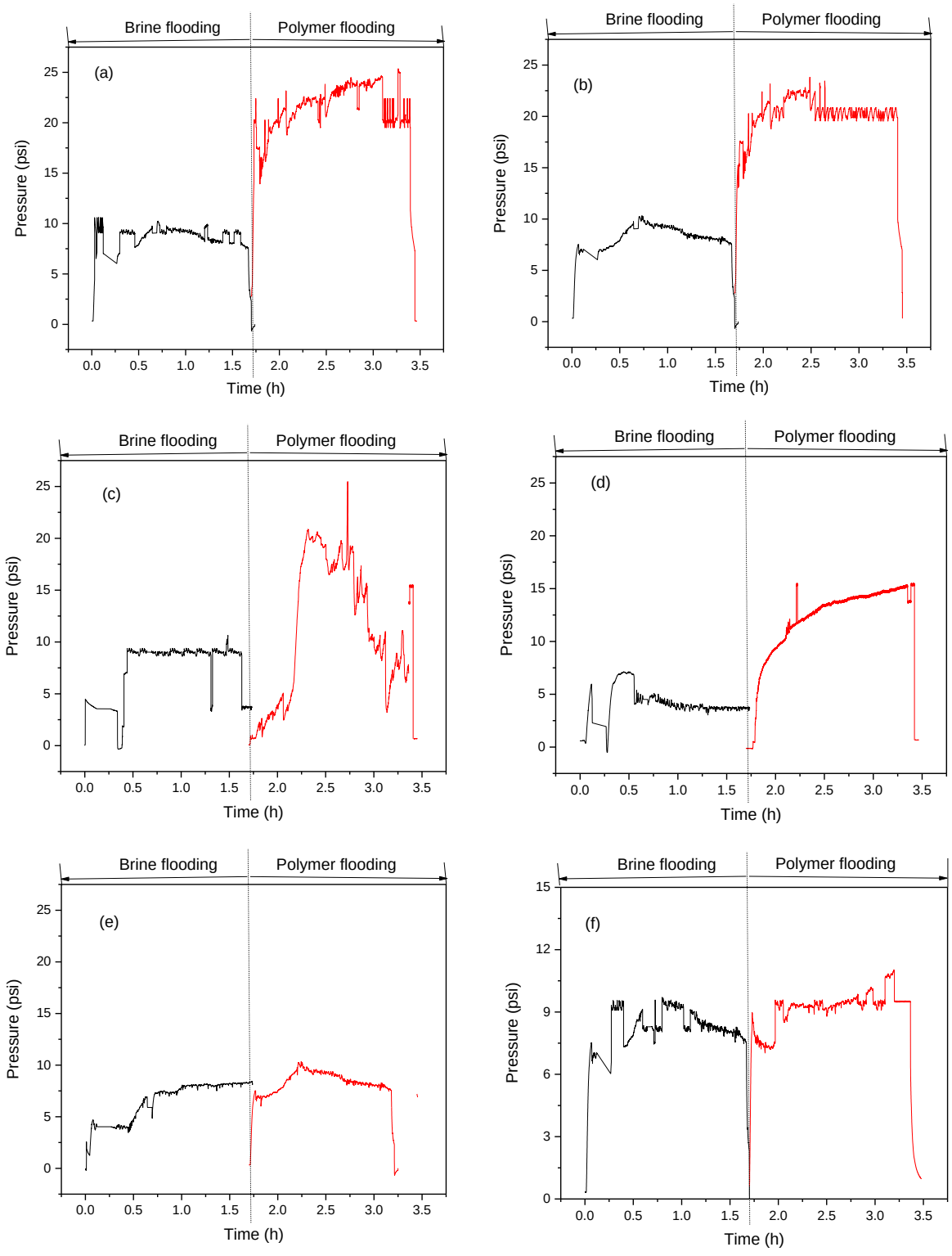

Figure 6.11. The Differential pressure recorded during the injection of (a) HPAM, HPAM/GO composites with different GO concentrations (b) 0.01 wt. %, (c) 0.04 wt. %, and (d) 0.1 wt. %, and zwitterionic-rGO-COPAM composites in (e) API brine and (f) FB brine.

6.5. Effect of surface modified SiO_2 NPs on polymers EOR at HT-HS conditions.

Before this investigation, surface-modified SiO_2 was formulated to reduce the problems associated with conventional SiO_2 used in enhancing the performance of polymer used in EOR as described in **Section 4.3**. The characterizations of the obtained materials were conducted and reported in **Section 4.3.5**, also, their rheological analysis was thoroughly performed in **Section 5.3.4.**

Increasing reservoirs sweep efficiency is the most important aspect in PF-EOR [2, 31, 385, 386]. This technique is based on altering the mobility ratio between oil and injection fluid by the addition of polymers to improve vertical and areal sweep efficiencies and thereby reducing viscous fingering [36, 46]. Notwithstanding, the PF efficiency is affected by several situations including pore throats blockage because of the polymer aggregation [26, 28], polymer degradation with the influence of extreme temperature and salinity conditions [334, 369, 387-389] and polymer adsorption onto the surface of the porous media [390, 391], these hinder the PF performance, causing huge economic expenditures and severe viscosity reduction. In this Section, a series of six core-flooding experiments were employed to examine the effect of NP-free COPAM, SiO_2/COPAM, and M_SiO_2/COPAM on the incremental oil recovery HT-HS conditions. The experimental conditions and the comparisons of overall oil recoveries are tabulated in **Table 6.5,** and the obtained results of the accumulated oil recovery are shown in **Fig. 6.15.** The first 3 sets of the experiment were conducted using API brine at 85 °C, after injecting 3.0 PV of brine solution for each experiment around 50-52% of the oil was recovered relative to the original oil in place (OOIP), meaning that around 48-50% of the OOIP remain unrecovered by the means of conventional water flooding. Consequently, the overall oil recovery increase was 7.7% and 12.7% after NP-free COPAM and SiO_2/COPAM injection,

while a 17.5% increase in oil recovery was obtained after M_SiO_2/COPAM injection under the same condition. A similar trend of oil recovery was recorded under after using FB at the similar temperature with overall oil recovery increase of 6.2% and 9.6% for NP-free COPAM and SiO_2/COPAM, whereas 16.2% oil were recovered after injecting M_SiO_{2CO}/PAM solution, lower than that of API brine samples.

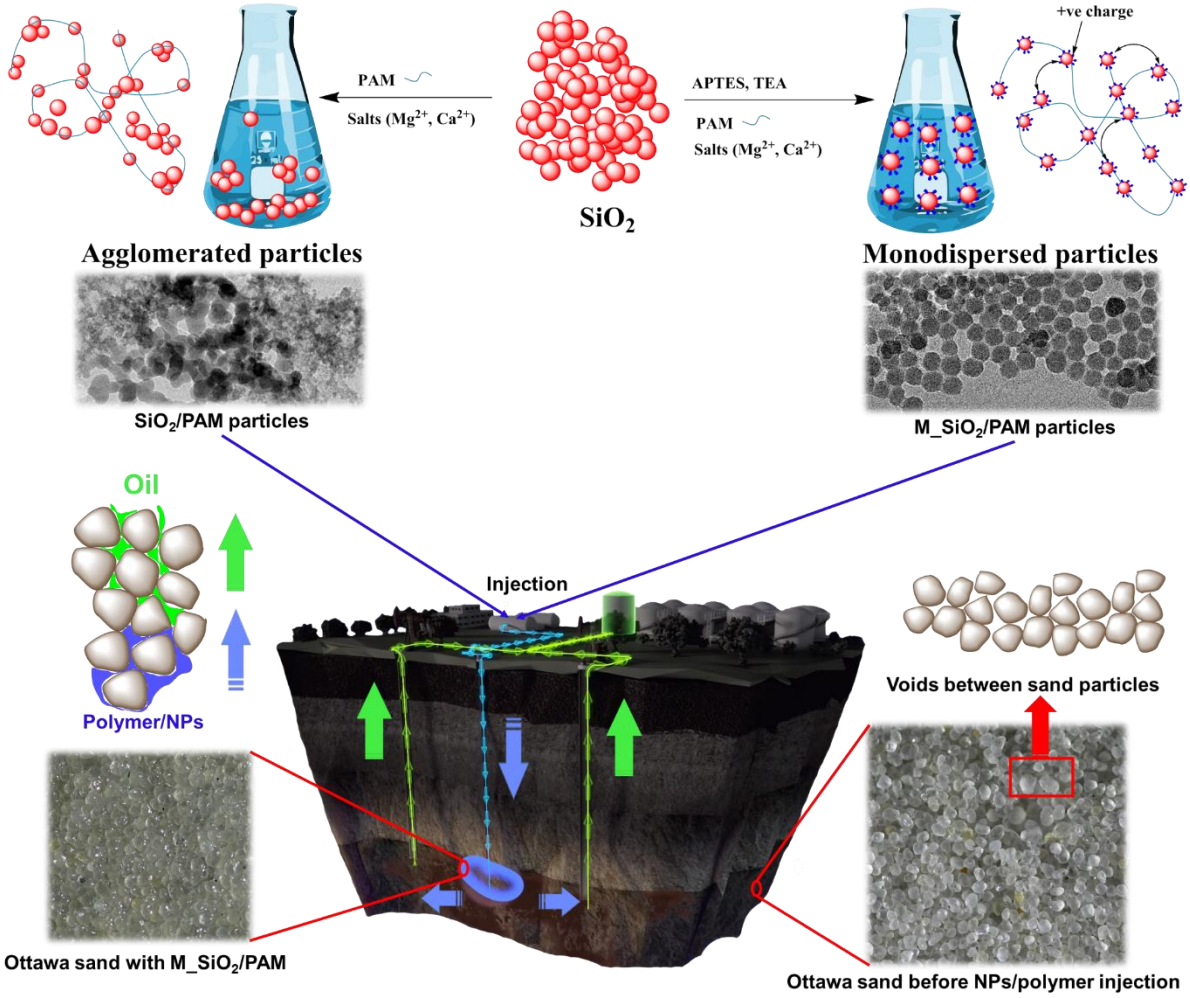

Figure 6.12. Schematic illustration showing how polymer nanoparticle mixture push oil through the sands.

The primary reason for greater oil recovery by M_SiO_2/COPAM is the ability of the M_SiO_2 to alter the oil/water mobility ratio. This could be associated with higher viscosity and improved stability after long-term aging at high temperature demonstrating a higher ability to be implemented under HT-HS without much decrease in viscosity. The M_SiO_2/COPAM also shows greater performance due to its fair viscous force when injected into the core, but the other two samples especially NP-free COPAM were believed to reduce their viscosity at HT-HS conditions because of poor stability. Thus, the highly stable solution could sweep the major core area without blocking the pores which makes more oil recovery to be achieved. These improved properties of M_SiO_2/COPAM were generated due to the incorporated amino functional groups present on the surface of added NPs, which results in the evolution of new electrostatic chemistry that occurs when the additional proton (H^+) from the amino group of M_SiO_2 react with the polymer ionic charges, reinforced the ability of polymer molecules to be adsorbed onto the M_SiO_2 NPs surface. During the core-flooding experiment, the differential pressure was recorded for all the tests as seen in **Fig. 6.16**. The pressure drop increases after injecting the polymer samples, this might be due to the high viscosity of the solution.

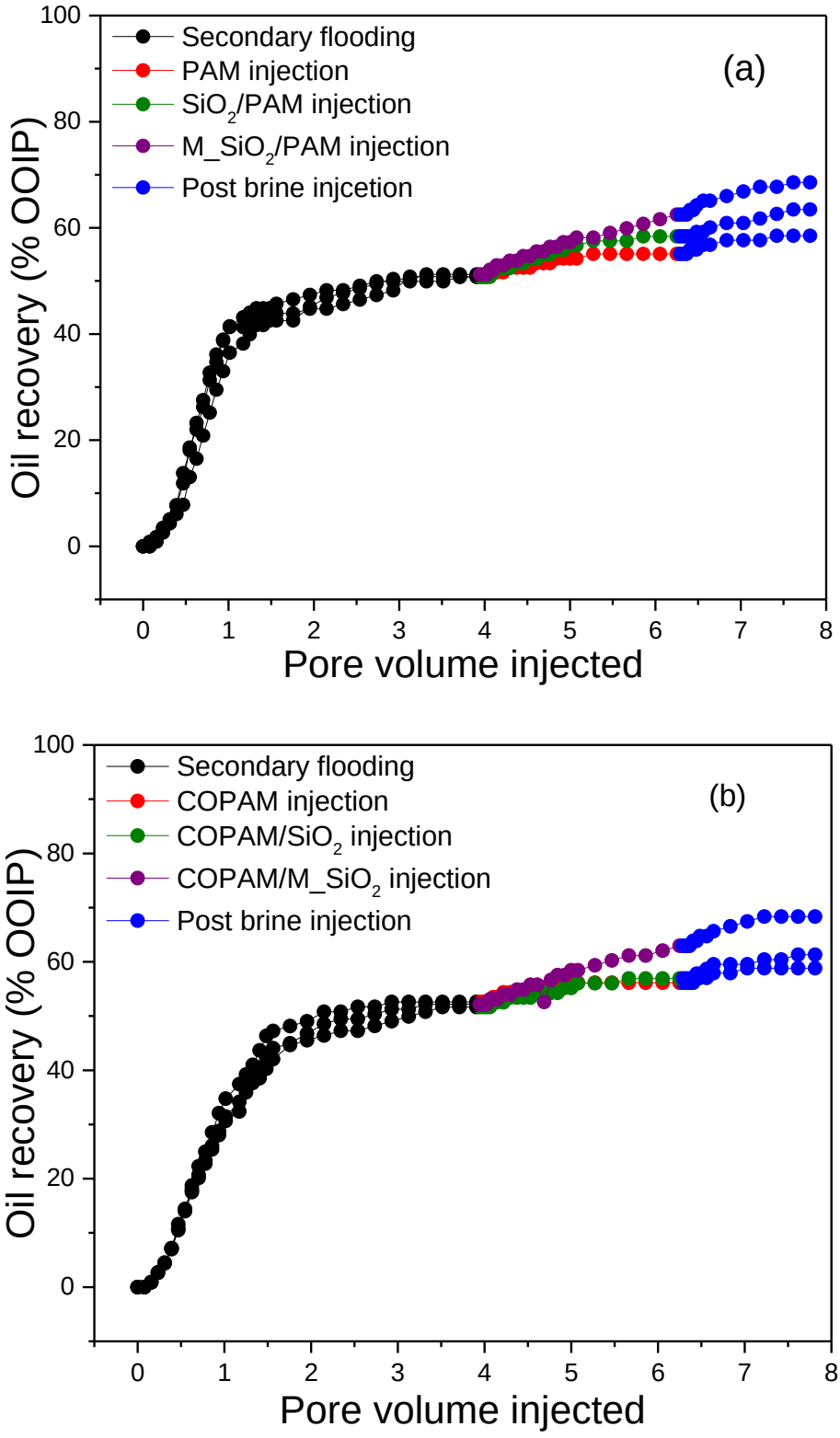

Figure 6.13. Tertiary oil recovery for NP-free COPAM, SiO_2/COPAM, and M_SiO_2/COPAM at HT-HS conditions (a) API brine and (b) FB brine.

Table 6.4. Oil recovery efficiency for NP-free COPAM, SiO_2/COPAM, and M_SiO_2/COPAM at HT-HS conditions (a) API brine and (b) FB brine.

Displacing Fluid		NP-free COPAM	SiO_2/COPAM	M_SiO_2/COPAM
(a)	Efficiency after brine flooding, % OOIP	50.77	50.76	51.21
	Efficiency after tertiary flooding, % OOIP	55.07	58.38	62.50
	Efficiency after post brine flooding, % OOIP	58.93	63.45	68.57
	EOR by sample, % OOIP	4.30	7.61	11.28
	EOR by chase water, % OOIP	3.44	5.08	6.18
	Overall oil recovery, % OOIP	7.74	12.68	17.46
(b)	Efficiency after brine flooding, % OOIP	52.58	51.66	52.16
	Efficiency after tertiary flooding, % OOIP	56.58	56.92	62.05
	Efficiency after post brine flooding, % OOIP	58.82	61.30	67.44
	EOR by sample, % OOIP	3.56	5.23	10.79
	EOR by chase water, % OOIP	2.67	4.37	5.40
	Overall oil recovery, % OOIP	6.23	9.60	16.20

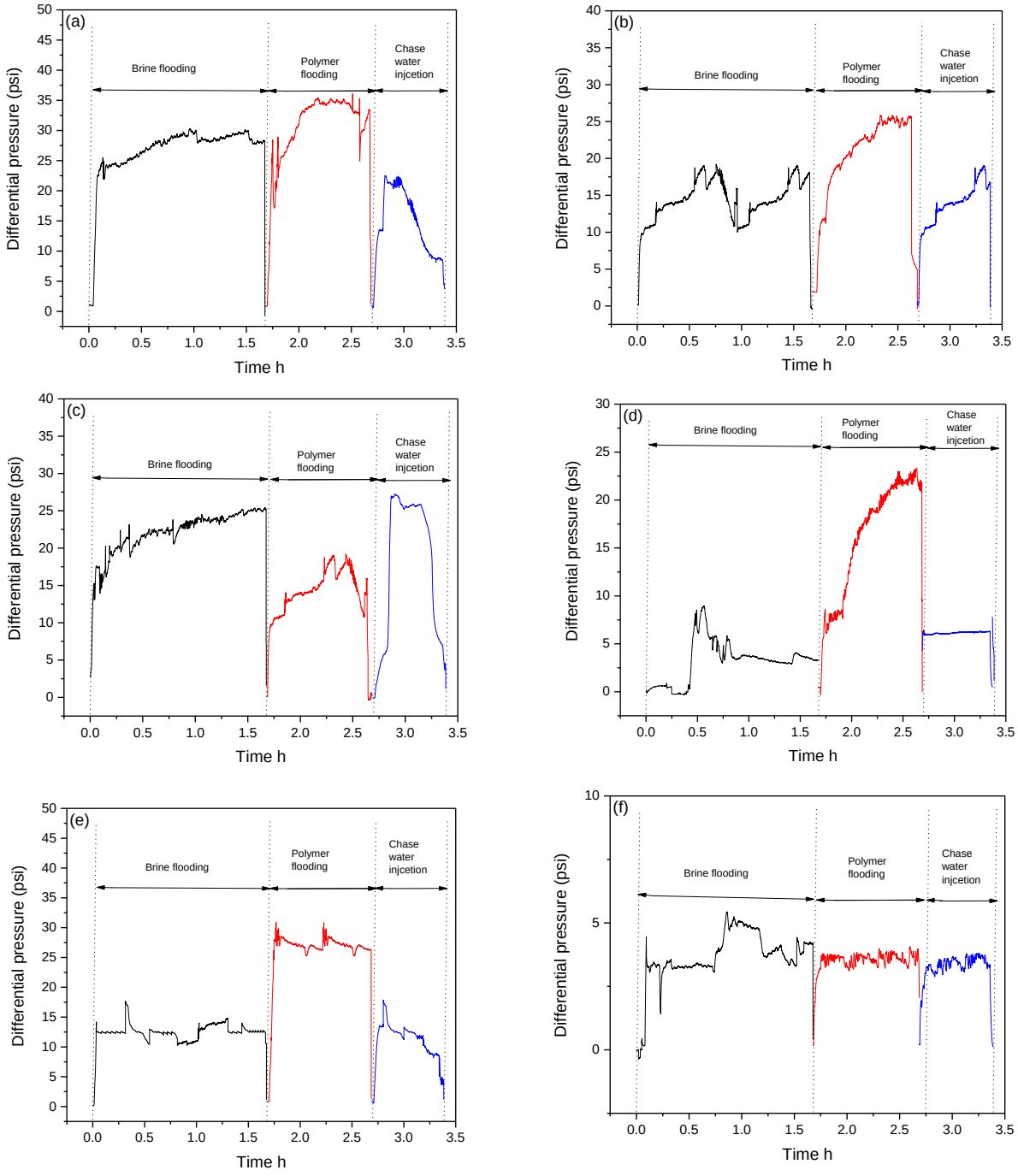

Figure 6.14. The Differential pressure for (a) COPAM flooding (b) SiO_2/COPAM flooding (c) M_SiO_2/COPAM flooding in the presence of API brine and (d) COPAM flooding (e) SiO_2/COPAM flooding (f) M_SiO_2/COPAM flooding in the presence of formation brine.

6.5. Chapter summary

In this Chapter, the effect of new materials produced in Chapters 3 and 4 was investigated on oil recovery efficiency using a core flooding experimental set-up. The EOR performance of different modified acrylamide co/ter-polymers/MWCNTs showed that in comparison to the pure polymer solution, the addition of MWCNTs to polyampholytic terpolymer and polyelectrolyte copolymer containing negative sulfonate groups improved the oil recovery efficiency at high temperature (85 °C) in the presence of both alkaline pH and API brine conditions, yet with a lower pressure drop, showing great promise for future EOR applications. Although lower interfacial tension and contact angle were observed with the addition of MWCNTs in polymer solutions at both conditions; but the desirability function indicated that viscosity was found to be the main factor responsible for high recovery. The improved oil recovery by the polyelectrolyte copolymer is due to the negative sulfonate groups in the polymer surface which resulted in a strong interaction of polymer/MWCNTs system, and prevented the collapse of the polymer backbone by attracting both mono and divalent ions in API brine, thereby protecting the chains repulsion of the acrylamide chains.

The influence of different GO concentration on the EOR performance of commercial HPAM is also investigated in comparison to the modified zwitterionic-rGO-COPAM. Since GO is considered to be amphiphilic, its interfacial and behaviour on the HPAM/GO composites were investigated before the core flooding analysis. The pilot core flooding investigation showed improved oil recovery by HPAM/GO composites more than that of pure HPAM. These enhanced performances could be as results of a two-dimensional (2D) layer or the amphiphilic behaviour of the GO sheets, which lead to improved stability, interfacial tension, and viscosity that is beneficial for enhanced oil recovery. On the other hand, zwitterionic-rGO-COPAM composite showed more oil recovery compared to HPAM and HPAM/GO materials,

generating about 16.67% in APIB and 15.56% FB, respectively due to better stability. These are because at high ionic strength brines, the presence of electrolyte ions can enhance the interactions of the ionic groups in the zwitterionic sulfobetaine polymers, creating the chain's expansion by providing adequate steric repulsion thereby preventing the flocculation/aggregation of the zwitterionic-rGO-COPAM and hence better stability.

The influence of M_SiO_2/COPAM in comparison to pure SiO_2/COPAM and NP-free COPAM solution for EOR performance were investigated at high temperatures and complex brine solution after 90 days of aging at 80 °C. The outcome showed that the M_SiO_2/COPAM solution provided more oil recovery than those from SiO_2/COPAM and NP-free COPAM solutions in HT-HS conditions. These improved properties of M_SiO_2/COPAM were generated due to the incorporation of amino functional groups on the surface of the SiO_2 NPs, which result in the formation of electrostatic attraction that reinforced the bonding of COPAM molecules with modified SiO_2, and inhibit thermal degradation of the polymer and safeguard its backbone to prevent the polymer molecule from rupture under HT-HS conditions.

Chapter 7 Conclusion and recommendations for future work

7.1 Thesis conclusion

Polymer flooding is a traditional chemical EOR process, in which polymer is dispersed in displacing water to reduce viscous fingering and increase sweep efficiency, leading to more oil production. Despite some progress in polymer EOR, there are still many drawbacks that hinder their wide applications due to polymer degradation and instability in harsh reservoir conditions such as high temperature and high salinity (HT-HS).

This project aims to improve the stability, rheology, and flooding performance of polymers in HT-HS conditions by two approaches, i.e., reinforcing polymer chains with desirable NPs to form composites and engineering new temperature-resistant polymers. In addition, a novel synthesis approach to produce suitable nanoparticles *in-situ* in polymers is developed to further improve the polymer performance. Newly formed materials were carefully characterised, and their stability and rheological properties under HT-HS conditions were investigated, as well as their EOR performance in a pilot core-flooding facility.

The finding suggested that the modified composites samples synthesized *in-situ* have better stability, rheological performance, and more oil recovery efficiency at HT-HS condition, than those prepared via a direct mixture of polymer/NPs solutions, showing great promise for future EOR applications. The main conclusions drawn from each Chapter are summarized as below:

1. ***Synthesis and characterization of polymer and polymer nanocomposites via direct mixing process.***

    - The dispersion stability observed using Turbiscan analysis showed HPAM/GO and HPAM/CQDs composites exhibited excellent stability in the presence of NaCl, but unstable when API brine and complex brines were used.

- The FT-IR spectral data confirmed the formation of the covalent linkage and the electrostatic hydrogen bond between GO and HPAM functional groups, which helps to strengthen the hybrid stability. The analyses also suggest the evolution of chemical linkage between segments of HPAM and those of the GO sheets.
- The ATR-FTIR analysis suggests the evolution of chemical linkage between segments of HPAM and those of CQDs. Thus, results in the formation of strong covalent bonding between HPAM/CQDs which occur between the deaminated amine in the polymer backbone and the hydroxyl group in the CQDs.
- The addition of MWCNTs into the polyampholytic terpolymer and polyelectrolyte copolymer containing negative sulfonate groups showed better enhancement in the dispersion stability in both alkali pH and API brine solution, respectively, which could be considered when to select the proper polymer that stabilized under harsh reservoir condition.
- This improvement showed that the copolymer containing sulfonate groups can withstand divalent ions and sustain the steric repulsive forces between polymer branches and the solubility of skeleton acrylamide at high salt contents, by preventing the collapse of the polymer backbone which attracted both mono and divalent ions in the API brine solution, thereby protecting the chains repulsion of the acrylamide chains. Although, the prepared composites are not very stable in a complex brine solution, but showed a great promise for future EOR applications.

2. *In-situ synthesis and characterization of modified polymer nanocomposites under the influence of high ionic strength brines.*

- The copolymer of acrylamide was covalently attached to the rGO via free radical polymerization and further reacted with 1, 3-propane sultone to accomplish zwitterionic groups.
- Comparing to GO-COPAM, zwitterionic-rGO-COPAM dispersions showed that there was no noticeable sedimentation or flocculation observed after visual inspection.
- The particle size measured was smaller with large zeta potentials compared to that of an unmodified solution.
- The instability index derived from Lumisizer was smaller over a storage of 120 days at 80 °C under both APIB and FB conditions. It also showed that the dispersion stability was better in APIB than FB, where the GO sheet conjugated structure may have been altered after 90 days in the formation brine.
- FTIR and other chemical analysis suggested that the formation of zwitterionic character on the rGO-COPAM composites was responsible for the excellent temperature stability and dispersibility in the presence of high salinity and high temperature.
- Such results suggest that the zwitterionic molecules could be used as a stability enhancer for different particles, and the zwitterionic-polyacrylamide-graphene oxide systems possess greater potential for future enhanced oil recovery applications.
- On the other hand, the SiO_2 NPs were successfully functionalised with (3-aminopropyl) triethoxysilane to create positively charged active sites on the surface to form a stable NP dispersion, which facilitates the formation of strong coordination bond with the negatively charged COPAM chain. Three samples including M_SiO_2/COPAM, pure SiO_2/COPAM, and NP-free COPAM were synthesised *in-situ* via free radical polymerisation.

- The outcome of the finding revealed that M_SiO_2 could inhibit the thermal degradation of the polymer and safeguard its backbone to prevent the polymer molecule from rupture under HT-HS conditions. As a result, M_SiO_2/COPAM possessed excellent temperature tolerance and thermal stability in a harsh environment after 90 days of aging.

3. Investigation of the rheological properties of the produced polymers and polymer nanocomposites

- For materials prepared via direct mixing, the viscosity of HPAM/GO composites showed a significant increase with the increasing GO concentrations, while HPAM/CQDs composites showed a decrease in viscosity demonstration a phenomenon which contradicts the expression normally derived from Einstein-Batchelor law for the viscosity of particle suspension.
- The addition of GO increased long-term thermal stability significantly due to the formation of electrostatic hydrogen bonding between the GO and the HPAM functional groups. After aging for 30 days at 80 °C, the viscosity of the composites solution decreases very slightly while a 59 % reduction was observed for pure HPAM solution.
- However, despite the improvement in long-term thermal stability and salinity tolerance of the HPAM/GO composite, the zwitterion-rGO-COPAM composite showed much better thermal and brine stability after aging. These are because at high ionic strength brines, the presence of electrolyte ions can enhance the interactions of the ionic groups in the zwitterionic sulfobetaine polymers, creating the chain's expansion by providing adequate steric repulsion.

- Increasing the GO content increases both storage and loss modulus the HPAM solution, making them favourable for EOR applications, while CQDs decreases the storage and the loss moduli of HPAM as when CQDs concentration increases.
- The increase in HPAM viscosity by the addition of GO could be due to the formation of covalent linkage and the electrostatic hydrogen bond between GO and HPAM functional groups, which helps to strengthen the polymer molecules.
- Two possible schemes are proposed for the decreased viscosity phenomenon, which is: 1- formation of carboxylic acid groups on the COPAM backbone, giving rise to a reaction with hydroxyl groups on the CQDs and the subsequent formation of ester bonds; 2- breakage of long macromolecular chains in the COPAM into smaller chains, with the CQDs being able to protonate the carboxylate groups in the COPAM ($–COO^-$ to –COOH), which make it more acidic and eventually cause a conformational transition of the polymer to change from a stretch-state into a coiled-state.

- The polyampholytic ter-polymer and polyelectrolyte copolymer containing negative sulfonate groups showed better enhancement in both stability and viscosity of MWCNTs/polymer dispersions in alkali and API brine solution respectively.

- The modifier SiO_2 improved COPAM viscosity more than the pure SiO_2, while SiO_2/COPAM and NP-free COPAM had 45 and 78% viscosity reduction after 90 days of aging, only 10% reduction was observed in M_SiO_2/COPAM. Showing better promising compared to traditional SiO_2 NPs. This could be a result of electrostatic attraction that reinforced the bonding of COPAM molecules with modified SiO_2 and inhibit thermal degradation of the polymer that safeguards its backbone from rupture under HT-HS conditions.

4. Enhanced oil recovery using nanoparticles modified polymer solutions

- The pilot core flooding investigation showed a slight increase in oil recovery by HPAM/GO composites than pure HPAM. Whereas zwitterionic-rGO-COPAM composite showed more oil recovery enhancement compared to HPAM and HPAM/GO, respectively, generating about 16.67% and 15.56% in API and FB brine conditions, respectively, with even lower pressure drop. This enhanced performance by zwitterionic-rGO-COPAM could be a result of excelling stability and higher viscosity. Hence, the improved performance by the composite could be a result of the 2D layer of the GO sheets, and the formation of strong linkage and the electrostatic bonding between modified rGO and polymer functional groups, which helps to strengthen the hybrid stability.

- Comparing to the pure polymer solution, the addition of MWCNTs improved the oil recovery efficiency at high temperature (85 °C) in the presence of both alkaline pH and API brine conditions, yet with a lower pressure drop, showing great promise for future EOR applications. The desirability function indicated that viscosity is the main factor responsible for high oil recovery using polymer/MWCNTs at both APIB and alkaline conditions.

- The core flooding experiments showed that the modified SiO_2/COPAM solution provided more oil recovery than those from SiO_2/COPAM and NP-free COPAM solutions in HT-HS conditions. These improved properties of M_SiO_2/COPAM were generated due to the incorporation of amino functional groups on the surface of the SiO_2 NPs, which result in the formation of electrostatic attraction that reinforced the bonding of COPAM molecules with M_SiO_2.

7.2. Recommendation for future work

This project has made progress in finding the materials with excellent thermal, brine, and dispersion stability and prove their potential for future EOR applications. However, to further explore the use of this material for field application, the following recommendations are suggested for future work.

- Develop advanced set-up for core flooding experiments at high temperature and high-pressure conditions.
- Build a high-pressure experimental set-up for the rheological investigation to further explore the potential use of these materials in high-pressure conditions.
- Investigate the adsorption and desorption of polymer/surfactant and their mixture with nanoparticles under reservoir-like conditions.
- More experiments on nanoparticle/polymer-carriers in different reservoir rocks.
- Explore novel ways to apply different nanoparticles as reservoir sensor.
- Explore the method to retrieve the used materials in core flooding to reduce the cost of production.
- Investigate the transport behaviour of polymer and polymer-nanoparticle composite in porous media.
- Understanding the migration behaviour of the nanoparticles, polymers, and their composites with the influence of the oil phase.
- Conduct a numerical simulation analysis of the prepared materials to compare with the experimental findings.
- Future work will also focus on the economic evaluation of the overall project, especially the cost related to the newly produced polymers and polymer-nanocomposites in comparison to the conventional polymers used in traditional EOR. This will actualize the applicability of the new materials for future EOR applications.

List of references

1. Zekri, A. and K. Jerbi, *Economic evaluation of enhanced oil recovery.* Oil & Gas Science and Technology, 2002. **57**(3): p. 259-267.
2. Hashemi, R., N.N. Nassar, and P.P. Almao, *Nanoparticle technology for heavy oil in-situ upgrading and recovery enhancement: Opportunities and challenges.* Applied Energy, 2014. **133**: p. 374-387.
3. Energy Outlook. *Energy Consumption World Wide*. 2017; Available from: https://www.confusedaboutenergy.co.uk/index.php/climate-and-the-environment/56-energy-consumption-world-wide#.WIXjZFOLSUk.
4. Agarwal, A.K., *Biofuels (alcohols and biodiesel) applications as fuels for internal combustion engines.* Progress in energy and combustion science, 2007. **33**(3): p. 233-271.
5. Hite, J.R. and P.L. Bondor. *Planning EOR Projects*. in *SPE International Petroleum Conference in Mexico*. 2004. Society of Petroleum Engineers.
6. Lu, J., et al., *New surfactant developments for chemical enhanced oil recovery.* Journal of Petroleum Science and Engineering, 2014. **120**: p. 94-101.
7. Terry, R.E., *Enhanced oil recovery.* Encyclopedia of physical science and technology, 2001. **18**: p. 503-518.
8. Lake, L., *W., 1989, Enhanced Oil Recovery*. 1989, Englewood Cliffs, New Jersey, USA: Prentice Hall.
9. Meyers, R.A., *Encyclopedia of physical science and technology*. 1987: Academic Press.
10. Gozalpour, F., S. Ren, and B. Tohidi, *CO2 EOR and storage in oil reservoir.* Oil & gas science and technology, 2005. **60**(3): p. 537-546.
11. Broze, G., *Handbook of Detergents, Part A: Properties*. 1999, CRC Press.
12. Schramm, L.L., *Surfactants: fundamentals and applications in the petroleum industry*. 2000: Cambridge University Press.
13. Green, D.W. and G.P. Willhite, *Enhanced oil recovery*. 1998: Richardson, Tex.: Henry L. Doherty Memorial Fund of AIME, Society of Petroleum Engineers.
14. Goddard, E.D. and K.P. Ananthapadmanabhan, *Interactions of surfactants with polymers and proteins*. 1993: CRC press.
15. Samanta, A., et al., *Mobility control and enhanced oil recovery using partially hydrolysed polyacrylamide (PHPA).* International Journal of Oil, Gas and Coal Technology, 2013. **6**(3): p. 245-258.
16. Buckley, S.E. and M. Leverett, *Mechanism of fluid displacement in sands.* Transactions of the AIME, 1942. **146**(01): p. 107-116.
17. Lyons, W., *Working Guide to Reservoir Engineering*. 2009: Gulf Professional Publishing.
18. Neil, J., H. Chang, and T. Geffen, *Waterflooding and improved waterflooding.* Improved Oil Recovery, 1983.
19. Cossé, R., *Basics of reservoir engineering: oil and gas field development techniques*. 1993: Éditions Technip.
20. Thomas, A., *Polymer Flooding*, in *Chemical Enhanced Oil Recovery (cEOR)-a Practical Overview*. 2016, InTech.
21. Ju, B., et al. *A study of wettability and permeability change caused by adsorption of nanometer structured polysilicon on the surface of porous media*. in *SPE Asia Pacific Oil and Gas Conference and Exhibition*. 2002. Society of Petroleum Engineers.
22. Krishnamoorti, R., *Extracting the benefits of nanotechnology for the oil industry.* Journal of petroleum technology, 2006. **58**(11): p. 24-26.
23. Wen, D., et al., *Review of nanofluids for heat transfer applications.* Particuology, 2009. **7**(2): p. 141-150.

24. El-Diasty, A.I. and A.M.S. Ragab. *Applications of Nanotechnology in the Oil & Gas Industry: Latest Trends Worldwide & Future Challenges in Egypt*. in *North Africa Technical Conference and Exhibition*. 2013. Society of Petroleum Engineers.
25. Bennetzen, M.V. and K. Mogensen. *Novel Applications of Nanoparticles for Future Enhanced Oil Recovery*. in *International Petroleum Technology Conference*. 2014. International Petroleum Technology Conference.
26. Green, D.W. and G.P. Willhite, *Enhanced oil recovery*. Vol. 6. 1998: Henry L. Doherty Memorial Fund of AIME, Society of Petroleum Engineers Richardson, TX.
27. Zhu, D., et al., *Laboratory study on the potential EOR use of HPAM/VES hybrid in high-temperature and high-salinity oil reservoirs.* Journal of Chemistry, 2013. **2013**.
28. Sorbie, K.S., *Polymer-improved oil recovery*. 2013: Springer Science & Business Media.
29. Broseta, D., et al., *Polymer Adsorption/Retention in porous media: Effects of core wettability on residual oil.* SPE Advanced Technology Series, 1995. **3**(01): p. 103-112.
30. Chiappa, L., et al., *Polymer adsorption at the brine/rock interface: the role of electrostatic interactions and wettability.* Journal of petroleum science and engineering, 1999. **24**(2): p. 113-122.
31. Sheng, J.J., B. Leonhardt, and N. Azri, *Status of polymer-flooding technology.* Journal of Canadian Petroleum Technology, 2015. **54**(02): p. 116-126.
32. Sheng, J.J., *Enhanced Oil Recovery Field Case Studies: Chapter 3. Polymer Flooding — Fundamentals and Field Cases*. 2013: Elsevier Inc. Chapters.
33. Wang, D., et al. *Sweep improvement options for the Daqing oil field*. in *SPE/DOE symposium on improved oil recovery*. 2006. Society of Petroleum Engineers.
34. Hussein, I.A., et al., *Rheological behavior of associating ionic polymers based on diallylammonium salts containing single-, twin-, and triple-tailed hydrophobes.* European Polymer Journal, 2010. **46**(5): p. 1063-1073.
35. Li, X.e., et al., *Comparative studies on enhanced oil recovery: Thermoviscosifying polymer versus polyacrylamide.* Energy & Fuels, 2017. **31**(3): p. 2479-2487.
36. Chen, Q., et al., *Thermoviscosifying polymer used for enhanced oil recovery: rheological behaviors and core flooding test.* Polymer bulletin, 2013. **70**(2): p. 391-401.
37. Deng, Y., et al., *Bonding between polyacrylamide and smectite.* Colloids and Surfaces A: Physicochemical and Engineering Aspects, 2006. **281**(1-3): p. 82-91.
38. Littman, W., *Polymer Flooding: Developments in Petroleum Science*. 1998, Elsevier, Amsterdam.
39. Atesok, G., P. Somasundaran, and L. Morgan, *Charge effects in the adsorption of polyacrylamides on sodium kaolinite and its flocculation.* Powder technology, 1988. **54**(2): p. 77-83.
40. Lee, L., J. Lecourtier, and G. Chauveteau, *Influence of calcium on adsorption properties of enhanced oil recovery polymers*. 1989, ACS Publications.
41. Cook, R.L., H. King Jr, and D.G. Peiffer, *High-pressure viscosity of dilute polymer solutions in good solvents.* Macromolecules, 1992. **25**(11): p. 2928-2934.
42. Lecourtier, J., L. Lee, and G. Chauveteau, *Adsorption of polyacrylamides on siliceous minerals.* Colloids and Surfaces, 1990. **47**: p. 219-231.
43. Mandal, A. and A. Bera, *Surfactant stabilized nanoemulsion: characterization and application in enhanced oil recovery.* World Academy of Science, Engineering and Technology, International Journal of Chemical, Molecular, Nuclear, Materials and Metallurgical Engineering, 2012. **6**(7): p. 537-542.
44. Morel, D.C., et al., *First polymer injection in deep offshore field Angola: recent advances in the Dalia/Camelia field case.* Oil and Gas Facilities, 2012. **1**(02): p. 43-52.
45. Zitha, P., K. Van Os, and K. Denys. *Adsorption of Linear Flexible Polymers during Laminar Flow through Porous Media*. in *SPE/DOE improved oil recovery symposium*. 1998. Society of Petroleum Engineers.

46. Jung, J.C., et al., *Rheology and polymer flooding characteristics of partially hydrolyzed polyacrylamide for enhanced heavy oil recovery.* Journal of Applied Polymer Science, 2013. **127**(6): p. 4833-4839.
47. Spildo, K. and E.I. Sæ, *Effect of Charge Distribution on the Viscosity and Viscoelastic Properties of Partially Hydrolyzed Polyacrylamide.* Energy & Fuels, 2015. **29**(9): p. 5609-5617.
48. Zhu, D., et al., *Enhancing rheological properties of hydrophobically associative polyacrylamide aqueous solutions by hybriding with silica nanoparticles.* Journal of Applied Polymer Science, 2014. **131**(19).
49. Lu, H., et al., *Retention behaviors of hydrophobically associating polyacrylamide prepared via inverse microemulsion polymerization through porous media.* Journal of Macromolecular Science, Part A: Pure and Applied Chemistry, 2010. **47**(6): p. 602-607.
50. Sheng, J., *Modern chemical enhanced oil recovery: theory and practice*. 2010: Gulf Professional Publishing.
51. Zhang, G. and R. Seright, *Effect of concentration on HPAM retention in porous media.* SPE Journal, 2014. **19**(03): p. 373-380.
52. Gbadamosi, A.O., et al., *An overview of chemical enhanced oil recovery: recent advances and prospects.* International Nano Letters, 2019: p. 1-32.
53. Pospíšil, J., et al., *Degradation and aging of polymer blends I. Thermomechanical and thermal degradation.* Polymer Degradation and Stability, 1999. **65**(3): p. 405-414.
54. Wang, W., Y. Liu, and Y. Gu, *Application of a novel polymer system in chemical enhanced oil recovery (EOR).* Colloid and Polymer Science, 2003. **281**(11): p. 1046-1054.
55. Mothé, C., et al., *Thermal and rheological study of polysaccharides for enhanced oil recovery.* Journal of thermal analysis and calorimetry, 2006. **85**(1): p. 31-36.
56. Seright, R.S., et al., *Stability of partially hydrolyzed polyacrylamides at elevated temperatures in the absence of divalent cations.* Spe Journal, 2010. **15**(02): p. 341-348.
57. Erdlac Jr, R., et al. *Ongoing resource assessment of geothermal energy from sedimentary basins in Texas*. in *Proceedings, thirty-second workshop on geothermal reservoir engineering, Stanford University, Stanford, SGP-TR-183*. 2007.
58. Kopperud, H.M., F.K. Hansen, and B. Nyström, *Effect of surfactant and temperature on the rheological properties of aqueous solutions of unmodified and hydrophobically modified polyacrylamide.* Macromolecular Chemistry and Physics, 1998. **199**(11): p. 2385-2394.
59. Shaikh, S., et al., *Synthesis and solution properties of poly (acrylamide - styrene) block copolymers with high hydrophobic content.* Polymer Engineering & Science, 1999. **39**(10): p. 1962-1968.
60. McCormick, C.L., T. Nonaka, and C.B. Johnson, *Water-soluble copolymers: 27. Synthesis and aqueous solution behaviour of associative acrylamideN-alkylacrylamide copolymers.* Polymer, 1988. **29**(4): p. 731-739.
61. Samanta, A., et al., *Effects of alkali, salts, and surfactant on rheological behavior of partially hydrolyzed polyacrylamide solutions.* Journal of Chemical & Engineering Data, 2010. **55**(10): p. 4315-4322.
62. Sabhapondit, A., A. Borthakur, and I. Haque, *Characterization of acrylamide polymers for enhanced oil recovery.* Journal of applied polymer science, 2003. **87**(12): p. 1869-1878.
63. Zhu, D., et al., *Aqueous hybrids of silica nanoparticles and hydrophobically associating hydrolyzed polyacrylamide used for EOR in high-temperature and high-salinity reservoirs.* Energies, 2014. **7**(6): p. 3858-3871.
64. Dawson, R. and R.B. Lantz, *Inaccessible pore volume in polymer flooding.* Society of Petroleum Engineers Journal, 1972. **12**(05): p. 448-452.
65. Littmann, W., *Polymer flooding*. Vol. 24. 1988: Elsevier.
66. Schramm, G., *A practical approach to rheology and rheometry*. 1994: Haake Karlsruhe.
67. Lasfargues, M., *Nitrate based high temperature nano-heat-transfer-fluids: formulation & characterisation*. 2014, University of Leeds.

68. Vermolen, E., M. Van Haasterecht, and S. Masalmeh. *A systematic study of the polymer visco-elastic effect on residual oil saturation by core flooding*. in *SPE EOR Conference at Oil and Gas West Asia*. 2014. Society of Petroleum Engineers.
69. Mezger, T.G., *The rheology handbook: for users of rotational and oscillatory rheometers*. 2006: Vincentz Network GmbH & Co KG.
70. Løbø Viken, A., T. Skauge, and K. Spildo, *Rheological properties of a hydrophobically modified anionic polymer: effect of varying salinity and amount of hydrophobic moieties.* Journal of Applied Polymer Science, 2016.
71. Masuda, Y., et al., *1D simulation of polymer flooding including the viscoelastic effect of polymer solution.* SPE reservoir engineering, 1992. **7**(02): p. 247-252.
72. Delshad, M., et al. *Mechanistic interpretation and utilization of viscoelastic behavior of polymer solutions for improved polymer-flood efficiency*. in *SPE Symposium on Improved Oil Recovery*. 2008. Society of Petroleum Engineers.
73. Pye, D.J., *Improved secondary recovery by control of water mobility.* Journal of Petroleum technology, 1964. **16**(08): p. 911-916.
74. Jennings, R., J. Rogers, and T. West, *Factors influencing mobility control by polymer solutions.* Journal of Petroleum Technology, 1971. **23**(03): p. 391-401.
75. Seright, R.S., J.M. Seheult, and T. Talashek. *Injectivity characteristics of EOR polymers*. in *SPE annual technical conference and exhibition*. 2008. Society of Petroleum Engineers.
76. Seright, R.S., et al., *Rheology of a new sulfonic associative polymer in porous media.* SPE Reservoir Evaluation & Engineering, 2011. **14**(06): p. 726-734.
77. Sun, Y., L. Saleh, and B. Bai, *Measurement and impact factors of polymer rheology in porous media.* Rheology, InTech, 2012: p. 187-202.
78. Elias, H.-G., *Macromolecules, Volume 3: Physical Structures and Properties*. Vol. 3. 2008: Wiley-VCH.
79. Dong, H., et al. *Review of practical experience & management by polymer flooding at Daqing*. in *SPE Symposium on Improved Oil Recovery*. 2008. Society of Petroleum Engineers.
80. Zhang, X., et al. *A Novel Method of Optimizing the Moelcular Weight of Polymer Flooding*. in *SPE Enhanced Oil Recovery Conference*. 2011. Society of Petroleum Engineers.
81. Maerker, J., *Mechanical degradation of partially hydrolyzed polyacrylamide solutions in unconsolidated porous media.* Society of Petroleum Engineers Journal, 1976. **16**(04): p. 172-174.
82. Aluhwal, O.K.H. and O. Kalifa, *Simulation study of improving oil recovery by polymer flooding in a Malaysian reservoir.* Masters disserta-tion, University Technology of Malaysia, 2008.
83. Taylor, K. and H. Nasr-El-Din. *Hydrophobically associating polymers for oil field applications*. in *Canadian International Petroleum Conference*. 2007. Petroleum Society of Canada.
84. Gao, C., *Viscosity of partially hydrolyzed polyacrylamide under shearing and heat.* Journal of Petroleum Exploration and Production Technology, 2013. **3**(3): p. 203-206.
85. Kelsall, R.W., I.W. Hamley, and M. Geoghegan, *Nanoscale science and technology*. 2005: Wiley Online Library.
86. Mongillo, J.F., *Nanotechnology 101*. 2007: ABC-CLIO.
87. Engeset, B., *The Potential of Hydrophilic Silica Nanoparticles for EOR Purposes: A literateur review and an experimental study.* 2012.
88. Hendraningrat, L., S. Li, and O. Torsæter, *A coreflood investigation of nanofluid enhanced oil recovery.* Journal of Petroleum Science and Engineering, 2013. **111**: p. 128-138.
89. Miranda, C.R., L.S.d. Lara, and B.C. Tonetto. *Stability and mobility of functionalized silica nanoparticles for enhanced oil recovery applications*. in *SPE International Oilfield Nanotechnology Conference and Exhibition*. 2012. Society of Petroleum Engineers.
90. Nazari Moghaddam, R., et al., *Comparative study of using nanoparticles for enhanced oil recovery: wettability alteration of carbonate rocks.* Energy & Fuels, 2015. **29**(4): p. 2111-2119.

91. Cheraghian, G. and L. Hendraningrat, *A review on applications of nanotechnology in the enhanced oil recovery part B: effects of nanoparticles on flooding.* International Nano Letters, 2016. **6**(1): p. 1-10.
92. Cheraghian, G., *Effects of titanium dioxide nanoparticles on the efficiency of surfactant flooding of heavy oil in a glass micromodel.* Petroleum Science and Technology, 2016. **34**(3): p. 260-267.
93. Cheraghian, G., *Effects of nanoparticles on wettability: A review on applications of nanotechnology in the enhanced Oil recovery.* International Journal of Nano Dimension, 2015. **6**(5): p. 443-452.
94. Jafarnezhad, M., M.S. Giri, and M. Alizadeh, *Impact of SnO2 nanoparticles on enhanced oil recovery from carbonate media.* Energy Sources, Part A: Recovery, Utilization, and Environmental Effects, 2017. **39**(1): p. 121-128.
95. Shokrlu, Y.H. and T. Babadagli. *Transportation and interaction of nano and micro size metal particles injected to improve thermal recovery of heavy-oil*. in *SPE Annual Technical Conference and Exhibition*. 2011. Society of Petroleum Engineers.
96. Alomair, O.A., K.M. Matar, and Y.H. Alsaeed. *Nanofluids application for heavy oil recovery*. in *SPE Asia Pacific Oil & Gas Conference and Exhibition*. 2014. Society of Petroleum Engineers.
97. Tarboush, B.J.A. and M.M. Husein, *Adsorption of asphaltenes from heavy oil onto in situ prepared NiO nanoparticles.* Journal of colloid and interface science, 2012. **378**(1): p. 64-69.
98. Kazemzadeh, Y., et al., *Behavior of asphaltene adsorption onto the metal oxide nanoparticle surface and its effect on heavy oil recovery.* Industrial & Engineering Chemistry Research, 2015. **54**(1): p. 233-239.
99. Luo, D., et al., *Nanofluid of graphene-based amphiphilic Janus nanosheets for tertiary or enhanced oil recovery: High performance at low concentration.* Proceedings of the National Academy of Sciences, 2016. **113**(28): p. 7711-7716.
100. Tongwa, P. and B. Bai, *Degradable nanocomposite preformed particle gel for chemical enhanced oil recovery applications.* Journal of Petroleum Science and Engineering, 2014. **124**: p. 35-45.
101. Ye, Z., et al., *Synthesis and performance of an acrylamide copolymer containing nano-SiO 2 as enhanced oil recovery chemical.* Journal of Chemistry, 2013. **2013**.
102. Thomas, A., N. Gaillard, and C. Favero, *Some key features to consider when studying acrylamide-based polymers for chemical enhanced oil recovery.* Oil & Gas Science and Technology–Revue d'IFP Energies nouvelles, 2012. **67**(6): p. 887-902.
103. Heller, H. and R. Keren, *Anionic polyacrylamide polymers effect on rheological behavior of sodium-montmorillonite suspensions.* Soil Science Society of America Journal, 2002. **66**(1): p. 19-25.
104. Nair, N., et al., *Coarse-Grained Simulations of Polymer-Grafted Nanoparticles: Structural Stability and Interfacial Behavior.* The Journal of Physical Chemistry B, 2016. **120**(35): p. 9523-9539.
105. Kumar, S.K. and R. Krishnamoorti, *Nanocomposites: structure, phase behavior, and properties.* Annual review of chemical and biomolecular engineering, 2010. **1**: p. 37-58.
106. El-Diasty, A.I. and A.M. Aly. *Understanding the Mechanism of Nanoparticles Applications in Enhanced Oil Recovery*. in *SPE North Africa Technical Conference and Exhibition*. 2015. Society of Petroleum Engineers.
107. Maghzi, A., et al., *The impact of silica nanoparticles on the performance of polymer solution in presence of salts in polymer flooding for heavy oil recovery.* Fuel, 2014. **123**: p. 123-132.
108. Hu, Z., et al., *Rheological Properties of Partially Hydrolyzed Polyacrylamide Seeded by Nanoparticles.* Industrial & Engineering Chemistry Research, 2017. **56**(12): p. 3456-3463.
109. Sharma, T., S. Iglauer, and J.S. Sangwai, *Silica nanofluids in an oilfield polymer polyacrylamide: interfacial properties, wettability alteration, and applications for chemical*

enhanced oil recovery. Industrial & Engineering Chemistry Research, 2016. **55**(48): p. 12387-12397.
110. Saito, Y., H. Ogura, and Y. Otsubo, *Rheological behavior of silica suspensions in aqueous solutions of associating polymer.* Colloid and polymer science, 2008. **286**(13): p. 1537-1544.
111. Cheraghian, G., *Thermal resistance and application of nanoclay on polymer flooding in heavy oil recovery.* Petroleum Science and Technology, 2015. **33**(17-18): p. 1580-1586.
112. Suleimanov, B., F. Ismailov, and E. Veliyev, *Nanofluid for enhanced oil recovery.* Journal of Petroleum Science and Engineering, 2011. **78**(2): p. 431-437.
113. Ehtesabi, H., M.M. Ahadian, and V. Taghikhani, *Enhanced heavy oil recovery using TiO2 nanoparticles: investigation of deposition during transport in core plug.* Energy & Fuels, 2014. **29**(1): p. 1-8.
114. Tarek, M. and A.H. El-Banbi. *Comprehensive investigation of effects of nano-fluid mixtures to enhance oil recovery*. in *SPE North Africa technical conference and exhibition*. 2015. Society of Petroleum Engineers.
115. Ogolo, N., O. Olafuyi, and M. Onyekonwu. *Enhanced oil recovery using nanoparticles*. in *SPE Saudi Arabia Section Technical Symposium and Exhibition*. 2012. Society of Petroleum Engineers.
116. Nares, H.R., et al. *Heavy-crude-oil upgrading with transition metals*. in *Latin American & caribbean petroleum engineering conference*. 2007. Society of Petroleum Engineers.
117. Kashefi, S., M.N. Lotfollahi, and A. Shahrabadi, *Investigation of asphaltene adsorption onto zeolite beta nanoparticles to reduce asphaltene deposition in a silica sand pack.* Oil & Gas Sciences and Technology–Revue d'IFP Energies nouvelles, 2018. **73**: p. 2.
118. Iglauer, S., et al., *New surfactant classes for enhanced oil recovery and their tertiary oil recovery potential.* Journal of Petroleum Science and Engineering, 2010. **71**(1): p. 23-29.
119. Howe, A.M., et al., *Visualising surfactant enhanced oil recovery.* Colloids and Surfaces A: Physicochemical and Engineering Aspects, 2015. **480**: p. 449-461.
120. Roustaei, A., S. Saffarzadeh, and M. Mohammadi, *An evaluation of modified silica nanoparticles' efficiency in enhancing oil recovery of light and intermediate oil reservoirs.* Egyptian Journal of Petroleum, 2013. **22**(3): p. 427-433.
121. Mohajeri, M., M. Hemmati, and A.S. Shekarabi, *An experimental study on using a nanosurfactant in an EOR process of heavy oil in a fractured micromodel.* Journal of Petroleum Science and Engineering, 2015. **126**: p. 162-173.
122. Moradi, B., et al. *Application of SiO 2 nano particles to improve the performance of water alternating gas EOR process*. in *SPE Oil & Gas India Conference and Exhibition*. 2015. Society of Petroleum Engineers.
123. Hu, Z., et al., *Nanoparticle-assisted water-flooding in Berea sandstones.* Energy & Fuels, 2016. **30**(4): p. 2791-2804.
124. Zhang, H., A. Nikolov, and D. Wasan, *Enhanced oil recovery (EOR) using nanoparticle dispersions: underlying mechanism and imbibition experiments.* Energy & Fuels, 2014. **28**(5): p. 3002-3009.
125. Frijters, S., F. Günther, and J. Harting, *Effects of nanoparticles and surfactant on droplets in shear flow.* Soft Matter, 2012. **8**(24): p. 6542-6556.
126. Ahmadi, M.A. and S.R. Shadizadeh, *Induced effect of adding nano silica on adsorption of a natural surfactant onto sandstone rock: experimental and theoretical study.* Journal of Petroleum Science and Engineering, 2013. **112**: p. 239-247.
127. Bagrezaie, M.A. and P. Pourafshary, *Improvement of Surfactant Flooding Performance by Application of Nanoparticles in Sandstone Reservoirs.* Journal of the Japan Petroleum Institute, 2015. **58**(2): p. 97-102.
128. Hendraningrat, L. and L. Shidong. *A glass micromodel experimental study of hydrophilic nanoparticles retention for EOR project*. in *SPE Russian Oil and Gas Exploration and Production Technical Conference and Exhibition*. 2012. Society of Petroleum Engineers.

129. Morrow, N.R., *Wettability and its effect on oil recovery.* Journal of Petroleum Technology, 1990. **42**(12): p. 1,476-1,484.
130. Ju, B., T. Fan, and M. Ma, *Enhanced oil recovery by flooding with hydrophilic nanoparticles.* China Particuology, 2006. **4**(01): p. 41-46.
131. Han, D., et al. *The effect of wettability on oil recovery by alkaline/surfactant/polymer flooding*. in *SPE Annual Technical Conference and Exhibition*. 2006. Society of Petroleum Engineers.
132. Nwidee, L.N., et al., *Nanoparticles influence on wetting behaviour of fractured limestone formation.* Journal of Petroleum Science and Engineering, 2017. **149**: p. 782-788.
133. Jiang, R., K. Li, and R. Horne. *A mechanism study of wettability and interfacial tension for EOR using silica nanoparticles*. in *SPE Annual Technical Conference and Exhibition*. 2017. Society of Petroleum Engineers.
134. Hendraningrat, L., S. Li, and O. Torsaeter. *Enhancing oil recovery of low-permeability berea sandstone through optimised nanofluids concentration*. in *SPE enhanced oil recovery conference*. 2013. Society of Petroleum Engineers.
135. Shahrabadi, A., et al. *Experimental investigation of hlp nanofluid potential to enhance oil recovery: A mechanistic approach*. in *SPE International Oilfield Nanotechnology Conference and Exhibition*. 2012. Society of Petroleum Engineers.
136. Hendraningrat, L. and O. Torsæter, *Metal oxide-based nanoparticles: revealing their potential to enhance oil recovery in different wettability systems.* Applied Nanoscience, 2015. **5**(2): p. 181-199.
137. Chengara, A., et al., *Spreading of nanofluids driven by the structural disjoining pressure gradient.* Journal of colloid and interface science, 2004. **280**(1): p. 192-201.
138. Wasan, D.T. and A.D. Nikolov, *Spreading of nanofluids on solids.* Nature, 2003. **423**(6936): p. 156-159.
139. Wasan, D., A. Nikolov, and K. Kondiparty, *The wetting and spreading of nanofluids on solids: Role of the structural disjoining pressure.* Current Opinion in Colloid & Interface Science, 2011. **16**(4): p. 344-349.
140. Karimi, A., et al., *Wettability alteration in carbonates using zirconium oxide nanofluids: EOR implications.* Energy & Fuels, 2012. **26**(2): p. 1028-1036.
141. Joonaki, E. and S. Ghanaatian, *The application of nanofluids for enhanced oil recovery: effects on interfacial tension and coreflooding process.* Petroleum Science and Technology, 2014. **32**(21): p. 2599-2607.
142. Hendraningrat, L. and O. Torsaeter. *Unlocking the potential of metal oxides nanoparticles to enhance the oil recovery*. in *Offshore Technology Conference-Asia*. 2014. Offshore Technology Conference.
143. Li, S., et al. *Effect of silica nanoparticles adsorption on the wettability index of Berea sandstone*. in *Paper SCA2013-059 presented at the international symposium of the society of core analysts held in Napa Valley, California, USA*. 2013.
144. Maghzi, A., et al., *Monitoring wettability alteration by silica nanoparticles during water flooding to heavy oils in five-spot systems: A pore-level investigation.* Experimental Thermal and Fluid Science, 2012. **40**: p. 168-176.
145. Vafaei, S., et al., *Effect of nanoparticles on sessile droplet contact angle.* Nanotechnology, 2006. **17**(10): p. 2523.
146. Hendraningrat, L. and O. Torsæter. *Understanding fluid-fluid and fluid-rock interactions in the presence of hydrophilic nanoparticles at various conditions*. in *SPE Asia Pacific Oil & Gas Conference and Exhibition*. 2014. Society of Petroleum Engineers.
147. Li, S., L. Hendraningrat, and O. Torsaeter. *Improved Oil Recovery by Hydrophilic Silica Nanoparticles Suspension: 2 Phase Flow Experimental Studies*. in *IPTC 2013: International Petroleum Technology Conference*. 2013.

148. Roustaei, A. and H. Bagherzadeh, *Experimental investigation of SiO 2 nanoparticles on enhanced oil recovery of carbonate reservoirs.* Journal of Petroleum Exploration and Production Technology, 2015. **5**(1): p. 27-33.
149. Mcelfresh, P.M., D.L. Holcomb, and D. Ector. *Application of nanofluid technology to improve recovery in oil and gas wells*. in *SPE International Oilfield Nanotechnology Conference and Exhibition*. 2012. Society of Petroleum Engineers.
150. Sethumadhavan, G.N., A.D. Nikolov, and D.T. Wasan, *Stability of liquid films containing monodisperse colloidal particles.* Journal of colloid and interface science, 2001. **240**(1): p. 105-112.
151. Kondiparty, K., et al., *Wetting and spreading of nanofluids on solid surfaces driven by the structural disjoining pressure: statics analysis and experiments.* Langmuir, 2011. **27**(7): p. 3324-3335.
152. Skauge, T., K. Spildo, and A. Skauge. *Nano-sized particles for EOR*. in *SPE Improved Oil Recovery Symposium*. 2010. Society of Petroleum Engineers.
153. Sun, X., et al., *Application of nanoparticles in enhanced oil recovery: a critical review of recent progress.* Energies, 2017. **10**(3): p. 345.
154. Yu, J., et al. *Transport study of nanoparticles for oilfield application*. in *SPE International Conference on Oilfield Scale*. 2010. Society of Petroleum Engineers.
155. Kanj, M.Y., J.J. Funk, and Z. Al-Yousif. *Nanofluid coreflood experiments in the ARAB-D*. in *SPE Saudi Arabia Section Technical Symposium*. 2009. Society of Petroleum Engineers.
156. Onyekonwu, M.O. and N.A. Ogolo. *Investigating the use of nanoparticles in enhancing oil recovery*. in *Nigeria Annual International Conference and Exhibition*. 2010. Society of Petroleum Engineers.
157. Jordan, J., et al., *Experimental trends in polymer nanocomposites—a review.* Materials science and engineering: A, 2005. **393**(1): p. 1-11.
158. Hanemann, T. and D.V. Szabó, *Polymer-nanoparticle composites: from synthesis to modern applications.* Materials, 2010. **3**(6): p. 3468-3517.
159. Schmidt, G. and M.M. Malwitz, *Properties of polymer–nanoparticle composites.* Current opinion in colloid & interface science, 2003. **8**(1): p. 103-108.
160. Chatterjee, T. and R. Krishnamoorti, *Rheology of polymer carbon nanotubes composites.* Soft Matter, 2013. **9**(40): p. 9515-9529.
161. Tanahashi, M., *Development of fabrication methods of filler/polymer nanocomposites: With focus on simple melt-compounding-based approach without surface modification of nanofillers.* Materials, 2010. **3**(3): p. 1593-1619.
162. Khan, W.S., N.N. Hamadneh, and W.A. Khan, *Polymer nanocomposites–synthesis techniques, classification and properties.* Science and applications of Tailored Nanostructures: One Central Press (OCP), 2016.
163. Jin, L., C. Bower, and O. Zhou, *Alignment of carbon nanotubes in a polymer matrix by mechanical stretching.* Applied physics letters, 1998. **73**(9): p. 1197-1199.
164. Coleman, J.N., et al., *High performance nanotube - reinforced plastics: Understanding the mechanism of strength increase.* Advanced Functional Materials, 2004. **14**(8): p. 791-798.
165. Cadek, M., et al., *Reinforcement of polymers with carbon nanotubes: the role of nanotube surface area.* Nano Letters, 2004. **4**(2): p. 353-356.
166. Cadek, M., et al., *Morphological and mechanical properties of carbon-nanotube-reinforced semicrystalline and amorphous polymer composites.* Applied physics letters, 2002. **81**(27): p. 5123-5125.
167. Nourafkan, E., et al., *Improved rheological properties and stability of multiwalled carbon nanotubes/polymer in harsh environment.* Journal of Applied Polymer Science, 2018: p. 47205.
168. Jia, Z., et al., *Study on poly (methyl methacrylate)/carbon nanotube composites.* Materials Science and Engineering: A, 1999. **271**(1-2): p. 395-400.

169. Cheng, Y., et al., *Preparation and properties of transparent bulk polymer nanocomposites with high nanophase contents.* Journal of Materials Chemistry, 2008. **18**(34): p. 4062-4068.
170. Shen, Y., et al., *High dielectric performance of polymer composite films induced by a percolating interparticle barrier layer.* Advanced Materials, 2007. **19**(10): p. 1418-1422.
171. Althues, H., et al., *Synthesis and characterization of transparent luminescent ZnS: Mn/PMMA nanocomposites.* Chemistry of materials, 2006. **18**(4): p. 1068-1072.
172. Li, H., et al., *A Highly Transparent and Luminescent Hybrid Based on the Copolymerization of Surfactant‐Encapsulated Polyoxometalate and Methyl Methacrylate.* Advanced Materials, 2005. **17**(22): p. 2688-2692.
173. Liu, H., S. Zheng, and K. Nie, *Morphology and thermomechanical properties of organic–inorganic hybrid composites involving epoxy resin and an incompletely condensed polyhedral oligomeric silsesquioxane.* Macromolecules, 2005. **38**(12): p. 5088-5097.
174. Demir, M.M., et al., *Optical properties of composites of PMMA and surface-modified zincite nanoparticles.* Macromolecules, 2007. **40**(4): p. 1089-1100.
175. Khrenov, V., et al., *Surface functionalized ZnO particles designed for the use in transparent nanocomposites.* Macromolecular Chemistry and Physics, 2005. **206**(1): p. 95-101.
176. Demir, M.M., et al., *PMMA/zinc oxide nanocomposites prepared by in‐situ bulk polymerization.* Macromolecular Rapid Communications, 2006. **27**(10): p. 763-770.
177. Liu, Y., et al., *High clay content nanocomposite hydrogels with surprising mechanical strength and interesting deswelling kinetics.* Polymer, 2006. **47**(1): p. 1-5.
178. Sirousazar, M., et al., *Polyvinyl alcohol/Na-montmorillonite nanocomposite hydrogels prepared by freezing–thawing method: Structural, mechanical, thermal, and swelling properties.* Journal of Macromolecular Science, Part B, 2012. **51**(7): p. 1335-1350.
179. Haraguchi, K., et al., *Mechanism of forming organic/inorganic network structures during in-situ free-radical polymerization in PNIPA–clay nanocomposite hydrogels.* Macromolecules, 2005. **38**(8): p. 3482-3490.
180. Haraguchi, K., T. Takehisa, and S. Fan, *Effects of clay content on the properties of nanocomposite hydrogels composed of poly (N-isopropylacrylamide) and clay.* Macromolecules, 2002. **35**(27): p. 10162-10171.
181. Aalaie, J. and A. Rahmatpour, *Preparation and swelling behavior of partially hydrolyzed polyacrylamide nanocomposite hydrogels in electrolyte solutions.* Journal of Macromolecular Science, Part B, 2007. **47**(1): p. 98-108.
182. Haraguchi, K. and T. Takehisa, *Nanocomposite hydrogels: a unique organic-inorganic network structure with extraordinary mechanical, optical, and swelling/de-swelling properties.* Advanced Materials, 2002. **14**(16): p. 1120.
183. Tongwa, P., R. Nygaard, and B. Bai, *Evaluation of a nanocomposite hydrogel for water shut-off in enhanced oil recovery applications: Design, synthesis, and characterization.* Journal of Applied Polymer Science, 2013. **128**(1): p. 787-794.
184. Okay, O. and W. Oppermann, *Polyacrylamide–Clay Nanocomposite Hydrogels: Rheological and Light Scattering Characterization.* Macromolecules, 2007. **40**(9): p. 3378-3387.
185. Aalaie, J., et al., *Effect of montmorillonite on gelation and swelling behavior of sulfonated polyacrylamide nanocomposite hydrogels in electrolyte solutions.* European Polymer Journal, 2008. **44**(7): p. 2024-2031.
186. Zolfaghari, R., et al., *Preparation and characterization of nanocomposite hydrogels based on polyacrylamide for enhanced oil recovery applications.* Journal of applied polymer science, 2006. **100**(3): p. 2096-2103.
187. Aalaie, J. and M. Youssefi, *Study on the dynamic rheometry and swelling properties of the polyacrylamide/laponite nanocomposite hydrogels in electrolyte media.* Journal of Macromolecular Science, Part B, 2012. **51**(6): p. 1027-1040.

188. Hu, G., et al., *Low percolation thresholds of electrical conductivity and rheology in poly (ethylene terephthalate) through the networks of multi-walled carbon nanotubes.* Polymer, 2006. **47**(1): p. 480-488.
189. Xu, G., et al., *Rheology of a low‐filled polyamide 6/montmorillonite nanocomposite.* Journal of applied polymer science, 2008. **108**(3): p. 1501-1505.
190. Saito, Y., H. Ogura, and Y. Otsubo, *Rheological behavior of silica suspensions in aqueous solutions of associating polymer.* Colloid and polymer science, 2008. **286**(13): p. 1537.
191. Bhardwaj, P., et al., *Nanosize polyacrylamide/SiO2 composites by inverse microemulsion polymerization.* International Journal of Polymeric Materials, 2008. **57**(4): p. 404-416.
192. Giraldo, L.J., et al., *The effects of SiO2 nanoparticles on the thermal stability and rheological behavior of hydrolyzed polyacrylamide based polymeric solutions.* Journal of Petroleum Science and Engineering, 2017. **159**: p. 841-852.
193. Maghzi, A., et al., *An experimental investigation of silica nanoparticles effect on the rheological behavior of polyacrylamide solution to enhance heavy oil recovery.* Petroleum Science and Technology, 2013. **31**(5): p. 500-508.
194. Zeyghami, M., R. Kharrat, and M. Ghazanfari, *Investigation of the Applicability of Nano Silica Particles as a Thickening Additive for Polymer Solutions Applied in EOR Processes.* Energy Sources, Part A: Recovery, Utilization, and Environmental Effects, 2014. **36**(12): p. 1315-1324.
195. Minagawa, N. and J.L. White, *The influence of titanium dioxide on the rheological and extrusion properties of polymer melts.* Journal of Applied Polymer Science, 1976. **20**(2): p. 501-523.
196. Zhang, L., T. Tao, and C. Li, *Formation of polymer/carbon nanotubes nano-hybrid shish–kebab via non-isothermal crystallization.* Polymer, 2009. **50**(15): p. 3835-3840.
197. Nezhad, S.S.K. and G. Cheraghian, *Mechanisms behind injecting the combination of nano-clay particles and polymer solution for enhanced oil recovery.* Applied Nanoscience, 2016. **6**(6): p. 923-931.
198. Chen, G., et al., *An Attenuated Total Reflection FT‐IR Spectroscopic Study of Polyamide 6/Clay Nanocomposite Fibers.* Macromolecular rapid communications, 2004. **25**(11): p. 1121-1124.
199. Tjong, S.C., *Structural and mechanical properties of polymer nanocomposites.* Materials Science and Engineering: R: Reports, 2006. **53**(3): p. 73-197.
200. Nourafkan, E., et al., *Synthesis of stable iron oxide nanoparticle dispersions in high ionic media.* Journal of Industrial and Engineering Chemistry, 2017. **50**: p. 57-71.
201. Fu, P., et al., *Preparation, stability and rheology of polyacrylamide/pristine layered double hydroxide nanocomposites.* Journal of Materials Chemistry, 2010. **20**(19): p. 3869-3876.
202. Hu, Z. and G. Chen, *Novel nanocomposite hydrogels consisting of layered double hydroxide with ultrahigh tensibility and hierarchical porous structure at low inorganic content.* Advanced Materials, 2014. **26**(34): p. 5950-5956.
203. Kmetz, A.A., et al., *Improved Mobility of Magnetite Nanoparticles at High Salinity with Polymers and Surfactants.* Energy & Fuels, 2016. **30**(3): p. 1915-1926.
204. Mackay, M.E., et al., *General strategies for nanoparticle dispersion.* Science, 2006. **311**(5768): p. 1740-1743.
205. Tuteja, A., et al., *Effect of ideal, organic nanoparticles on the flow properties of linear polymers: non-Einstein-like behavior.* Macromolecules, 2005. **38**(19): p. 8000-8011.
206. Tuteja, A., P.M. Duxbury, and M.E. Mackay, *Multifunctional nanocomposites with reduced viscosity.* Macromolecules, 2007. **40**(26): p. 9427-9434.
207. Schmidt, R.G., et al., *A critical size ratio for viscosity reduction in poly (dimethylsiloxane)–polysilicate nanocomposites.* Macromolecules, 2010. **43**(23): p. 10143-10151.

208. Gordon, G.V., et al., *Impact of Polymer Molecular Weight on the Dynamics of Poly (dimethylsiloxane)−Polysilicate Nanocomposites.* Macromolecules, 2010. **43**(23): p. 10132-10142.
209. Einstein, A., *On the motion of small particles suspended in liquids at rest required by the molecular-kinetic theory of heat.* Annalen der physik, 1905. **17**: p. 549-560.
210. Kropka, J.M., et al., *Origin of dynamical properties in PMMA−C60 nanocomposites.* Macromolecules, 2007. **40**(15): p. 5424-5432.
211. Mu, M., et al., *Polymer tracer diffusion exhibits a minimum in nanocomposites containing spherical nanoparticles.* Macromolecules, 2010. **44**(2): p. 191-193.
212. de Luzuriaga, A., *Key role of entropy in nanoparticle dispersion: polystyrene-nanoparticle/linear-polystyrene nanocomposites as a model system.* Physical Chemistry Chemical Physics, 2008. **10**(5): p. 650-651.
213. Li, Y., M. Kröger, and W.K. Liu, *Nanoparticle effect on the dynamics of polymer chains and their entanglement network.* Physical review letters, 2012. **109**(11): p. 118001.
214. Kalathi, J.T., G.S. Grest, and S.K. Kumar, *Universal viscosity behavior of polymer nanocomposites.* Physical review letters, 2012. **109**(19): p. 198301.
215. Kim, D., et al., *Polymer nanocomposites: polymer and particle dynamics.* Soft Matter, 2012. **8**(42): p. 10813-10818.
216. Cho, J. and D. Paul, *Nylon 6 nanocomposites by melt compounding.* Polymer, 2001. **42**(3): p. 1083-1094.
217. Schulze, D., et al., *Rheological evidence of modifications of polypropylene by β-irradiation.* Rheologica acta, 2003. **42**(3): p. 251-258.
218. Jain, S., et al., *Strong decrease in viscosity of nanoparticle-filled polymer melts through selective adsorption.* Soft Matter, 2008. **4**(9): p. 1848-1854.
219. Mackay, M.E., et al., *Nanoscale effects leading to non-Einstein-like decrease in viscosity.* Nature materials, 2003. **2**(11): p. 762.
220. Haruna, M.A., et al., *Improved rheology and high‐temperature stability of hydrolyzed polyacrylamide using graphene oxide nanosheet.* Journal of Applied Polymer Science, 2019: p. 47582.
221. Haruna, M.A., et al., *Improved Polymer Flooding in Harsh Environment by Free-Radical Polymerization and the Use of Nanomaterials.* Energy & Fuels, 2019.
222. Kadhum, M.J., et al., *Polymer-Stabilized Multi-Walled Carbon Nanotube Dispersions in High-Salinity Brines.* Energy & Fuels, 2017. **31**(5): p. 5024-5030.
223. Abduo, M., et al., *Comparative study of using Water-Based mud containing Multiwall Carbon Nanotubes versus Oil-Based mud in HPHT fields.* Egyptian Journal of Petroleum, 2016. **25**(4): p. 459-464.
224. Arake, T., et al., *Dispersion of multi-walled carbon nanotube using soluble polysilsesquioxane containing alkylammonium side chains and triiodide counterions.* Polymer, 2013. **54**(21): p. 5643-5647.
225. Xu, L., et al., *Noncovalent solubilization of multi-walled carbon nanotubes in common low-polarity organic solvents with branched Pd–diimine polyethylenes: Effects of polymer chain topology, molecular weight and terminal pyrene group.* Polymer, 2014. **55**(14): p. 3120-3129.
226. Han, B., et al., *Transport of multi-walled carbon nanotubes stabilized by carboxymethyl cellulose and starch in saturated porous media: Influences of electrolyte, clay and humic acid.* Science of the Total Environment, 2017. **599**: p. 188-197.
227. Sakellariou, G., D. Priftis, and D. Baskaran, *Surface-initiated polymerization from carbon nanotubes: strategies and perspectives.* Chemical Society Reviews, 2013. **42**(2): p. 677-704.
228. Hwang, C.-C., et al., *Highly stable carbon nanoparticles designed for downhole hydrocarbon detection.* Energy & Environmental Science, 2012. **5**(8): p. 8304-8309.

229. Vasantha, V.A., et al., *Water swelling, brine soluble imidazole based zwitterionic polymers–synthesis and study of reversible UCST behaviour and gel–sol transitions.* Chemical communications, 2014. **50**(1): p. 46-48.
230. Bagaria, H.G., et al., *Iron oxide nanoparticles grafted with sulfonated copolymers are stable in concentrated brine at elevated temperatures and weakly adsorb on silica.* ACS applied materials & interfaces, 2013. **5**(8): p. 3329-3339.
231. Portehault, D., et al., *Hybrid thickeners in aqueous media.* Colloids and Surfaces A: Physicochemical and Engineering Aspects, 2006. **278**(1-3): p. 26-32.
232. Petit, L., et al., *Responsive hybrid self-assemblies in aqueous media.* Langmuir, 2007. **23**(1): p. 147-158.
233. LeBaron, P.C., Z. Wang, and T.J. Pinnavaia, *Polymer-layered silicate nanocomposites: an overview.* Applied clay science, 1999. **15**(1-2): p. 11-29.
234. Oberdisse, J., *Aggregation of colloidal nanoparticles in polymer matrices.* Soft matter, 2006. **2**(1): p. 29-36.
235. Wang, X., et al., *Facile surface modification of silica nanoparticles with a combination of noncovalent and covalent methods for composites application.* Composites Science and Technology, 2014. **104**: p. 1-8.
236. Graham, T., *XIV. On the properties of silicic acid and other analogous colloidal substances.* Proceedings of the Royal Society of London, 1864. **13**: p. 335-341.
237. Aalaie, J., *Rheological behavior of polyacrylamide/laponite nanoparticle suspensions in electrolyte media.* Journal of Macromolecular Science, Part B, 2012. **51**(6): p. 1139-1147.
238. Rahman, I.A. and V. Padavettan, *Synthesis of silica nanoparticles by sol-gel: size-dependent properties, surface modification, and applications in silica-polymer nanocomposites—a review.* Journal of Nanomaterials, 2012. **2012**: p. 8.
239. Lerf, A., et al., *13C and 1H MAS NMR studies of graphite oxide and its chemically modified derivatives.* Solid State Ionics, 1997. **101**: p. 857-862.
240. Li, W., et al., *Simultaneous surface functionalization and reduction of graphene oxide with octadecylamine for electrically conductive polystyrene composites.* Carbon, 2011. **49**(14): p. 4724-4730.
241. Zheng, D., et al., *In situ thermal reduction of graphene oxide for high electrical conductivity and low percolation threshold in polyamide 6 nanocomposites.* Composites Science and Technology, 2012. **72**(2): p. 284-289.
242. Liu, R., et al., *Tough and highly stretchable graphene oxide/polyacrylamide nanocomposite hydrogels.* Journal of Materials Chemistry, 2012. **22**(28): p. 14160-14167.
243. Shen, J., et al., *Study on graphene-oxide-based polyacrylamide composite hydrogels.* Composites Part A: Applied Science and Manufacturing, 2012. **43**(9): p. 1476-1481.
244. Bai, H., et al., *Graphene oxide/conducting polymer composite hydrogels.* Journal of Materials Chemistry, 2011. **21**(46): p. 18653-18658.
245. Potts, J.R., et al., *Graphene-based polymer nanocomposites.* Polymer, 2011. **52**(1): p. 5-25.
246. Fan, J., et al., *Glycidyl methacrylate-modified gum arabic mediated graphene exfoliation and its use for enhancing mechanical performance of hydrogel.* Polymer, 2013. **54**(15): p. 3921-3930.
247. Nguyen, B.D., et al., *The impact of graphene oxide particles on viscosity stabilization for diluted polymer solutions using in enhanced oil recovery at HTHP offshore reservoirs.* Advances in Natural Sciences: Nanoscience and Nanotechnology, 2014. **6**(1): p. 015012.
248. Rodewald, P.G., *Oil recovery by waterflooding employing graphite oxide for mobility control*. 1976, Google Patents.
249. Stankovich, S., et al., *Graphene-based composite materials.* nature, 2006. **442**(7100): p. 282.
250. Ramanathan, T., et al., *Functionalized graphene sheets for polymer nanocomposites.* Nature nanotechnology, 2008. **3**(6): p. 327.

251. Reimer, L., *Scanning electron microscopy: physics of image formation and microanalysis*. Vol. 45. 2013: Springer.
252. Reimer, L., *Transmission electron microscopy: physics of image formation and microanalysis*. Vol. 36. 2013: Springer.
253. Gabbott, P., *Principles and applications of thermal analysis*. 2008: John Wiley & Sons.
254. Gazulla, M.F., et al., *Determination of carbon, hydrogen, nitrogen and sulfur in geological materials using elemental analysers.* Geostandards and geoanalytical research, 2012. **36**(2): p. 201-217.
255. Barr, T.L., *Modern ESCAThe Principles and Practice of X-Ray Photoelectron Spectroscopy*. 1994: CRC press.
256. Hebishy, E., et al., *Physical and oxidative stability of whey protein oil-in-water emulsions produced by conventional and ultra high-pressure homogenization: Effects of pressure and protein concentration on emulsion characteristics.* Innovative Food Science & Emerging Technologies, 2015. **32**: p. 79-90.
257. Doyle, W.M., *Principles and applications of Fourier transform infrared (FTIR) process analysis.* Process Control Qual, 1992. **2**(1): p. 11-41.
258. Lahaye, L. and G. Prado, *Fundamentals of the physical-chemistry of pulverized coal combustion*. Vol. 137. 2012: Springer Science & Business Media.
259. Hummers Jr, W.S. and R.E. Offeman, *Preparation of graphitic oxide.* Journal of the american chemical society, 1958. **80**(6): p. 1339-1339.
260. Gao, H., D. Wen, and G.B. Sukhorukov, *Composite silica nanoparticle/polyelectrolyte microcapsules with reduced permeability and enhanced ultrasound sensitivity.* Journal of Materials Chemistry B, 2015. **3**(9): p. 1888-1897.
261. Gao, H., et al., *In Situ Synthesis of Fluorescent Carbon Dots/Polyelectrolyte Nanocomposite Microcapsules with Reduced Permeability and Ultrasound Sensitivity.* ACS nano, 2016. **10**(10): p. 9608-9615.
262. Shen, C., et al., *Kinetics of coupled primary-and secondary-minimum deposition of colloids under unfavorable chemical conditions.* Environmental science & technology, 2007. **41**(20): p. 6976-6982.
263. Wu, J., et al., *Solvothermal synthesis and characterization of sandwich-like graphene/ZnO nanocomposites.* Applied Surface Science, 2010. **256**(9): p. 2826-2830.
264. Cai, D. and M. Song, *Preparation of fully exfoliated graphite oxide nanoplatelets in organic solvents.* Journal of Materials Chemistry, 2007. **17**(35): p. 3678-3680.
265. Srivastava, S., et al., *Faster response of NO2 sensing in graphene–WO3 nanocomposites.* Nanotechnology, 2012. **23**(20): p. 205501.
266. Wang, G., et al., *Facile Synthesis and Characterization of Graphene Nanosheets.* The Journal of Physical Chemistry C, 2008. **112**(22): p. 8192-8195.
267. Yi, M., et al., *Achieving concentrated graphene dispersions in water/acetone mixtures by the strategy of tailoring Hansen solubility parameters.* Journal of Physics D: Applied Physics, 2012. **46**(2): p. 025301.
268. Guerrero-Contreras, J. and F. Caballero-Briones, *Graphene oxide powders with different oxidation degree, prepared by synthesis variations of the Hummers method.* Materials Chemistry and Physics, 2015. **153**: p. 209-220.
269. An, Y.-X., et al., *The assembly of a composite based on nano-sheet graphene oxide and montmorillonite.* Petroleum Science: p. 1-9.
270. Ni, Y., et al., *Preparation, characterization, and optical, electrochemical property research of CdS/PAM nanocomposites.* The Journal of Physical Chemistry B, 2006. **110**(35): p. 17347-17352.
271. Cheng, Q.-Y., et al., *Supramolecular self-assembly induced graphene oxide based hydrogels and organogels.* Langmuir, 2012. **28**(5): p. 3005-3010.

272. Wang, X., D. Hu, and J. Yang, *Synthesis of PAM/TiO2 composite microspheres with hierarchical surface morphologies.* Chemistry of materials, 2007. **19**(10): p. 2610-2621.
273. Gao, H., et al., *Bifunctional ultraviolet/ultrasound responsive composite TiO 2/polyelectrolyte microcapsules.* Nanoscale, 2016. **8**(9): p. 5170-5180.
274. Kavitha, T., S.I.H. Abdi, and S.-Y. Park, *pH-sensitive nanocargo based on smart polymer functionalized graphene oxide for site-specific drug delivery.* Physical Chemistry Chemical Physics, 2013. **15**(14): p. 5176-5185.
275. Kejun, Y. and Z. Guowei, *Synthesis and rheological properties in aqueous solution of poly (acrylamide‐co‐sodium allylsulfonate).* Journal of applied polymer science, 1992. **44**(1): p. 1-7.
276. Chen, W., et al., *Fabricating a flocculant with controllable cationic microblock structure: characterization and sludge conditioning behavior evaluation.* Industrial & Engineering Chemistry Research, 2016. **55**(10): p. 2892-2902.
277. Phuoc, T.X., M. Massoudi, and R.-H. Chen, *Viscosity and thermal conductivity of nanofluids containing multi-walled carbon nanotubes stabilized by chitosan.* International Journal of Thermal Sciences, 2011. **50**(1): p. 12-18.
278. Teng, T.-P., L. Lin, and C.-C. Yu, *Preparation and characterization of carbon nanofluids by using a revised water-assisted synthesis method.* Journal of Nanomaterials, 2013. **2013**: p. 133.
279. Li, X., D. Zhu, and X. Wang, *Evaluation on dispersion behavior of the aqueous copper nano-suspensions.* Journal of colloid and interface science, 2007. **310**(2): p. 456-463.
280. Chen, Y., et al., *Mechanically strong and pH-responsive carboxymethyl chitosan/graphene oxide/polyacrylamide nanocomposite hydrogels with fast recoverability.* Journal of Biomaterials Science, Polymer Edition, 2017. **28**(16): p. 1899-1917.
281. Chen, J., et al., *Synthesis of silica-based carbon dot/nanocrystal hybrids toward white LEDs.* Journal of materials science, 2014. **49**(21): p. 7391-7398.
282. Vázquez-Nakagawa, M., et al., *Chirality transfer from graphene quantum dots.* Chemical Communications, 2016. **52**(4): p. 665-668.
283. Gaabour, L., *Spectroscopic and thermal analysis of polyacrylamide/chitosan (PAM/CS) blend loaded by gold nanoparticles.* Results in physics, 2017. **7**: p. 2153-2158.
284. Al-Sabagh, A., et al., *Synthesis and characterization of high molecular weight hydrophobically modified polyacrylamide nanolatexes using novel nonionic polymerizable surfactants.* Egyptian Journal of Petroleum, 2013. **22**(4): p. 531-538.
285. Zhu, D., et al., *Dispersion behavior and thermal conductivity characteristics of Al 2 O 3–H 2 O nanofluids.* Current Applied Physics, 2009. **9**(1): p. 131-139.
286. Mahdavian, A.R., M. Abdollahi, and H.R. Bijanzadeh, *Kinetic study of radical polymerization. III. Solution polymerization of acrylamide by 1H‐NMR.* Journal of applied polymer science, 2004. **93**(5): p. 2007-2013.
287. Durmaz, S. and O. Okay, *Acrylamide/2-acrylamido-2-methylpropane sulfonic acid sodium salt-based hydrogels: synthesis and characterization.* Polymer, 2000. **41**(10): p. 3693-3704.
288. Rosa, F., J. Bordado, and M. Casquilho, *Hydrosoluble copolymers of acrylamide‐(2‐acrylamido‐2‐methylpropanesulfonic acid). Synthesis and characterization by spectroscopy and viscometry.* Journal of applied polymer science, 2003. **87**(2): p. 192-198.
289. Liao, Y., et al., *UV-initiated polymerization of hydrophobically associating cationic polyacrylamide modified by a surface-active monomer: a comparative study of synthesis, characterization, and sludge dewatering performance.* Industrial & Engineering Chemistry Research, 2014. **53**(27): p. 11193-11203.
290. Li, X., et al., *Optimized preparation of micro-block CPAM by response surface methodology and evaluation of dewatering performance.* RSC Advances, 2017. **7**(1): p. 208-217.
291. Sahoo, N.G., et al., *Polymer nanocomposites based on functionalized carbon nanotubes.* Progress in polymer science, 2010. **35**(7): p. 837-867.

292. Bilalis, P., et al., *Non-covalent functionalization of carbon nanotubes with polymers.* Rsc Advances, 2014. **4**(6): p. 2911-2934.
293. Fujigaya, T. and N. Nakashima, *Non-covalent polymer wrapping of carbon nanotubes and the role of wrapped polymers as functional dispersants.* Science and technology of advanced materials, 2015. **16**(2): p. 024802.
294. Pramanik, C., et al., *Carbon Nanotube Dispersion in Solvents and Polymer Solutions: Mechanisms, Assembly, and Preferences.* ACS nano, 2017. **11**(12): p. 12805-12816.
295. Noguchi, Y., et al., *Single-walled carbon nanotubes/DNA hybrids in water are highly stable.* Chemical Physics Letters, 2008. **455**(4-6): p. 249-251.
296. Ranka, M., P. Brown, and T.A. Hatton, *Responsive stabilization of nanoparticles for extreme salinity and high-temperature reservoir applications.* ACS applied materials & interfaces, 2015. **7**(35): p. 19651-19658.
297. Nativ-Roth, E., et al., *Physical adsorption of block copolymers to SWNT and MWNT: a nonwrapping mechanism.* Macromolecules, 2007. **40**(10): p. 3676-3685.
298. Yang, M., V. Koutsos, and M. Zaiser, *Interactions between polymers and carbon nanotubes: a molecular dynamics study.* The Journal of Physical Chemistry B, 2005. **109**(20): p. 10009-10014.
299. Ansari, R., S. Ajori, and S. Rouhi, *Structural and elastic properties and stability characteristics of oxygenated carbon nanotubes under physical adsorption of polymers.* Applied Surface Science, 2015. **332**: p. 640-647.
300. Bagaria, H.G., et al., *Stabilization of iron oxide nanoparticles in high sodium and calcium brine at high temperatures with adsorbed sulfonated copolymers.* Langmuir, 2013. **29**(10): p. 3195-3206.
301. McCormick, C.L. and D. Elliott, *Water-soluble copolymers. 14. Potentiometric and turbidimetric studies of water-soluble copolymers of acrylamide: comparison of carboxylated and sulfonated copolymers.* Macromolecules, 1986. **19**(3): p. 542-547.
302. Lowe, A.B. and C.L. McCormick, *Synthesis and solution properties of zwitterionic polymers.* Chemical reviews, 2002. **102**(11): p. 4177-4190.
303. Zuniga, C.A., et al., *Long-Term High-Temperature Stability of Functionalized Graphene Oxide Nanoplatelets in Arab-D and API Brine.* ACS applied materials & interfaces, 2016. **8**(3): p. 1780-1785.
304. Israelachvili, J.N., *Intermolecular and surface forces*. 2011: Academic press.
305. Quintana, R., et al., *Sulfobetaine-based polymer brushes in marine environment: Is there an effect of the polymerizable group on the antifouling performance?* Colloids and surfaces B: Biointerfaces, 2014. **120**: p. 118-124.
306. Wever, D., F. Picchioni, and A. Broekhuis, *Polymers for enhanced oil recovery: a paradigm for structure–property relationship in aqueous solution.* Progress in Polymer Science, 2011. **36**(11): p. 1558-1628.
307. Compton, O.C. and S.T. Nguyen, *Graphene oxide, highly reduced graphene oxide, and graphene: versatile building blocks for carbon‐based materials.* small, 2010. **6**(6): p. 711-723.
308. Dreyer, D.R., A.D. Todd, and C.W. Bielawski, *Harnessing the chemistry of graphene oxide.* Chemical Society Reviews, 2014. **43**(15): p. 5288-5301.
309. Wang, H., et al., *Graphene-wrapped sulfur particles as a rechargeable lithium–sulfur battery cathode material with high capacity and cycling stability.* Nano letters, 2011. **11**(7): p. 2644-2647.
310. Sreejith, S., X. Ma, and Y. Zhao, *Graphene oxide wrapping on squaraine-loaded mesoporous silica nanoparticles for bioimaging.* Journal of the American Chemical Society, 2012. **134**(42): p. 17346-17349.
311. Ma, X., et al., *Graphene oxide wrapped gold nanoparticles for intracellular Raman imaging and drug delivery.* Journal of Materials Chemistry B, 2013. **1**(47): p. 6495-6500.

312. Nguyen, K.T. and Y. Zhao, *Integrated graphene/nanoparticle hybrids for biological and electronic applications.* Nanoscale, 2014. **6**(12): p. 6245-6266.
313. Xu, L., et al., *Synthesis and thermal degradation property study of N-vinylpyrrolidone and acrylamide copolymer.* RSC Advances, 2014. **4**(63): p. 33269-33278.
314. Haruna, M.A., et al., *Influence of carbon quantum dots on the viscosity reduction of polyacrylamide solution.* Fuel, 2019. **248**: p. 205-214.
315. Avşar, A., et al., *A novel catalyst system for the synthesis of N, N′-Methylenebisacrylamide from acrylamide.* Designed monomers and polymers, 2017. **20**(1): p. 434-440.
316. Cao, J., et al., *Application of Amino-Functionalized Nanosilica in Improving the Thermal Stability of Acrylamide-Based Polymer for Enhanced Oil Recovery.* Energy & fuels, 2017. **32**(1): p. 246-254.
317. Lerf, A., et al., *Structure of graphite oxide revisited.* The Journal of Physical Chemistry B, 1998. **102**(23): p. 4477-4482.
318. Szabó, T., et al., *Evolution of surface functional groups in a series of progressively oxidized graphite oxides.* Chemistry of materials, 2006. **18**(11): p. 2740-2749.
319. Li, D., et al., *Processable aqueous dispersions of graphene nanosheets.* Nature nanotechnology, 2008. **3**(2): p. 101.
320. Walter, J., et al., *New possibilities of accurate particle characterisation by applying direct boundary models to analytical centrifugation.* Nanoscale, 2015. **7**(15): p. 6574-6587.
321. Chiu, H.-T., et al., *Using analytical centrifugation to characterize the dispersibility and particle size distributions of organic/inorganic composite coatings.* Journal of Polymer Research, 2011. **18**(6): p. 1587-1596.
322. Hondow, N., et al., *Quantitative characterization of nanoparticle agglomeration within biological media.* Journal of Nanoparticle Research, 2012. **14**(7): p. 977.
323. Simon, A., et al., *Study of two grafting methods for obtaining a 3-aminopropyltriethoxysilane monolayer on silica surface.* Journal of colloid and interface science, 2002. **251**(2): p. 278-283.
324. Al-Oweini, R. and H. El-Rassy, *Synthesis and characterization by FTIR spectroscopy of silica aerogels prepared using several Si (OR) 4 and R′′′ Si (OR′) 3 precursors.* Journal of Molecular Structure, 2009. **919**(1-3): p. 140-145.
325. Zhang, H., et al., *In situ synthesis of poly (methyl methacrylate)/SiO 2 hybrid nanocomposites via Grafting Onto strategy based on UV irradiation in the presence of iron aqueous solution.* Journal of Nanomaterials, 2012. **2012**: p. 3.
326. Lin, B. and S. Zhou, *Poly (ethylene glycol)-grafted silica nanoparticles for highly hydrophilic acrylic-based polyurethane coatings.* Progress in Organic Coatings, 2017. **106**: p. 145-154.
327. Ranjan, R. and W.J. Brittain, *Combination of living radical polymerization and click chemistry for surface modification.* Macromolecules, 2007. **40**(17): p. 6217-6223.
328. Bergström, L., C.H. Schilling, and I.A. Aksay, *Consolidation behavior of flocculated alumina suspensions.* Journal of the American Ceramic Society, 1992. **75**(12): p. 3305-3314.
329. Lange, F. and K. Miller, *PRESSURE FILTRATION: CONSOLIDATION KINETICS AND MECHANICS.* AM. CERAM. SOC. BULL. Am. Ceram. Soc. Bull., 1987. **66**(10): p. 1498.
330. Alhreez, M. and D. Wen, *Controlled releases of asphaltene inhibitors by nanoemulsions.* Fuel, 2018. **234**: p. 538-548.
331. Dong, A., et al., *Synthesis of N-halamine-functionalized silica–polymer core–shell nanoparticles and their enhanced antibacterial activity.* Nanotechnology, 2011. **22**(29): p. 295602.
332. Gao, Y., Y. Hu, and K. Yao, *Surface molecularly imprinted polymers for solid-phase extraction of (–)-epigallocatechin gallate from toothpaste.* Frontiers of Chemical Science and Engineering, 2015. **9**(4): p. 467-478.
333. Albonico, P. and T.P. Lockhart, *pH effects on the solubility of polyacrylamides in hard brines.* Journal of applied polymer science, 1995. **55**(1): p. 69-73.

334. Muller, G., J. Fenyo, and E. Selegny, *High molecular weight hydrolyzed polyacrylamides. III. Effect of temperature on chemical stability.* Journal of Applied Polymer Science, 1980. **25**(4): p. 627-633.
335. Al-Sabagh, A., et al., *Solution properties of hydrophobically modified polyacrylamides and their potential use for polymer flooding application.* Egyptian Journal of Petroleum, 2016. **25**(4): p. 433-444.
336. Yeo, S.-D., I.-S. Kang, and E. Kiran, *Critical polymer concentrations of polyethylene solutions in pentane.* Journal of Chemical & Engineering Data, 2002. **47**(3): p. 571-574.
337. Grassl, B., et al., *Poly (ethylene oxide) - and poly (acrylamide) - based water - soluble associative polymers: synthesis, characterisation, properties in solution.* Polymer international, 2006. **55**(10): p. 1169-1176.
338. Zhao, X., et al., *Enhanced mechanical properties of graphene-based poly (vinyl alcohol) composites.* Macromolecules, 2010. **43**(5): p. 2357-2363.
339. Zhang, H., D. Zhai, and Y. He, *Graphene oxide/polyacrylamide/carboxymethyl cellulose sodium nanocomposite hydrogel with enhanced mechanical strength: preparation, characterization and the swelling behavior.* RSC Advances, 2014. **4**(84): p. 44600-44609.
340. Feng, Y., et al., *Hydrophobically associating polyacrylamides and their partially hydrolyzed derivatives prepared by post-modification. 2. Properties of non-hydrolyzed polymers in pure water and brine.* Polymer, 2005. **46**(22): p. 9283-9295.
341. Levitt, D. and G.A. Pope. *Selection and screening of polymers for enhanced-oil recovery*. in *SPE Symposium on Improved Oil Recovery*. 2008. Society of Petroleum Engineers.
342. Mitchell, J., et al., *Viscoelastic polymer flows and elastic turbulence in three-dimensional porous structures.* Soft matter, 2016. **12**(2): p. 460-468.
343. Wei, B., *Flow characteristics of three enhanced oil recovery polymers in porous media.* Journal of Applied Polymer Science, 2015. **132**(10).
344. ZHANG, L.-j. and X.-a. Yue, *Mechanism for viscoelastic polymer solution percolating through porous media.* Journal of Hydrodynamics, Ser. B, 2007. **19**(2): p. 241-248.
345. Hu, Z. and G. Chen, *Aqueous dispersions of layered double hydroxide/polyacrylamide nanocomposites: preparation and rheology.* Journal of Materials Chemistry A, 2014. **2**(33): p. 13593-13601.
346. Fan, J., et al., *Mechanically strong graphene oxide/sodium alginate/polyacrylamide nanocomposite hydrogel with improved dye adsorption capacity.* Journal of Materials Chemistry A, 2013. **1**(25): p. 7433-7443.
347. Yang, Y., S. Song, and Z. Zhao, *Graphene oxide (GO)/polyacrylamide (PAM) composite hydrogels as efficient cationic dye adsorbents.* Colloids and Surfaces A: Physicochemical and Engineering Aspects, 2017. **513**: p. 315-324.
348. Imperiali, L., et al., *A simple route towards graphene oxide frameworks.* Materials Horizons, 2014. **1**(1): p. 139-145.
349. Song, Y., C. Xu, and Q. Zheng, *Styrene–butadiene–styrene copolymer compatibilized carbon black/polypropylene/polystyrene composites with tunable morphology, electrical conduction and rheological stabilities.* Soft Matter, 2014. **10**(15): p. 2685-2692.
350. Bai, L., et al., *Localizing graphene at the interface of cocontinuous polymer blends: Morphology, rheology, and conductivity of cocontinuous conductive polymer composites.* Journal of Rheology, 2017. **61**(4): p. 575-587.
351. Lepoittevin, B., et al., *Poly (ε-caprolactone)/clay nanocomposites prepared by melt intercalation: mechanical, thermal and rheological properties.* Polymer, 2002. **43**(14): p. 4017-4023.
352. Otsubo, Y. and K. Umeya, *Adsorption of polyacrylamide on silica particles and its effect on the rheological properties of suspensions.* Journal of colloid and interface science, 1983. **95**(1): p. 279-282.

353. Ikeda, S. and K. Nishinari, *"Weak Gel"-type rheological properties of aqueous dispersions of nonaggregated κ-carrageenan helices.* Journal of agricultural and food chemistry, 2001. **49**(9): p. 4436-4441.
354. Casson, N., *A new flow equation for pigment oile-suspension of the printing ink type.* Rheology of disperse systems, 1959.
355. Magami, S.M., et al., *The physical–chemical behaviour of amino cross-linkers and the effect of their chemistry on selected epoxy can coatings' hydrolysis to melamine and to formaldehyde into aqueous food simulants.* Progress in Organic Coatings, 2015. **78**: p. 325-333.
356. Einstein, A., *Zur theorie der brownschen bewegung.* Annalen der physik, 1906. **324**(2): p. 371-381.
357. Tuteja, A., et al., *Breakdown of the continuum Stokes–Einstein relation for nanoparticle diffusion.* Nano letters, 2007. **7**(5): p. 1276-1281.
358. Kim, S.H., S.H. Ahn, and T. Hirai, *Crystallization kinetics and nucleation activity of silica nanoparticle-filled poly (ethylene 2, 6-naphthalate).* Polymer, 2003. **44**(19): p. 5625-5634.
359. Henckens, A., et al., *Synthesis of 3, 4-diphenyl-substituted poly (thienylene vinylene), low-band-gap polymers via the dithiocarbamate route.* Macromolecules, 2005. **38**(1): p. 19-26.
360. Des Cloizeaux, J., *Double reptation vs. simple reptation in polymer melts.* EPL (Europhysics Letters), 1988. **5**(5): p. 437.
361. Li, H., et al., *Water‐soluble fluorescent carbon quantum dots and photocatalyst design.* Angewandte Chemie International Edition, 2010. **49**(26): p. 4430-4434.
362. Yang, W., et al., *Cationic carbon dots for modification-free detection of hyaluronidase via an electrostatic-controlled ratiometric fluorescence assay.* Analytical chemistry, 2017. **89**(16): p. 8384-8390.
363. Zhou, J., et al., *Cationic carbon quantum dots derived from alginate for gene delivery: One-step synthesis and cellular uptake.* Acta biomaterialia, 2016. **42**: p. 209-219.
364. Saito, S., *Salt effect on polymer solutions.* Journal of Polymer Science Part A‐1: Polymer Chemistry, 1969. **7**(7): p. 1789-1802.
365. Gaillard, N., D.B. Sanders, and C. Favero. *Improved oil recovery using thermally and chemically protected compositions based on co-and ter-polymers containing acrylamide*. in *SPE improved oil recovery symposium*. 2010. Society of Petroleum Engineers.
366. Caulfield, M.J., G.G. Qiao, and D.H. Solomon, *Some aspects of the properties and degradation of polyacrylamides.* Chemical reviews, 2002. **102**(9): p. 3067-3084.
367. Xin, X., et al., *Interaction between sodium oleate and partially hydrolyzed polyacrylamide: A rheological study.* Colloids and Surfaces A: Physicochemical and Engineering Aspects, 2008. **326**(1-2): p. 1-9.
368. Chen, J., et al., *Fluorescence studies on hydrophobic associations of fluorocarbon-modified poly (acrylic acid) solutions.* Macromolecules, 1999. **32**(15): p. 4861-4866.
369. Caulfield, M.J., et al., *Degradation on polyacrylamides. Part I. Linear polyacrylamide.* Polymer, 2003. **44**(5): p. 1331-1337.
370. Yasuda, K., K. Okajima, and K. Kamide, *Study on Alkaline Hydrolysis of Polyacrylamide by 13 C NMR.* Polymer journal, 1988. **20**(12): p. 1101.
371. Ma, Q., et al., *Theoretical studies of hydrolysis and stability of polyacrylamide polymers.* Polymer Degradation and Stability, 2015. **121**: p. 69-77.
372. Hirasaki, G.J., C.A. Miller, and M. Puerto. *Recent advances in surfactant EOR*. in *SPE Annual Technical Conference and Exhibition*. 2008. Society of Petroleum Engineers.
373. Pötschke, P., et al., *Rheological and dielectrical characterization of melt mixed polycarbonate-multiwalled carbon nanotube composites.* Polymer, 2004. **45**(26): p. 8863-8870.
374. Cassagnau, P., *Linear viscoelasticity and dynamics of suspensions and molten polymers filled with nanoparticles of different aspect ratios.* Polymer, 2013. **54**(18): p. 4762-4775.

375. Hu, Z., et al., *Microemulsions stabilized by in-situ synthesized nanoparticles for enhanced oil recovery.* Fuel, 2017. **210**: p. 272-281.
376. Kedar, V. and S.S. Bhagwat, *Effect of salinity on the IFT between aqueous surfactant solution and crude oil.* Petroleum Science and Technology, 2018. **36**(12): p. 835-842.
377. Bera, A., A. Mandal, and B. Guha, *Synergistic effect of surfactant and salt mixture on interfacial tension reduction between crude oil and water in enhanced oil recovery.* Journal of Chemical & Engineering Data, 2013. **59**(1): p. 89-96.
378. Nikolov, A., K. Kondiparty, and D. Wasan, *Nanoparticle self-structuring in a nanofluid film spreading on a solid surface.* Langmuir, 2010. **26**(11): p. 7665-7670.
379. Wasan, D.T. and A.D. Nikolov, *Spreading of nanofluids on solids.* Nature, 2003. **423**(6936): p. 156.
380. Tangparitkul, S., *Evaluation of effecting factors on oil recovery using the desirability function.* Journal of Petroleum Exploration and Production Technology, 2018: p. 1-10.
381. Sun, Z., T. Feng, and T.P. Russell, *Assembly of graphene oxide at water/oil interfaces: tessellated nanotiles.* Langmuir, 2013. **29**(44): p. 13407-13413.
382. Whitby, C.P., et al., *Properties of fatty amine–silica nanoparticle interfacial layers at the hexane–water interface.* The Journal of Physical Chemistry C, 2012. **116**(4): p. 3050-3058.
383. Gamot, T.D., et al., *Synthesis and stability of water-in-oil emulsion using partially reduced graphene oxide as a tailored surfactant.* Langmuir, 2017. **33**(39): p. 10311-10321.
384. Haruna, M.A. and D. Wen, *Stabilization of Polymer Nanocomposites in High-Temperature and High-Salinity Brines.* ACS omega, 2019. **4**(7): p. 11631-11641.
385. Kulicke, W.-M., et al., *Effect of molecular weight and molecular weight distribution on the rheological properties of aqueous poly (ethylene oxide) solution.* polymer bulletin, 1983. **9**(4): p. 190-197.
386. Needham, R.B. and P.H. Doe, *Polymer flooding review.* Journal of Petroleum Technology, 1987. **39**(12): p. 1,503-1,507.
387. Pu, W., et al., *Synthesis and evaluation of β-cyclodextrin-functionalized hydrophobically associating polyacrylamide.* RSC Advances, 2016. **6**(98): p. 96006-96014.
388. Ramsden, D. and K. McKay, *The degradation of polyacrylamide in aqueous solution induced by chemically generated hydroxyl radicals: Part II—Autoxidation of Fe2+.* Polymer degradation and stability, 1986. **15**(1): p. 15-31.
389. Seright, R., *Potential for polymer flooding reservoirs with viscous oils.* SPE Reservoir Evaluation & Engineering, 2010. **13**(04): p. 730-740.
390. Ali, M. and H.B. Mahmud. *The effects of concentration and salinity on polymer adsorption isotherm at sandstone rock surface*. in *IOP Conference Series: Materials Science and Engineering*. 2015. IOP Publishing.
391. Clarke, A., et al., *Mechanism of anomalously increased oil displacement with aqueous viscoelastic polymer solutions.* Soft Matter, 2015. **11**(18): p. 3536-3541.